Using a tephrostratigraphic framework to determine the past 40,000 yrs of fault rupture and paleohydrothermal activity on the east strand of the Whirinaki Fault, Ngakuru Graben, central Taupo Volcanic Zone

A thesis submitted in partial fulfilment

of the requirements for the degree

of

Masters of Science (Research) in Earth Science

at

The University of Waikato

by

Remedy Charlotte Loame

The University of Waikato
2016

THE UNIVERSITY OF
WAIKATO
Te Whare Wānanga o Waikato

Abstract

The Ngakuru Graben in the central Taupo Volcanic Zone, North Island, New Zealand, is largely thermally inactive, but several fossil geothermal systems have been mapped throughout the area parallel to the Whirinaki Fault (WF). A fossil geothermal system was identified on the northeast section of the east strand of the WF at a location on Hossack Road hereafter referred to as the Meade-Hossack site. The aim of this study was to establish a history of fault rupture and sinter development at the Meade-Hossack site, and to relate the observed faulting and paleogeothermal activity to that at other locations on the WF. The objectives were to (i) describe the stratigraphy exposed in a trench and outcrop, (ii) identify (correlate) tephras using stratigraphic principles, ferromagnesian mineralogical assemblages, and electron microprobe-determined major-element compositions of glass shards, and (iii) restore tectonic deformation at the site using tephrochronology to date the timing of fault movement and the development of sinter formation.

A paleoseismic trench was excavated across the northeast section of the east strand of the WF. The stratigraphy and deformation in the trench were logged. Samples of tephras were taken for mineral and glass shard analysis by microscope petrography and electron microprobe analysis, respectively. Eight tephras were identified, namely the Kaharoa (AD 1314 ± 12 or 636 ± 12 cal. yr. BP) (95% probability age range), Taupo (AD 232 ± 10 or 1718 ± 10 cal. yr. BP), Rotoma (9423 ± 120 cal. yr. BP), Rotorua (15635 ± 412 cal. yr. BP), Okareka (21858 ± 290 cal. yr. BP), Kawakawa (25358 ± 162 cal. yr. BP), Poihipi (28446 ± 670 cal. yr. BP), and Tahuna (c. 40 ka), as well as the Ohakuri Ignimbrite (c. 240 ka).

Five fault rupture events were identified in the trench (MH1–5). The trench logs were used to reconstruct earlier stages of the stratigraphic succession at the site prior to deformation by each rupture events. The tephra ages were used to constrain the timing of fault movement. The slip rates and the vertical displacement measurements were also calculated using tephrochronology, and correlated with trends (fast-slow-fast) for events of similar ages observed in other trenches on the WF.

Rupture event MH1 occurred between the Taupo and Kaharoa eruption episodes at a slip rate of 0.87 ± 0.37 mm/yr, MH2 between the Rotoma and Taupo eruptions at a rate of 0.11 ± 0.20 mm/yr, MH3 between the Rotorua and Rotoma eruptions at a rate of 0.20 ± 0.22 mm/yr, MH4 between the Okareka and Rotorua eruptions at a rate of 0.13 ± 0.27 mm/yr, and MH5 between the Ohakuri and Okareka eruptions at a rate of 0.53 ± 0.24 mm/yr. The recurrence interval during the last 21.8 kyrs was calculated to be 1.8–5.4 kyrs, which fits within recurrence intervals calculated for other trenches on the WF.

The rupture events at the Meade-Hossack site show evidence of stress transfer from the southeast section of the east strand as well as the northwest section of the west strand of the WF, indicating that the strands are connected at depth. Sinter deposition mirrors that on the west strand from ~40–10 ka, indicating that the paleogeothermal fields were fed by the same source at depth.Sinter deposition mirrors that on the west strand from ~40–10 ka, indicating that the paleogeothermal fields were fed by the same source at depth. Fault rupture MH3 at the Meade-Hossack site altered the local fluid flow regime, leading to the cessation of sinter development on the east strand by 9423 ± 120 cal. yr. BP.

Acknowledgements

Firstly I must express gratitude to my triumvirate of advisors at the University of Waikato, Prof. David Lowe, Dr. Adrian Pittari, and Dr. Shaun Barker, for their excellent guidance, encouragement, and editorial advice. In addition to the solid home base of support, Dr. Pilar Villamor and Dr. Andrew Rae of GNS Science granted me the opportunity to work on this fascinating investigation and gave useful feedback along the way. The financial support I gratefully received from The University of Waikato Summer Research Scholarship, University of Waikato Masters Scholarship, and the Broad Memorial Fund made life on a student budget a little less stressful.

The trenching campaign would have been incredibly difficult without permission from the landowner Colin Meade and his family, the cosy shearers' quarters provided by John and Catherine Ford, and the help and good humour of my field support crew, Gaby Gómez, Manuel Martínez Martos, and Sarah Milicich. Many thanks to Ian Nairn and Anna Eames for joining us in the trenches for a day, and to Annette Rodgers and Dean Sandwell for bringing the vibrocorer all the way out to Ngakuru.

Back in the lab, Renat Radosinsky taught me the ins and outs of sample preparation, Will Ries at GNS Science helped me get started on digitisation of trench logs, and Ian Schipper at Victoria University of Wellington sorted me out with the electron microprobe. I would also like to thank Janine Ryburn, Kirsty Vincent, Gangqing Xu, Ryan Lee, and Helen Turner for additional technical support.

I greatly appreciate the chats I had about the field area with Roger Briggs, Bob Brathwaite, and Rob Langridge, as well as the administrative support from the School of Science office, particularly Sydney Wright. Last but not least, my wonderful officemates Lizzie Cook, Hannah Julian, and Elham Yousefzadeh. It was inspiring to be working alongside strong women all throughout this process, and I'm going to miss the coffee breaks.

You all rock.

Table of contents

List of figures

Chapter 2

Chapter 3

Chapter 4

Chapter 5

Chapter 5 ctd.

Chapter 5 ctd.

Chapter 5 ctd.

Chapter 6

List of tables

Chapter 1: Introduction

1.1: Topic background and significance

Areas of high heat flow and crustal weakness on the Earth's surface often host active geothermal systems. The geothermal systems are recharged at depth by meteoric water, which travels through deep fractures caused by faulting, is heated by magma bodies, and rises in convective plumes, erupting at the surface from hydrothermal vents. The Taupo Volcanic Zone (TVZ) in the central North Island of New Zealand is one such area of high heat flow and crustal weakness, characterised by volcanism, faulting, and geothermal fields within an active extensional setting (Rowland and Sibson, 2004).

Geothermal fields in the central Taupo Volcanic Zone (TVZ) follow a northeast-trending alignment, similar to the alignment of the volcanic centres and the trend of major faults in the region. The Ngakuru Graben in the central TVZ is largely thermally inactive (Brathwaite, 2003), but hosts evidence of fossil geothermal systems along the northern parts of the east and west strands of the NE-trending NW-dipping Whirinaki Fault (Drake et al., 2014).

Siliceous sinter deposits at the Hossack Road site, on the northeast section of the east strand of the Whirinaki Fault, have previously been examined by Alder and Sharp (1988) in a technical report examining gold prospects, and by Holland (2000) in an MSc thesis. The technical report was of limited scope, with descriptions mainly focused on epithermal mineralisation resulting in gold and silver deposits. The thesis by Holland examined and described the sinters in detail, but the timing of sinter formation was poorly constrained. Holland (2000) mapped several sinter outcrops in the Ngakuru Graben and estimated a surficial area extent of 63,000 m^2 but did not provide a map of the estimated historic extent of surface or subsurface features.

This thesis project was conceived as a complement to a summer research project assessing fault segmentation of the Whirinaki Fault, one of the major faults in the Ngakuru Graben, and analysing relationships

between fault rupture events and hydrothermal activity using tephrochronology.

The proposed study will provide new information on the geological history of the Ngakuru Graben with regard to the extent and age range of paleohydrothermal activity and its relationship with fault rupture events along the Whirinaki Fault. Information about the paleoseismic activity of the study site will contribute to the National Seismic Hazard database.

1.2: Research questions

Although Holland (2000) observed that there were tephras present at the Hossack Road site, he was not able to identify them within the scope of his study. A study by Canora-Catalán et al. (2008) collected fault rupture information on the southeast section of the east strand and the northwest section of the west strand of the Whirinaki Fault, but did not trench the northeast section of the east strand. Drake et al. (2014) described and dated sinters on the west strand of the Whirinaki Fault, and attempted to relate sinter formation to local tectonism, but lacked information on the east strand parallel to their study area. The gaps in knowledge from the aforementioned studies gave rise to the following research questions to be addressed in my thesis:

- What are the stratigraphic relationships between the tephras and sinter deposits at the Hossack Road site?
- What are the distinguishing characteristics of the tephras, and can the tephras be identified or linked to known eruption events so that the associated ages can be used to date the sinters using tephrochronology?
- What is the age range and paleoenvironment of hydrothermal activity in the Hossack Road area?
- How many fault rupture events have occurred in the Hossack Road area?

- What are the ages of the fault rupture events?
- Is there evidence of a causal relationship between the fault rupture events and hydrothermal activity in the study area?
- Is there evidence of a relationship between fault rupture events in the Hossack Road area and those elsewhere on the Whirinaki Fault?
- Is there evidence of a relationship between the hydrothermal systems on the east and west strands of the Whirinaki Fault?

1.3: Research aim

The aim of the study is to establish a geological history of the Ngakuru sinter-tephra succession in relation to rupture events associated with movement along the Whirinaki Fault and the development of the paleogeothermal field.

1.4: Objectives

In order to achieve my aim, I will:

1. Document the stratigraphic succession and fault structure at the Hossack Road site.
2. Determine the mineralogy of the tephras using petrographic microscopy.
3. Examine the major and minor element geochemistry of the volcanic glass shards from the tephras.
4. Incorporate the identified tephras into a framework for reconstructing the stratigraphy with regard to timing of fault movement and paleohydrothermal deposits.

1.5: Thesis structure and chapter outline

Chapter 2 is a review of literature relevant to the regional geology including tephrostratigraphy, structural setting, and hydrothermal features around the study area at Hossack Road. In Chapter 3 I provide stratigraphic descriptions of the tephra-sinter successions in the outcrop and the paleoseismic trench at Hossack Road, including site photographs and a stratigraphic log. In Chapter 4 I present the mineralogical descriptions of the tephras based on petrographic microscopy. In Chapter 5 the results of major and minor element analysis based on electron microprobe analysis are presented. In Chapter 6 the results of the trench log restoration, slip rate calculations, and recurrence interval calculations are presented. The main conclusions of the study are presented in Chapter 7. Research methods for the fieldwork and each analytical technique are presented in each of their respective chapters. Raw data not suitable for results chapters are presented in the appendices.

Chapter 2: Geological background

2.1: Introduction

The Hossack Road area is located within the Ngakuru Graben in the central Taupo Volcanic Zone (Figures 1 and 2) where subduction-related extension during the Quaternary has contributed to a rift system comprising active volcanism, closely-spaced NE-trending normal faults, and geothermal fields (Nairn, 2002).

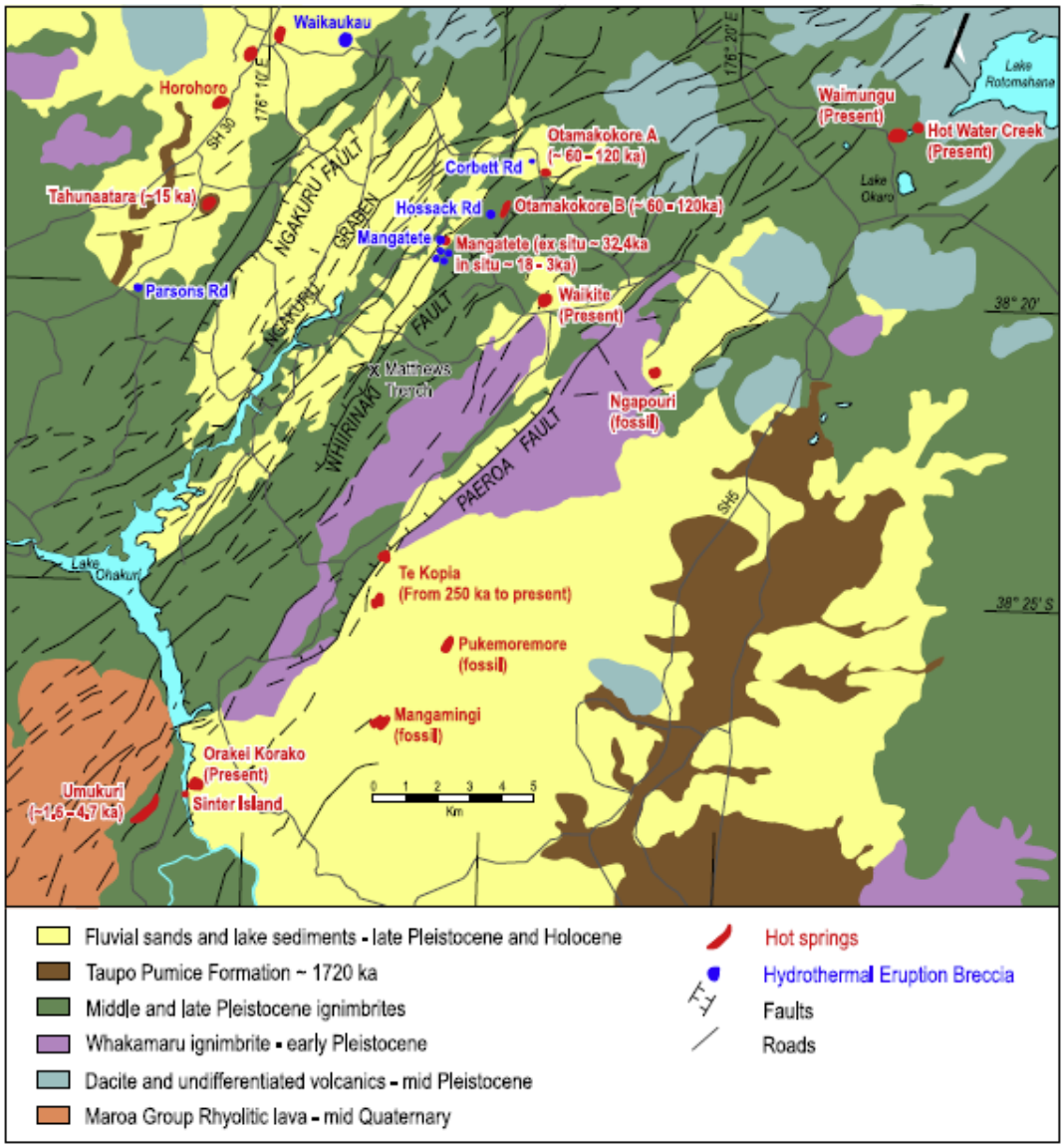

Figure 1. Composite map of the regional geology, structure, and hydrothermal features (hot springs and eruption breccia) around the Hossack Road area (Drake et al., 2014).

Sinters found close to Hossack Road, Ngakuru, contain multiple silicified tephras which remain largely unidentified and uncorrelated (Holland, 2000). Attempts have previously been made to correlate hydrothermal activity at depth or at the surface with fault ruptures, for example in Te Kopia geothermal field in New Zealand (cf. Martin, 2000) and in Dixie Valley, Nevada (Lutz et al., 2002). However, establishing the timing of sinter precipitation and fault ruptures observed within the sinters is difficult because there are few reliable methods of directly dating the sinters if no material suitable for radiocarbon (^{14}C) dating is present (assuming the deposits are within the ^{14}C age-range, $\leq$ c. 60,000 years for optimum dating material).

Tephrochronology offers a way to constrain the ages of sinters (Jones et al., 2007) and fault ruptures using stratigraphy, mineralogy, and geochemical fingerprinting techniques (Lowe, 2011). The application of tephrochronology to the sinters at Hossack Road would provide insight into the history of hydrothermal activity, faulting, and volcanism in the wider region. Gathering further geochemical and petrographic data about the tephras found in the study area could aid in establishing heterogeneities between them, particularly those from the Okataina Volcanic Centre (Smith et al., 2005; Lowe et al., 2008; Shane et al., 2008; Wilson et al., 2009).

The following literature review is a summary of the geological and structural setting of the Hossack Road site in the Ngakuru Graben.

2.2: Geological and structural setting

2.2.1: Taupo Volcanic Zone

The Taupo Volcanic Zone (TVZ; Figure 2) is a 300-km-long volcano-tectonic depression which lies above the Taupo-Hikurangi subduction system (Nairn, 2002; Leonard et al., 2010), where the Pacific plate is obliquely subducting under the Australian Plate at a rate of around 50 mm/yr (Figure 2). The subduction process is associated with rapid onshore extension, high heat flow, and active volcanism, all significant features of the TVZ (Bibby et al., 1995).

The earliest volcanism in the TVZ occurred along the eastern margin around 1.89 Ma, comprising deep andesitic lavas (Chambefort et al., 2014). Although four main magma compositions (basalt, andesite, rhyolite, and dacite) are found within the TVZ, the central TVZ volcanic centres have been largely dominated by rhyolite since around 1.6 Ma (Wilson et al., 1995, 2009; Nairn, 2002).

The central TVZ can be broadly divided into two rift basins: the Taupo Rift (also known as the Taupo Fault Belt, TFB) to the northwest, and the Taupo-Reporoa Basin to the southeast (Downs et al., 2014a). The Taupo Rift is a 20 km-wide seismically active basin that has been subsiding at a rate of 3-4 mm/yr since 61 ka (ka = x1000 years ago), driven by largely orthogonal rifting associated with subduction (Downs et al., 2014a), with the clockwise rotation of the North Island allowing the rift to open (Villamor and Berryman, 2006). The Taupo-Reporoa Basin (TRB) is located 25 km northeast of Lake Taupo and is bounded by the Kaingaroa fault scarp in the east, the Paeroa fault block in the west, and the margins of the Taupo and Okataina calderas to the south and north, respectively (Kaya et al., 2014). Most of the active geothermal fields in the TVZ are located in or near the TRB, and it is less seismically active than the Taupo Rift (Downs et al., 2014a).

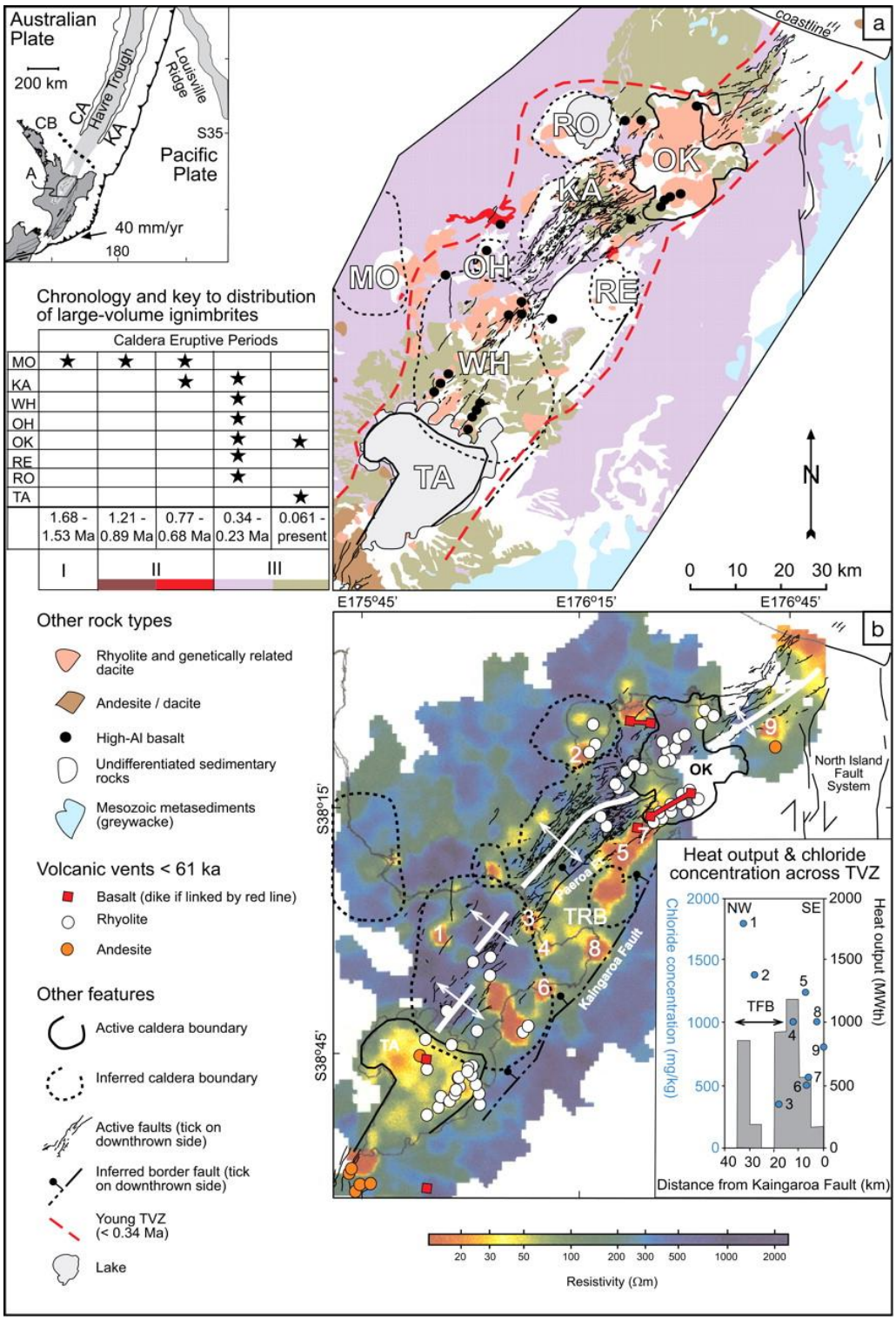

Figure 2. Geologic setting of the Taupo Volcanic Zone, with the location of the TVZ in the North Island (top left), active and inferred caldera boundaries and geology of the TVZ (a), vent locations, electrical resistivity, heat output, and chloride concentration across the TVZ (b), and active faults (a and b). The white lines with arrows indicate extension (Rowland and Simmons, 2012).

2.2.2: Geological units

Much of the Taupo Rift is covered by Ohakuri Ignimbrite (~240 ka) overlain by Huka Group sediments and tuffs, which in turn are typically overlain by the Hinuera Formation and multiple pyroclastic deposits.

A mineral report by Alder and Sharp (1988) showed eight geological units in the Hossack Road area (Figure 3). Some of the units are poorly described (Haparangi Rhyolite and Paeroa Ignimbrite), or not described at all (Ignimbrite A and Ignimbrite B), though site-specific descriptions are available for other units and thus may be useful for correlation.

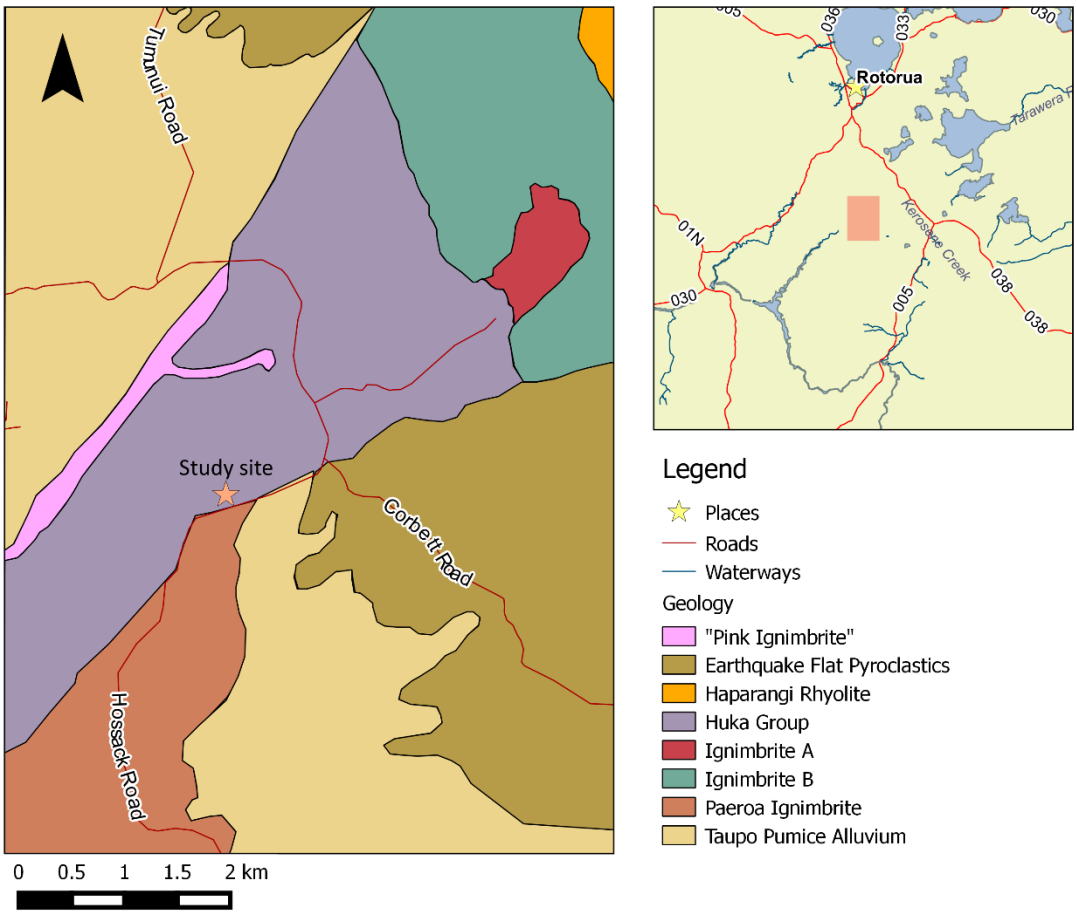

Figure 3. Main geological units of the Hossack Road area as classified by Alder and Sharp (1988) in relation to the proposed study site for this thesis.

The “Pink Ignimbrite” crops out along the scarp of the Whirinaki Fault. It has a moderately welded, crystal-rich, devitrified groundmass and is pink in colour with some orange weathered pumice clasts. It contains < 10%

phenocrysts, and lithic fragments < 5 mm in diameter. Evidence of propylitic alteration occurs in the form of fine pyrite crystals.

In outcrop southwest of the proposed study site, the Paeroa Ignimbrite is light grey, moderately welded, and crystal rich.

Along Corbett Road, the Earthquake Flat Pyroclastics crop out as weakly compacted pumiceous flow units and interbedded fall tephras.

The Kawakawa Tephra (not mapped) can also be observed along Corbett Road as a 300-mm-thick layer of pumice lapilli directly underlying alluvial deposits. However, it is possible that the unit was wrongly identified by Alder and Sharp (1988), because Kawakawa Tephra is typically more fine-grained.

The Huka Group is a thick (>130 m) sequence of interbedded volcaniclastic lacustrine and fluvial sediments and pyroclastic deposits, and can be divided broadly into upper and lower subunits. The upper subunit of the Huka Group is a lithified silty ash with some sandstone lenses. The lower subunit of the Huka Group is a coarse lithic- and crystal-rich tuff with clasts of pink-coloured ignimbrite, old ignimbrite, and rhyolite. The Huka Group has undergone supergene silicification and weak argillic alteration (Alder and Sharp, 1988).

In contrast to the work by Alder and Sharp (1988), Nairn (2002) described the Earthquake Flat Pyroclastics as crystal-rich biotite-hornblende rhyolitic pyroclastic flow and fall deposits in low-angle fans. The Huka Group are lacustrine sandstones and siltstone with minor diatomite, interbedded gravels, and primary pyroclastic deposits. The Hinuera Formation consists of coarse cross-bedded pumice and rhyolite sands and gravels deposited during the last glaciation, with the coarser fraction derived from reworked Earthquake Flat Pyroclastics and the finer fraction derived from Ohakuri Ignimbrite. The Taupo Ignimbrite Member is a white, low-density rhyolite pumice ash and lapilli valley-confined pyroclastic flow deposit which may be reworked to alluvium.

No basement units have been mapped as cropping out within the OVC, though Wilson et al. (1995) stated the upper part of the crust in the

TVZ is comprised of Mesozoic greywacke, which Seebeck (2008) suggested is incorporated by the volcanics in the Taupo and Okataina centres, possibly influencing magma composition, eruption style, and the location of volcanism.

2.2.3: Tephras

Tephras are unconsolidated deposits of pyroclastic material of any grain size, derived from explosive volcanic eruptions, and emplaced by either pyroclastic falls or density currents (Lowe, 2011; Lowe and Alloway, 2015).

Multiple tephras from both the Okataina and Taupo Volcanic Centres are anticipated to be found in the study area. Holland (2000) observed silicified tephras within sinter deposits in the area around Hossack Road, Otamakokore Stream, and Corbett Road, and tentatively estimated the age of the sinter formation to be between 260 ka and 60 ka based on the stratigraphic positions of the Ohakuri Ignimbrite and the Kawakawa/Oruanui Tephra. Holland (2000) attempted to identify the tephras by conducting X-ray fluorescence spectrometry (XRF) analyses of several bulk samples of tephra, and compared the major element data against averages for the TVZ from Ewart (1966), determining the values to be similar, though attempts to fingerprint the tephras by Zr/Y ratios did not give meaningful results.

Although some geochemical data for the bulk samples of tephras are available in the thesis by Holland (2000), the lack of accompanying information in terms of stratigraphic position of sample points, physical descriptions, or petrography, along with the narrow breadth of only six analysed samples, makes unit-to-unit comparison difficult. In addition, modern tephra fingerprinting demands analyses of major/minor and trace elements for individual glass shards or crystals using the electron microprobe (EMPA) and laser ablation inductively coupled plasma mass spectrometry (LA-ICP-MS), not bulk analyses which have limited effectiveness (e.g. Lowe, 2011; Pearce et al., 2014; Lowe and Alloway, 2015). In addition, the suggested upper constraining age of “60 ka” is

inconsistent with the putative identification of Kawakawa/Oruanui Tephra, which is dated at c. 25.4 calendar (cal) ka.

Based mainly on tephra isopach maps in Nairn (2002), and earlier mapping, the tephra deposits proposed to most likely occur at the Hossack Road site study area are listed in Table 1.

Table 1. Known tephras that could occur in the Hossack Road area, including most recently determined ages, general mineralogy, and diagnostic field characteristics.

Tephra Name	Age (cal yr BP)	Ferromagnesian mineralogy	Diagnostic characteristics	Estimated tephra thickness in field area
Taupo	1718 ± 10[2, 13]	Hypersthene ± augite (± minor hornblende)[3]	White low density rhyolitic pumice ash and lapilli[4]	
Whakatane	5526 ± 145[2]	Cummingtonite abundant, (± minor hypersthene, hornblende ± augite)[3]	Pale grey very fine ash[5]	0.4 - 0.2 m [1]
Rotoma	9423 ± 120[2]	Cummingtonite abundant[1], ± minor hypersthene, hornblende ± augite)[3]	Weathered to yellow-brown, best preserved at base with pale yellow and pale grey fine ash. ≤ 1 m thick. Overlain by brown or reddish-brown sandy paleosol[4]	0.5 - 1 m [1]
Waiohau	14009 ± 155[2]	Crystal-poor; hypersthene[1]	Coarse lower: Pink-red pumiceous & glassy ash, lapilli, blocks of hypersthene-hornblende rhyolite. Upper: ~2 m of interbedded ash and lapilli beds. Encloses fine-grained low-angle cross-bedded surge deposits[1]. Yellow-grey, grey, and light brown fine and coarse ash ≤ 1 m thick, lower third contains 6-8 cm thick bed with abundant black glass[4]	0.5 - 1 m [1]
Rotorua Tephra	15635 ± 412[2]	Hypersthene, hornblende and augite ± biotite[3]	Coarse sandy ash and sparse lapilli, overlain by yellow-brown silty paleosol[4]	0.3 - 0.5 m [1]
Rerewhakaaitu Tephra	17496 ± 462[2]	Crystal-rich with hornblende and biotite; crystal-poor with hypersthene and hornblende[1]	Grey coarse ash overlain by thick yellow-brown clayey paleosol[4]	0.2 - 0.4 m [1]

Tephra Name	Age (cal yr BP)	Ferromagnesian mineralogy	Diagnostic characteristics	Estimated tephra thickness in field area
Okareka Tephra	21858 ± 290[2]	Hornblende and biotite rhyolite, hypersthene and hornblende rhyolite[1]	Typically occurs within a loess unit; grey and brown base of coarse and fine ash grading upward into yellowish-brown fine ash[4]	0.4 - 0.5 m [1]
Te Rere Tephra	25171 ± 964[2]	Poor or absent in quartz[1]	Yellowish-brown fine ash overlying pale yellowish-brown coarse ash; white basal lapilli and ash[6]	0.5 - 1 m [1]
Kawakawa Tephra	25358 ± 162[2]	Hypersthene + hornblende ± augite[3]	White fine ash base with pale brown sand upper[6]	
Poihipi Tephra	28446 ± 670[2]	Hypersthene + hornblende ± augite[3]	Cemented blue-grey fine ash[12]	
Okaia Tephra	28621 ± 1428[2]	Hypersthene + hornblende ± augite[3]		< 0.6 m [12]
Mangaone Tephra	~33 ka[7]	Hypersthene + hornblende ± augite[3]	Contains fresh-looking hard white pumice clasts[8]	< 1 m [11]
Rotoiti Tephra /Rotoehu Ash	45.1 ± 3.3 ka[10]	Crystal-rich[1]; cummingtonite abundant, ± minor hypersthene, hornblende ± augite[3]	Compact pale yellow coarse ash base[6]	1 – 1.2 m [1]
Earthquake Flat Pyroclastics/Rifle Range Ash	45.1 ± 2.9 ka[10]	Crystal-rich, hornblende and biotite[1]		

[1]Nairn (2002), [2]Lowe et al. (2013), [3]Froggatt and Lowe (1990), [4]Villamor and Berryman (2001), [5]Vucetich and Pullar (1973), [6]Vucetich and Pullar (1969), [7]Charlier and Wilson (2010), [8]Smith et al. (2002), [9]Green et al. (2014), [10]Danišík et al. (2012), [11]Howorth (1975), [12]Vucetich and Pullar (1976), [13]Hogg et al. (2012).

2.2.4: Geothermal systems

Geothermal systems exist in areas of thin or weakened crust and high heat flow, such as the central TVZ, host to many of the active geothermal fields in New Zealand (Figure 4). The locations of the geothermal fields have been delineated by areas of low electrical resistivity because the high-temperature salt-rich hydrothermal fluids are highly conductive, and dispersed throughout a porous rock matrix (Bibby et al., 1995). Surface features of geothermal systems may include hot springs, geysers, sinter deposits, fumaroles, and thermal ground.

The geothermal fields in the TVZ are often linearly aligned, trending NE-SW like many of the faults and volcanic vents in the region. The fields tend to be located close to the margins of volcanic centres or at the tips of faults, suggesting an influence of geological boundaries or structure on the hydrology of geothermal activity, or both (Kaya et al., 2014). TVZ geothermal systems are generally spaced around 10–15 km apart and have an estimated lifespan of thermal activity between 50 and 250 kyr (Rowland and Simmons, 2012).

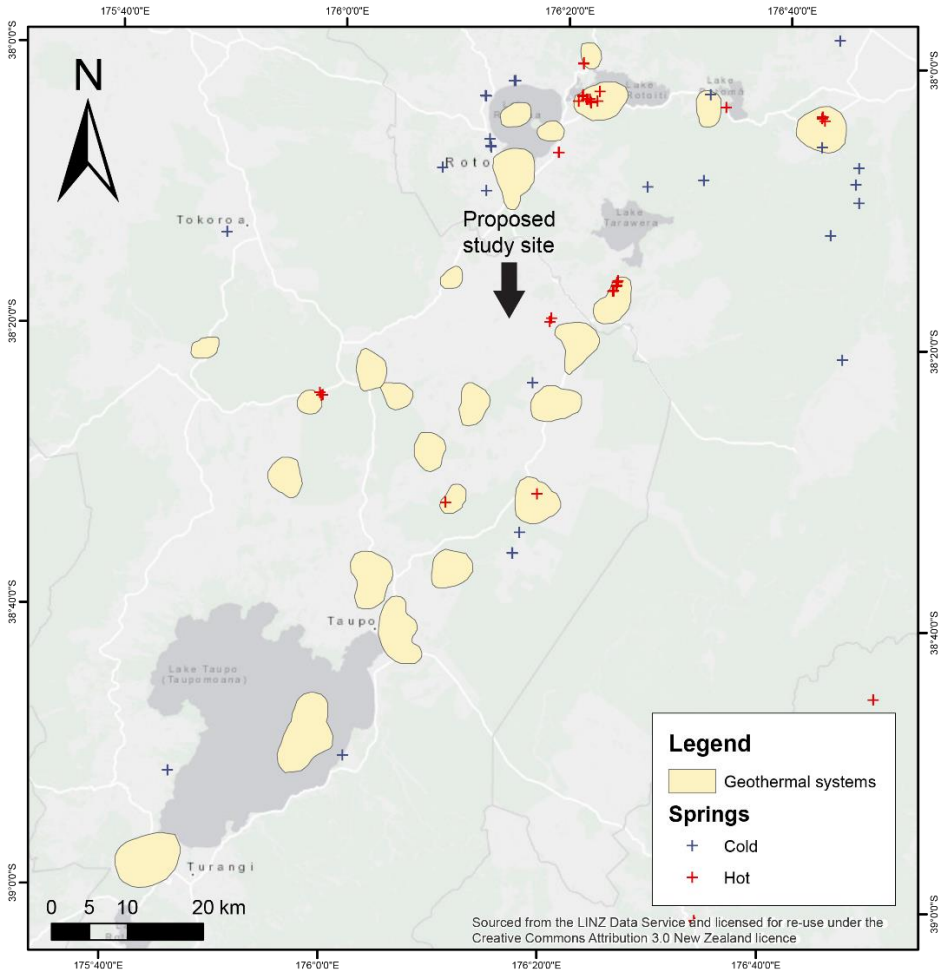

Figure 4. Simplified map of current geothermal systems and springs within the Taupo Volcanic Zone (after Bibby et al., 1995).

The model for geothermal activity in the TVZ was described by Bibby et al. (1995) as a series of convecting hydrothermal plumes carrying hot fluids to the surface, recharged by inputs of cold meteoric water which flows down and is heated by either dike intrusions or a nearby pluton. A geothermal field is the surface expression of a convective subsurface hydrothermal system (Rowland and Simmons, 2012).

In the TVZ, meteoric water enters geothermal systems via the ground surface and circulates to over 5 km depth, where it is heated and incorporates magmatic volatiles from a nearby magmatic intrusion. The meteoric water may also interact with country rock, eventually becoming buoyant neutral chloride water which rises and is directed to geothermal fields by horizontal permeability, groundwater flow, and near-surface structural variations (Bertrand et al., 2012; Rowland and Simmons, 2012).

The Taupo-Reporoa Basin in the central TVZ is an area of intense geothermal activity, with a 6–8 km deep convective zone at a temperature of around 350°C, made permeable by a combination of faults and displacement associated with caldera collapse. The convective zone overlies a ductile zone which extends to 15 km depth. Ductile mantle and partially melted interconnected structures in the mantle wedge have been detected in deeper parts of the system (Heise et al., 2007; Kaya et al., 2014).

2.2.5: Sinters

Siliceous sinters are surface features typically associated with geothermal systems. They occur as aprons around hot springs and geysers and are formed by the precipitation of non-crystalline opal-A as geothermal fluids are discharged and cooled at the ground surface (Preston, et al., 2008).

Holland (2000) mapped and sampled several siliceous sinter deposits in the area around Hossack Road and proposed the “Whirinaki Sinter Formation” as a new geological unit, though it has not been recognised as such in more recent maps (cf. Nairn, 2002), nor in other literature. Campbell et al. (2003) acknowledged Holland’s work but preferred to simply recognise a significant sinter deposit at Otamakokore Stream.

The sinters mapped by Holland (2000) were tentatively dated between 160 ka and 60 ka based on the stratigraphic juxtapositions of the Ohakuri Ignimbrite and the Kawakawa Tephra (as noted above). Holland suggested that because all mineralogical stages of sinter maturation were observed in the study area, then the sinter must have been deposited over at least a 10,000-year period within the wider timeframe, and by many fluid discharges from multiple vents during that time.

Better constraint of the age and deposition period of the sinters at the Hossack Road location could be achieved by more detailed analysis of

the tephras found in association with the sinter units, including more accurate identification based on volcanic glass shard geochemistry and more up-to-date ^{14}C ages where deposits are in the appropriate age range.

On the west strand of the Whirinaki Fault, ~3 km southwest of the proposed study site at Hossack Road, sinters at Mangatete (Figure 1) ~36–3 ka in age are exposed on terraces at different elevations. The Mangatete sinters exhibit a variety of lithofacies indicative of a range of paleoenvironments and fluid types. Drake et al. (2014) proposed that the paleohydrothermal activity in the Ngakuru Graben is related to enhanced permeability caused by faulting, as well as magmatism in the past ~60 kyr.

2.2.6: Fault history

Hossack Road and the surrounding area are located within the Ngakuru Graben of the centre of the active Taupo Rift (Villamor et al., 2011). The Taupo Rift is a Late Quaternary extensional feature (Nairn, 2002) characterised by earthquake swarms as deep as 8 km, and some moderate to large earthquakes (Canora-Catalán et al., 2008). Faults within the Taupo Rift are typically NNE-trending normal faults (Figures 2 and 5), displacing the Earthquake Flat Pyroclastics and other tephras including the Rotoma Tephra (Nairn, 2002).

The Ngakuru Graben is a 14-km-wide structure formed by tectonically-driven faults which mainly strike 040°. As the extent of the faults approaches the Okataina caldera margin, the strike bends to 060° (Villamor et al., 2011). The displacement rates on faults in the Hossack Road area have varied over the past 18,000 years, with a range of 0.1 to 3.6 mm/yr (Canora-Catalán et al., 2008). Four major faults are identified in the study area: the Maleme Fault Zone, the Whirinaki Fault, the Te Weta Fault, and the Paeroa Fault (Figure 5).

The Maleme Fault Zone (Figure 5) is a NE-trending, NW- and SE-dipping group of closely-spaced normal faults on the Ngakuru Graben in the

central Taupo Rift (Villamor and Berryman, 2001). McClymont et al. (2009) used a paleoseismic trench to correlate reflection horizons from 3D ground-penetrating radar to a stratigraphic sequence of tephra deposits, paleosols, and alluvial deposits. A paleosol is a soil of a past environment or landscape (Lowe and Tonkin, 2010). Additionally, the authors used tephrochronology to constrain the ages of the surfaces of the alluvium deposits and the initial displacements in order to obtain the vertical slip rates, determining an average total vertical slip rate of 0.20 ± 0.03 mm/yr over the past 25,000 years.

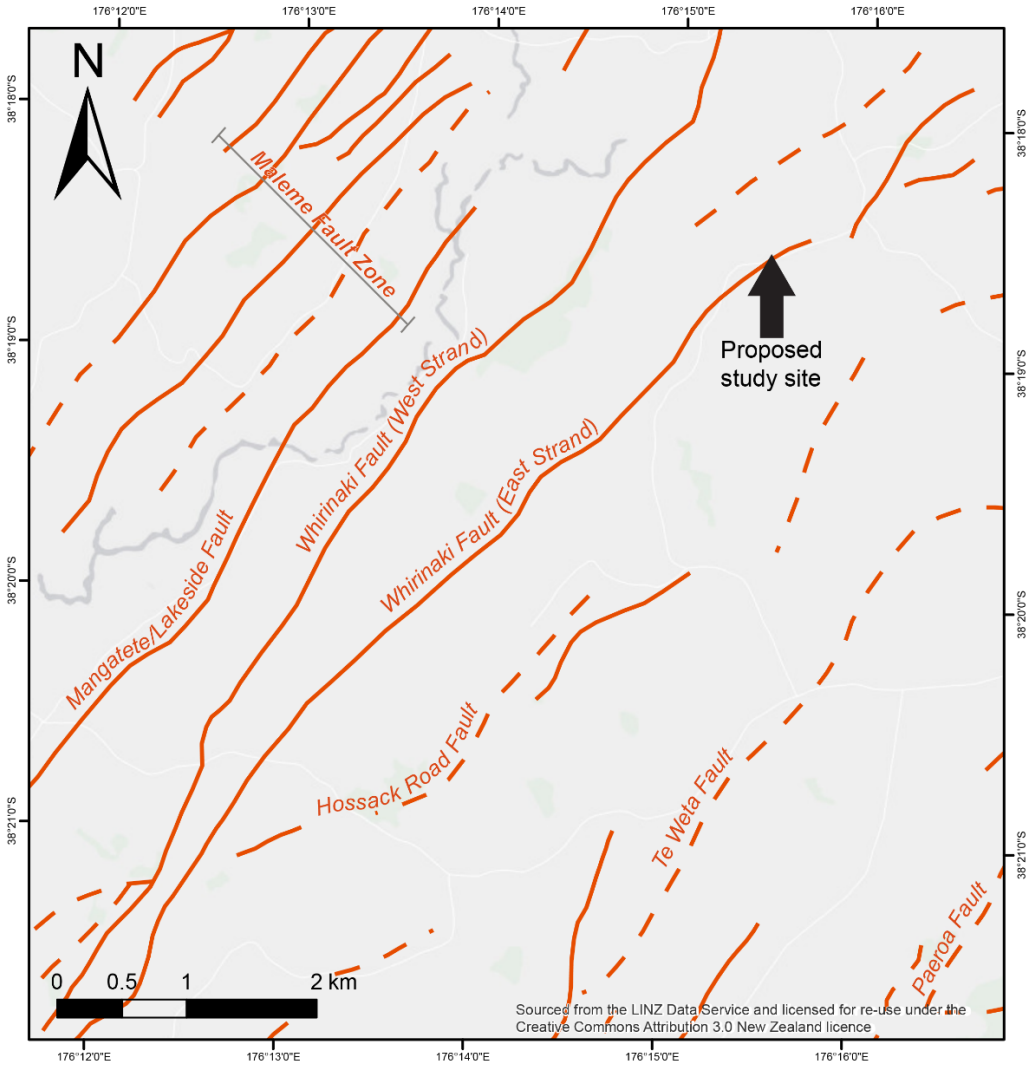

Figure 5. The main active faults in the area of the proposed study site at Hossack Road, Ngakuru.

The Whirinaki Fault (Figure 5) is a NE-trending NW-dipping normal fault on the eastern flank of the Ngakuru Graben in the central Taupo Rift.

Single-event displacements on the Whirinaki Fault vary from 0.2 to 4 m over the past 27000 years, with the overall slip rate increasing from 0.3 mm/yr to 1.3 mm/yr and the rupture recurrence interval decreasing in the last 2000 years (Canora-Catalán et al., 2008).

The Te Weta Fault (Figure 5) is a 35 km long fault bounding the western side of the Te Weta Range, and has fault traces dipping both NW and SE. The vertical slip rate has been estimated at 0.43 ± 0.15 mm/yr for the last ~13,000 years (Villamor and Berryman, 2001).

The Paeroa Fault is a 25–30 km long active normal dip-slip fault striking 040° to 050°, with an associated upstanding footwall block (the Paeroa Block). The Paeroa Fault inception was around 339 ± 5 ka and is a major structural contributor to seismic hazards in the area (Berryman et al., 2008; Downs et al., 2014a). It is the northwest boundary for the Taupo-Reporoa Basin (Downs et al., 2014a) and the southeast boundary of the Ngakuru Graben. The fault scarp of the Paeroa Fault has a "whaleback morphology", increasing in elevation from southwest to northeast, then decreasing again north of the Ngapouri Fault (Downs et al., 2014b). Average slip rate is estimated to be between 1.1-1.7 mm/yr, but it is likely that fault displacement has resulted from sporadic caldera-forming eruptive events rather than having a constant rate of slip (Downs et al., 2014a).

Some of the tephra marker bed ages used for constraining rupture timing in the studies by Villamor and Berryman (2001), Canora-Catalán et al. (2008), and McClymont et al. (2009) have changed slightly since the slip rates were calculated, and the slip rates may need to be updated accordingly.

Villamor et al. (2011) looked for relationships between the timing of fault rupture events and eruptive episodes in the Okataina Volcanic Centre (OVC), using tephrostratigraphy to constrain fault timing. The authors determined four categories of temporal relationship (Table 2). The authors concluded that faulting in the OVC is driven by tectonic activity and that dike intrusion plays a role only in some cases, at ranges less than 5 km from vents. However, they suggested near-failure faults may have been triggered to rupture by magmatic activity in the area.

Table 2. Summary of the types of temporal relationships between fault rupture timing and timing of single eruptive tephra deposition observed in the Okataina Volcanic Centre (Villamor et al., 2011).

Relationship between rupture and single eruptive tephra deposition	**Field description**
Rupture during tephra deposition	Lower beds displaced, upper beds may be slightly deformed or undeformed
Rupture slightly before tephra deposition	Deformation features are preserved, fissures filled with tephra as opposed to colluvium
Rupture slightly after tephra deposition	Colluvial wedge present without underlying paleosol
None	Signs of erosion, may have paleosol underlying colluvial wedge

Chapter 3: Stratigraphy and unit descriptions of the Hossack Road trench and outcrop

3.1: Introduction

Paleoseismological analysis uses geophysical, stratigraphic, and geomorphic evidence to interpret characteristics and reconstruct the frequency-magnitude history of prehistoric earthquakes (McCalpin, 2009; Payne et al., 2009).

Mapping the paleoseismic deformation in exposed subsurface units during trenching aids in finding event indicators (Table 3), the “morphologic and sedimentologic evidence of ground deformation”. Event indicators can be ranked by quality and abundance, and if determined to be earthquake-related are referred to as “earthquake horizons” (McCalpin, 2009).

Table 3. Classification of primary event indicators, created by tectonic deformation, with examples of geomorphic and stratigraphic features (McCalpin, 2009).

Location	On-fault		Off-fault	
Timing	Coseismic	Postseismic	Coseismic	Postseismic
Geomorphic expression	Fault scarps, fissures, folds, pressure ridges	Afterslip contributions, colluvial aprons	Tilted surfaces, uplifted or subsided shorelines	Tectonic alluvial terraces, afterslip contributions
Stratigraphic expression	Faulted or folded strata, unconformities, disconformities	Scarp-derived colluvial wedges, fissure fills	Tsunami deposits, erosional unconformities caused by tsunami	Erosional unconformities, deposits induced by uplift, subsidence, tilting
Abundance of similar nonseismic features	Few	Few	Some	Common

In the TVZ, it is also necessary to consider that extension and earthquake swarms in the region have a history of association with lateral or vertical dike propagation because the intrusion of magma can cause surface faulting. The magnitude of the cumulative fault throw at the surface above an intrusion as well as the horizontal displacement are proportional to the thickness of the intrusion. Basaltic dikes are typically 1–4 m thick, and will cause less horizontal displacement than rhyolitic dikes, which can be tens of metres thick.

Similarly, graben width can also be related to the intrusion, with deeper dikes resulting in wider grabens (Payne et al., 2009). The width of the Ngakuru Graben, which hosts the paleohydrothermal system at Hossack Road, is 14 km (Villamor et al., 2011) and there does not appear to be any known or mapped dikes in the area surrounding this strand of the Whirinaki Fault. However, the presence of the paleohydrothermal system indicates a heat source was present at some point in the past.

The excavation of a paleoseismic trench across the strand of the Whirinaki Fault at Hossack Road in this study aims to reveal stratigraphic evidence of event indicators. Once interpreted, the indicators will add further information to the history of faulting in the Ngakuru Graben and segmentation along the Whirinaki Fault. If sinters are uncovered in the trench, they will provide new information about the extent and development of the paleohydrothermal system at the site.

3.2: Field methods and limitations

A sinter outcrop was observed during the initial field visit in September, 2014 on a small hill adjacent to the proposed paleoseismic trench site. Several units of sinter, tephras and loess could be differentiated based solely on field observations, and a rough field stratigraphic log of ~6 m thickness was sketched out. A small pit of ~1 m depth was excavated at the base of the outcrop and the stratigraphy added to the log. Some samples were collected at the initial visit, sample codes are prefaced with “HR” (Hossack Road).

In November, 2014, the paleoseismic trench was excavated and the main outcrop was cleaned back using a 13 ton backhoe digger hired from Harrison Contracting Ltd. The double-bench style trench measured 23 m long, 5 m wide, and 3 m deep, with benches of up to 1.5 m depth at the deepest end. Although it is possible to dig larger and deeper paleoseismic trenches, this study was limited by time, a perched water table, and the difficulty of digging through sinter. The University of Waikato vibrocorer was used in an attempt to examine the stratigraphy below the trench floor and

on either side of the exposed fault. The trench is referred to as Meade-Hossack, after the Meade family who owned the land at the excavation site, and the name of the nearest road (Hossack).

The trench walls were further cleaned back using Niwashi hand tools. A 1 x 1 m reference grid was projected onto the southwest (SW) and northeast (NE) walls of the trench using a laser level. The grid was marked out with nails and string, and numbered with spray paint. Geological boundaries were identified and marked out with coloured pins. The trench stratigraphy was measured and logged onto drafting paper. Smaller representative sections from both the SW and NE walls were selected for unit descriptions and individual field stratigraphic logs. Units were loosely grouped and given numerical identifiers based on field-identifiable deposit characteristics. Further detail on the methods of paleoseismic trenching is available in McCalpin (2009).

Individual field stratigraphic logs were transcribed into SedLog (Zervas et al., 2009), and edited in Adobe Illustrator. Trench logs were digitised into ArcGIS and exported into Adobe Illustrator for preparation to restore the stratigraphy (Chapter 6). Field sample codes for samples collected in the trench were prefaced with “HT” (Hossack Trench). All sample codes and corresponding PETLAB numbers are listed in Appendix 1.

A consideration that should be made by researchers planning to trench any location would be to allow more than one week for a trenching campaign to allow for bad weather days when it is unsafe to work in a large trench, technical issues with equipment (GPS batteries, corers, diggers, laser level), and sufficient time for thorough documentation (trench logs, stratigraphic logs, field descriptions, field photographs). The study at Meade-Hossack limited trenching to one week including excavation and setup (cleaning back walls, creating reference grid, pinning unit boundaries), more detail could have been gathered with more time.

3.3: Results

3.3.1: Unit descriptions

The units found in the Meade-Hossack trench are described in Table 4 and accompanied by photographs. Unit-specific features visible in photographs have been annotated where possible with text and arrows. The unit ID numbers in the table correspond to the unit codes given on the Meade-Hossack trench logs (Figures 6 and 7).

Units included massive ignimbrite, unconsolidated pumice lapilli, banded siliceous sinters, and a variety of what may be weathered Holocene-age tephras and/or paleosols developed on tephras.

Table 4. Field descriptions and photographs of the stratigraphic units exposed in the trench at Hossack Road. Unit ID corresponds to units on the Meade-Hossack trench logs. The colours of units are described using the Munsell system.

UNIT ID#	DESCRIPTION	PHOTO
1	2.5Y 2/1 black to 5YR 3/1 brownish black massive ungraded poorly sorted slightly clayey sandy silt with few very fine to fine pumice lapilli in base, many very fine to medium roots. Charcoal-rich.	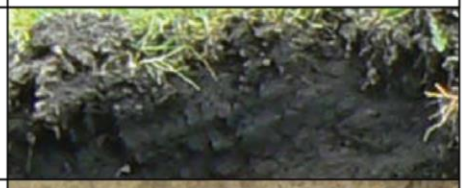
2	2.5Y 4/6 olive brown to 10 YR 3/4 massive ungraded poorly sorted dark brown silt to coarse sand with very fine to fine pumice lapilli and few fine roots.	
3	5Y 6/2 greyish olive grain-supported medium to very coarse sand with few fine pumice lapilli. 30% dark grains. Includes lenses of quartz-rich 5Y 7/3 light yellow silt in medium laminae with few coarse sand grains. Scoured into underlying unit.	
4a	10YR 6/3 dull yellow orange massive ungraded poorly sorted very fine to fine sand with coarse pumice ash, coarse sand-sized lithics, and fine to medium pumice lapilli (MP: 40 mm). Contains pieces of charcoal 20 mm to 240 mm in size. Often shows "chimney" type gas or fluid escape structures of coarse ash and fine to medium pumice lapilli, containing 10-20% dark grains. TAUPO UNIT Y.	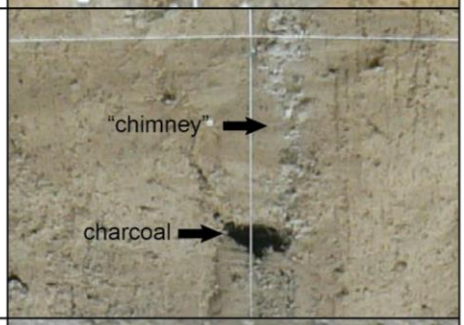
4b	2.5Y 5/2 dark greyish yellow very fine to fine sand with medium sand and few fine pumice lapilli. ~1% dark grains. Charcoal occurs mostly in the base of the unit, typically in association with "chimney" escape structures. TAUPO UNIT Y.	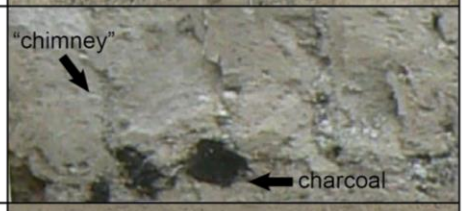
4b1	2.5Y 5/3 yellowish brown fine sand with few medium and coarse sand-size grains and few very fine pumice lapilli. 10% dark grains. Charcoal occurs mostly in top of unit. TAUPO UNIT Y.	
4c	10YR 6/3 dull yellow orange very fine to fine sand with few fine to medium pumice lapilli. 5-10% dark grains. Contains charcoal typically associated with "chimney" escape structures of medium pumice ash to medium pumice lapilli and 10-20% dark grains. TAUPO UNIT Y.	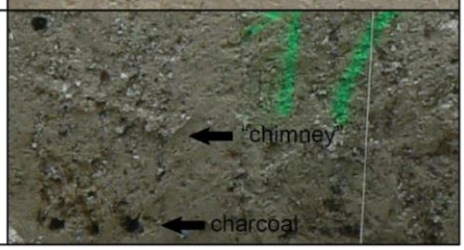

Table 4 continued.

UNIT ID#	DESCRIPTION	PHOTO
4d	5Y 8/2 light grey poorly sorted grain supported unconsolidated fine to coarse pumice lapilli and fine to medium pebble lithics (5Y 4/1 grey and 5Y 4/6 reddish brown). Discontinuous but mantles paleotopography. Extremely loose, falls out of face with a light brush. TAUPO UNIT Y.	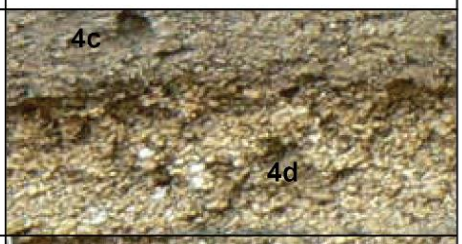
4e	10YR 4/1 brownish grey to 5Y 4/1 grey fine to medium ash. Discontinuous but mantles topography in association with 4d.	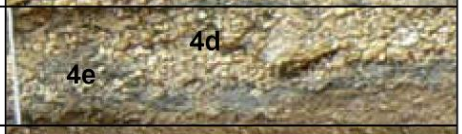
10	10 YR 5/8 yellowish brown moderately sorted very fine to medium sandy clay with few very coarse sand grains and MnO_2 nodules (<3 mm). 5% dark grains.	
11	10YR 6/8 bright yellowish brown fine to coarse sandy clay with fine subangular pebble lithics and few MnO_2 nodules (<3 mm). < 5% dark grains.	
12	10YR 5/6 yellowish brown poorly sorted very fine to very coarse sandy clay with hard, glassy, angular fine to coarse pebble sinter lithics coloured white, dark grey, or alternating both. Also contains 5Y 7/1 light grey soft (~3 Mohs) speckled subangular to subrounded fine to coarse pebble lithics, some of which have MnO_2 coatings.	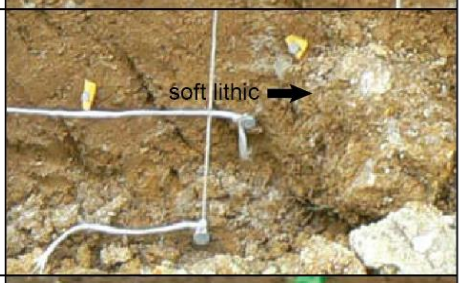
20	2.5Y 4/4 olive brown ungraded poorly sorted medium to very coarse pumice ashy clay with MnO_2 nodules (< 3mm). 5% dark grains.	
20x	10YR 5/8 yellowish brown clayey fine to medium sand with few coarse sand grains and very fine to fine pumice lapilli.	
21	10YR 4/6 brown fine sand with flecks of charcoal and few fine to very fine roots. Often contains “cream cakes” (21a) in base.	
21a	2.5Y 7/3 light yellow moderately well sorted fine ash with few coarse ash grains. 1% dark grains. “Cream cakes” in 21.	

Table 4 continued.

UNIT ID#	DESCRIPTION	PHOTO
22	10YR 5/6 yellowish brown massive clayey very fine to medium sand with few very coarse sand grains and few very fine roots.	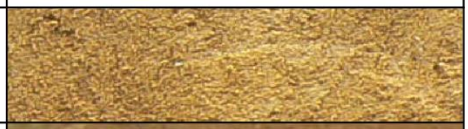
23	10YR 5/8 yellowish brown well sorted clayey fine to medium sand.	
24	10 YR 5/8 yellowish brown massive moderately well sorted clayey fine to medium sand with few coarse sand grains and few very fine to fine root fragments. ~1% dark grains.	
25	2.5Y 5/6 yellowish brown normal graded moderately well sorted slightly clayey biotite-rich fine to very coarse ash. In base, grain supported unconsolidated medium to very coarse pumice ash and 20% dark grains. In top, fine to medium pumice ash with few coarse ash grains and 10% dark grains. Base is very loose, easily brushed from face. Top is slightly more cohesive.	
30	10YR 7/6 bright yellowish brown poorly sorted sandy clay with medium to very coarse sand, many 5Y 8/1 light grey soft (Mohs ~3) angular granule to coarse pebble lithics and glassy angular fine pebble to cobble lithics of silicified material.	
30x	2.5Y 7/6 bright yellowish brown non-sticky clay with 2.5Y 8/1 light grey soft angular pebbles and few white medium to coarse sand grains. Mottled 10YR 7/8 yellow orange to 7.5YR 6/8 orange.	
31	2.5Y 6/8 bright yellowish brown massive ungraded poorly sorted medium to very coarse sandy clay with angular fine pebble to cobble lithics of grey and white sinter. MnO_2 coatings common on lithics. 1-5% dark grains.	
40x	Grey and white alternating thin laminae to thin beds of hard glassy silicic sinter with subvertical fractures. Intermixed with 30x on NE wall.	

Table 4 continued.

UNIT ID#	DESCRIPTION	PHOTO
41	5Y 7/3 light yellow massive poorly sorted non-sticky clay with 5Y 8/1 soft (Mohs ~3) angular lithics and MnO_2 nodules (<3 mm). <1% dark grains. Slightly mottled to 10YR 7/8 yellow orange.	
42	Alternating thin wavy beds of 5YR 8/1 light grey and 5N 7/0 grey sinter with sharp contacts between beds. Weathered silicified material at contacts with underlying and overlying units. Has many round porelike structures from <1 mm to ~2 mm diameter, some infilled to give a concentric/radial pattern. May be silicified twigs.	
43	7.5Y 7/3 light grey massive clay. Sharp slightly weathered contact with underlying unit. Highly weathered contact with overlying unit, strong mottling 10YR 6/8 bright yellowish brown.	
44	Thin wavy alternating beds of 5Y 8/1 light grey and 5Y 5/1 grey hard, glassy sinter, often brecciated. Intermixed with 7.5YR 7/8 yellow orange sandy clay with MnO_2 nodules 1 mm to 6 mm.	
45	**Weathered:** 2.5Y 8/6 yellow very poorly sorted non-sticky medium to coarse sandy clay with many 7.5Y 8/1 light grey angular pebble to cobble lithics (Mohs ~3) and 10YR 7/8 mottles. **Unweathered:** 2.5Y 8/1 light grey moderately well sorted siltstone with few coarse sand grains. 10-20% dark grains. Mohs ~4.5.	 
SZ	Brecciated sinter and 5Y 8/2 light grey soft nonsticky clay clasts up to cobble sizes. 10YR 7/8 yellow orange weathering in between poorly defined and fragmented sinter horizons. Shear zone. Sinter fragments appear to have been sheared in an upwards motion.	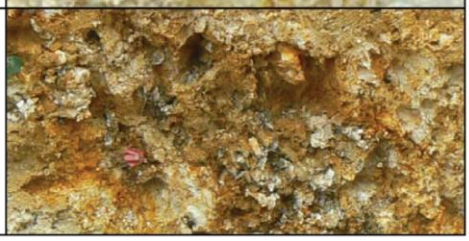

3.3.2: Paleoseismic trench logs

Two paleoseismic logs were produced from the Meade-Hossack trench, one from the northeast wall (Figure 6) and one from the southwest wall (Figure 7). Cores taken in the trench have been added to the log at the appropriate depth. The cores were examined upon return to the University of Waikato and correlations were based on descriptions of core units compared with trench units.

In the northern part of the trench, there is a succession of weathered Holocene-age tephras and/or paleosols (Units 20 through 25) overlying a variably weathered ignimbrite (Unit 45). Thin Taupo Unit Y deposits, mainly the Taupo Pumice Lapilli [Taupo plinian pumice, equivalent to Taupo subunit Y5] (Wilson, 1993) and Rotongaio Ash [Taupo subunit Y4], overlie the Holocene tephras. The succession is topped by a charcoal-rich topsoil (Unit 1). In the southern part of the trench on the hanging wall, Taupo Unit Y is dominant, with up to 2.5 m of Taupo Ignimbrite [Taupo subunit Y7] (Wilson, 1985; Wilson and Walker, 1985) exposed in the deepest part of the trench and very little Holocene tephra (< 0.5 m in thickness).

Core taken from the deepest part of the trench showed reduced thicknesses of Holocene tephras and around 0.5 m of fine to medium sandy deposits uncorrelatable with other units observed in the trench.

Fault deformation is visible on both logs, largely between vertical batters 9 to 11 on both walls, affecting deposits as young as Taupo Unit Y (~1.8 ka). Several other units stratigraphically below Taupo Unit Y have also been deformed, including 24, 25, 30, 40x, and 45. A zone of shear is visible in the SW wall (Figure 7), with dark sinter fragments sheared upwards along the hanging wall of the fault plane (Figure 8). The fault associated with the shear zone has a strike/dip of 025/69NW, while most of the other faults and fractures along the SW wall close to the shear zone are dipping in the opposite direction and have a strike greater than 040°.

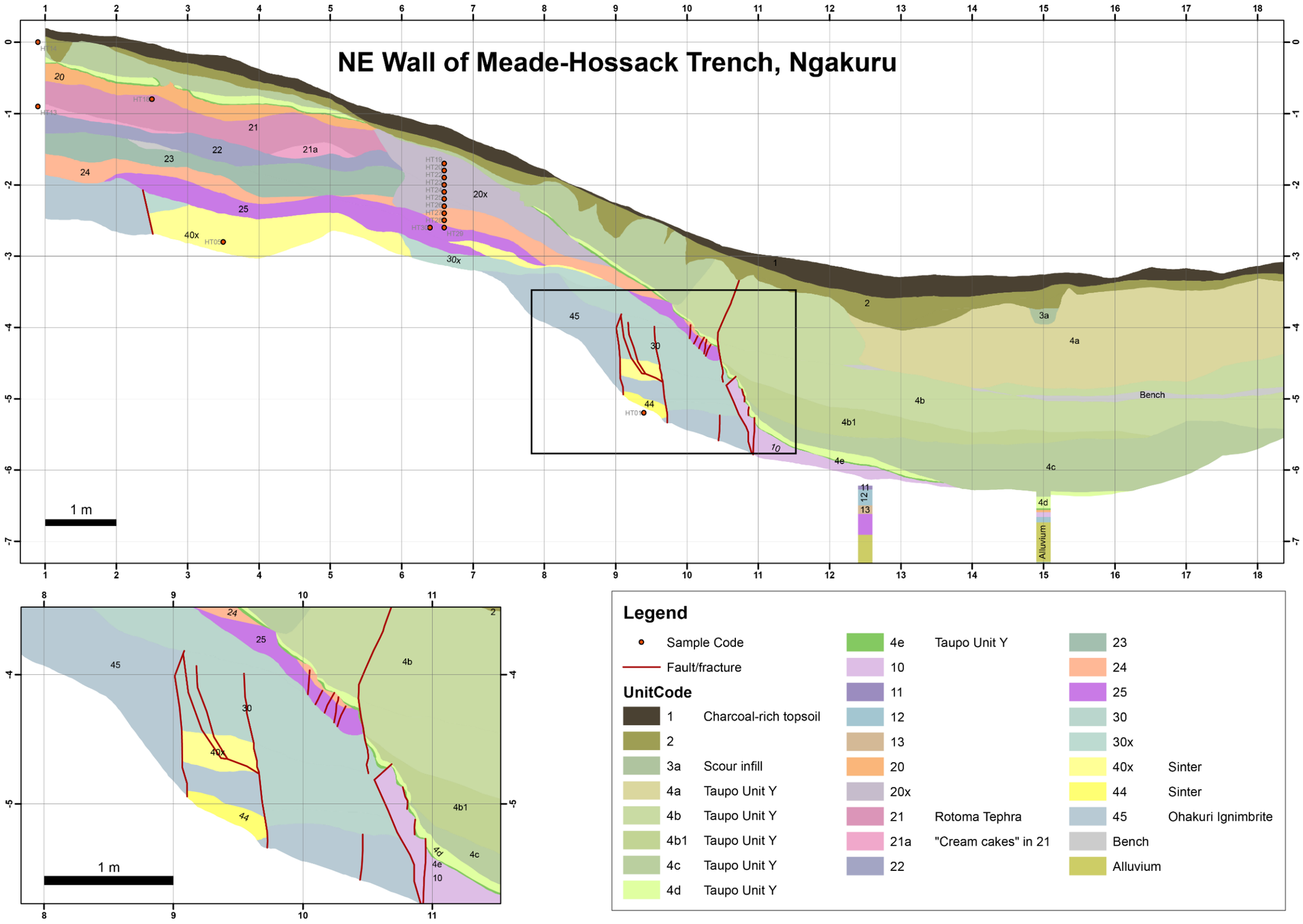

Figure 6. Paleoseismic trench log for the northeast (NE) wall of the trench at Hossack Road, Ngakuru, with inset highlighting deformed strata. Horizontal batters are marked from top to bottom on the sides of the figure. Vertical batters are marked from left to right at the top and bottom of the figure. Sample locations have an error margin of 0.1 m.

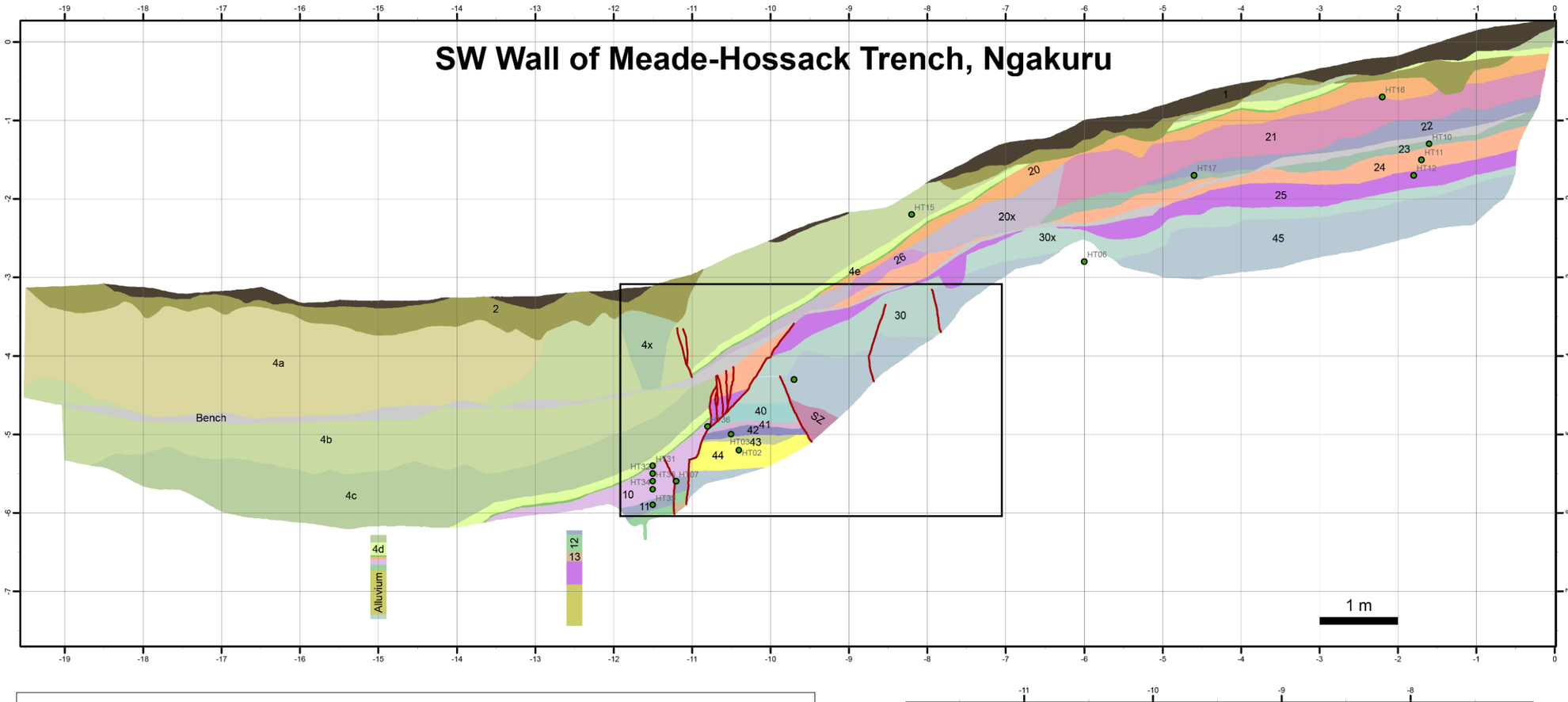

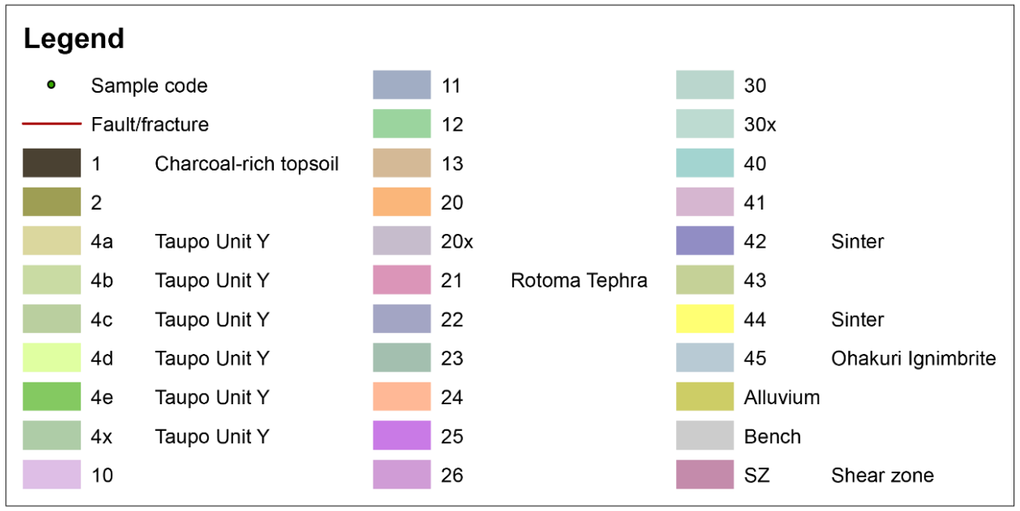

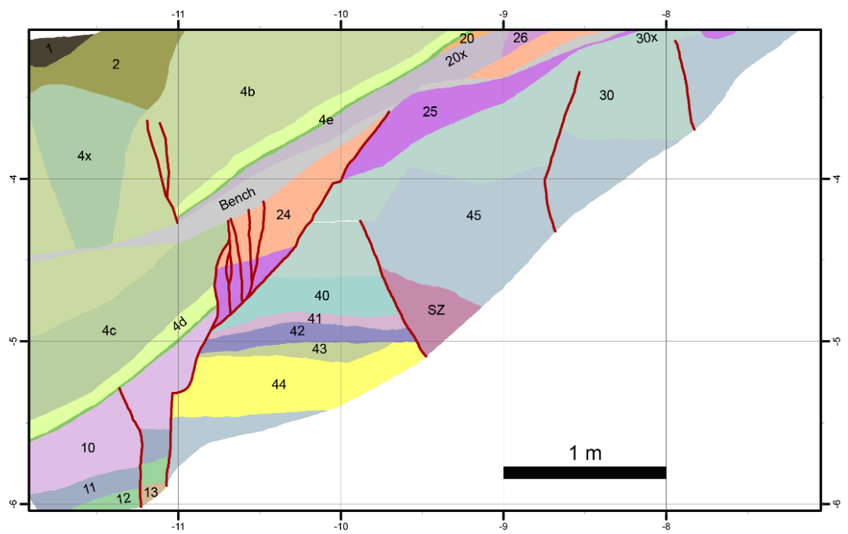

Figure 7. Paleoseismic trench log for the southwest (SW) wall of the trench at Hossack Road, Ngakuru, and inset highlighting the deformed strata. Horizontal batters are marked from top to bottom on the sides of the figure. Vertical batters are marked from left to right at the top and bottom of the figure. Sample locations have an error margin of 0.1

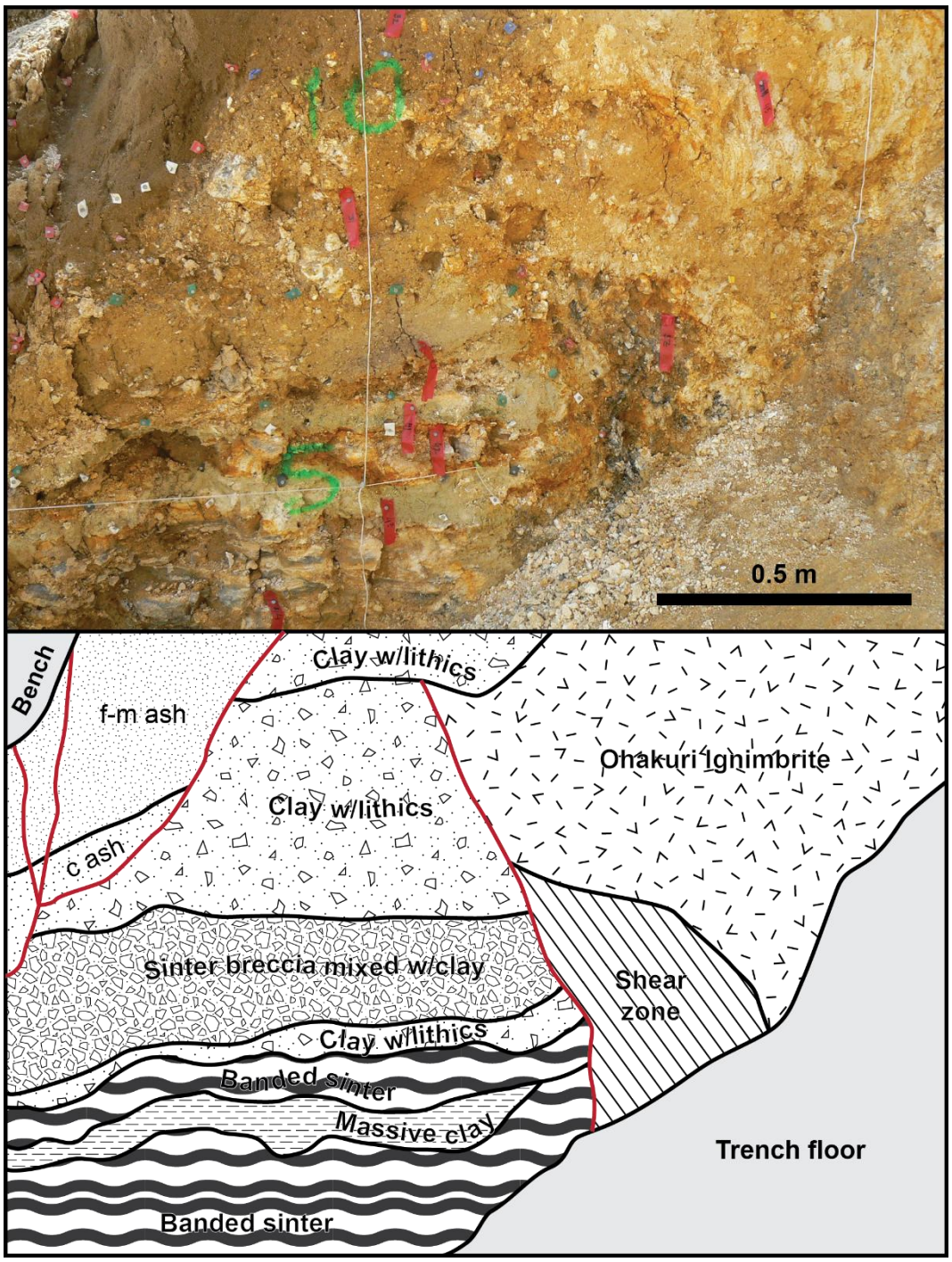

Figure 8. Detail photograph and sketch of the units surrounding the shear zone in the SW wall of the Meade-Hossack trench.

3.3.3: Stratigraphic logs

The stratigraphic logs (and encapsulated physical properties of constituent units) aid in capturing the spatial variations in units throughout the length and across the width of the trench. The logs were recorded at roughly the same grid reference points on each of the trench walls.

At vertical batter 2.5 on the NE wall (Figure 9), the deepest visible unit is 40x, a brecciated sinter containing some round cavities filled with pale yellow orange clay. Overlying the sinter is 30x, a bright yellowish brown clay containing blocks of light grey clay. Unit 25 overlies 30x, and is a normally graded tephra of around 0.3 m thickness with a coarser, grain-supported base and a finer, more cohesive top. Unit 24 is a clayey fine to medium sand noted initially as a paleosol developed on 25. 23, another fine to medium sand or ash, overlies 24 and provides the surface for the bench at the northern end of the trench. Unit 22 is a massive yellowish brown clayey sand, mostly visible just above the bench. Unit 21 is the thickest tephra unit, at around 0.5 m thickness. 21 contains pale yellow “cream cakes” (21a), discontinuous patches of fine ash of around 50 mm diameter, typically in the base of 21. Unit 20 is a coarse sandy clay of ~ 0.1 m thickness overlying 21. Around 20 mm of the Rotongaio Ash (4e) of Taupo Unit Y overlies 20, followed by around 120 mm of Taupo Pumice Lapilli (4d). 4d contains grey and reddish brown lithics, with a maximum lithic size of 18 mm and a maximum pumice size of 55 mm. Overlying 4d is a 0.18 m-thick Taupo Ignimbrite deposit (4c) with some small pieces of charcoal in the base. On top of the ignimbrite is 2, a massive fine sandy unit containing some very fine pumice lapilli. The uppermost horizon is 1, a brownish black charcoal-rich unit containing very fine pumice lapilli and many roots.

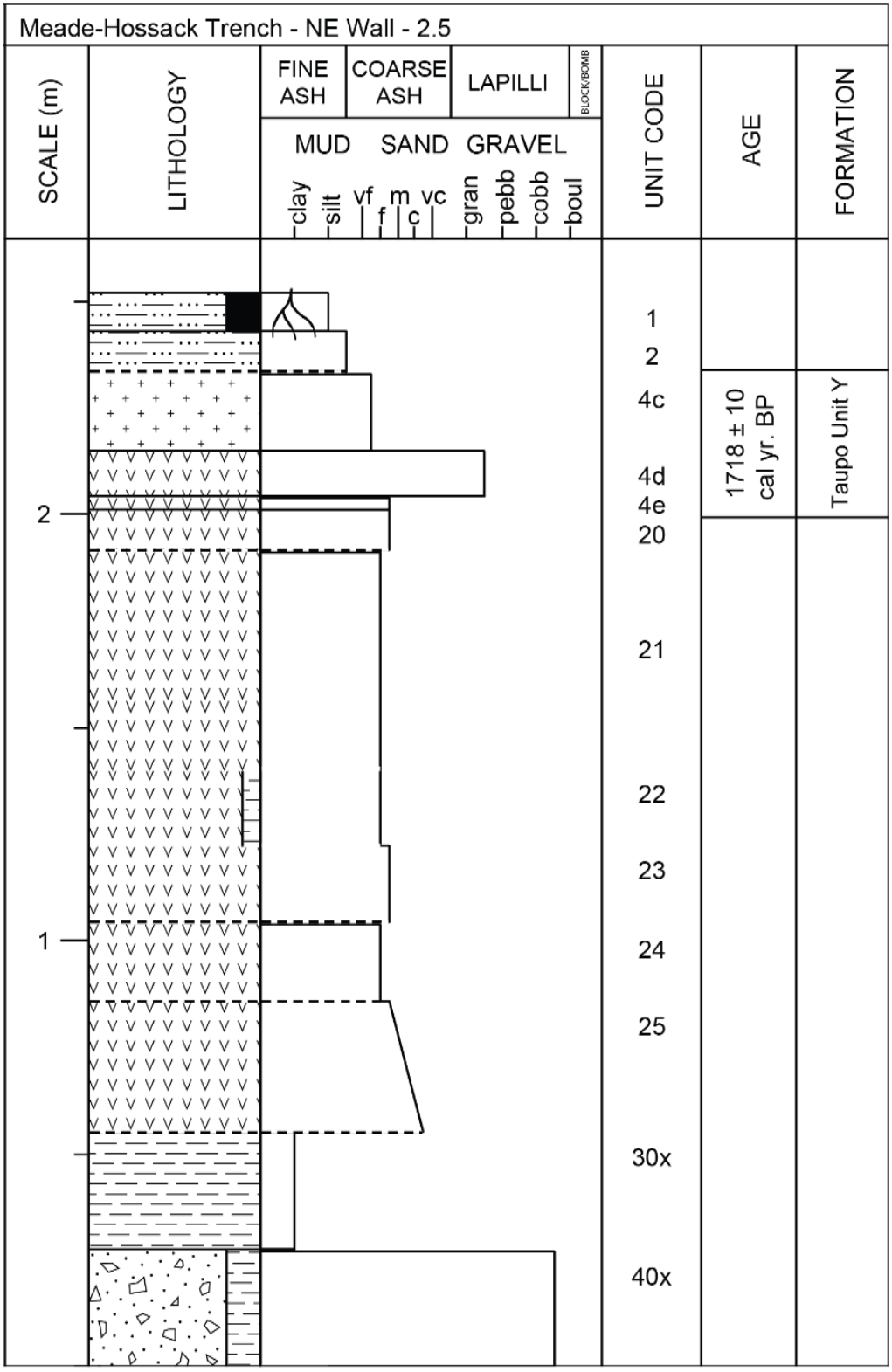

Figure 9. Stratigraphy of the NE wall at vertical batter 2.5 on Figure 6. Unit codes correspond to codes on Figure 6 and unit descriptions in Table 4. Gradational boundaries are delineated with a dashed black line. Sharp boundaries are delineated with a bold black line. Age for Taupo Unit Y from Hogg et al. (2012).

On the SW wall (Figure 10), the 40x sinter is not observed at the 2.5 vertical batter, in contrast with the NE wall. The deepest unit is a 0.5 m thickness of greenish clay identified in the field as Ohakuri Ignimbrite. 30x, 25, 24, and 23 follow at similar positions and thicknesses to the same units on the NE wall. Unit 22 is indistiguishable from 23 at this point in the trench, and fewer “cream cakes” are visible in Unit 21. Neither Rotongaio Ash nor Taupo Ignimbrite are present, with Taupo Pumice Lapilli the only visible component of Taupo Unit Y deposits. Unit 2 is very thin, at only around 20 mm thickness. Unit 1 is similar in thickness to the deposit on the NE wall.

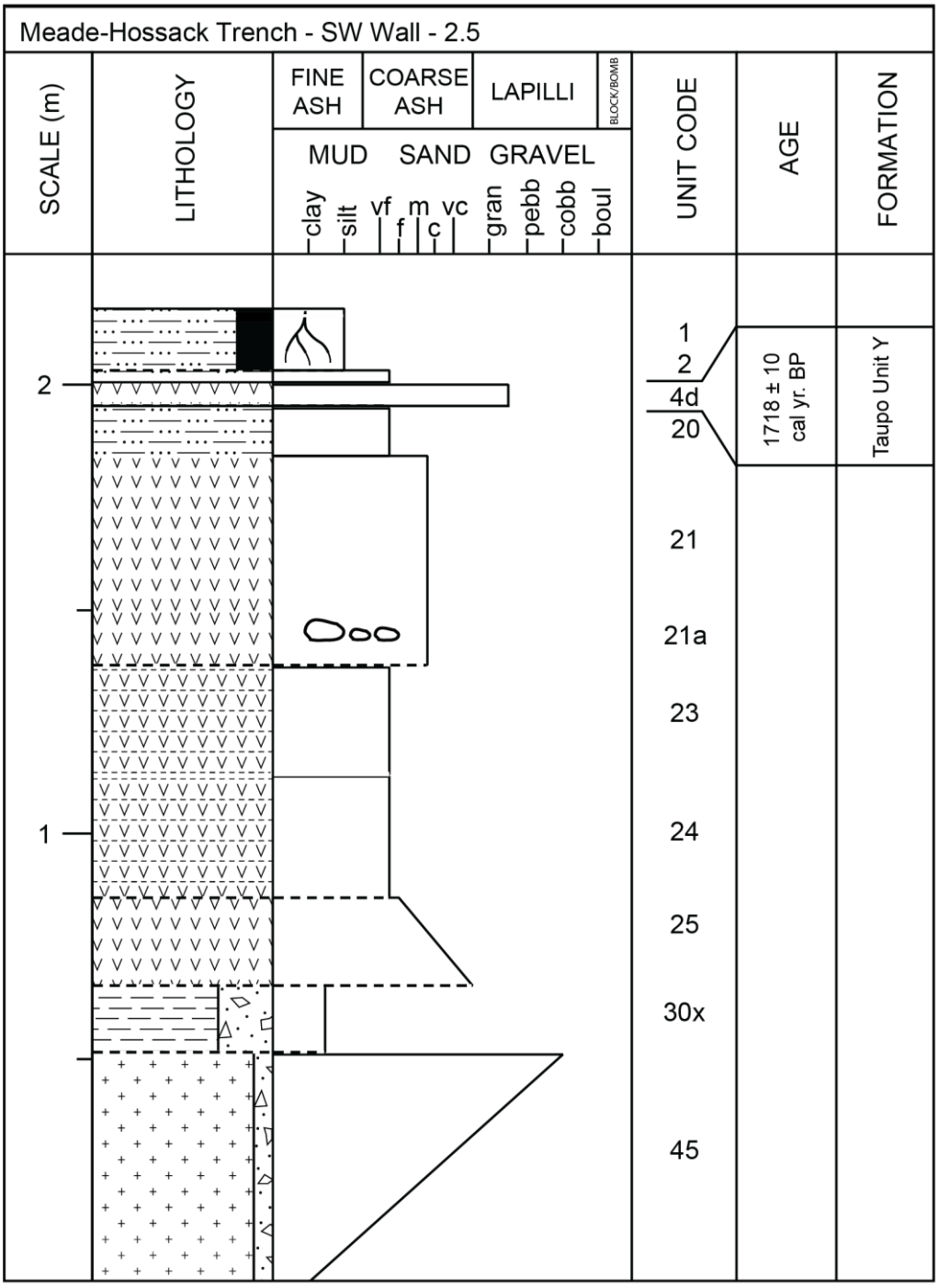

Figure 10. Stratigraphy of the SW wall at vertical batter 2.5 on Figure 7. Unit codes correspond to codes on Figure 7 and unit descriptions in Table 4. Gradational boundaries are delineated with a dashed black line. Sharp boundaries are delineated with a bold black line. Age for Taupo Unit Y from Hogg et al. (2012).

At vertical batter 7.5 on the NE wall (Figure 11), the deepest unit is 30x, at a thickness of 0.5 m. The lower part of 30x is a fine to coarse sandy clay containing round clasts of light grey clay ranging 10-50 mm in diameter. The upper part of 30x is the same sandy clay but contains many angular clasts of white sinter breccia of up to 40 mm in size. 30x is overlain by a thin layer of 25. Above the bench is a 0.2-m thick deposit of the 40x sinter, consisting of grey and white laminae grading to thin beds, with few fractures; it is brecciated in parts with clay formed in the voids. The sinter is overlain by a further 0.1-m thick deposit of Unit 25, which is overlain by around 0.2 m of Unit 24. On 24 is a 0.5-m thick mixed unit 20x, comprised of paleosols and/or tephra. Around 0.2 m of 4c follows, containing a fine pumice lapilli within the base. 4c is capped by 0.1 m of Unit 2 and around 60 mm of the charcoal-rich topsoil making up Unit 1.

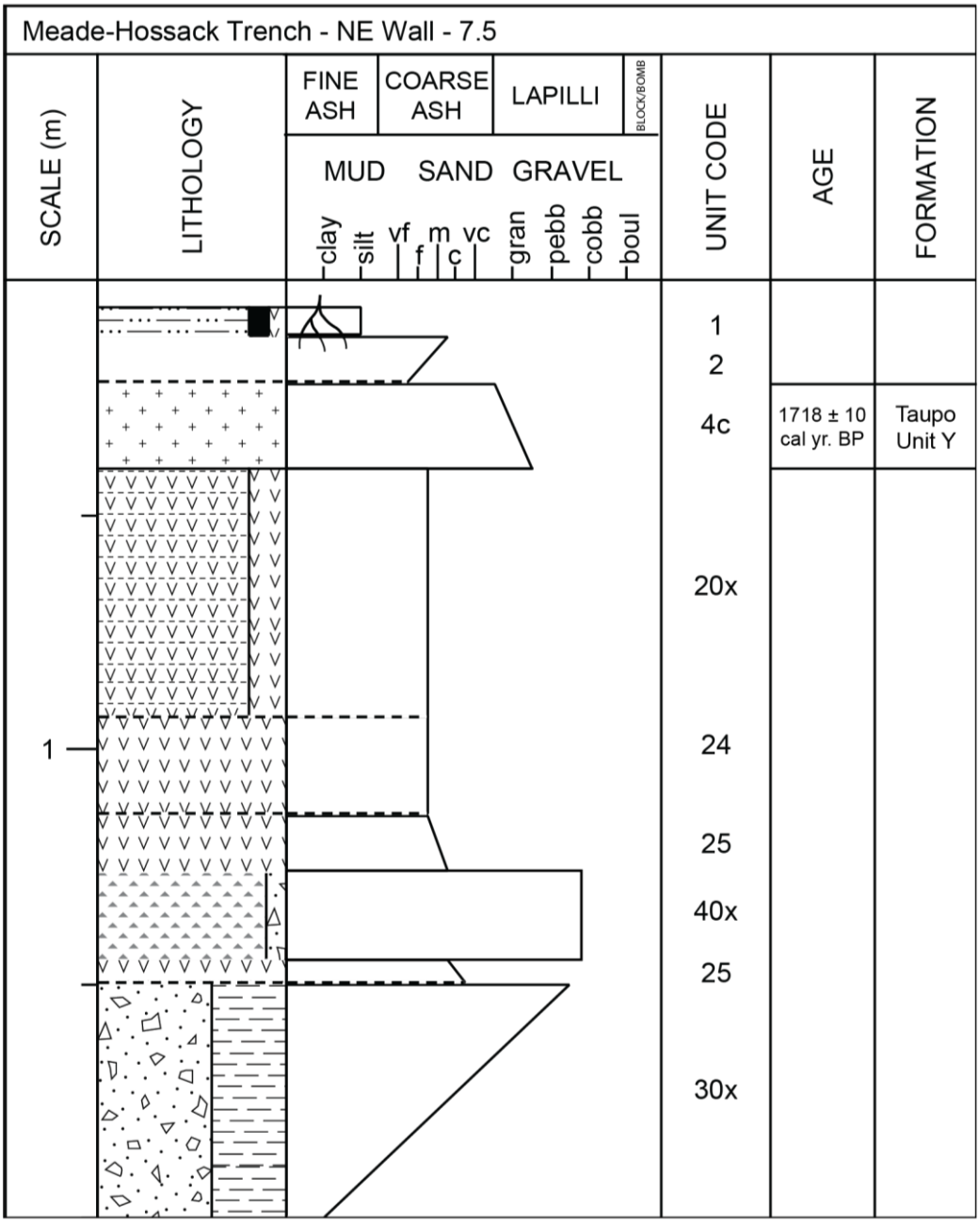

Figure 11. Stratigraphy of the NE wall at vertical batter 7.5 on Figure 6. Unit codes correspond to codes on Figure 6 and unit descriptions in Table 4. Gradational boundaries are delineated with a dashed black line. Sharp boundaries are delineated with a bold black line. Age for Taupo Unit Y from Hogg et al. (2012).

The 7.8 vertical batter on the SW wall of the trench was preferred for a stratigraphic log (Figure 12) over the 7.5 point as there is a fracture running through, giving two different thicknesses for some of the strata. The deepest unit is a 0.5 m thickness of weathered Ohakuri Ignimbrite (45) overlain by less than 0.1 m of 30x. Around 0.15 m of Unit 25 follows, then nearly 0.4 m of 24, which is overlain by 0.2 m of Unit 21. There were no visible “cream cakes” of 21a within 21 at the log location. Around 0.15 m of Unit 20 overlies 21, followed by almost 0.5 m of Taupo Unit Y deposits, including 4e, 4d, and ignimbrite 4b. Units 2 and 1 are thin at the log location, comprising just a few tens of millimetres.

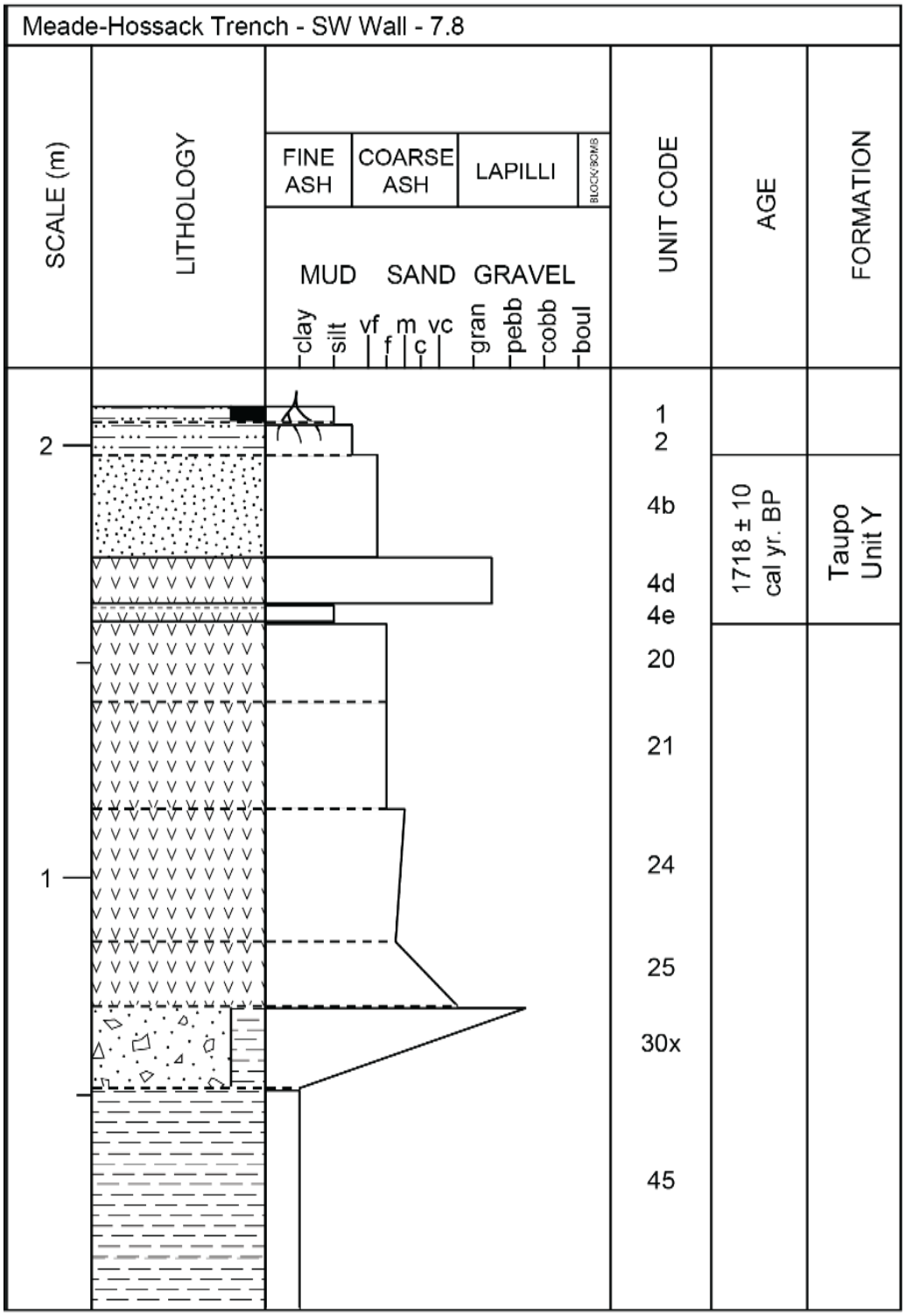

Figure 12. Stratigraphy of the SW wall at vertical batter 7.8 on Figure 7. Unit codes correspond to codes on Figure 7 and unit descriptions in Table 4. Gradational boundaries are delineated with a dashed black line. Sharp boundaries are delineated with a bold black line. Age for Taupo Unit Y from Hogg et al. (2012).

The log for the NE wall at the 12.5 vertical batter (Figure 13) marks a shift to a stratigraphy dominated by Taupo Unit Y deposits. The 0.16 m-thick manganese-bearing Unit 20 is at the bottom of the trench, overlain by 30 mm of Rotongaio Ash (4e). The 4d pumice lapilli is next (above), at a thickness of around 0.1 m. Almost 0.3 m of 4c follows, the ignimbrite contains medium to very coarse pumice lapilli throughout, and charred logs or branches in the upper half of the unit. The tops of the “chimney” gas escape structures associated with the charcoal pieces form a linear boundary at the top of the unit. Just over 0.3 m of 4b1 lies above, comprising an ignimbrite lacking in pumice clasts and containing only small pieces of charred plant material in the top 10-20 mm of the unit. Overlying 4b1 is >0.5 m of 4b ignimbrite, which exhibits slight reverse grading and contains fine pumice lapilli. Large charcoal branches are close to the base of the unit, and are associated with the “chimney” gas escape structures previously seen in 4c. Above the bench, around 0.7 m thickness of ignimbrite 4a, which also has the charcoal/”chimney” association in the base of the unit. At the log location the total observed thickness of the Taupo Unit Y deposits is almost 2 m. Taupo Unit Y is capped by 0.25 m of Unit 2, which contains fine to coarse pumice lapilli. At the top, around 0.1 m of Unit 1 completes the stratigraphy.

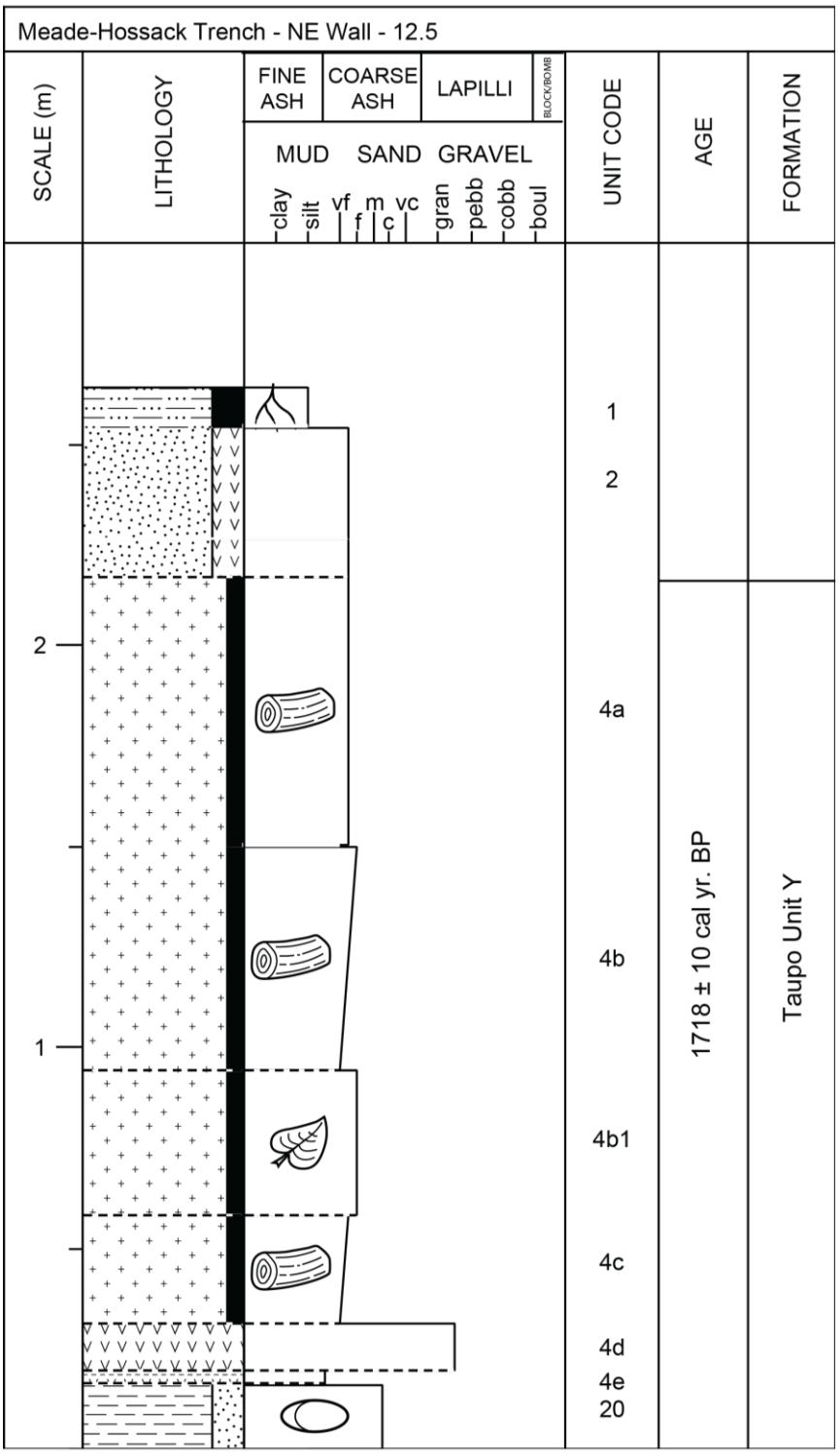

Figure 13. Stratigraphy of the NE wall at vertical batter 12.5 on Figure 6. Unit codes correspond to codes on Figure 6 and unit descriptions in Table 4. Gradational boundaries are delineated with a dashed black line. Sharp boundaries are delineated with a bold black line. Tree log symbols represent carbonised tree logs and branches. The elliptical symbol represents MnO_2 concretions. Age for Taupo Unit Y from Hogg et al. (2012).

The stratigraphic log for the SW wall at vertical batter 12.5 (Figure 14) is very similar to that for the NE wall (Figure 13), starting off at the base with 0.15 m of Unit 20, followed by 10 mm of 4e and around 0.1 m of 4d. Almost 0.3 m of the 4c ignimbrite follows, then around 1.5 m of what is identified as the 4b ignimbrite but may be 4b in the lower part below the bench, and 4a above the bench. The lack of charcoal and “chimney” structures in the upper part of the unit makes the distinction difficult as these features tend to appear at the base of the ignimbrite subunits. The combined thickness of Taupo Unit Y deposits on the SW wall at the log location is just under 2 m, similar to the thickness at the NE wall. The ignimbrite is topped with around 0.4 m of Unit 2, and 40 mm of Unit 1.

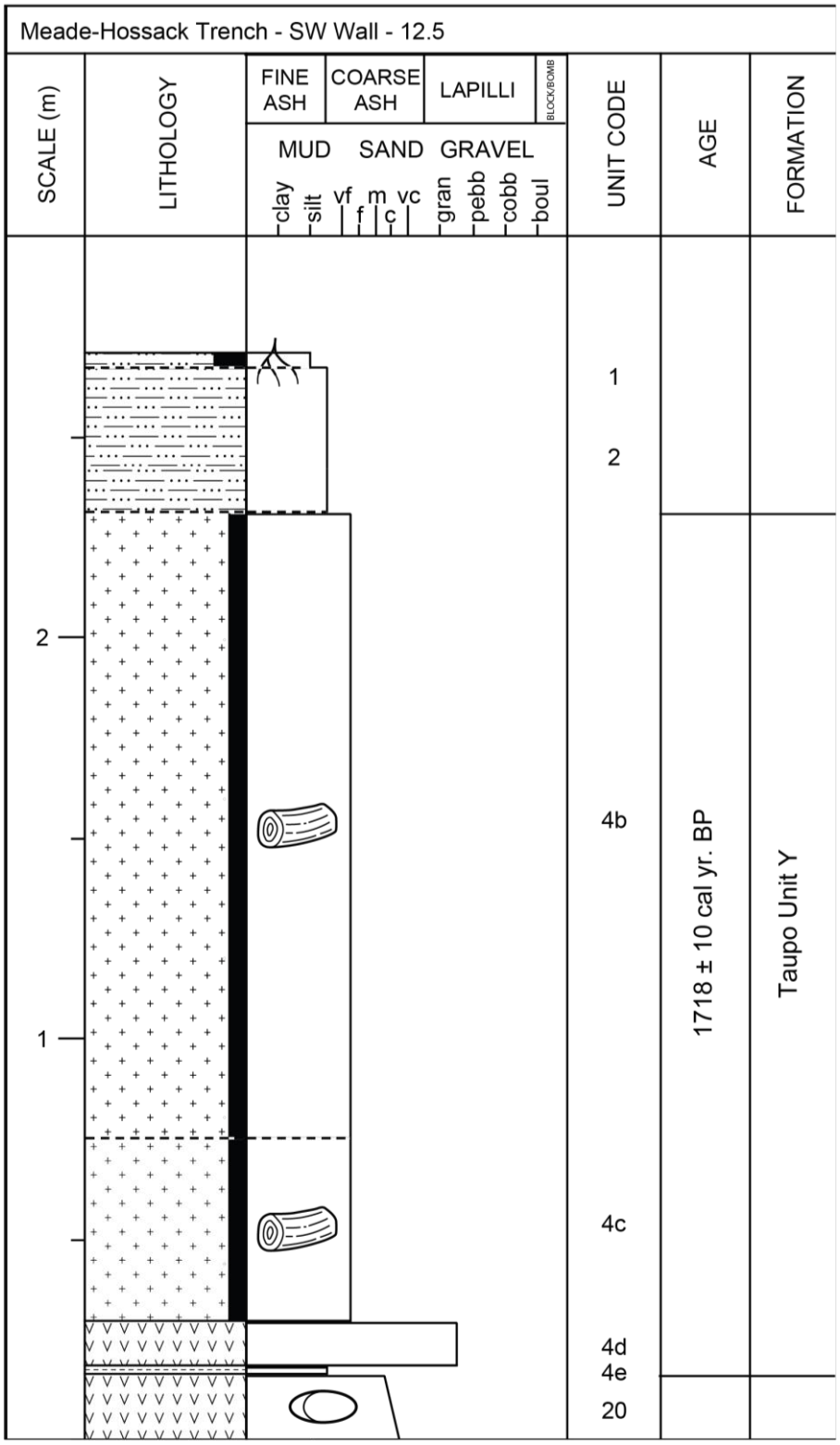

Figure 14. Stratigraphy of the SW wall at vertical batter 12.5 on Figure 7. Unit codes correspond to codes on the Figure 7 and unit descriptions in Table 4. Gradational boundaries are delineated with a dashed black line. Sharp boundaries are delineated with a bold black line. Tree log symbols represent carbonised tree logs and branches. The elliptical symbol represents MnO_2 concretions. Age for Taupo Unit Y from Hogg et al. (2012).

On the NE wall at vertical batter 15 (Figure 15), the stratigraphy is still dominated by Taupo Unit Y deposits, with no older units observed at this location. The deepest unit is a 20 mm thick deposit of the upper part of the 4d pumice lapilli, which is overlain by around 0.65 m of the 4c ignimbrite. A relatively thin zone of 4b1 follows, at under 0.1 m thickness, then around 0.6 m of the 4b ignimbrite. 4b is overlain by around 0.9 m of 4a, which contains charcoal plant remains up to 0.24 m in diameter. The total exposed thickness of Taupo Unit Y deposits at this batter is around 2.1 m. 3a is a grain-supported medium to coarse ash unit, of around 0.2 m thickness and containing fine pumice lapilli and lenses of light yellow very fine ash. 3a lies in a scored depression in the top of 4a, and is overlain by around 0.2 m of Unit 2, and just under 0.1 m of Unit 1.

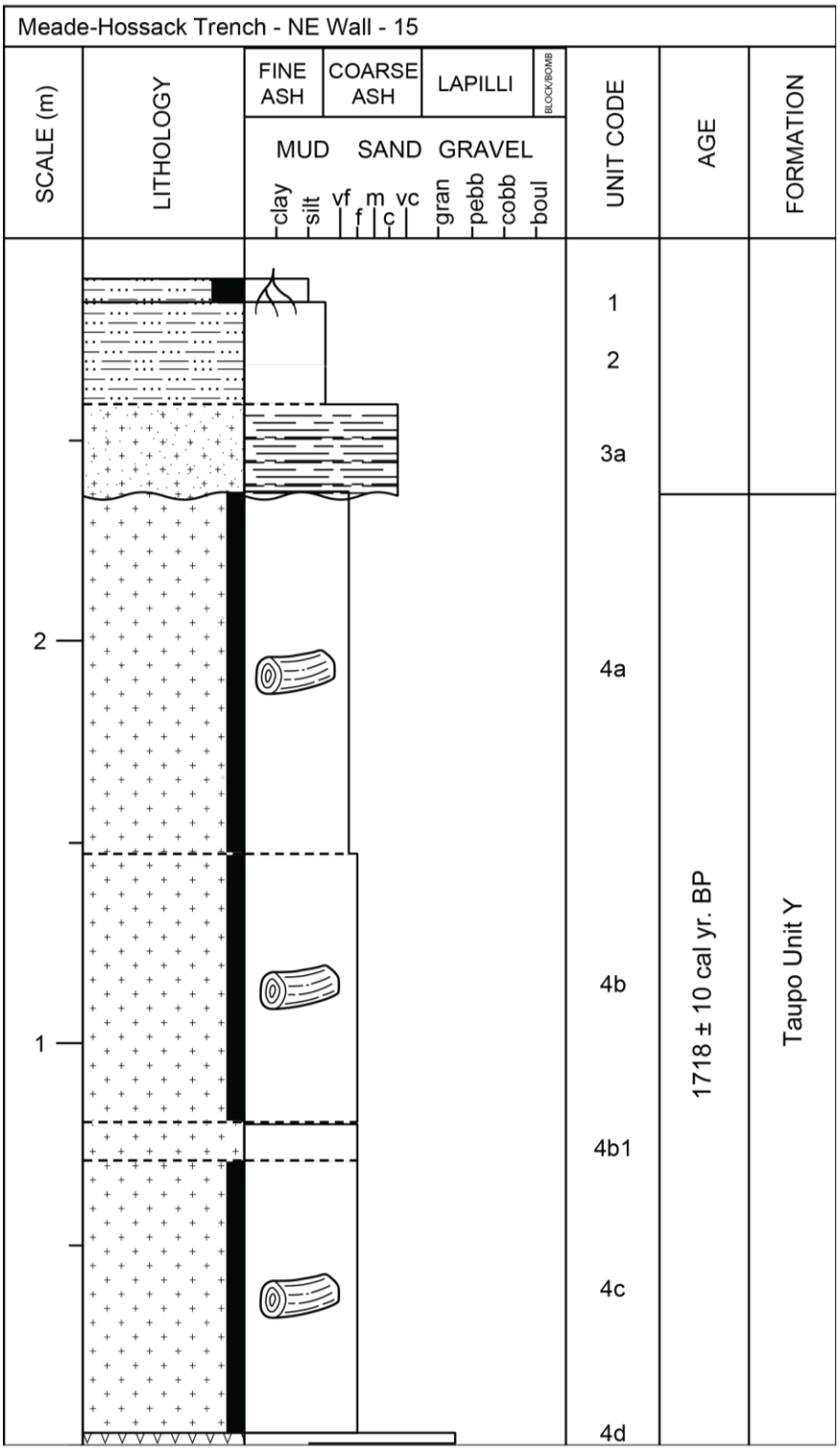

Figure 15. Stratigraphy of the NE wall at vertical batter 15 on Figure 6. Unit codes correspond to codes on Figure 6 and unit descriptions in Table 4. Gradational boundaries are delineated with a dashed black line. Sharp boundaries are delineated with a bold black line. Tree log symbols represent carbonised tree logs and branches. Age for Taupo Unit Y from Hogg et al. (2012).

The SW wall at vertical batter 15 is also dominated by Taupo Unit Y deposits, although 4d is not exposed on the wall at this location (Figure 16). Unit 4c is the deepest in the stratigraphy, at a thickness of around 0.7 m. It contains logs up to 0.8 m long and 0.3 m in width, with associated “chimney” gas escape structures. 4a is overlain by around 0.5 m of 4b, and the sequence is completed with 1 m of 4a. The total exposed thickness of the Taupo Unit Y deposits at this batter is around 2.2 m. The ignimbrite is overlain by around 0.4 m of Unit 2, and 40 mm of Unit 1.

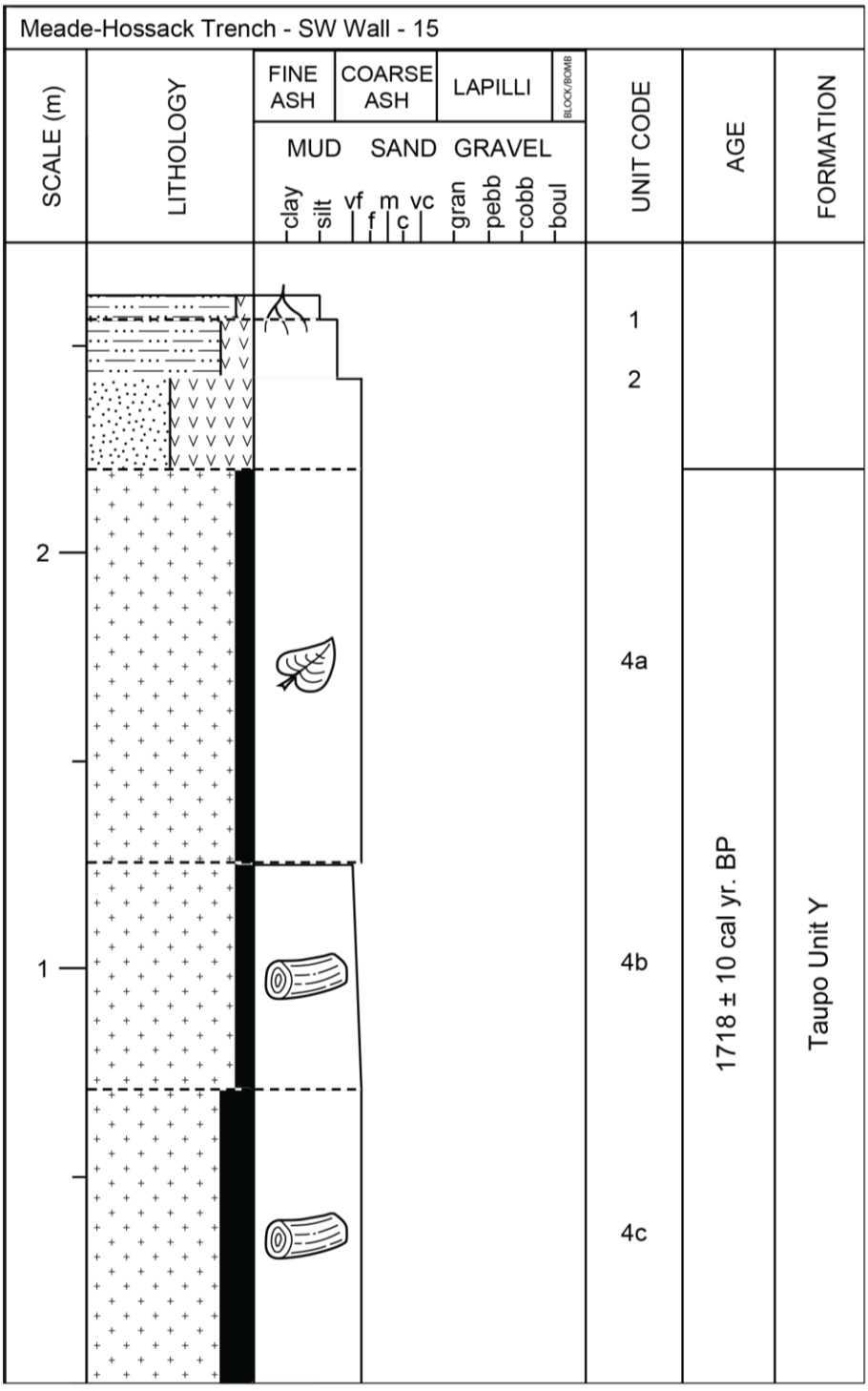

Figure 16. Stratigraphy of the SW wall of the trench at vertical batter 15 on Figure 7. Unit codes correspond to codes on Figure 7 and unit descriptions in Table 4. Gradational boundaries are delineated with a dashed black line. Tree log symbol represents carbonised tree logs and branches, leaf symbol represents smaller carbonised plant material. Age for Taupo Unit Y from Hogg et al. (2012).

3.3.4: Outcrop stratigraphy and photographs

Around 50 m northwest of the trench site, on a hill ~410 m asl and 15 m above the northernmost edge of the trench, tephras and siliceous sinters are exposed (Figure 17). Although the outcrop is not the main focus of the study, some of the observed units could immediately be correlated with units in the trench.

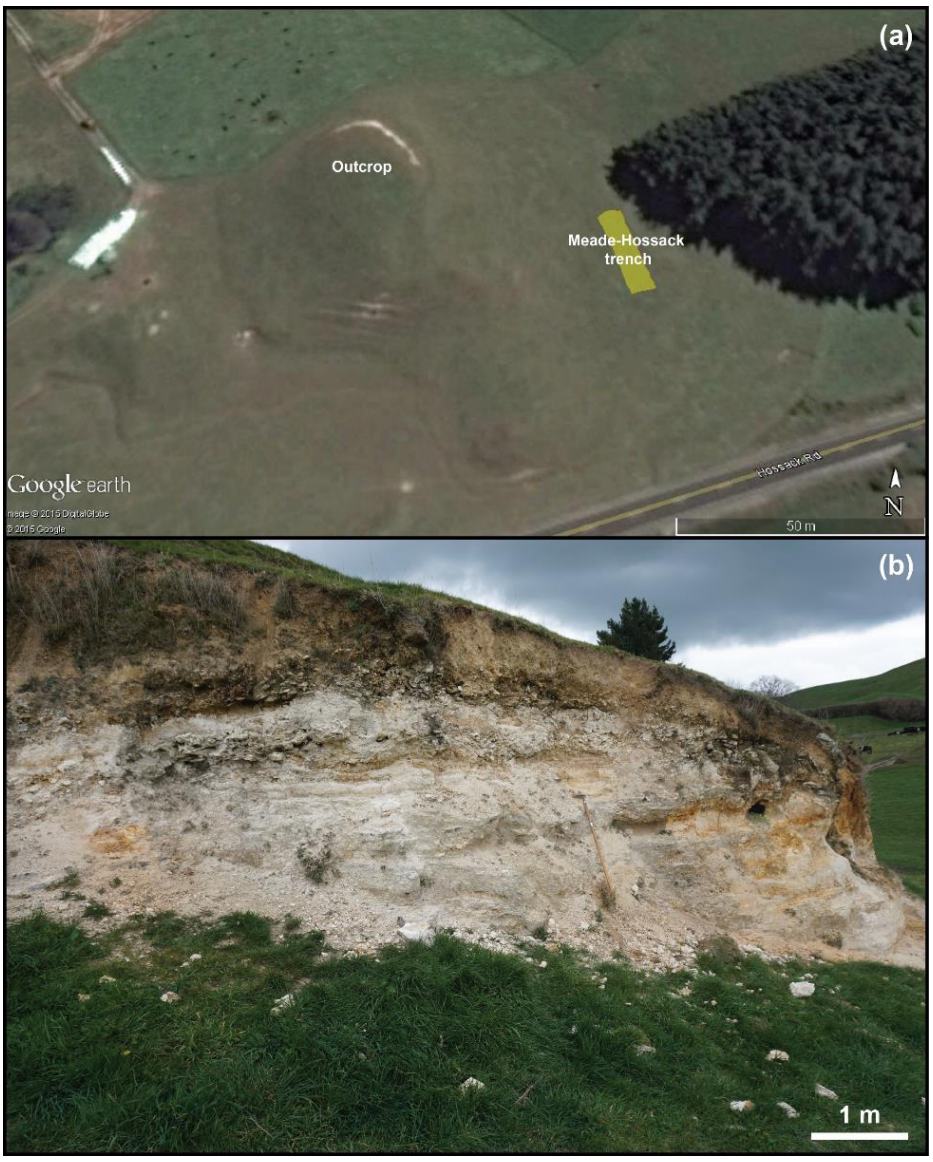

Figure 17. a) Location of the outcrop in relation to the Meade-Hossack trench (shown as a rectangle). b) Photograph of outcrop from southeast (left) to northwest (right).

A basic stratigraphy of the outcrop and short descriptions of some units were collected with a mind to incorporate the outcrop information into the overall timeline for sinter development in the area, as well as informing possible models of paleotopography and fluid flow.

The stratigraphy from top to bottom (Figure 18) includes hard white pumice lapilli, probably Kaharoa Tephra (AD 1314 ± 12 years) (Hogg et al., 2003), overlying a thin deposit of Taupo Unit Y ignimbrite which has a discontinuous charcoal-rich base. Several ashy layers overlie the youngest sinter deposit. A layer of ashy colluvium separates the youngest sinter from another, older and slightly thicker sinter deposit which overlies a buried soil. A thin yet distinctive pink pumiceous ignimbrite overlies the next oldest sinter deposit. A fine white ash containing lithics and accretionary lapilli overlies a thick sinter deposit filled with silicified plant material, largely twigs. The twigs were dated by radiocarbon to give a conventional radiocarbon age of 34360 ± 460 ^{14}C yr BP (NZA 33105), and calibrated using Intcal13 (Reimer et al., 2013), resulting in an age of 38,850 ± 1118 cal. yr. BP. Underneath the dated sinter is a succession of grey and white laminated ash alternating with thin (< 50 mm) glassy black sinter horizons. A hydrothermal vent breccia underlies the succession. A thin pumice lapilli and glassy black sinter horizon then overlie an unknown thickness of Ohakuri Ignimbrite exposed in the small pit excavated at the base of the outcrop.

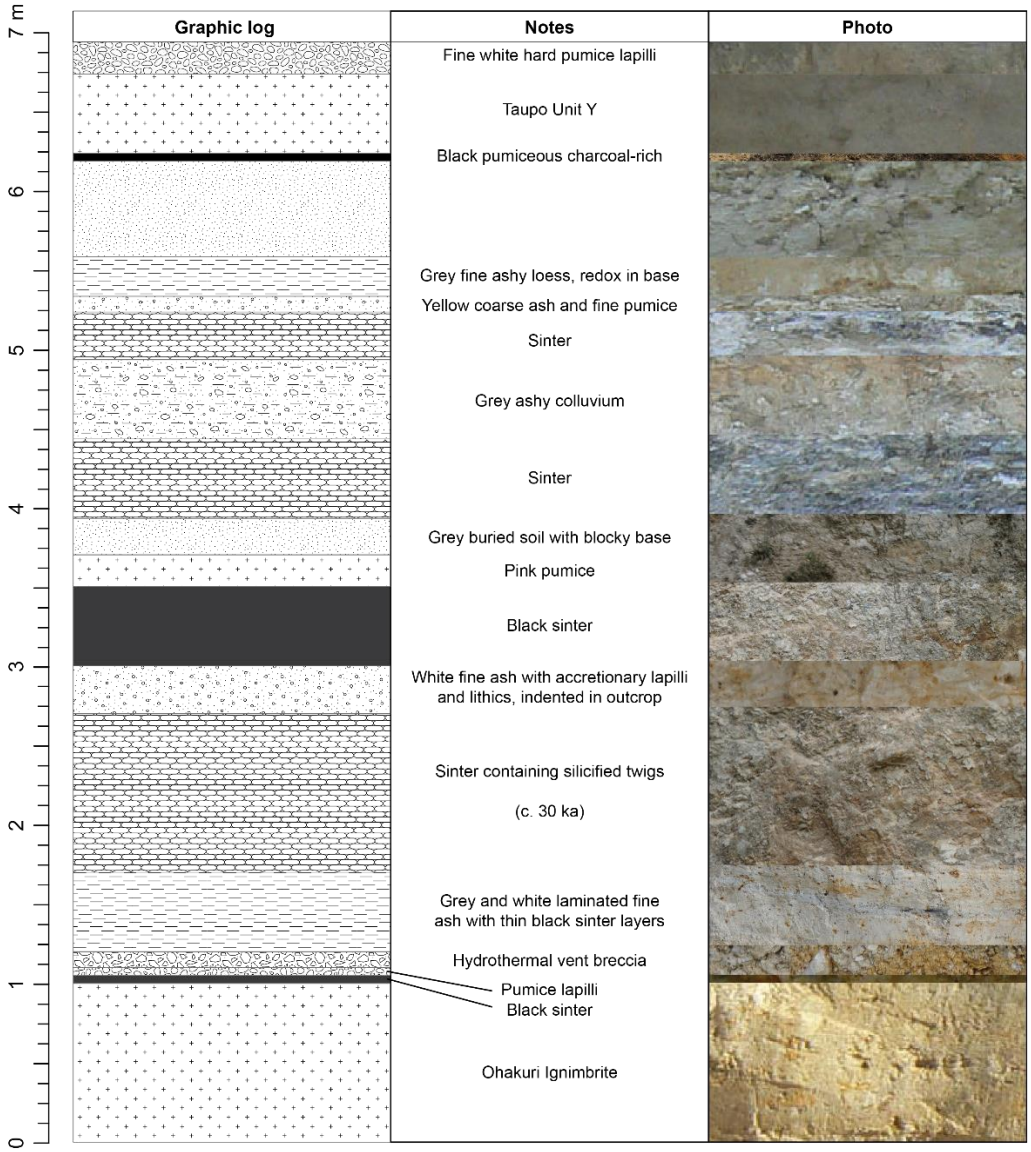

Figure 18. Simplified stratigraphic log of the outcrop at Hossack Road, including a small pit dug during trench excavation.

A block sag was observed within the breccia bed on the outcrop (Figure 19). The difference in the steepness of the sides suggests a low angle of ejection from the vent. The location of the vent from which the breccia originated is proposed as being south or southeast of the outcrop, as the steeper side of the sag more sharply impacted appears to be oriented towards the northwest.

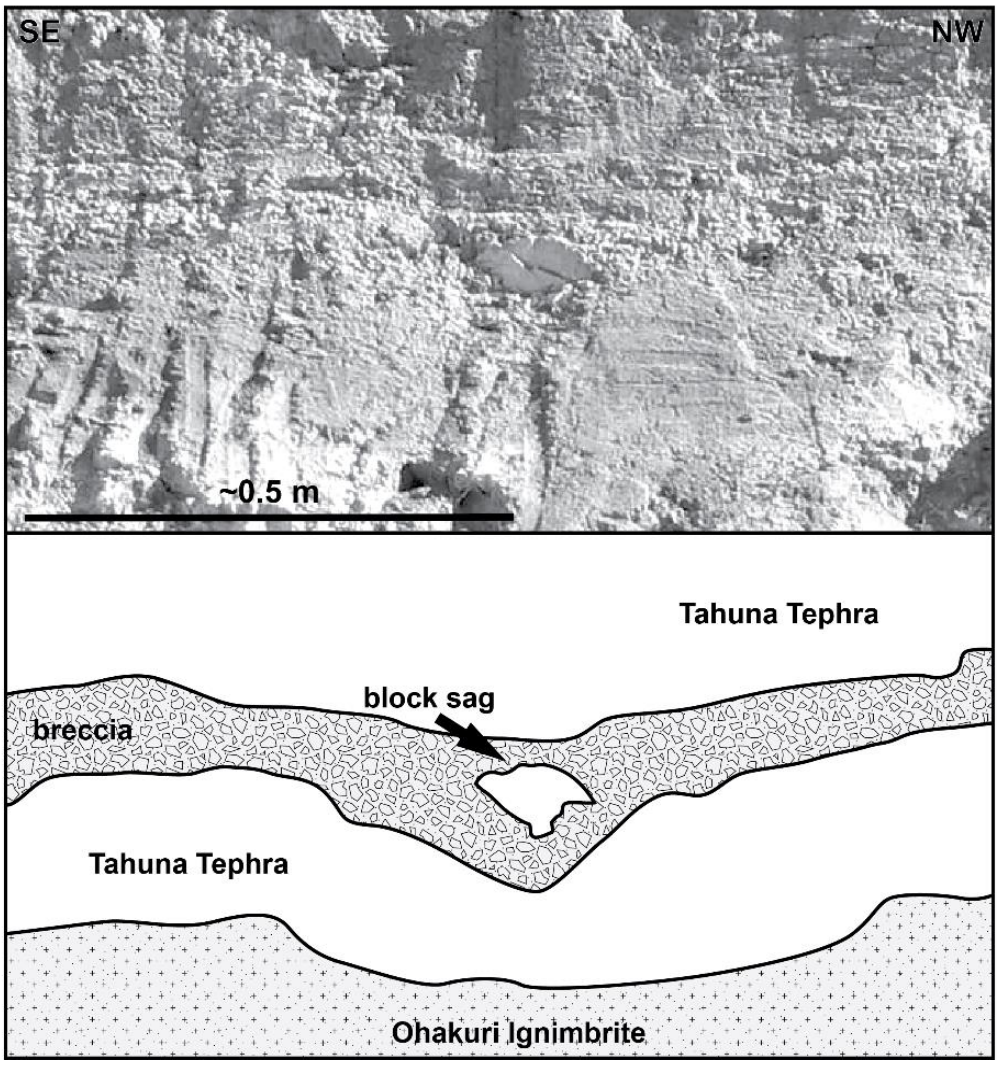

Figure 19. Photo and accompanying simple sketch of the block sag within hydrothermal vent breccia on the outcrop at the Meade-Hossack site.

3.4: Interpretations

There were few clear examples of marker tephras or other units immediately identifiable based on physical (field) properties and stratigraphy.

Units 4a through 4e, including the Taupo Ignimbrite, Taupo (Plinian) Pumice and Rotongaio Ash (1718 ± 10 cal yr BP; Hogg et al., 2012), were easily identified based on their physical properties and surficial stratigraphic position. More tentatively, Unit 25 was suggested by I.A. Nairn (pers. comm. Nov. 2014) to be Rotorua Tephra (15,635 ± 412 cal yr BP; Lowe et al., 2013), based on the texture and high biotite content. Units 21 and 21a were suggested by I.A. Nairn (pers. comm. Nov 2014) to be the Rotoma Tephra (9423 ± 120 cal yr BP; Lowe et al., 2013), which could be partly confirmed by the abundance of cummingtonite in the ferromagnesian mineralogical assemblage (Nairn, 2002), although Whakatane Tephra (5526 ± 145 cal yr BP; Lowe et al., 2013) also contains cummingtonite (Froggatt and Lowe, 1990), thus a more detailed geochemical profile would be necessary to discern one from the other (unless one was stratigraphically above the other and able to be separated chronologically via an intervening paleosol). I.A. Nairn (pers. comm. Nov. 2014) identified Unit 45, which at first glance appeared to be lake sediments, as Ohakuri Ignimbrite. Unit 45 could be part of the Ngakuru Formation of the Huka Group lake sediments, but the age of the sediments is not known at the location of the study site and the deposits may be outside the age range for ^{14}C dating. Unit 45 hereafter is assumed to be Ohakuri Ignimbrite as it can provide a known age constraint for sinter formation and fault activity, but further testing is recommended.

Units 4b, 4b1, and 4a may be reworked Taupo Ignimbrite from lahars immediately following deposition from the initial pyroclastic density current. Alternately, this group of units could represent deposits from pulses of pyroclastic density currents over the course of the eruption, perhaps occurring on different days. Unit 3a, the interbedded deposit infilling a scour in the top of 4a, is likely to be Taupo Pumice Alluvium.

The variable thickness in Taupo Unit Y deposits in the trench, being < 0.2 m thick in the northern end of the trench and >2 m thick in the southern end of the trench, as well as the downward-draping shape of the undeformed tephras (Units 20 through 25 between vertical batters 0 and 10 on each wall), indicate the presence of a paleovalley. Taupo Unit Y is also the youngest deformed unit in the trench, disrupted by the largest observed fault plane. The paleovalley was unlikely to have been formed exclusively during the most recent movement on the fault plane disrupting Taupo Unit Y; rather, Taupo Unit Y has infilled a pre-existing paleovalley, the size of which may have been exaggerated by fault movement.

Sinter in the trench is observed within Unit 45, the Ohakuri Ignimbrite, and also within Unit 25 on the NE wall. If *in situ*, the sinters in both cases could be subsurface depositions as they are found within units, rather than strictly above or below. The age of the respective sinters can be constrained to < 240 ka (post-Ohakuri) and < 15.6 ka (post-Rotorua) using the field-based identifications. The age constraints fit with the stratigraphy of sinters observed on the outcrop, which are also post-Ohakuri. The youngest sinters on the outcrop are not well-constrained chronologically, but sinter has continued to form more recently than c. 39 ka at the Hossack Road location on the basis of the ^{14}C age on the sinter reported earlier. Sinter deposition appears to have ceased entirely well before Taupo Unit Y was emplaced.

The sinters in the trench are not readily correlated with those on the outcrop in terms of their field-identifiable (physical) characteristics. It is possible that the outcrop sinters have largely been deposited at the surface, resulting in clear-cut boundaries and sub-horizontal position, with silicification of twigs in one of the horizons. The paleohydrothermal system may therefore have been concurrently depositing silica at both the surface and in the subsurface. The terrace-like nature of the sinter within the Ohakuri Ignimbrite in the trench in a position below the elevation of sinter of a similar age range in the outcrop also brings to mind a cascading effect with possible analogy to the modern-day Orakei Korako geothermal area.

3.5: Conclusions

Paleoseismic trenching at the Meade-Hossack site revealed a succession of sinters, tephras, paleosols, and ignimbrites disrupted by multiple fault planes. Field-identifiable marker beds include Taupo Unit Y and Ohakuri Ignimbrite, which are both correlatable between the trench and the outcrop on the hill. Two more tentative identifications were made, with Unit 25 correlated with Rotorua Tephra (c. 15.6 ka) and Units 21 and 21a with Rotoma Tephra (c. 9.4 ka). The youngest disrupted unit in the trench is Taupo Unit Y, which indicates the most recent movement on the Whirinaki Fault strand at the Meade-Hossack site has occurred after 1718 ± 10 cal. yr. BP. The presence of sinter within the Ohakuri Ignimbrite deposits in the trench may be an indicator of subsurface deposition, which may have preferentially affected more permeable parts of the Ohakuri unit, and constrain the age of the sinter to < 240 ka, i.e. post-Ohakuri. If Unit 45 is instead revealed by future work to be lake sediments of the Huka Group, the sinter likely formed on top of it and was subsequently overlain by lake sediments. ^{14}C dating could better constrain sinter ages if Unit 45 is Huka Group provided suitable material was obtainable. If the identification of Unit 25 as Rotorua Tephra is correct, then the youngest sinter in the trench can be constrained as < 15.6 ka. The sinters on the outcrop are more likely to be surface depositions, but fit within the age constraints from the trench.

Chapter 4: Mineralogical descriptions of tephras at the Hossack Road site from microscopic petrography

4.1: Introduction

Smith et al. (2005) stated that it is possible to classify all deposits from the Okataina and Taupo Volcanic Centres solely by ferromagnesian mineralogy (Table 5). In practice, the stratigraphic position of a tephra (relative age) is used in addition to mineralogical assemblages to identify and correlate tephras (e.g. Lowe, 2011). Orthopyroxene is dominant across most deposits, so its scarcity is more diagnostic than its presence. Fe-Ti oxides are ubiquitous across all deposits and may only factor in when considering relative abundances. Cummingtonite and biotite are the most diagnostic minerals, being abundant in only a limited number of tephras.

Table 5. Summary of ferromagnesian mineral assemblages for deposits from the Okataina and Taupo Volcanic Centres (after Smith et al., 2005).

	Deposit	**Age**	**Ferromagnesian mineralogy**
Okataina Volcanic Centre	Low-K_2O Rotoiti	~50 ka	cgt[2] > fe-ti[4] >> hbl[5] + opx[6]
	High-K2O Rotoiti	~50 ka	bi[1] > hbl ± cgt > fe-ti ± opx
	Earthquake Flat Pyroclastics	~50 ka	bi > hbl ± cgt > fe-ti ± opx
	Old Mangaone Subgroup	40-35 ka	opx + hbl > cpx[3] + fe-ti
	Young Mangaone Subgroup	35-31.5 ka	opx + hbl > fe-ti
	Rotorua Subgroup	post-25 ka	opx + hbl ± cgt ± bio > fe-ti
	Te Rere	25 ka	opx + hbl > fe-ti > cpx
	Rotorua	15.6 ka	bio > hbl > fe-ti > opx
Taupo Volcanic Centre	Okaia Subgroup	42-27.3 ka	opx > hbl > fe-ti > bio
	Okaia	29 ka	opx > hbl > fe-ti
	Oruanui/Kawakawa	25.4 ka	opx > hbl > fe-ti
	Dacites	20.5-17 ka	opx > cpx > fe-ti
	Units B-E	11.7-10 ka	opx > fe-ti > cpx ± hbl
	Units F-S	7.05-3.55 ka	opx > fe-ti ± hbl
	Units U-V	2.85-2.8 ka	opx > fe-ti
	Units X-Y	2.2-1.8 ka	opx > fe-ti > cpx
	Unit Z	1.8 ka	opx > fe-ti

[1]biotite, [2]cummingtonite, [3]clinopyroxene, [4]Fe-Ti oxides, [5]hornblende, [6]orthopyroxene

Ferromagnesian assemblages from samples of key tephra beds in the Meade-Hossack trench may help narrow down and confirm the identification of units, or at least help to determine the volcanic centre of origin. The technique has limitations because abundances of ferromagnesian minerals can vary due to differences in dispersion, and other factors, resulting in different abundances for different locations (e.g. Juvigné and Porter, 1985; Lowe, 1988a).

4.2: Methods

4.2.1: Preparation by washing and sieving

Mineral grains (crystals) and glass shards were washed to remove any clay and organic matter in order to get clean surfaces for identification using a petrographic microscope and for single-grain geochemical analyses. Wet sieves were used to separate the size fractions of the washed grains. The procedure is as follows:

1. A subsample of bulk tephra was added to a clean 600 ml beaker. If the tephra was clayey, a larger subsample was used. Pumice clasts were crushed using a ceramic mortar and pestle.
2. Up to 250-300 ml of tap water was added to the beaker.
3. Beaker was placed into an ultrasonic bath. The model used here was the Astrason Ultrasonic Cleaner.
4. Every few minutes the beaker was retrieved from the bath and rested for 20 seconds to allow the more dense grains to settle. The water was carefully discarded along with any clay particles in suspension, then new water was added and the beaker was placed bath into the ultrasonic bath. The process was repeated until the water was clear, with only very fine sand particles in suspension.
5. The material was poured through clean stacked wetted sieves for > 1 mm, > 250 µm, and > 63 µm. Grains were washed through with a light squirt of water.
6. Grains were washed from the sieves into 100 ml beakers labelled with the appropriate size fraction (> 1 mm, > 250 µm < 1mm, and > 63 µ < 250 µm) and sample number. A vacuum pipette was used to draw off excess water once the material was transferred.
7. Beakers were placed in an oven set at 65°C until the grains were completely dry.

8. Dry grains of the > 1 mm fraction and the > 250 µm < 1 mm fraction were transferred into phials labelled with fraction details and sample number. The > 63 µm < 250 µm fraction was kept in its beaker until mineral separation.

4.2.2: Mineral separation

Electromagnetic separators were used to sort heavy mineral grains from light mineral grains and further isolate (purify) the volcanic glass shards. Separators were cleaned thoroughly with an air hose in between each sample to avoid contamination.

1. The > 63 µm < 250 µm fraction was poured through a clean vertical Frantz magnetic separator running at 2.0 A. Lighter, less magnetic minerals were collected onto a clean sheet of paper, transferred into a beaker, and set aside.
2. Another clean sheet of paper was placed underneath the chute of the magnetic separator and the machine was switched off. The heavy minerals fell from the sheet and were collected on the paper. Minerals still stuck on the chute were brushed through using a small, clean, dry paintbrush.
3. The heavy minerals were transferred into a labelled phial and set aside.
4. Steps 1-4 were repeated until the light mineral fraction appeared to be free of heavy mineral grains.
5. A clean tilted Frantz magnetic separator was set to 15°/15°, operating at 0.6 A, with the chute vibration setting at 2.
6. The lighter minerals were poured into the hopper, chute vibration was increased as needed to shake all of the grains down the chute.
7. The grains were collected into two cups, with the less magnetic in the front cup and more magnetic in the back cup. The less magnetic grains were transferred into a beaker and the cup set back into place.

8. Chute vibration was reset to 2, and the current increased to 0.8 A.
9. The less magnetic grains were poured into the hopper, and chute vibration increased as needed.
10. The non-magnetic (glass) and magnetic fractions were transferred into separate labelled phials.

4.2.3: Slide preparation

For each sample, a subsample of grains from each of the heavy mineral and more magnetic light fractions was transferred to a clean welled glass slide. A drop or two of clove oil was added to each well and the mixture was stirred to distribute the grains evenly. Slides were labelled with sample code and fraction type.

4.2.4: Mineral identification

Temporary slides were viewed under an Olympus BH-2 petrographic microscope. Minerals were identified by diagnostic optical properties under plane polarised light and cross-polarised light. Properties used included colour, pleochroism, relief, crystal habit, interference colours, birefringence, extinction angle, and special characteristics such as twinning.

Minerals and mineraloids (glass) were counted for each quadrant viewed, using the crosshairs as dividers. Counts were recorded on data sheets such as that in Figure 20, with multiple counts conducted for each subsample. Other observations were also noted on the data sheets, such as whether selvedges were present or not on mineral grains, presence of microlites or embayments on crystals, and any compositional zoning.

SAMPLE	Ferromags					Glass		Felsics		
#	Hyp	Hbl	Aug	Cgt	Bio	Brown	Clear	Quartz	Fspar	Other/Notes

Figure 20. Example of datasheet used for recording initial mineralogical observations.

4.3: Results

The samples from the trench tended to show the same small group of minerals in varying abundances (Table 6). Fe-Ti oxides, orthopyroxenes, clinopyroxenes and hornblende were common to all samples. Biotite was found in most samples, and cummingtonite was found in five of the samples.

Table 6. Summary table of ferromagnesian mineral percentage distributions of samples from the Meade-Hossack trench. Sample locations are on Figures 7 and 8.

Sample Code	**Hbl**[1] **%**	**Opx**[2] **%**	**Cpx**[3] **%**	**Cgt**[4] **%**	**Bi**[5] **%**	**Fe-Ti**[6] **%**
HT10	9.8	26.2	13.1	1.6	27.9	21.3
HT11	27.0	16.9	5.6	-	33.7	16.9
HT12	12.6	26.6	13.1	-	0.5	48.7
HT13	10.6	31.9	14.9	19.2	2.1	21.3
HT14	15.4	28.2	30.8	-	-	34.7
HT15	8.2	34.7	16.3	-	-	40.8
HT16	8.2	44.9	12.2	-	-	34.7
HT17	20.4	42.7	14.0	-	0.6	22.3
HT18	13.6	43.2	14.8	-	-	28.4
HT19	10.9	50.0	14.1	-	3.1	18.8
HT20	6.2	31.0	15.9	4.4	0.9	38.4
HT23	0.7	44.5	21.2	2.1	0.7	30.8
HT24	1.4	35.6	21.9	-	2.7	38.4
HT25	4.5	39.9	21.1	-	0	34.6
HT26	14.8	53.1	13.6	-	3.7	14.8
HT27	11.0	51.2	12.2	-	0.0	25.6
HT28	8.4	36.1	24.1	-	1.2	30.1
HT29	12.8	27.7	5.0	-	9.9	44.7
HT30	4.4	16.8	5.8	-	3.7	69.3
HT31	3.4	47.5	17.0	-	-	27.1
HT35	1.5	32.6	22.2	-	1.5	42.2
HT36	11.5	21.8	9.2	5.8	6.9	44.8

[1]hornblende, [2]orthopyroxene, [3]clinopyroxene (predominantly augite), [4]cummingtonite, [5]biotite, [6]Fe-Ti oxides

4.4: Interpretations

HT10 (Unit 23) and HT11 (Unit 24) are biotite-rich, which (assuming an age range younger than c. 25 ka) narrows the list of likely tephras to Kaharoa, Rotorua, Rotoma, Rerewhakaaitu, Okareka, and Puketarata. Biotite abundances in percentage terms are higher than in Smith et al. (2005) for any known eruptives, though HT11 aligns quite well with Rotoma in terms of overall ferromagnesian mineralogy (bi > hbl > fe-ti + opx). HT10 mineralogy is summarised as bi > opx > fe-ti + hbl, which aligns best with Rotorua Subgroup deposits. However, the associated unit is stratigraphically younger than that for HT11, so if Unit 23 is Rotorua, Unit 24 cannot be Rotoma. However, the high biotite content in samples HT10 and HT11 does suggest that Units 23 and 24 are likely to have originated from the Okataina Volcanic Centre.

HT27 (opx > fe-ti > hbl + cpx) is from the same stratigraphic unit as HT11, though the sample was taken from the NE wall of the trench rather than the SW wall. The absence of biotite in this sample does not match with the high biotite content of HT11. It may be the case that the unit boundary has been incorrectly determined, or spatial variability has resulted in a biotite-poor pocket. HT28 (opx > fe-ti > cpx > hbl) is taken from just below HT27, in the base of Unit 24 on the NE wall. It is dissimilar to samples from other units in terms of percentage abundances and loosely fits within the profile for Taupo Units B through E.

HT12 (Unit 25) is from the unit tentatively identified in the field as Rotorua, but the biotite content is low in the ferromagnesian mineral assemblage (fe-ti > opx > hbl + cpx), observed only in trace (<1%) amounts. Unit 25 is therefore unlikely to be Rotorua. The shiny dark grains observed in the field may have been Fe-Ti oxides or obsidian flakes. It is unlikely that the biotite was lost during sample processing as nothing differed about the method used to process this sample compared with the other samples.

HT30 is from Unit 25 on the NE wall of the trench and was expected to have a similar assemblage to that of HT12. The minerals present are similar, though abundances have slight differences in that Fe-Ti oxides are higher by ~20%, giving lower abundances for hornblende, orthopyroxenes,

and clinopyroxenes. HT29, also from Unit 25, is similar to HT12, although with higher biotite and lower clinopyroxene abundances. Note that HT29 is near the boundary with Unit 24, and may be intermixed.

HT13 and HT18 are in stratigraphic association (from units 21a and 21, respectively). Both are high in orthopyroxenes. Units 21 and 21a were tentatively identified as Rotoma Tephra, and although the orthopyroxene percentages are close to the range of 49-69% given by Smith et al. (2005), the overall assemblage and relative abundances in HT13 (opx > fe-ti > cgt > cpx + hbl) do not correlate well with any of the known tephras, and HT18 (opx > fe-ti + cpx + hbl) fits closer to Taupo Units B through E.

HT15 was collected from what was identified in the field as Taupo Unit Y. The ferromagnesian mineralogy fits with the field identification, dominated by orthopyroxene, Fe-Ti oxides, and clinopyroxene. The relative abundance of hornblende is <15% which accords with the findings of Froggatt & Lowe (1990). HT14, collected from the same unit on the NE wall, has a similar mineral assemblage (cpx > opx > fe-ti + hbl) but is higher in clinopyroxene.

HT16 (opx > fe-ti > hbl > cpx) was taken from the top of Unit 21 on the SW trench wall. It fits into the mineralogical profile for Okataina deposits in general, but does not closely align with any specific tephra. HT17 is taken from Unit 23 on the SW trench wall and shares a similar mineralogical composition in terms of overall abundance (opx > fe-ti > hbl > cpx), but contains over twice as much hornblende as HT16, and trace amounts of biotite.

Samples HT19, HT20, HT23, HT24, HT25, and HT26 are all taken from Unit 20x on the NE trench wall, weathered tephric material that may have resulted from developmental upbuilding, with no discernible horizonation. It is expected that samples will share similar compositions to other samples taken from other units at similar points in the stratigraphy, but weathering may have had an effect on abundances.

HT19 (opx > fe-ti > cpx > hbl + bi) is from the upper part of Unit 20x. The closest fit for mineralogy is with Taupo Units B through E, though there may be more biotite in the sample than might be expected from

Taupo tephras. HT20 (fe-ti > opx > cpx > hbl + cgt), taken from around 0.1 m beneath HT19, does not match any assemblage particularly well. The closest match is Taupo Units X and Y. Sample HT23 (opx > fe-ti > cpx) is taken from the middle of Unit 20x, at a similar stratigraphic level to the top of Unit 23 or the base of Unit 22 if the curve of the paleotopographic surface is followed. The ferromagnesian minerals are overall closest to Taupo Units X and Y, but there are trace amounts of biotite and hornblende, and the sample contains ~2% cummingtonite. HT24 (fe-ti > opx > cpx + hbl + bi) is also taken from the middle of Unit 20x, at a similar stratigraphic level to Unit 23. It contains far less biotite and more Fe-Ti oxides than samples from Unit 23, giving further support to the identification of 20x as a mixed unit. HT25 (opx > fe-ti > cpx + hbl) is also at a similar level to Unit 23, but contained no biotite. HT26 (opx > fe-ti + hbl > cpx + bi) is taken from the lower part of Unit 20x, at a similar stratigraphic level to the top of Unit 24. The ferromagnesian assemblage shares similarities with deposits from both the TVC and the OVC.

HT31 (opx > fe-ti > cpx + hbl) is taken from the upper part of Unit 10, on the hanging wall of the main fault plane on the SW trench wall. Unit 10 needs to be correlated with one of the other units in the trench. The ferromagnesian assemblage is similar to that of HT12 (Unit 25), HT16 (Unit 21), and HT18 (Unit 21). In terms of abundances, HT31 is closer to HT16 and HT18 than to HT12, which is higher in hornblende and Fe-Ti oxides, and lower in orthopyroxenes. It is likely that Unit 10 is the downthrown part of Unit 21. HT36 (fe-ti > opx > hbl > cpx > bi) was taken from a different section of Unit 10, notably less downthrown than that of sample HT31. It contains higher hornblende and biotite contents and lower pyroxene content than HT31. It is not similar enough to any other samples to make a conclusive correlation, expect perhaps HT29 (Unit 25).

HT35 (fe-ti > opx > cpx > bi + hbl) is taken from Unit 11, another unit on the hanging wall on the SW side of the trench. The assemblage is somewhat similar to that of sample HT24, which is from 20x, the mixed/undifferentiated unit on the NE wall.

As an aside, the subsample of HT30 contained 2 rounded grains of riebeckite, identified by their distinctive blue pleochroism. Riebeckite (an

amphibole) is unreported in the mineral assemblages for tephras from the TVC and OVC, but does appear in deposits from Mayor Island, a peralkaline caldera volcano ~26 km offshore in the western Bay of Plenty (Buck et al., 1981; Houghton et al., 1992) and defined as the locus of the Tuhua Volcanic Centre by Froggatt and Lowe (1990). Shane et al. (2006) mentioned that Pillans and Wright (1992) found Mayor Island tephras (pre-Tuhua) mixed with OVC tephras "at ~13.8, 33, and 45 ka" up to 125 km NNE of the island, Manighetti et al. (2003) identified Tuhua Tephra in a core off the coast of the North Island, around 140 km east of Cape Turnagain, and the Tuhua Tephra has been observed onshore at multiple locations (e.g. Hogg and McCraw, 1983; Lowe, 1988; Lowe et al., 1999).

Dates given for the Mayor Island tephras are given in Table 7. Shane et al. (2006) also found Mayor Island cryptotephras within Rerewhakaaitu (17.8 ka), Te Rere (25.5 ka), and Hauparu (~35 ka) tephras. Lowe (1988b) also reported a Mayor Island-derived tephra aged c. 17 cal ka in the central Waikato region, likely to be the Te Paritu Tephra (Houghton et al., 1992). Kennedy and Froggatt (1984) reported the presence of peralkaline Tuhua Tephra, and W.R. Esler reported that the Te Paritu tephra and several older ones occurred as cryptotephras in the Rotorua area (pers. comm. with D.J. Lowe 2006). Given the potential extent of Mayor Island tephras based on existing isopach models for the Tuhua Tephra (Manighetti et al., 2003), and unpublished data, there may be a Mayor Island cryptotephra within Meade-Hossack Unit 25.

Another marker mineral for Mayor Island tephras, aegerine (Buck et al., 1981) was not observed in the HT30 slide, but crystals may be present in the rest of the sample, or could have been misidentified as augite. Contamination was considered another possibility, though the equipment used for processing samples had been cleaned thoroughly and had not recently been used for work on Mayor Island tephras.

Table 7. List of Mayor Island tephras and their dates from Shane et al. (2006).

Mayor Island Tephra	**Date (ka)**
M1	>45
M2	<45
M3	40.5
M4	37.4
M5	22.2
M6	14.2
M7 (Tuhua)	7

4.5: Conclusions

Units 23 and 24 are likely to have originated from the Okataina Volcanic Centre. Unit 25 is not Rotorua Tephra as first thought, but nevertheless is likely to be from the OVC. Grains of riebeckite in a sample from Unit 25 may indicate the presence of a Mayor Island-derived cryptotephra. Units 21 and 21a have a mineral profile closest to Taupo-derived Units B through E, but the correlation is not strong and some samples also fit with general OVC assemblages. The mineralogy for samples collected from the unit identified in the field as Taupo Unit Y (from its physical properties and stratigraphic position) confirm that identification. Unit 23 is likely to be sourced from the OVC. The samples from Unit 20x show some similarities with Taupo-derived Units B through E, or Taupo Units X and Y, but no definitive correlations can be made. Unit 10 may either be correlated with Unit 21 or Unit 25. Unit 11 is similar to one of the Unit 20x samples.

The results of the ferromagnesian mineralogy are largely inconclusive other than suggesting possible volcanic sources, and even then these may be somewhat ambiguous. Abundances are affected by high amounts of Fe-Ti oxides which may suggest reworking of tephra deposits has occurred. Errors in identification of minerals may also affect totals. The overall lack of diagnostic minerals and the narrow range of minerals represented, along with the discrepancy in ferromagnesian mineral abundances between trench units and known tephras, underscores the need for additional geochemical data when attempting to identify unknown deposits.

Chapter 5: Major and minor element composition of volcanic glass shards from tephras at the Hossack Road site

5.1: Introduction

Electron probe microanalysis (EPMA) of glass from tephras was first conducted by Smith and Westgate (1968), who used the major element data (as oxides) as a correlation tool. It is now universally used as a key technique in tephrochronology (Lowe, 2011), with numerous case studies both in New Zealand and overseas. For example, Giacco et al. (2014) used EPMA of glass in combination with Sr isotope compositions and $^{40}Ar/^{39}Ar$ dating to identify and correlate a succession of Middle Pleistocene tephras, establishing a new tephrostratigraphic record for the Mercure Basin, southern Italy, whereas Smith et al. (2005) have used EPMA to determine glass and mineral compositions of post-50 ka tephras from the Okataina Volcanic Centre (OVC) and the Taupo Volcanic Centre (TVC).

EPMA as a technique for analysing glass has inherent difficulties (including loss of Na and K because of volatilisation), and has been modified substantially regarding analytical protocols since 1968 (e.g. Froggatt, 1983, 1992; Kuehn et al., 2011; Hayward, 2012; Hall and Hayward, 2014). However, the fundamental basis of the method remains unchanged. An electron gun (Figure 21) focuses a beam of between 0.5 and 3 µm (usually wider for glass assay, ~10–20 µm) onto the surface of a flat sample, generating X-rays which pass through the sample and are received by a detector, such as wavelength dispersive spectrometer(s) (WDS) or a solid-state energy dispersive detector (EDS) (Wittke, 2006; Pearce et al., 2014).

Samples for EPMA can be prepared as either thin sections or blocks, but they must be flat to help counter absorption and fluorescence effects from the X-rays passing through the sample, though the latter can be corrected for with software (Pearce et al., 2014).

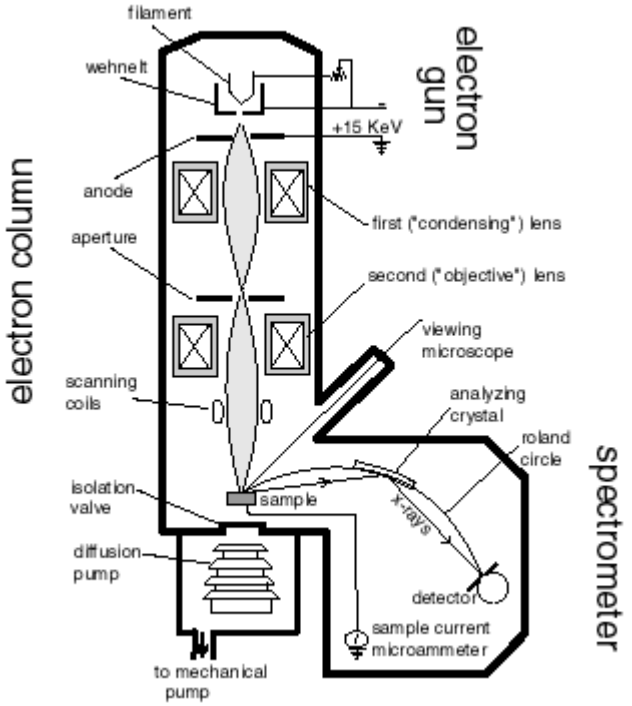

Figure 21. Schematic example of EPMA instrumentation (Wittke, 2006).

Hall and Hayward (2014) have devised a process of sample storage, transport, and preparation which facilitates EPMA of glass shards in the 10 to 50 µm size range. For storage and transport, Hall and Hayward (2014) recommend minimal handling, use of wide and shallow plastic containers for storage and transfers, only transferring samples when dry, and washing the grains in petroleum spirit to remove dust and residue. There are three main steps in sample preparation: mounting the samples onto a glass-backed rubber sheet with epoxy resin and fitting a ring mould, filling the ring mould with more resin and curing for at least 72 hours, and grinding and polishing. A general flowchart for sample preparation is summarised in Figure 22, with more specific details given in Hall and Hayward (2014), and a visual step-by-step chart for preparing multiple samples on the same block is presented in Figure 23. Ultrasonic cleaning is recommended immediately after grinding and polishing to remove residual abrasives from the polished sample, either in de-ionised water to remove alumina or petroleum spirit to remove oils (Hall and Hayward, 2014).

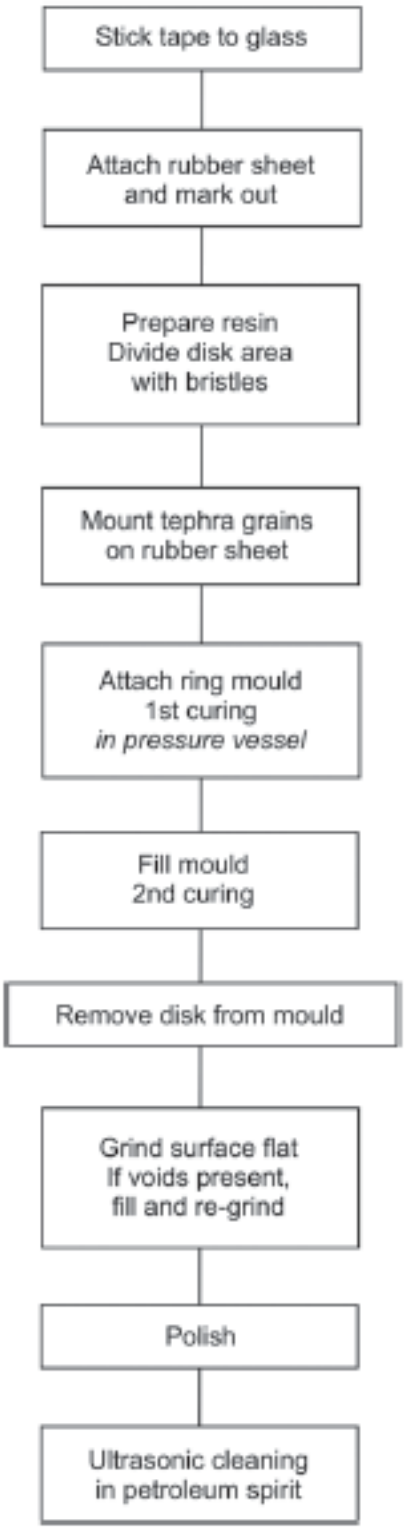

Figure 22. Summary flow diagram of sample preparation method for EPMA (Hall and Hayward, 2014).

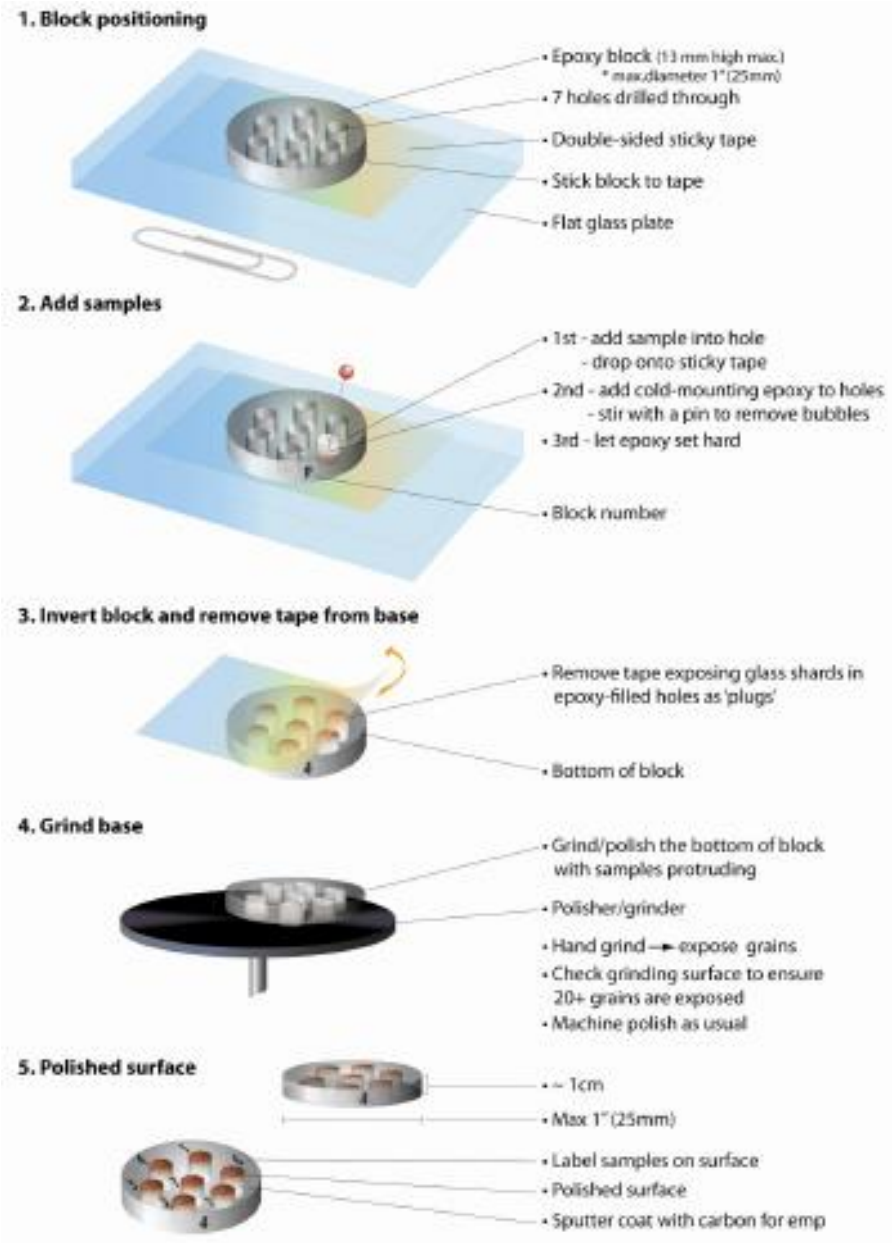

Figure 23. Method of preparing multiple samples of volcanic glass shards for electron microprobe analysis (Lowe, 2011).

Morgan and London (2005) made several recommendations for electron microprobe analysis to reduce and correct for the effects of Na migration on relative concentrations of other elements, based on the correlation between beam current density and elemental concentrations in EPMA results. For glasses of rhyolitic and andesitic compositions, the authors suggested using multiple beam conditions. The initial beam should be of a low current density (≤ 2 nA) for analysis of major components (Na, Al, Si, K, ± Ca), followed by a beam of higher current density (20–50 nA) for analysis of the remaining elements. Both beams should be of the same

spot size, at least 5 µm for a current density of 2 nA, and counting times should be scaled for sensitivity. If the instrument does not support multiple beam conditions, current density should be no more than ~0.5-1.0 nA/µm^2, and data corrections or primary calibration using glass standards is required to account for Na losses. Spot size should be kept the same across all samples for ease of data correction and comparison.

Additional recommendations are provided by Kuehn et al. (2011), including screening for outliers regarded as contamination prior to calculation of mean values, consideration of the number of sample points to be taken for adequate characterisation (15-20 for a homogeneous sample, 50-60 for a heterogeneous sample), and full disclosure of all experimental conditions and the data obtained. Kuehn (2014) gave a brief summary of the recommendations for data reporting from EPMA of tephras, and Pearce et al. (2014) emphasised that although normalisation is expected and often essential, it is also important to present data that can be recalculated from either raw to normalised form, or vice versa.

5.2: Methods

Glass shards were separated from the bulk 63-250 µm fraction using magnetic separation, as detailed in 4.2.2. Prefabricated disks were used and the method outlined in Figure 23 was followed. Holes in the disks were filled with sample grains to around a quarter of the available volume to ensure glass would be preserved after grinding. The resin used for filling the block mounts was Struers EpoFix, a low-viscosity epoxy resin suitable for vacuum impregnation.

A basic sample map was constructed for each block (Figure 24 and Appendix 2.6), with Roman numerals (I, II, III…) allocated to each block and Arabic numerals (1, 2, 3…) allocated to samples to create a code system that could be easily scribed onto the blocks. Five blocks were prepared for EPMA, each holding seven samples from both the Meade-Hossack trench and the outcrop, as well as two samples from the bottom of Core 3 (Figure 28).

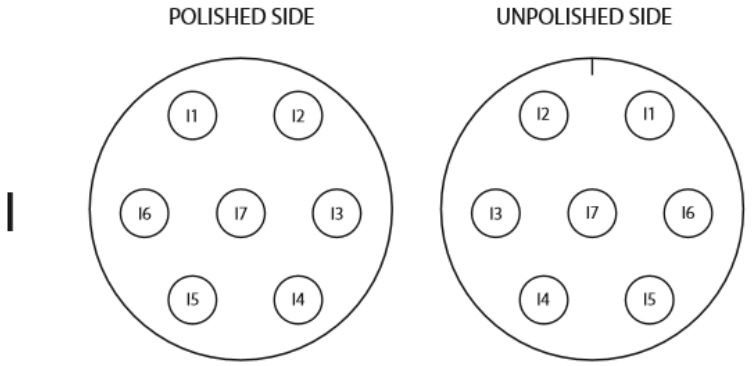

Block Code	Sample
I1	HT10
I2	HT11
I3	HT12
I4	HT13
I5	HT16
I6	HT17
I7	HT18

Figure 24. Example map of block mount for EPMA. The block code is comprised of a Roman numeral for the block and an Arabic numeral for the sample. The full maps and code lists are available in Appendix 2.6.

EPMA was conducted using the JEOL JXA-8200 SuperProbe Electron Probe Microanalyzer at Victoria University of Wellington. Operating conditions, standards, element analysis conditions, and peak/background count times are detailed in Appendix 2. Some samples prepared for EPMA were not probed because grains had been plucked out during the polishing process, and this was not observed until the blocks had been chambered in the system. Given that LA-ICP-MS analysis requires results from EPMA as standards and the same resin blocks are used (Pearce et al., 2011; Pearce, 2014), extra care needs to be taken when preparing blocks if both analyses are to be performed. Duplicate blocks should be prepared where possible and resin must be fully set before polishing to avoid grain plucking.

I recommend that at least one day for every two blocks is allowed for when scheduling EPMA, more heterogeneous samples require a greater number of shards analysed and therefore more time for shard selection and probing. The limited time and budget available for probing and decreased available time for analysis because of technical issues (system crashes) meant that the two blocks affected by plucking could not be re-prepared for analysis while in Wellington.

Major and minor element data were normalised in Excel and plotted using GCDkit 4.0, an open-source software package written in R language for use in igneous petrology (Janoušek et al., 2006, 2011).

5.3: Results and interpretation

5.3.1: Meade-Hossack Trench and Core 3

To identify the tephras in the Meade-Hossack trench, the results of major and minor elemental analyses of volcanic glass by EPMA (major element data were reported as oxides) were compared with mean EPMA values for volcanic glass from known late Quaternary TVZ-derived tephras as reported by Smith et al. (2005) and Lowe et al. (2008).

A summary of the identified units is provided in Figure 25, and mean values and standard deviations are given in Table 8. All raw EPMA data for glass shards are available in Appendix 2.

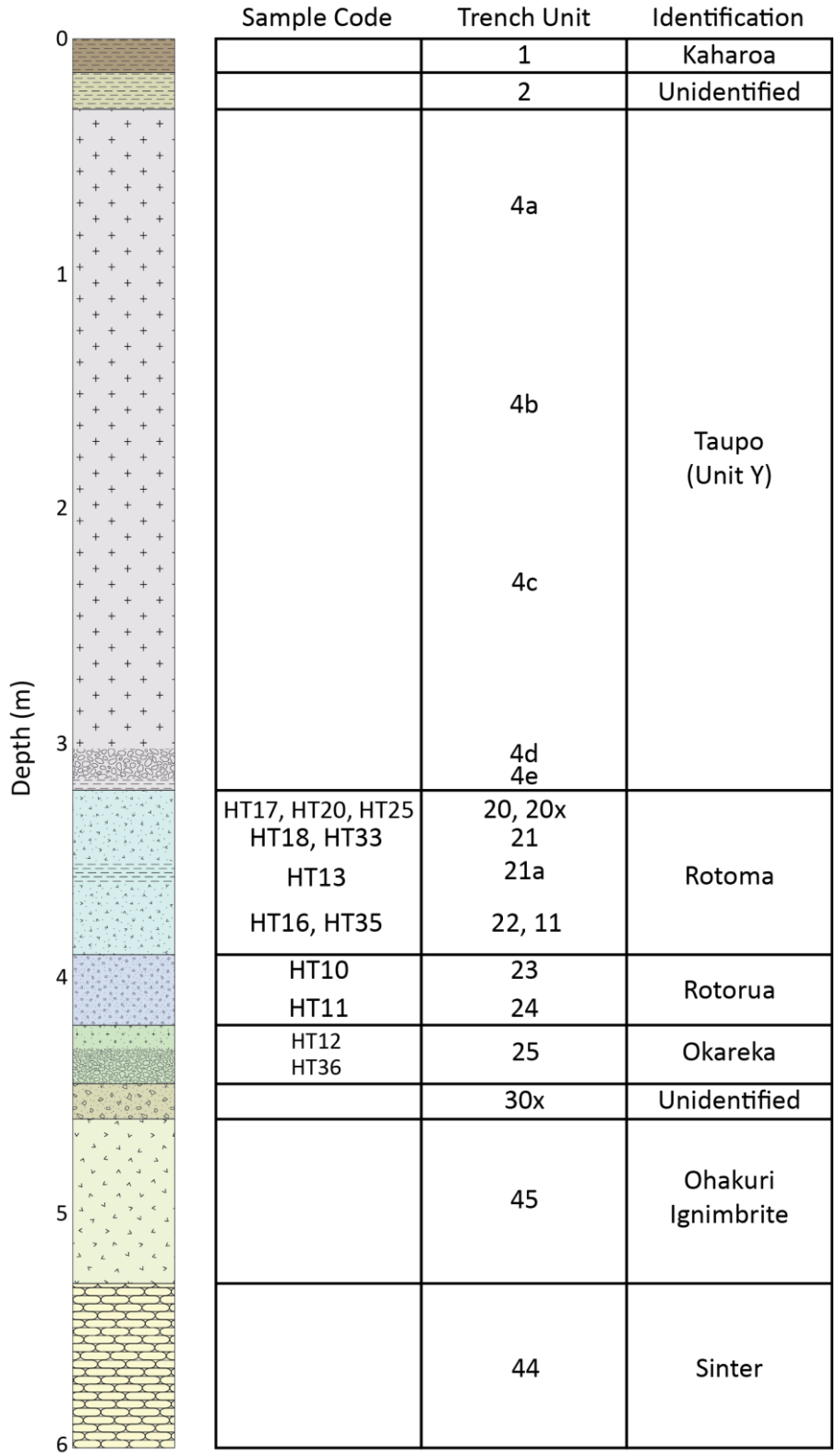

Sample Code	Trench Unit	Identification
	1	Kaharoa
	2	Unidentified
	4a	Taupo (Unit Y)
	4b	
	4c	
	4d 4e	
HT17, HT20, HT25	20, 20x	Rotoma
HT18, HT33	21	
HT13	21a	
HT16, HT35	22, 11	
HT10	23	Rotorua
HT11	24	
HT12 HT36	25	Okareka
	30x	Unidentified
	45	Ohakuri Ignimbrite
	44	Sinter

Figure 25. Generalised stratigraphic log of the units in the trench, the corresponding sample physical properties (from field descriptions), ferromagnesian mineral assemblages, and glass-shard EPMA results.

Table 8. Major element glass compositions of tephra samples from the Meade-Hossack trench. Analyses are in wt.%, normalised to 100% anhydrous, and provided as means with standard deviations italicised and in parentheses. Water by difference. Subpopulations within samples are signified by appending a, b… to the sample code. n is the number of analyses (individual shards). Raw data are reported in Appendix 2.

	SiO_2	TiO_2	Al_2O_3	FeOt*	MnO	MgO	CaO	Na_2O	K_2O	P_2O_5	Cl	H_2O	*n*
HT10a	77.91 *(0.09)*	0.05 *(0.01)*	12.56 *(0.07)*	4.27 *(0.06)*	0.06 *(0.02)*	0.05 *(0.01)*	0.65 *(0.05)*	3.40 *(0.11)*	4.27 *(0.18)*	0.01 *(0.01)*	0.16 *(0.01)*	2.68 *(1.76)*	13
HT10b	77.10 *(0.32)*	0.20 *(0.00)*	12.91 *(0.16)*	1.35 *(0.05)*	0.06 *(0.02)*	0.22 *(0.03)*	1.35 *(0.03)*	3.62 *(0.17)*	2.99 *(0.08)*	0.03 *(0.02)*	0.13 *(0.01)*	0.14 *(0.19)*	4
HT11a	77.83 *(0.12)*	0.06 *(0.01)*	12.54 *(0.09)*	0.87 *(0.05)*	0.05 *(0.01)*	0.06 *(0.01)*	0.66 *(0.05)*	3.40 *(0.07)*	4.32 *(0.07)*	0.01 *(0.01)*	0.16 *(0.01)*	3.39 *(0.64)*	12
HT11b	76.91 *(0.05)*	0.21 *(0.01)*	12.98 *(0.10)*	1.38 *(0.06)*	0.06 *(0.03)*	0.23 *(0.03)*	1.41 *(0.02)*	3.61 *(0.07)*	3.01 *(0.03)*	0.03 *(0.01)*	0.12 *(0.02)*	1.74 *(1.59)*	5
HT12a	77.89 *(0.17)*	0.07 *(0.01)*	12.50 *(0.04)*	0.089 *(0.07)*	0.05 *(0.02)*	0.06 *(0.01)*	0.69 *(0.07)*	3.36 *(0.11)*	4.29 *(0.15)*	0.01 *(0.01)*	0.15 *(0.01)*	3.08 *(1.18)*	5
HT12b	76.96 *(0.47)*	0.22 *(0.02)*	12.98 *(0.11)*	1.44 *(0.06)*	0.08 *(0.01)*	0.22 *(0.02)*	1.33 *(0.05)*	3.58 *(0.25)*	2.99 *(0.13)*	0.03 *(0.01)*	0.13 *(0.01)*	1.14 *(0.96)*	3
HT13	78.30 *(0.31)*	0.10 *(0.04)*	12.47 *(0.19)*	0.92 *(0.08)*	0.06 *(0.02)*	0.11 *(0.01)*	0.79 *(0.05)*	3.62 *(0.09)*	3.42 *(0.11)*	0.02 *(0.01)*	0.15 *(0.01)*	1.88 *(1.32)*	18
HT16	78.33 *(0.18)*	0.10 *(0.01)*	12.51 *(0.10)*	0.90 *(0.07)*	0.06 *(0.01)*	0.11 *(0.01)*	0.78 *(0.03)*	3.64 *(0.10)*	3.37 *(0.09)*	0.01 *(0.01)*	0.15 *(0.01)*	2.27 *(1.42)*	18
HT17	78.29 *(0.23)*	0.12 *(0.02)*	12.42 *(0.07)*	1.04 *(0.09)*	0.06 *(0.02)*	0.12 *(0.02)*	0.87 *(0.06)*	3.50 *(0.16)*	3.38 *(0.26)*	0.01 *(0.01)*	0.15 *(0.01)*	3.14 *(1.91)*	18
HT18	78.24 *(0.15)*	0.09 *(0.01)*	12.44 *(0.08)*	0.96 *(0.09)*	0.06 *(0.02)*	0.10 *(0.01)*	0.77 *(0.07)*	3.56 *(0.09)*	3.56 *(0.20)*	0.02 *(0.01)*	0.15 *(0.01)*	1.48 *(1.29)*	14
HT20	77.85 *(0.22)*	0.10 *(0.02)*	12.38 *(0.08)*	1.15 *(0.16)*	0.04 *(0.01)*	0.09 *(0.02)*	0.90 *(0.06)*	3.23 *(0.16)*	3.98 *(0.19)*	0.02 *(0.02)*	0.18 *(0.01)*	2.83 *(0.40)*	12

Table 8 continued.

	SiO_2	TiO_2	Al_2O3	FeOt*	MnO	MgO	CaO	Na_2O	K_2O	P_2O_5	Cl	H_2O	*n*
HT25	78.09 *(0.26)*	0.08 *(0.03)*	12.46 *(0.18)*	0.92 *(0.09)*	0.05 *(0.02)*	0.07 *(0.01)*	0.73 *(0.09)*	3.36 *(0.17)*	4.03 *(0.46)*	0.01 *(0.01)*	0.16 *(0.01)*	0.86 *(0.93)*	8
HT33a	78.24 *(0.06)*	0.10 *(0.01)*	12.53 *(0.04)*	0.93 *(0.03)*	0.05 *(0.02)*	0.11 *(0.01)*	0.79 *(0.03)*	3.62 *(0.04)*	3.40 *(0.04)*	0.02 *(0.02)*	0.15 *(0.01)*	0.82 *(0.58)*	5
HT33b	78.26 *(0.16)*	0.09 *(0.01)*	12.41 *(0.04)*	0.92 *(0.05)*	0.05 *(0.02)*	0.09 *(0.01)*	0.68 *(0.02)*	3.48 *(0.10)*	3.81 *(0.08)*	0.00 *(0.00)*	0.15 *(0.01)*	0.53 *(0.39)*	6
HT35	78.24 *(0.22)*	0.09 *(0.02)*	12.50 *(0.08)*	0.91 *(0.06)*	0.05 *(0.01)*	0.10 *(0.02)*	0.74 *(0.06)*	3.55 *(0.13)*	3.61 *(0.31)*	0.01 *(0.01)*	0.15 *(0.01)*	0.65 *(0.52)*	19
HT36	78.28 *(0.14)*	0.10 *(0.01)*	12.44 *(0.05)*	0.93 *(0.05)*	0.05 *(0.01)*	0.10 *(0.01)*	0.77 *(0.06)*	3.61 *(0.11)*	3.52 *(0.21)*	0.01 *(0.01)*	0.15 *(0.01)*	0.65 *(0.58)*	11
CR31a	77.96 *(0.24)*	0.07 *(0.02)*	12.48 *(0.14)*	0.89 *(0.06)*	0.06 *(0.01)*	0.07 *(0.03)*	0.69 *(0.09)*	3.36 *(0.15)*	4.21 *(0.33)*	0.01 *(0.01)*	0.15 *(0.01)*	1.15 *(1.45)*	8
CR31b	77.21 *(0.26)*	0.22 *(0.01)*	12.85 *(0.03)*	1.32 *(0.11)*	0.04 *(0.01)*	0.24 *(0.01)*	1.35 *(0.08)*	3.55 *(0.13)*	3.03 *(0.04)*	0.02 *(0.02)*	0.13 *(0.03)*	0.46 *(0.51)*	3
HT20a	78.10 *(0.19)*	0.10 *(0.03)*	12.54 *(0.09)*	1.02 *(0.11)*	0.05 *(0.01)*	0.11 *(0.04)*	0.81 *(0.11)*	3.49 *(0.13)*	3.58 *(0.41)*	1.02 *(0.11)*	0.15 *(0.02)*	0.90 *(0.74)*	8
HT20b	76.93 *(0.45)*	0.16 *(0.04)*	12.94 *(0.14)*	1.62 *(0.06)*	0.07 *(0.01)*	0.15 *(0.02)*	1.22 *(0.02)*	3.61 *(0.17)*	3.11 *(0.01)*	0.02 *(0.02)*	0.014 *(0.01)*	1.31 *(1.72)*	3
HT25a	78.49 *(0.44)*	0.11 *(0.03)*	12.52 *(0.16)*	0.90 *(0.18)*	0.05 *(0.02)*	0.11 *(0.02)*	0.84 *(0.07)*	3.52 *(0.11)*	3.25 *(0.24)*	0.01 *(0.01)*	0.14 *(0.01)*	1.19 *(1.01)*	8
HT25b	77.99 *(0.16)*	0.07 *(0.02)*	12.48 *(0.03)*	0.92 *(0.10)*	0.04 *(0.02)*	0.08 *(0.01)*	0.71 *(0.05)*	3.39 *(0.07)*	4.10 *(0.29)*	0.01 *(0.01)*	0.16 *(0.01)*	0.75 *(0.76)*	4

**Total Fe expressed as FeO*

The clearest identification based on comparing trench sample EPMA results with pre-existing EPMA data on TVZ tephras was for samples HT10 and HT11 (Units 23 and 24, respectively). The samples were taken from what were initially described and drawn as separate stratigraphic units on the trench logs, but displayed similar enough patterns to each another in the EPMA results that Units 23 and 24 may now be considered one and the same. The generalised stratigraphic log in Figure 25 therefore shows samples HT10 and HT11 as being derived from the same unit.

Compared to pre-existing data from Lowe et al. (2008), HT10 and HT11 showed the most similarity with the mean averages for Rotorua Tephra (Figure 26), showing a mix of both T1 (low-K) and T2 (high-K) magmas, with a majority of points from both samples plotting closer to the T2 magma/eruptive stage. The match in the SiO_2 plots is inexact, but the standard deviations show variations. Although the sample data follow the same pattern as Rotorua T1 and T2 across different plots, the values for SiO_2 from the samples appear to be consistently ~0.5% higher than those of the comparison data. In addition to the problem with SiO_2 values, those for Na_2O appear to be ~0.6% lower than the comparison data, possibly due to volatilisation during analysis despite precautionary measures taken to reduce losses. The similarity is better conveyed by plots without SiO_2 or Na_2O, such as those in Figure 27, in particular the CaO vs. K_2O and the MgO vs. FeOt plots. The sample data plot closely to the T1 and T2 points, with the majority falling around T2.

The EMPA-based glass shard major element compositional data for samples HT10 and HT11 are consistent with data from the ferromagnesian mineral assemblages. Therefore Units 23 and 24 in the trench are both identified as Rotorua Tephra, primarily T2 magma/eruptive stage. The calibrated age for Rotorua Tephra is 15635 ± 412 cal. yr BP (Lowe et al., 2013). The Rotorua Tephra was subsequently used as a key chronostratigraphic stratigraphic marker bed to help identify the other tephras in the trench using glass-shard compositional data.

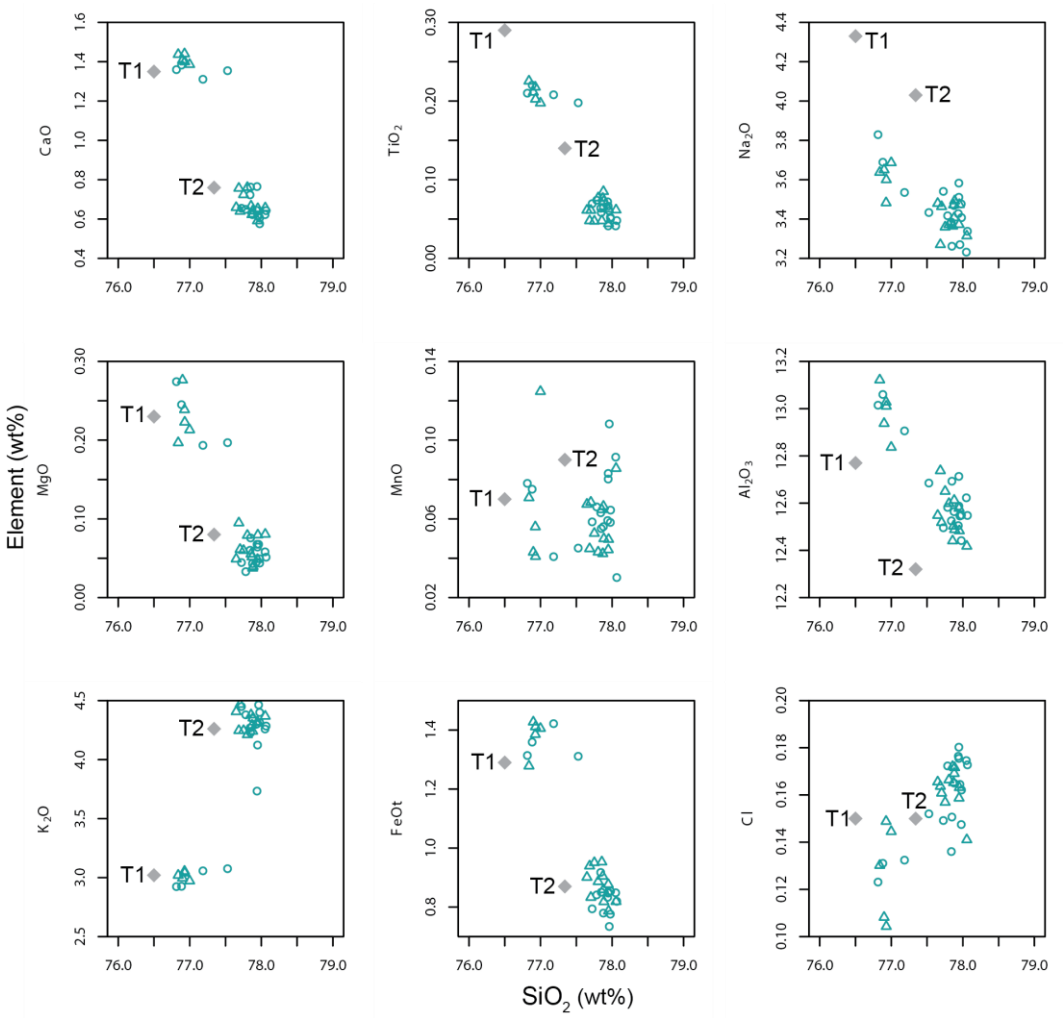

Figure 26. Major and minor element vs. SiO_2 glass chemistry for samples HT10 (circle) and HT11 (triangle), compared with Rotorua T1 and T2 data (diamond) from Lowe et al. (2008).

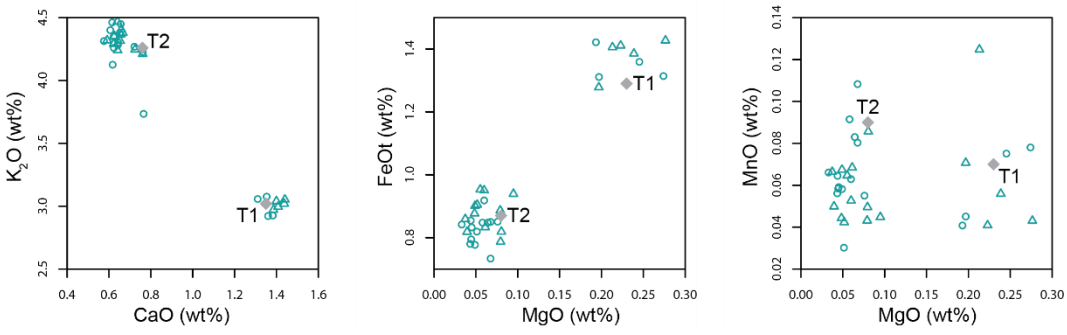

Figure 27. Plots of K_2O vs. CaO (left), FeOt vs. MgO (centre), and MnO vs. MgO (right) for samples HT10 (circle) and HT11 (triangle), compared with Rotorua T1 and T2 data (diamond) from Lowe et al. (2008).

Sample CR31 is from core taken ~21 m northwest of the northernmost edge of the Meade-Hossack trench (Figure 28). CR31 is a sample of the material at 2.13 m depth from surface.

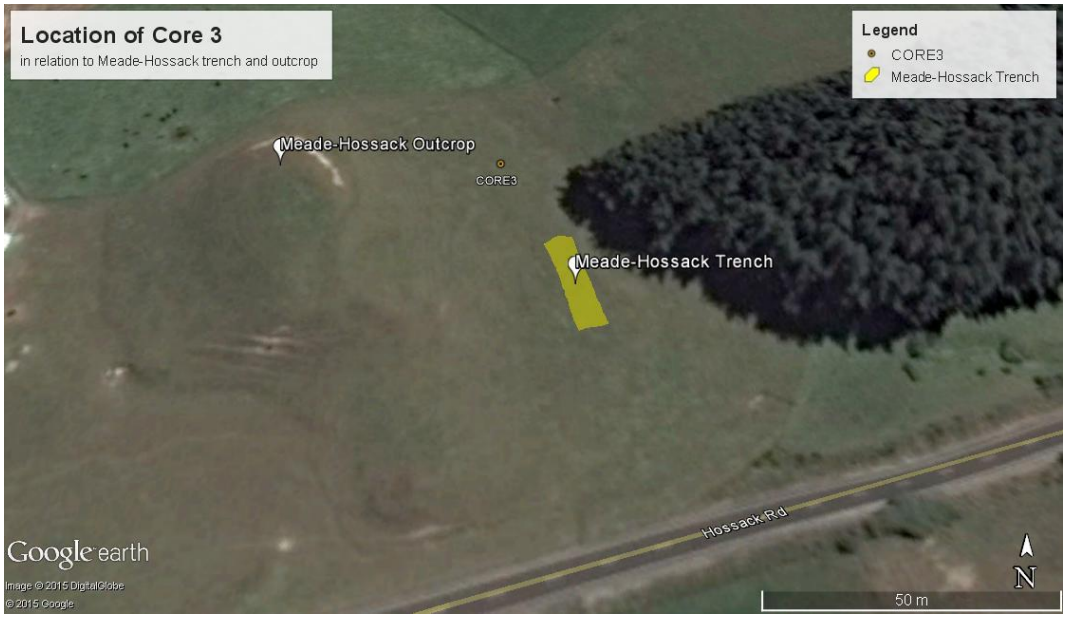

Figure 28. Location of Core 3 in relation to the Meade-Hossack trench and outcrop.

The major element composition of glass shards from sample CR31 (Figures 28 and 29) follows a similar pattern as that for samples HT10 and HT11 (Figures 25 and 26), with volatilisation issues affecting the sample to a similar degree as well for Na_2O. The CaO vs. K_2O plot and the MgO vs. FeOt plot (Figure 30) show the data points close to the mean averages for Rotorua T1 and T2, with the majority (excluding one outlier point) around T2. The geochemistry and the similarity in proportions of T1 vs. T2 points are evidence that the deposit CR31 is taken from is the same unit as that of HT10 and HT11, and that all of these samples are primarily Rotorua Tephra (T2 magma).

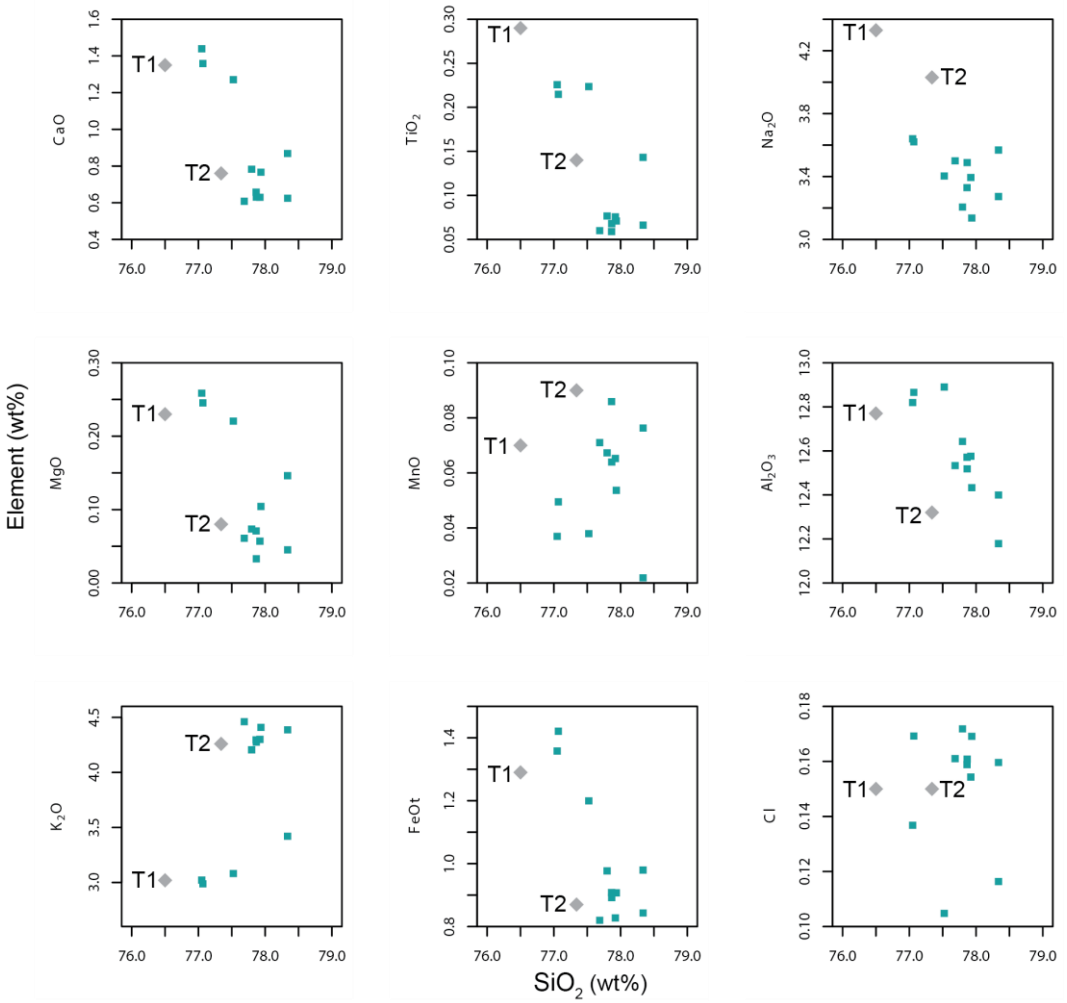

Figure 29. Major and minor element vs. SiO_2 glass chemistry for sample CR31 (square), compared with Rotorua T1 and T2 data (diamond) from Lowe et al. (2008).

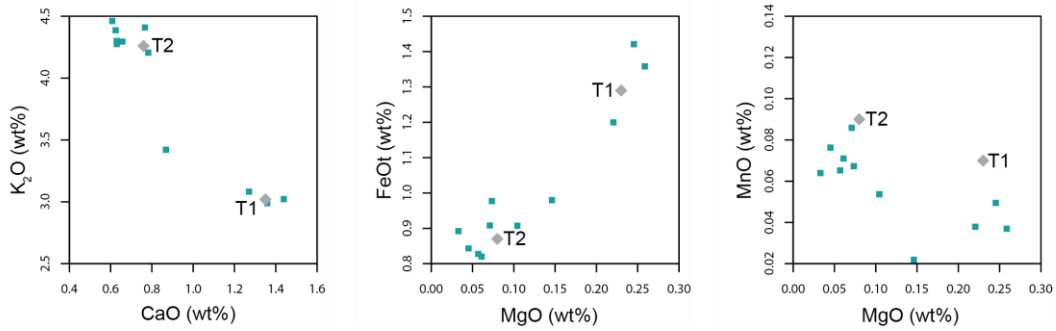

Figure 30. Plots of K_2O vs. CaO (left), FeOt vs. MgO (centre), and MnO vs. MgO (right) for sample CR31 (square), compared with Rotorua T1 and T2 data (diamond) from Lowe et al. (2008).

Having a distinctive marker bed (Rotorua Tephra) constrains the identifications of other units in the trench, assuming no overturning or reworking has occurred. Units in the undeformed stratigraphic succession beneath the Rotorua Tephra must therefore be older than c. 15.6 ka, and units higher in the succession must be younger. The age constraint is useful when trying to compare unknown units against compositionally similar known tephras from different time periods.

Sample CR32 is from the core taken ~21 m northwest of the edge of the Meade-Hossack trench (Figure 28). CR32 is a sample of the material at 2.33 m depth from surface, a lower stratigraphic position than that of the sample identified as Rotorua Tephra.

The glass-shard major element composition of CR32 is compared against Rotorua and Okareka tephras in Figures 30 and 31, as these known tephras were the closest in composition and age to the unknown. Assuming the CR32 data points have the same volatilisation issue as seen in the samples identified as Rotorua Tephra, an issue arises in that the Rotorua T2 mean is generally close in composition to the Okareka T1 and T2 means.

The convention for labelling magma types (e.g. Shane et al., 2008) puts T1 as the earliest magma type associated with an eruptive event, with T2, T3 and so on to indicate increasingly later eruptive phases of magma types. With the convention in mind, the absence of CR32 data points close to the mean for Rotorua T1 magma would suggest that it is unlikely CR32 is Rotorua Tephra. The closest fit then appears to be Okareka Tephra, though the dominant magma type is unclear. Most of the data points tend to be closer to T1 and T2, but in the SiO_2 vs. FeOt plot, they are close to T3 as well.

The unit that CR32 is sampled from may be a slightly mixed or reworked unit, or there may have been a degree of contamination caused by the vibrocoring process. There are also only eight data points available for this sample, which may not be enough to draw a strong conclusion where more than one glass population may be present. In this case, I tentatively correlate CR32 with the Okareka Tephra, the calibrated age of which is 21,858 ± 290 cal. yr BP (Lowe et al., 2013).

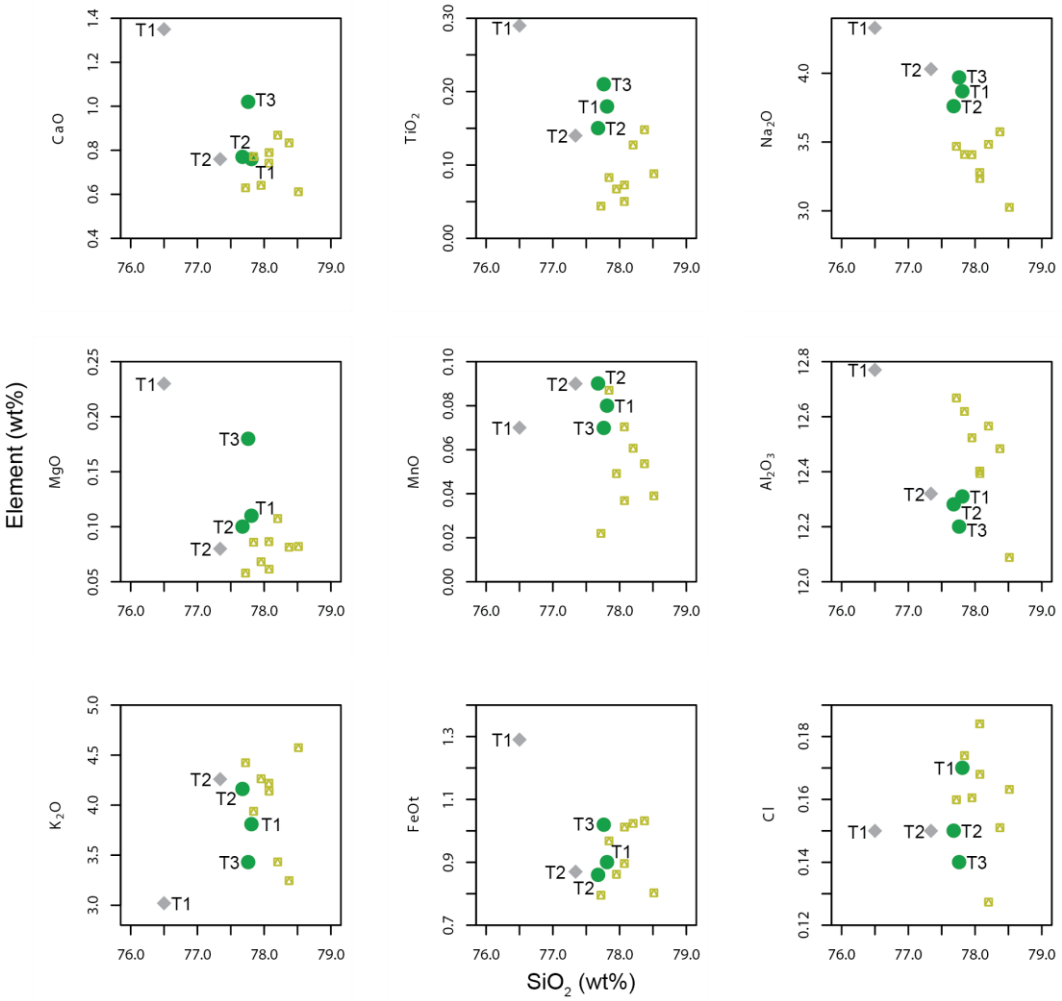

Figure 31. Major and minor element vs. SiO_2 glass chemistry for sample CR32 (square), compared with Okareka data (circle) from Smith et al. (2005) and Rotorua data (diamond) from Lowe et al. (2008).

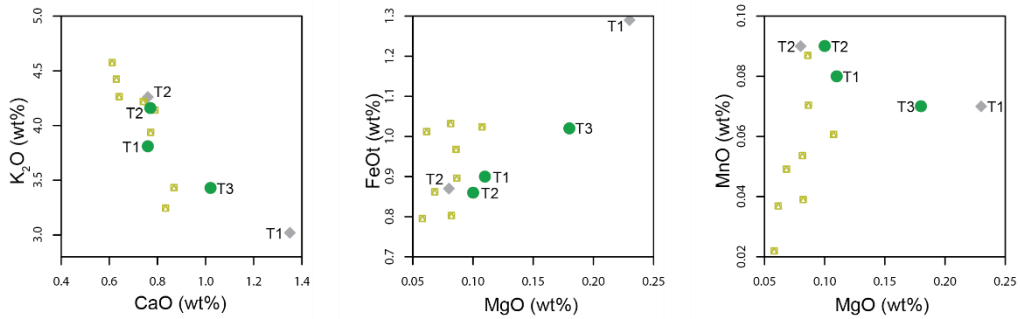

Figure 32. Plots of K_2O vs. CaO (left), FeOt vs. MgO (centre), and MnO vs. MgO (right) for sample CR32 (square), compared with Okareka data (circle) from Smith et al. (2005) and Rotorua data (diamond) from Lowe et al. (2008).

Sample HT36 is taken from a downthrown wedge of Unit 25 on the hanging wall of the most prominent normal fault plane on the SW wall of the Meade-Hossack trench.

The analytical data for HT36 were initially compared with the mean Rerewhakaaitu Tephra data from Smith et al. (2005), because Rerewhakaaitu is chronologically the next oldest OVC eruptive after the Rotorua Tephra, at 17,496 ± 462 cal. yr BP (Lowe et al. 2013). The SiO_2 vs. major element plots were not a good fit, even when taking the assumed ~0.5% silica discrepancy into account. Some of the more "stable" oxides such as K_2O, FeOt, and CaO were also dissimilar enough to suggest that a correlation with other known tephras was more likely.

The most similar OVC eruptive to HT36 that is older than the Rotorua Tephra is the Okareka Tephra, which correlates with the samples from Core 3. The SiO_2 vs major element plots (Figure 33) show a fairly strong similarity when the ~0.5% SiO_2 and ~0.6% Na_2O discrepancies are taken into account. Out of the non-SiO_2 plots (Figure 34), only the MgO vs. FeOt plot shows a similarity between the sample data and Okareka T1 and T2 data. The CaO vs. K_2O plot has a subset of sample data close to Okareka T1, but the rest are too low in CaO by ~0.2% to correlate with Okareka T3, and too low in K_2O by ~0.8% to correlate with Okareka T2.

The identification of Unit 25 as the Okareka Tephra based on sample HT36 geochemistry should be regarded as tentative. If Unit 25 is Okareka Tephra and Unit 24 is Rotorua Tephra, then there is an unconformity between the Rotorua and Okareka tephras at this location. Evidence of an unconformity was observed in the field as a weak paleosol formed on the uppermost part of Unit 25.

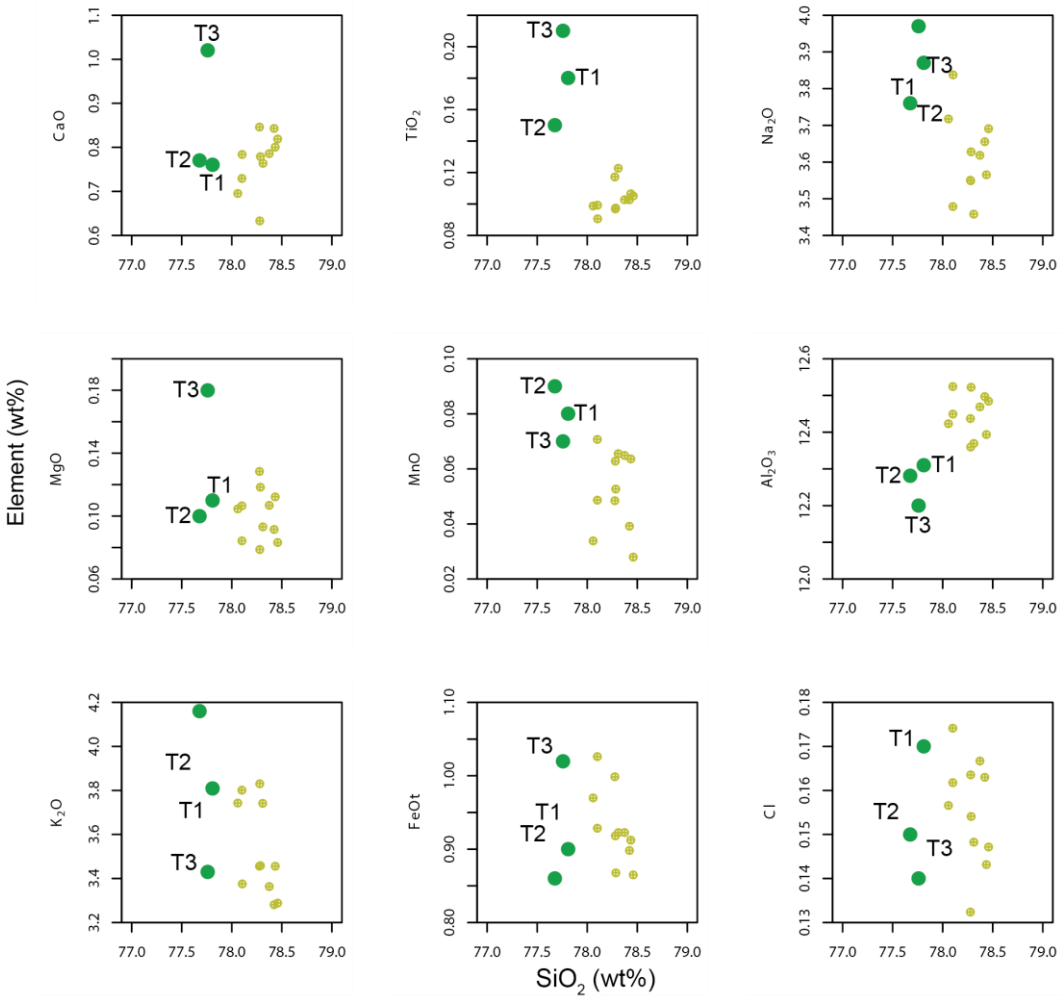

Figure 33. Major and minor element vs. SiO_2 glass chemistry for sample HT36 (small circle), compared with Okareka data (large circle) from Smith et al. (2005).

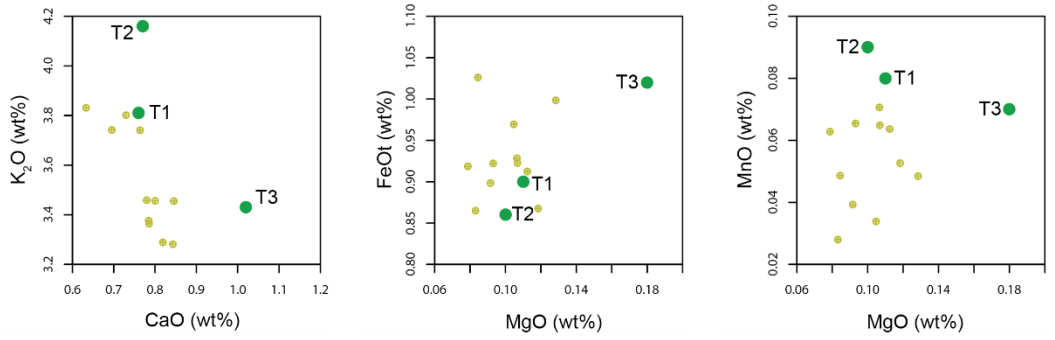

Figure 34. Plots of K_2O vs. CaO (left), FeOt vs. MgO (centre), and MnO vs. MgO (right) for sample HT36 (small circle), compared with Okareka data (large circle) from Smith et al. (2005).

Sample HT35 was taken from Unit 11, one of the lowest visible units on the downthrown hanging wall of the fault on the SW wall of the trench. It is important to identify Unit 11 because it is one of the units directly impacted by deformation caused by faulting. Taking the ~0.5% silica excess of the samples into account, the glass compositions (Figures 34 and 35) align best with the averages for glass from Rotoma Tephra and Okareka Tephra. The stratigraphic position of the sample, along with the absence of the unit identified as Rotorua Tephra above HT35, and the thickness of Rotoma Tephra at other locations in the trench, means that the sample is more likely to be Rotoma Tephra than Okareka Tephra.

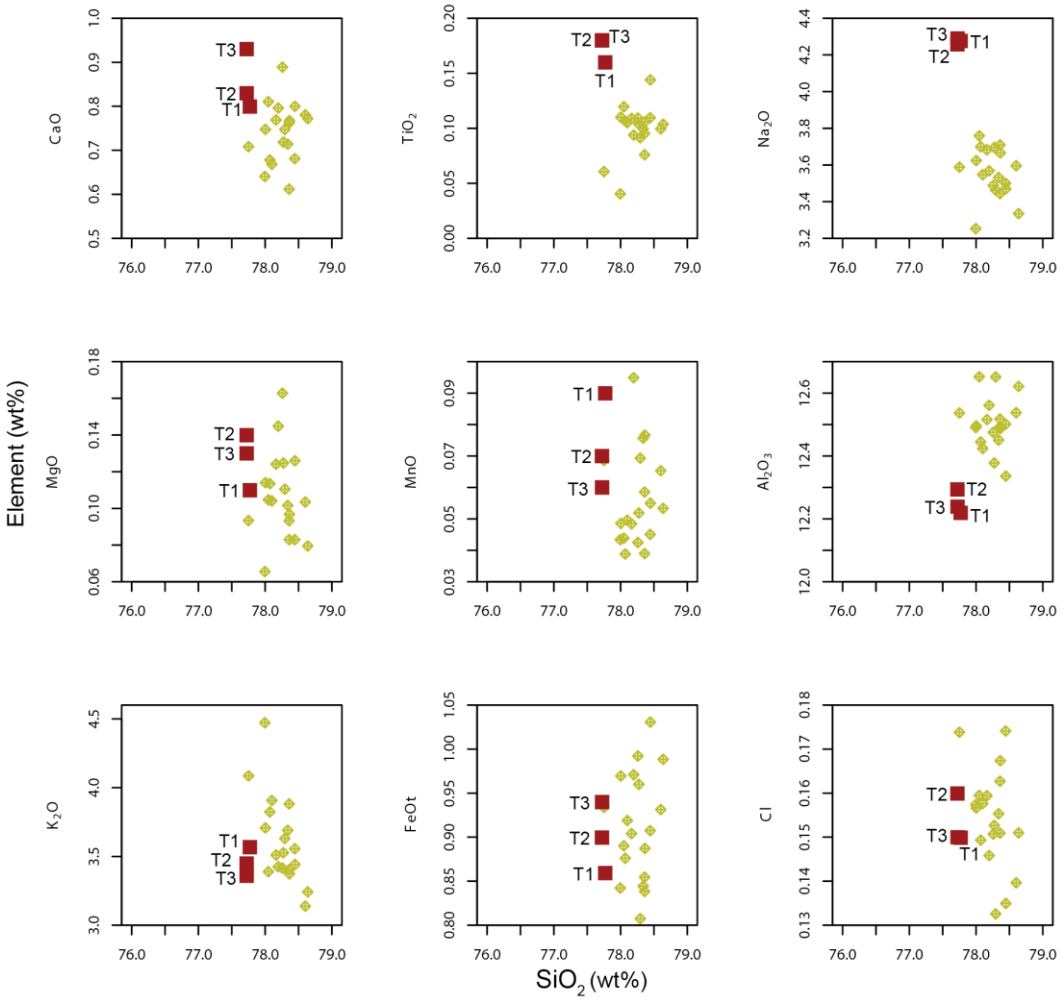

Figure 35. Major and minor element vs. SiO_2 glass chemistry for sample HT35 (diamond), compared with Rotoma data (square) from Smith et al. (2005).

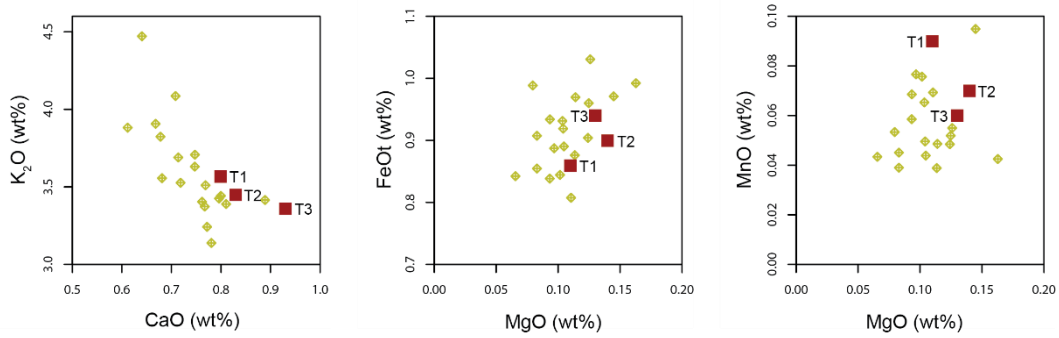

Figure 36. Plots of K_2O vs. CaO (left), FeOt vs. MgO (centre), and MnO vs. MgO (right) for sample HT35 (diamond), compared with Rotoma data (square) from Smith et al. (2005).

Samples HT13 and HT18 were taken from Units 21a and 21, respectively, in the Meade-Hossack trench. Unit 21a are “cream cakes” within Unit 21, and these two units were tentatively identified in the field collectively as Rotoma Tephra. The stratigraphic position of these units is higher than the Rotorua Tephra marker bed identified earlier, so Rotoma was still a possible correlative for samples HT13 and HT18.

Comparisons were made with mean data from all known post-Rotorua TVZ eruptives as recorded by Smith et al. (2005). The best fits for the sample data are Whakatane Tephra (T3 only) and Rotoma Tephra. Plotting the mean glass analyses for the samples against those from the Smith et al. (2005) dataset put HT18 and HT13 close to Rotoma T1 and T2 across most major and minor elements.

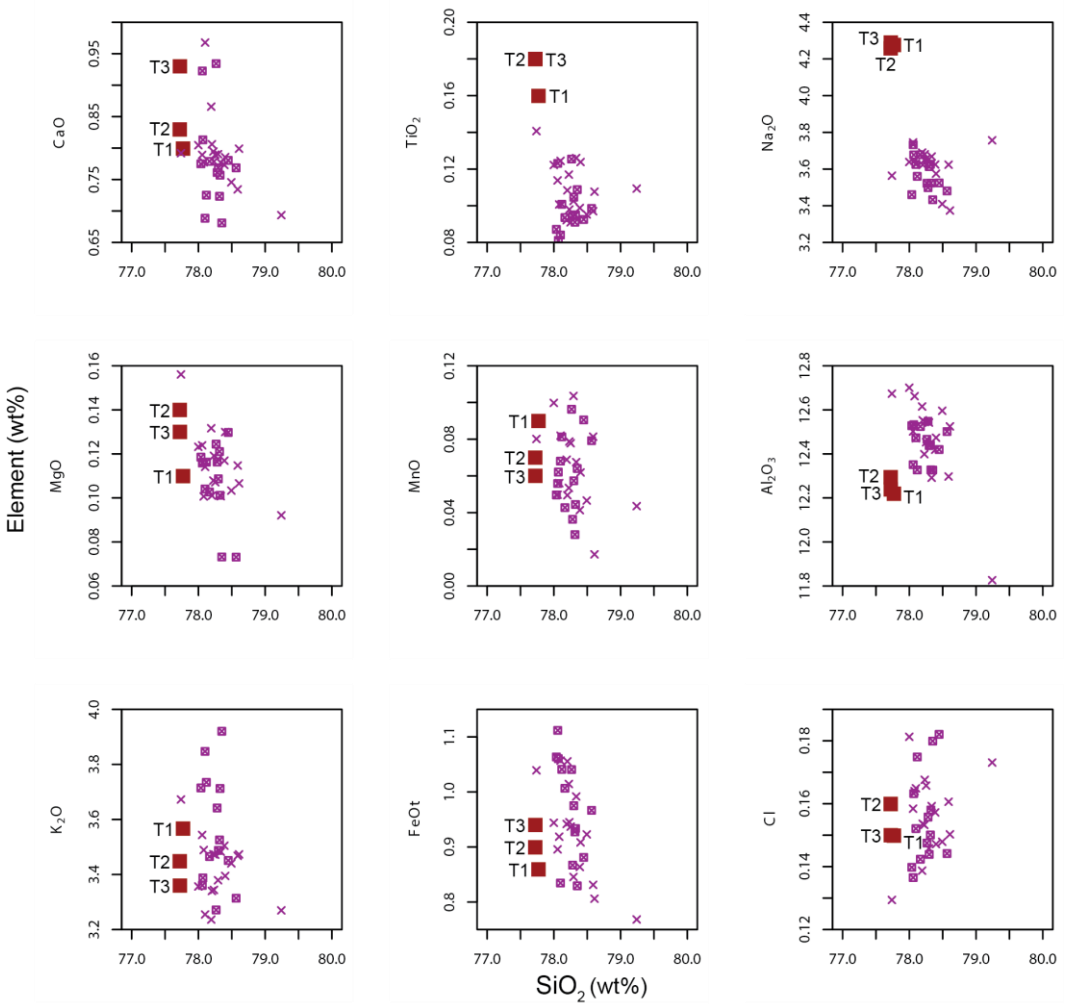

Figure 37. Major and minor element vs. SiO_2 glass chemistry for samples HT13 (cross) and HT18 (small square), compared with Rotoma data (large square) from Smith et al. (2005).

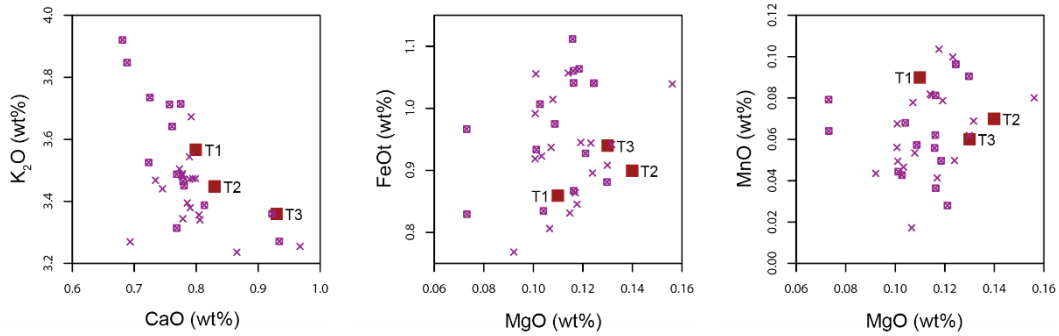

Figure 38. Plots of K_2O vs. CaO (left), FeOt vs. MgO (centre), and MnO vs. MgO (right) for HT13 (cross) and HT18 (small square), compared with Rotoma data (large square) from Smith et al. (2005).

Sample HT33 is from the upper part of Unit 10, on the downthrown hanging wall on the SW trench wall. The unit is directly below Taupo Unit Y and is expected to be Rotoma Tephra. The geochemistry for HT33 (Figure 39) supports the identification of Unit 10 as Rotoma Tephra, although there is a group of high-K/Low Ca samples (Figure 40) that may be an indicator of contamination or mixing in the soil environment. The group is also seen in sample HT18, for example, which is also identified as Rotoma Tephra (Figure 38). The grouping does not correlate with means for Rotorua Tephra nor with means for other known deposits within the appropriate age range. The conclusion is that all of Unit 10 is identified as Rotoma Tephra, and Unit 10 is the same unit as Unit 21 in the undeformed northern parts of the trench.

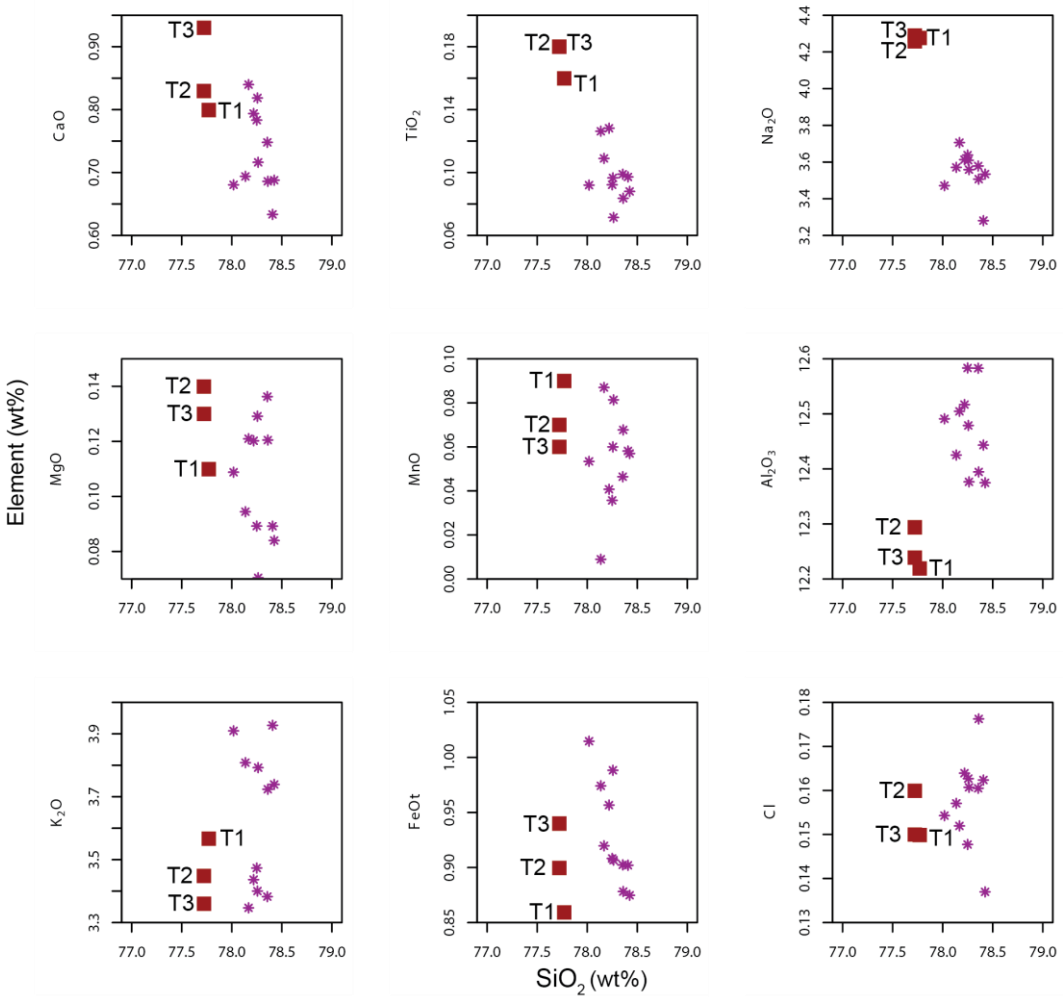

Figure 39. Major and minor element vs. SiO_2 glass chemistry for sample HT33 (star), compared with Rotoma data (square) from Smith et al. (2005).

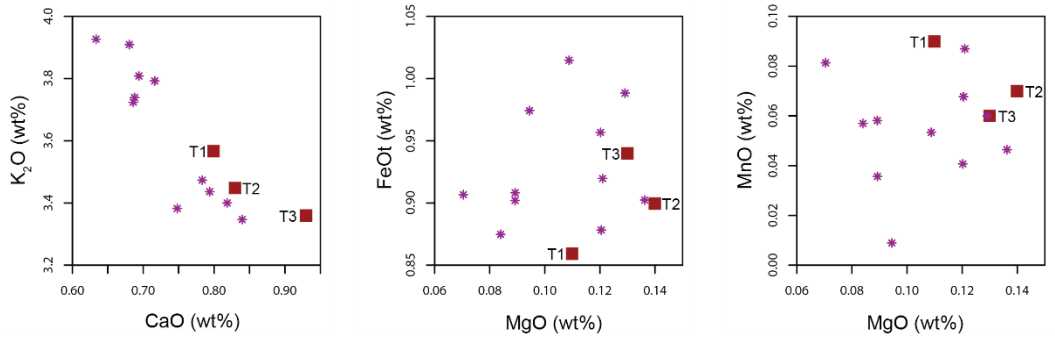

Figure 40. Plots of K_2O vs. CaO (left), FeOt vs. MgO (centre), and MnO vs. MgO (right) for sample HT33 (star), compared with Rotoma data (square) from Smith et al. (2005).

Sample HT12 is taken from the upper part of Unit 25 in the undeformed part of the SW wall. The data display a grouping similar to other samples identified as Rotorua, with most points correlating with the mean for Rotorua T2 (Figures 40 and 41). However, a problem arises in that the means for the Rotorua T2 magma type are compositionally similar to those for Okareka magma types, particularly Okareka T2, as noted for sample HT36.

HT12 may be affected by soil mixing between the upper part of the unit and the overlying Rotorua Tephra, or it may be that the upper boundary of the unit was incorrectly identified and should be lower at this location. Other samples from the same unit, HT36 and CR32, do not show any data points that can be correlated with Rotorua T1, particularly evident when the CaO and K_2O plots are compared to those of HT12. The overall identification of Unit 25 as Okareka is unchanged but the actual location of the HT12 sample is from a unit that may include Rotorua Tephra.

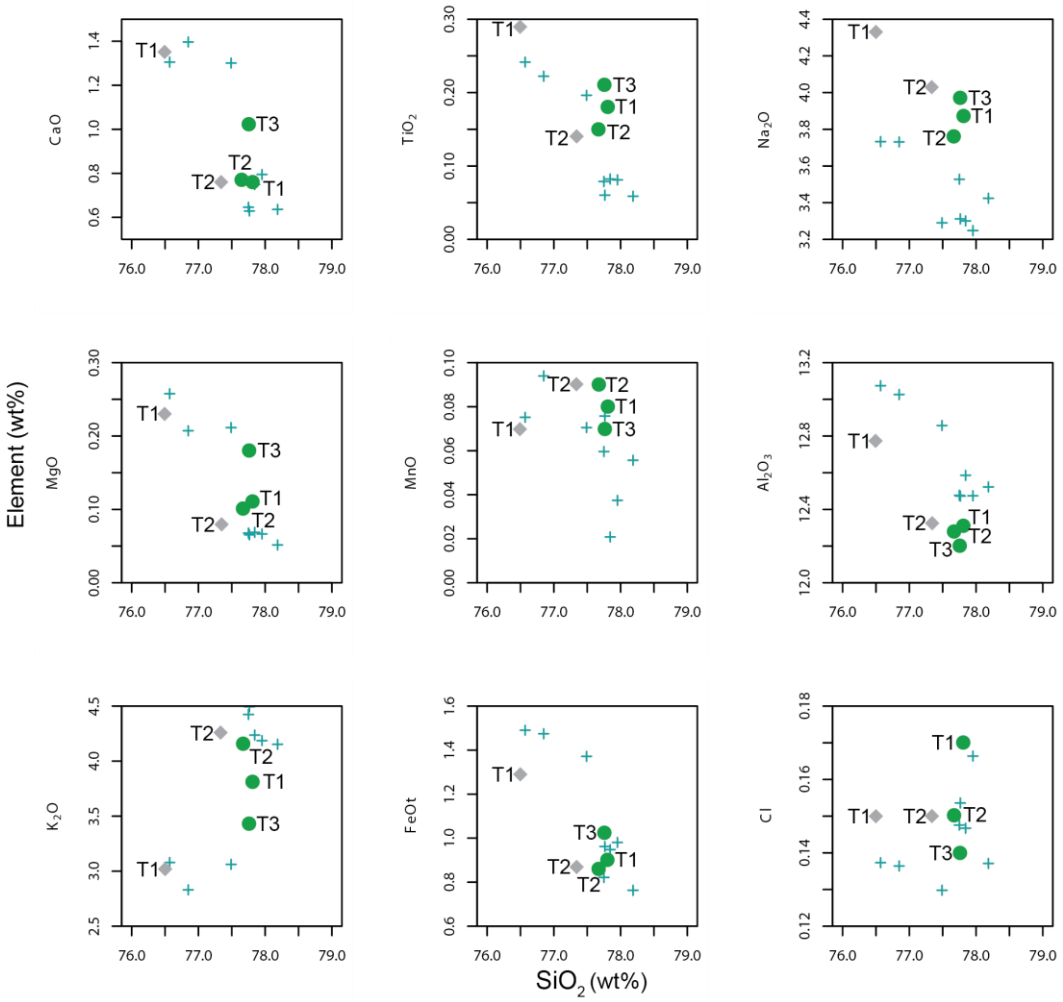

Figure 41. Major and minor element vs. SiO_2 glass chemistry for sample HT12 (cross), compared with Rotorua data (diamond) from Lowe et al. (2008) and Okareka data (circle) from Smith et al. (2005).

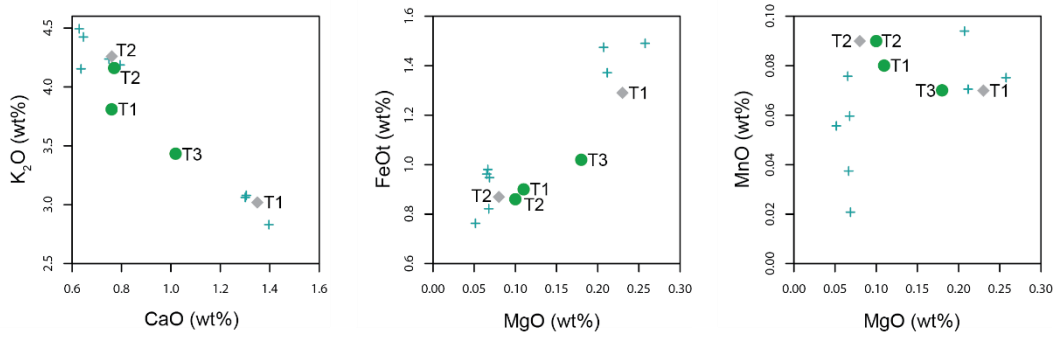

Figure 42. Plots of K_2O vs. CaO (left), FeOt vs. MgO (centre), and MnO vs. MgO (right) for sample HT12 (cross), compared with Rotorua data (diamond) from Lowe et al. (2008) and Okareka data (circle) from Smith et al. (2005).

Sample HT16 is taken from the base of Unit 20 on the SW wall of the trench, and HT17 is from the base of Unit 22 on the same wall. The samples display a geochemical overlap for most of the elements analysed, so they have been plotted together in Figures 42 and 43. Overall, HT17 is more closely correlated with the Rotoma T3 magma type with some T2 overlap, whereas HT16 is more closely correlated with the Rotoma T1 magma type, overlapping with T2.

Both samples HT16 and HT17 are identified as Rotoma Tephra, thus Units 20 and 22 are also identified as this tephra. The identification of Units 20 through 22 suggests a thickness of around 0.8 m for the undeformed Rotoma Tephra deposit in the northern end of the trench, which is within the estimated thickness range of 0.5 to 1 m from isopach maps (Table 1; Nairn, 2002).

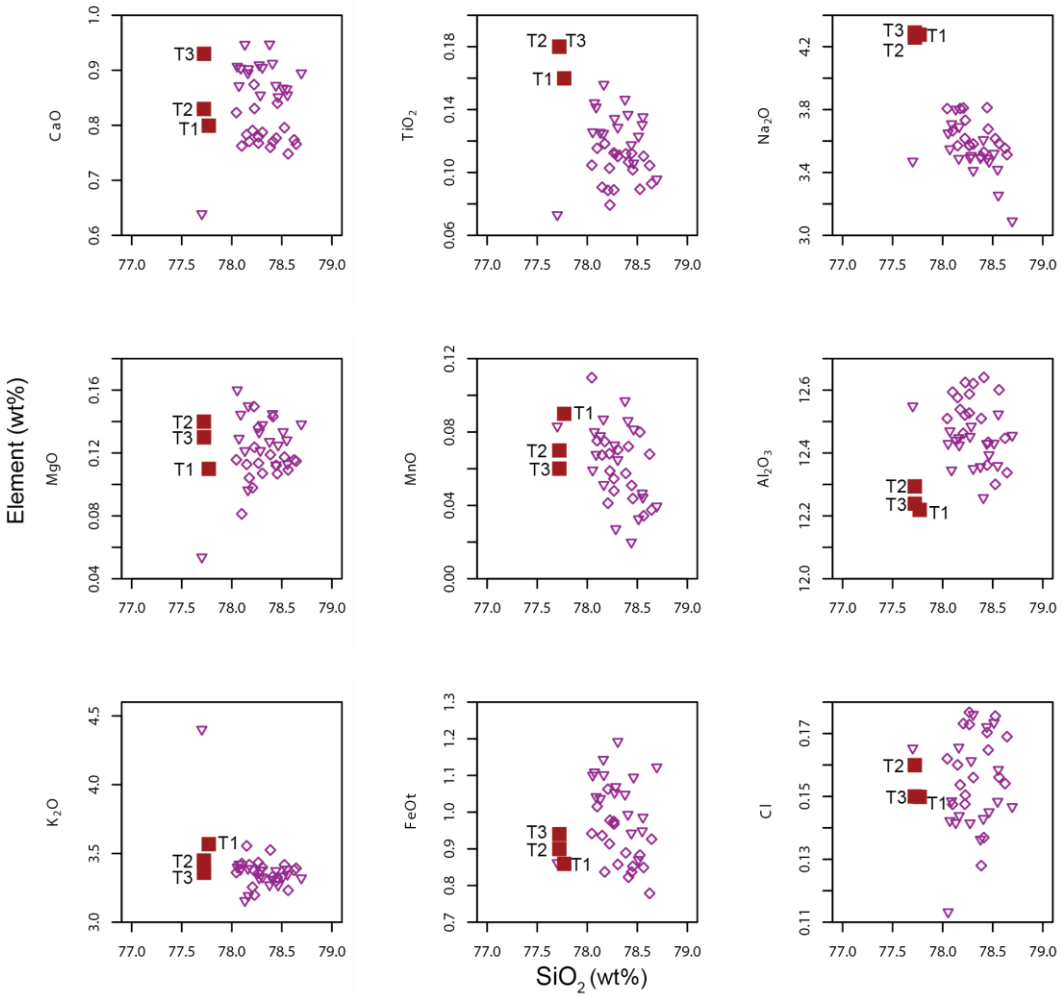

Figure 43. Major and minor element vs. SiO_2 glass chemistry for samples HT16 (diamond) and HT17 (triangle), compared with Rotoma data (square) from Smith et al. (2005).

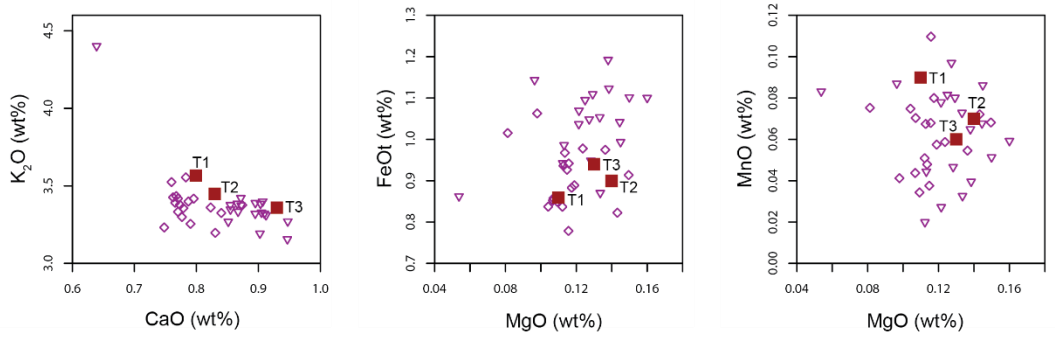

Figure 44. Plots of K_2O vs. CaO (left), FeOt vs. MgO (centre), and MnO vs. MgO (right) for samples HT16 (diamond) and HT17 (triangle), compared with Rotoma data (square) from Smith et al. (2005).

Samples HT20 and HT25 are taken from Unit 20x in the Meade-Hossack trench, a unit described as “mixed tephras and/or paleosol”. The glass analyses from these samples were compared against those of both Rotorua and Rotoma tephras on the basis of the position of Unit 20x in the trench, namely on the backslope, where transport of deposits is likely to be at a maximum. The analyses were not compared with those for Okareka Tephra because Unit 20x is stratigraphically higher than Unit 25, and separated by other units.

The major and minor element geochemistry (Figures 44 and 45) reveal that Unit 20x is largely Rotoma Tephra, with some Rotorua Tephra mixed into the unit by hillslope transport. The data points classed as Rotorua Tephra are particularly discernible in the CaO vs. K_2O plot in Figure 46.

For the purposes of reconstructing the stratigraphy of the trench, Unit 20x will be regarded as Rotoma Tephra.

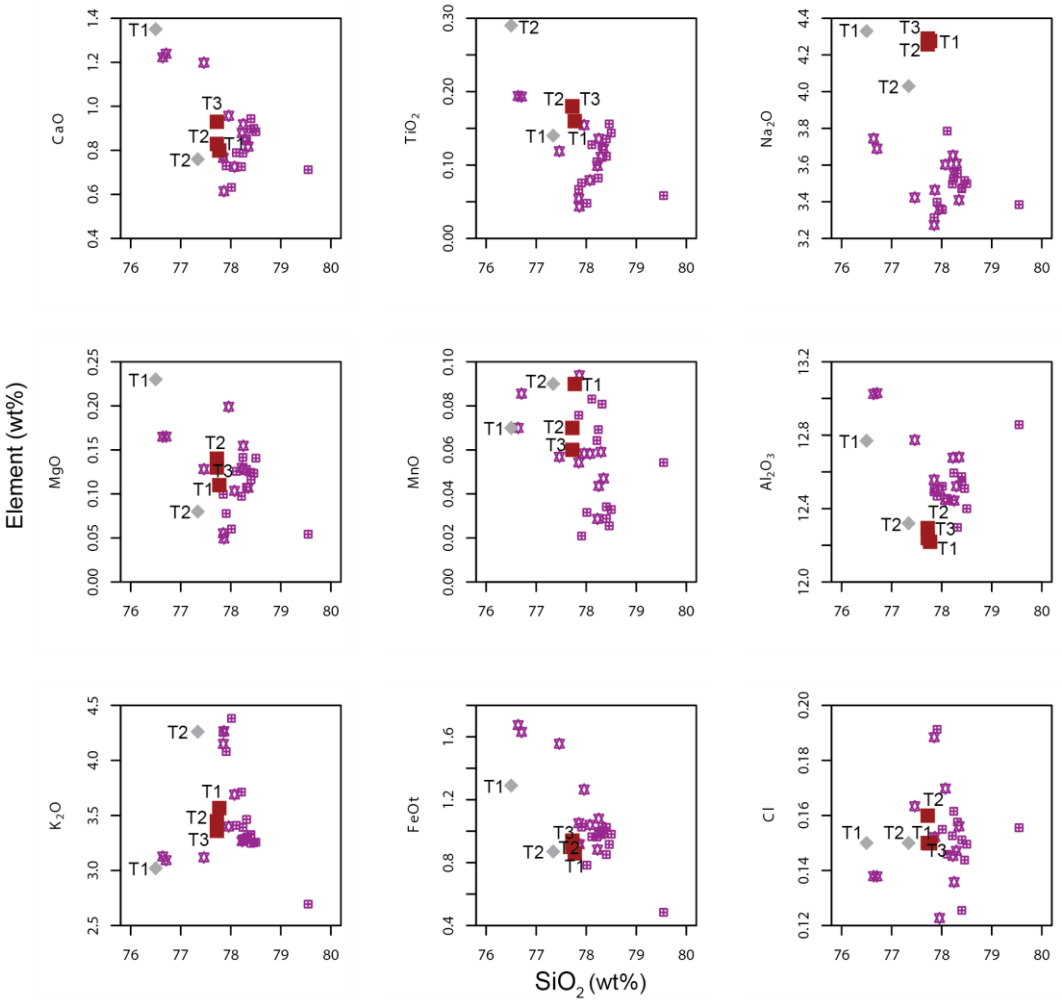

Figure 45. Major and minor element vs. SiO_2 glass chemistry for samples HT20 (star) and HT25 (small square), compared with Rotorua T1 and T2 data (diamond) from Lowe et al. (2008) and Rotoma data (large square) from Smith et al. (2005).

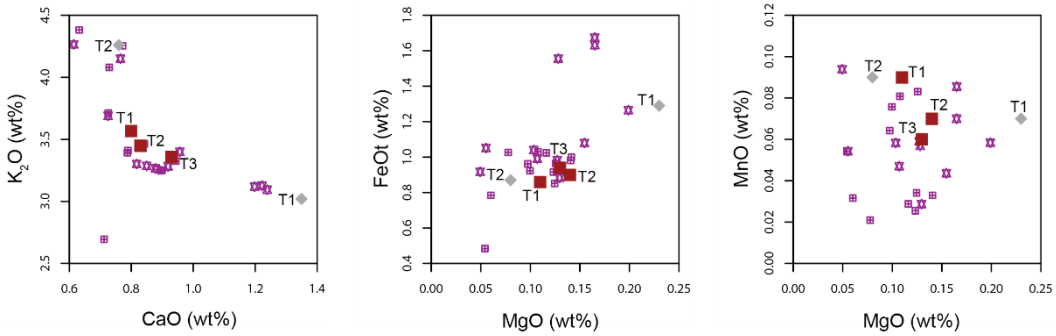

Figure 46. Plots of K_2O vs. CaO (left), FeOt vs. MgO (centre), and MnO vs. MgO (right) for samples HT20 (star) and HT25 (small square), compared with Rotorua T1 and T2 data (diamond) from Lowe et al. (2008) and Rotoma data (large square) from Smith et al. (2005).

5.3.2: Outcrop

Although the outcrop in Figure 17 is not the focus of the study, it would be helpful to be able to correlate units across where possible in order to aid in working out the paleotopography of the field area. However, few samples from the outcrop were able to be analysed by microprobe as the blocks affected by grain plucking during polishing were predominantly comprised of outcrop samples. Six of the outcrop samples were analysed, and the mean data are presented in Table 9, with the full set of raw data available in Appendix 2.

Table 9. Major element glass compositions of tephra samples from the Meade-Hossack outcrop. Analyses are in wt.% normalised to 100% anhydrous, and provided as means with standard deviations italicised and in parentheses. Water by difference. n is the number of analyses (individual shards). Raw data are reported in Appendix 2.

	SiO_2	TiO_2	Al_2O_3	FeOt*	MnO	MgO	CaO	Na_2O	K_2O	P_2O_5	Cl	H_2O	*n*
HP9	77.88 *(0.22)*	0.10 *(0.02)*	12.38 *(0.08)*	1.15 *(0.16)*	0.04 *(0.01)*	0.09 *(0.02)*	0.90 *(0.06)*	3.23 *(0.16)*	3.98 *(0.19)*	0.02 *(0.01)*	0.18 *(0.01)*	2.83 *(0.40)*	12
HP11	78.00 *(0.16)*	0.08 *(0.01)*	12.46 *(0.15)*	1.07 *(0.13)*	0.03 *(0.01)*	0.08 *(0.01)*	0.85 *(0.06)*	3.27 *(0.18)*	3.92 *(0.28)*	0.02 *(0.01)*	0.18 *(0.02)*	3.19 *(0.61)*	19
HR13	78.08 *(0.16)*	0.08 *(0.02)*	12.49 *(0.10)*	1.03 *(0.07)*	0.04 *(0.01)*	0.08 *(0.02)*	0.86 *(0.05)*	3.28 *(0.15)*	3.83 *(0.14)*	0.01 *(0.01)*	0.19 *(0.01)*	3.31 *(0.65)*	7
HR15	77.90 *(0.40)*	0.10 *(0.02)*	12.43 *(0.14)*	0.04 *(0.02)*	0.04 *(0.02)*	0.08 *(0.01)*	0.85 *(0.06)*	3.38 *(0.19)*	3.79 *(0.08)*	0.01 *(0.01)*	0.18 *(0.02)*	3.03 *(0.70)*	10
HR17	78.03 *(0.19)*	0.08 *(0.01)*	12.49 *(0.14)*	1.07 *(0.08)*	0.04 *(0.02)*	0.08 *(0.01)*	0.85 *(0.07)*	3.29 *(0.14)*	3.84 *(0.23)*	0.01 *(0.01)*	0.18 *(0.01)*	3.17 *(0.74)*	14
HR20	78.16 *(0.29)*	0.11 *(0.01)*	12.51 *(0.13)*	1.24 *(0.08)*	0.03 *(0.01)*	0.12 *(0.01)*	1.05 *(0.07)*	3.36 *(0.07)*	3.16 *(0.20)*	0.01 *(0.01)*	0.19 *(0.01)*	3.97 *(1.42)*	15

*Total Fe expressed as FeO

Sample HP9 is taken from a lens of fine lapilli ~0.55 m below the hydrothermal vent breccia close to the base of the outcrop, and ~0.5 mm above the upper boundary of the Ohakuri Ignimbrite observed in the excavated pit. The data points plotted in between the mean averages for several known tephras, including Whakatane, Tahuna, Rotoiti, and Earthquake Flat (Figures 46 and 47). The Whakatane Tephra can be disregarded for identification despite geochemical similarities, as stratigraphically the unit from which the sample was taken is below the sinter dated at c. 39 ka. Tahuna, Rotoiti, and Earthquake Flat tephras are all older than 39 ka and younger than 240 ka. Of those options, Tahuna tends to plot the closest to the mean average for HP9 more frequently than the others.

Smith and Shane (2002) described the geochemical characteristics of glass from several different subunits of the Tahuna Tephra, one of which is a fine lapilli. The HP9 data were replotted to compare with the data for the lapilli subunit of the Tahuna tephra (Figures 48 and 49). Taking into account the ~0.5% excess SiO_2 anomaly for my sample data, the means for sample HP9 are very close to those for the Tahuna lapilli subunit for SiO_2, CaO, MgO, and FeOt.

The outcrop unit from which HP9 was taken is thus tentatively identified as Tahuna Tephra, which has an age of 39,300 ± 2400 cal. BP (Molloy et al., 2009). The age of the Tahuna Tephra compared with the next oldest identifiable unit, the Ohakuri Ignimbrite, indicates the presence of an unconformity between them. Smith and Shane (2002) noted that the Tahuna tephra was erupted in a cooler climate and thus frequently appears in association with erosional boundaries, so an unconformity is not unexpected.

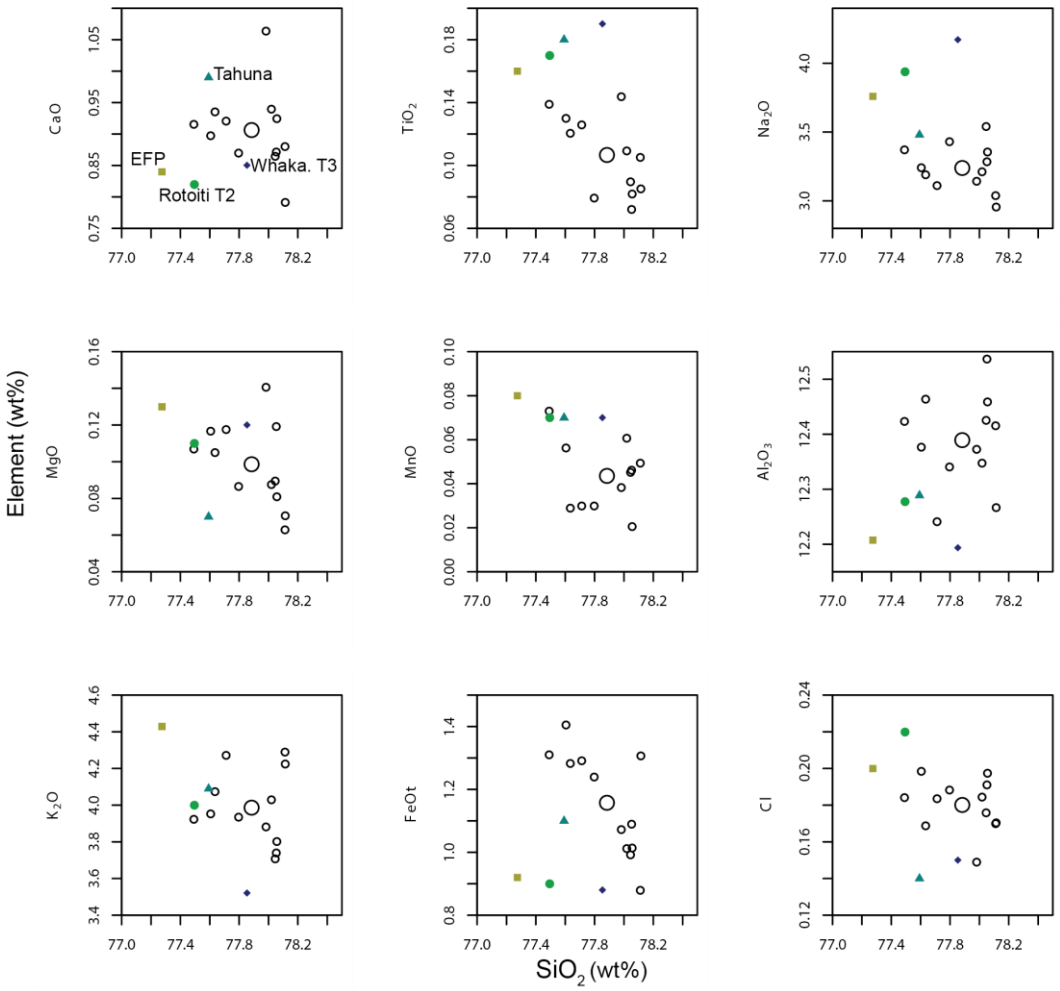

Figure 47. Major and minor element vs. SiO_2 glass chemistry for sample HP9 (hollow circle; mean represented by a larger hollow circle), compared with Tahuna (triangle), Whakatane T3 (diamond), Earthquake Flat Pyroclastics (EFP; square) and Rotoiti T2 (filled circle) data from Smith et al. (2005).

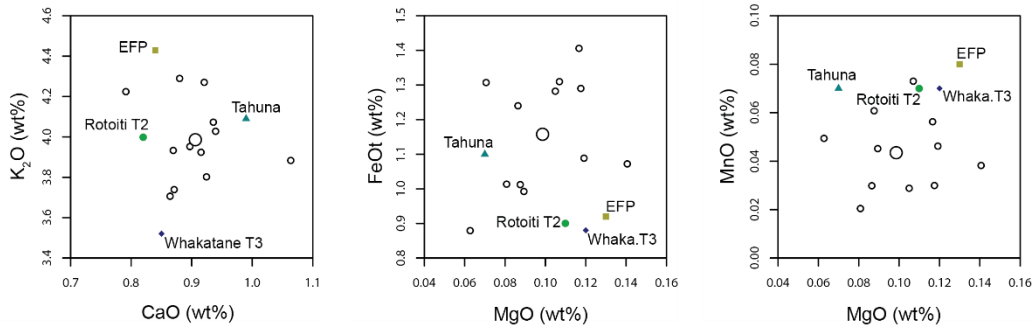

Figure 48. Plots of K_2O vs. CaO (left), FeOt vs. MgO (centre), and MnO vs. MgO (right) for sample HP9 (hollow circle; mean represented by a larger hollow circle), compared with Tahuna (triangle), Whakatane T3 (diamond), Earthquake Flat Pyroclastics (EFP; square) and Rotoiti T2 (filled circle) data from Smith et al. (2005).

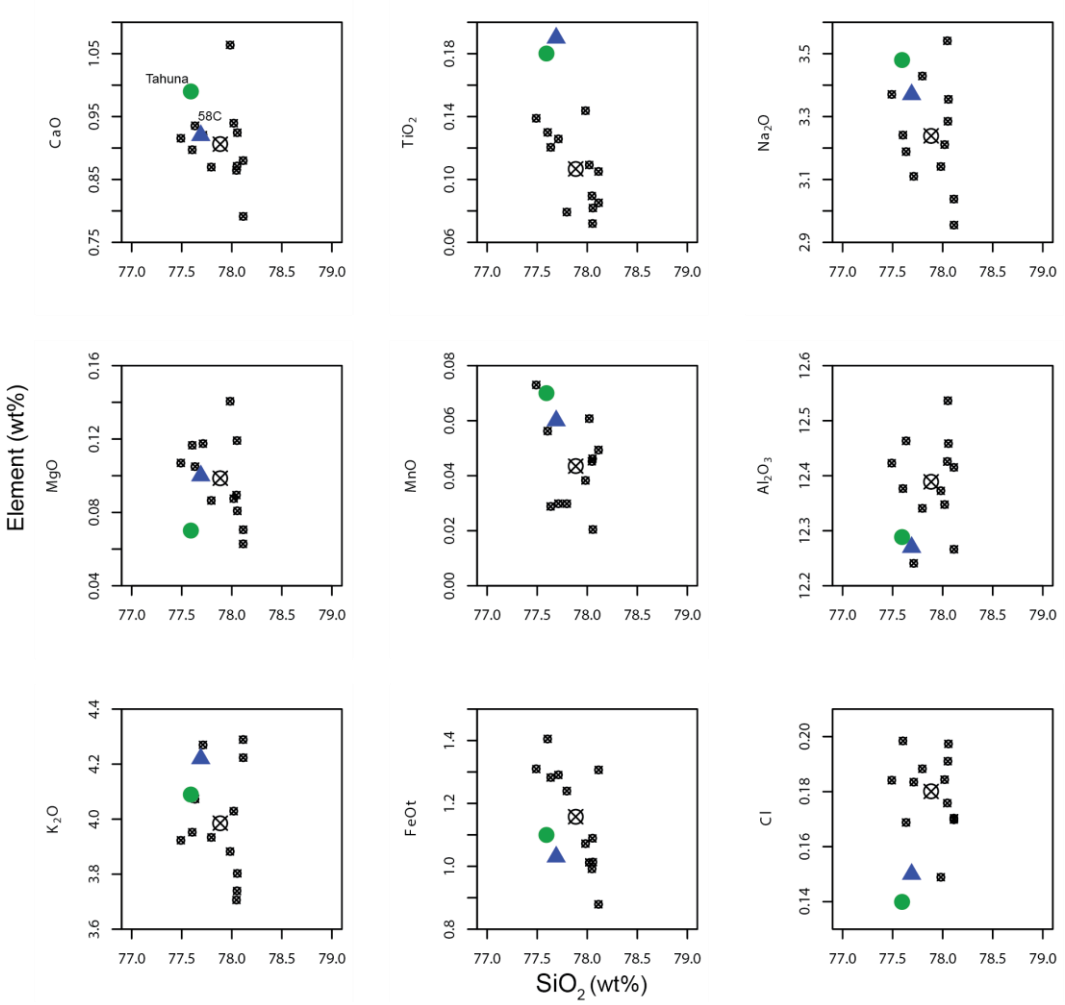

Figure 49. Major and minor element vs. SiO_2 glass chemistry for sample HP9 (hollow crossed circle; mean represented by a larger symbol), compared with mean Tahuna tephra data (filled circle) from Smith et al. (2005) and Tahuna lapilli subunit data (58C; triangle) from Smith & Shane (2002).

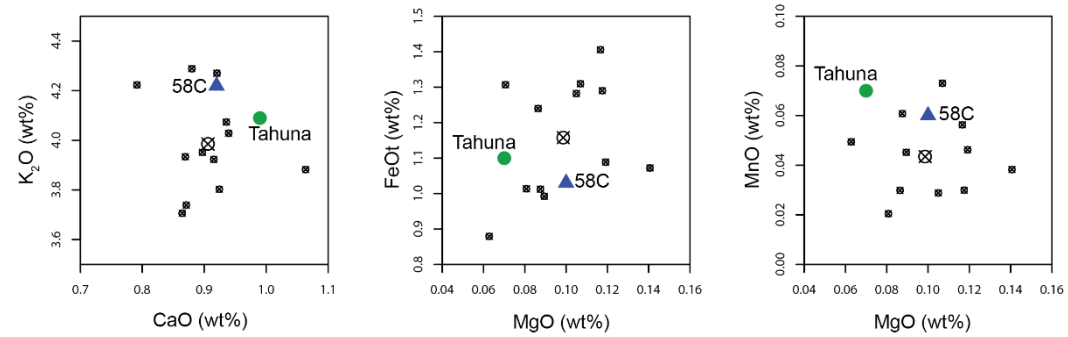

Figure 50. Plots of K_2O vs. CaO (left), FeOt vs. MgO (centre), and MnO vs. MgO (right) for sample HP9 (hollow crossed circle; mean represented by a larger symbol), compared with mean Tahuna tephra data (filled circle) from Smith et al. (2005) and Tahuna lapilli subunit data (58C; triangle) from Smith & Shane (2002).

Sample HP11 is from a pale grey ash unit directly above the hydrothermal vent breccia close to the base of the outcrop, and it is also stratigraphically below the c. 39 ka sinter and above the HP9 lapilli unit. As this unit is constrained chronologically by the c. 39 ka sinter and the ~240 ka Ohakuri Ignimbrite, only known tephras between these two ages were considered for comparison. The constraints removed the possibility of geochemically similar deposits such as Waihora and Rotoiti/Rotoehu tephras, leaving the Tahuna Tephra as a possible correlative.

The HP11 data were compared against the data from ashy subunits from Smith and Shane (2002) as well as the mean for Tahuna Tephra from Smith et al. (2005), as presented in Figures 50 and 51. The HP11 mean overall plots closest to the Tahuna 587 subunit, described in Smith and Shane (2002) as a coarse ash. The similarities are most evident in the plots for SiO_2 vs. Cl, K_2O vs. FeOt, and MgO vs. FeOt. HP11 is tentatively identified as a different subunit of the Tahuna Tephra to that of HP9. However, the general lithostratigraphy of the various subunits of the Tahuna Tephra is unclear from the Smith and Shane (2002) paper in terms of whether the 587 subunit is typically found above or below the 58C lapilli subunit.

Given that both HP9 and HP11 are identified as Tahuna Tephra, the age of the hydrothermal vent breccia is constrained to be concurrent with the Tahuna eruptive episode.

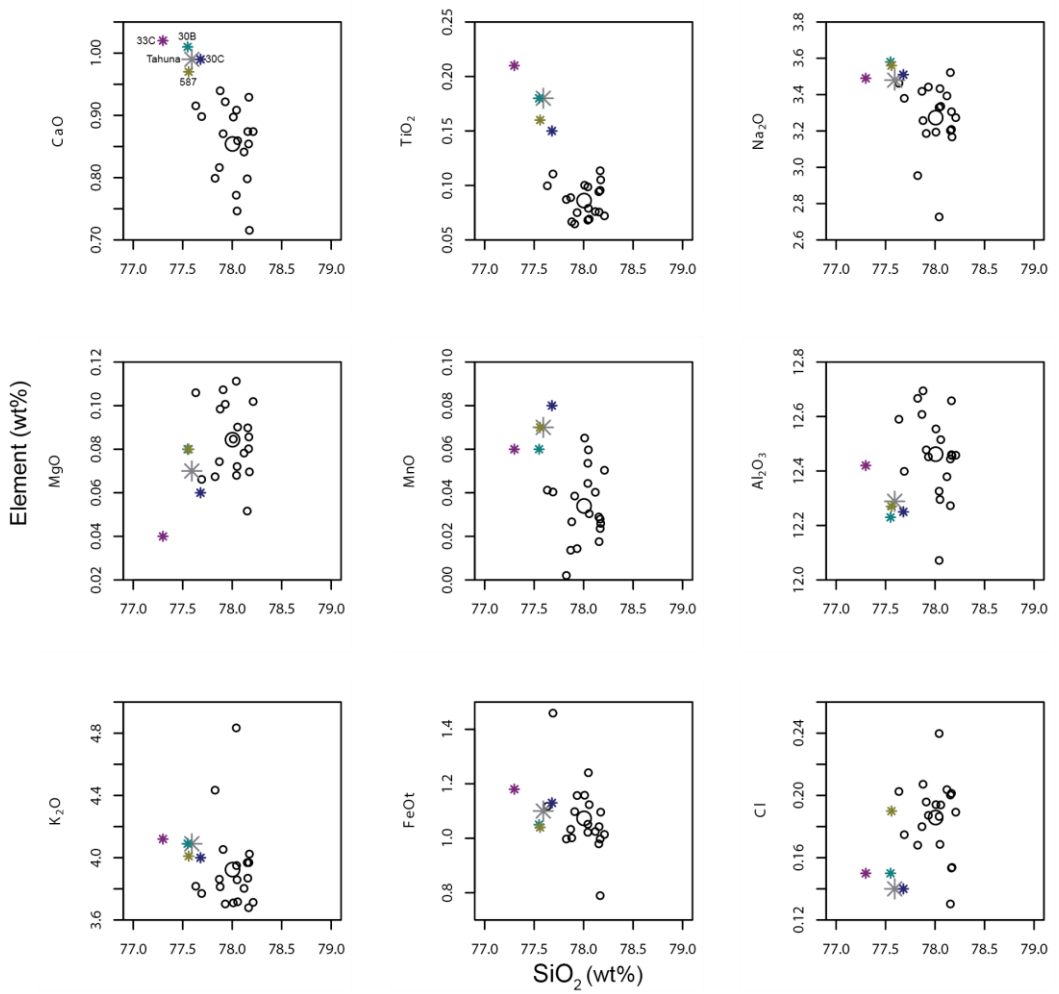

Figure 51. Major and minor element vs. SiO_2 glass chemistry for sample HP11 (circle; mean represented by a larger symbol), compared with mean Tahuna tephra data (large star) from Smith et al. (2005) and Tahuna subunit data (small stars) from Smith & Shane (2002).

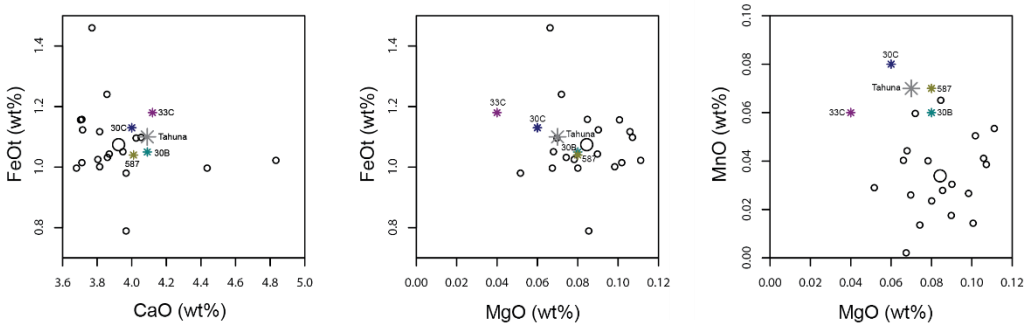

Figure 52. Plots of FeOt vs. K_2O (left), FeOt vs. MgO (centre), and MnO vs. MgO (right) for sample HP11 (circle; mean represented by a larger symbol), compared with mean Tahuna tephra data (large star) from Smith et al. (2005) and Tahuna subunit data (small stars) from Smith & Shane (2002).

Samples HR13 and HR15 are taken from a unit below the c. 39 ka sinter, containing a blocky buried soil and pink pumice (sample HR14, not analysed). The analyses of the samples are similar enough geochemically to be plotted together and are presented in Figures 52 and 53. However, results are inconclusive for the two samples, as they do not plot consistently near glass data analyses for any particular known tephra. Results are also complicated by the stratigraphic position, which puts the unit above the unit identified as Tahuna Tephra. The tephras HR13 and HR15 are closest in composition to include Tahuna Tephra, but also two tephras which are older than Tahuna Tephra (Tihoi and Waihora) and one tephra which is younger than Tahuna Tephra (Poihipi).

Even a tentative identification is not possible given the extent of the data available, and more EPMA may be needed for the samples, and more detailed comparison data (of individual shards) rather than solely mean data could also be helpful.

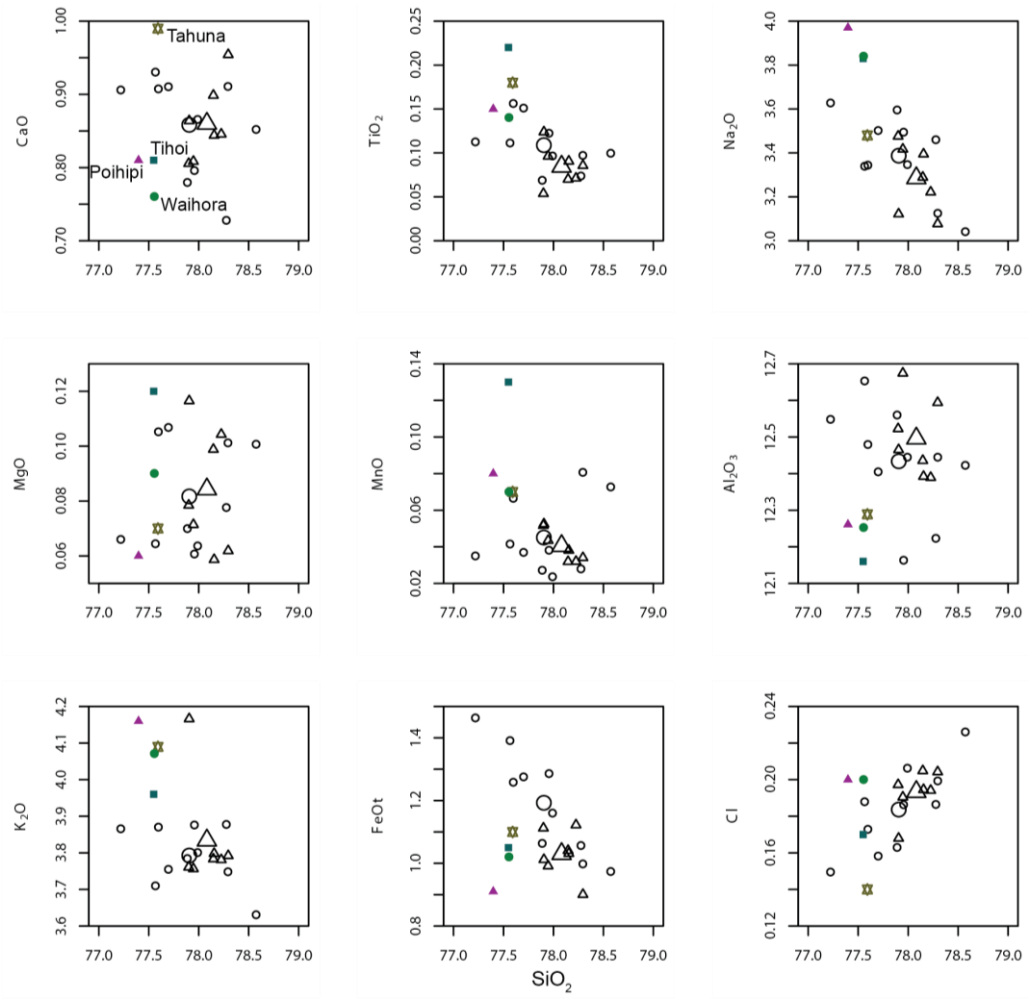

Figure 53. Major and minor element vs. SiO_2 glass chemistry for sample HR13 (hollow circle, mean represented by larger symbol) and HR15 (hollow triangle, mean represented by larger symbol) compared with Poihipi tephra (filled triangle), Tihoi tephra (filled square), Waihora tephra (filled circle) and Tahuna tephra (star) mean data from Smith et al. (2005).

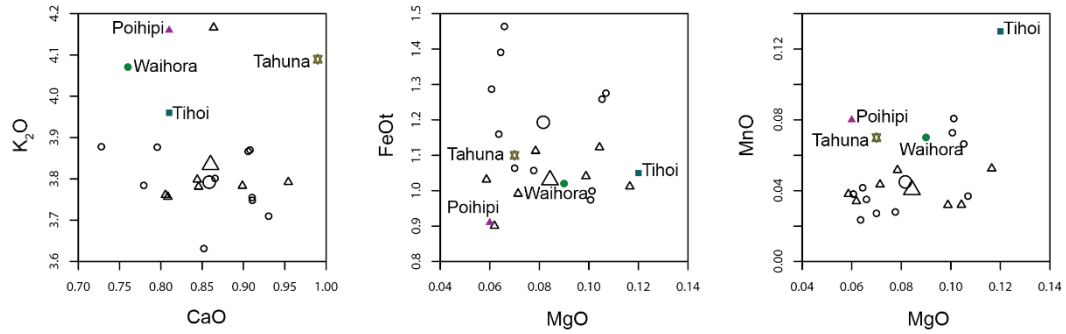

Figure 54. Plots of K_2O vs. CaO (left), FeOt vs. MgO (centre), and MnO vs. MgO (right) for sample HR13 (hollow circle, mean represented by larger symbol) and HR15 (hollow triangle, mean represented by larger symbol) compared with Poihipi tephra (filled triangle), Tihoi tephra (filled square), Waihora tephra (filled circle) and Tahuna tephra (star) mean data from Smith et al. (2005).

Sample HR17 was taken from the middle part of a normally graded ash unit underlain and overlain by sinter deposits, featuring coarse white ash in the base and fine to coarse grey ash with accretionary lapilli in the upper part. The unit was initially identified in the field as Poihipi Tephra in loess. The age of Poihipi Tephra (c. 28 ka; Lowe et al., 2013) fits within the age constraint provided by the underlying c. 39 ka sinter.

Major and minor elements of glass from sample HR17 are overall closest with those for Poihipi Tephra, particularly once the EPMA discrepancies are adjusted. The unadjusted plots are presented in Figures 54 and 55, with the SiO_2 vs. CaO and SiO_2 vs. Cl plots best supporting the initial identification. In the adjusted plots, SiO_2 vs. Ti_2O and SiO_2 vs. Na_2O also support the initial identification (Appendix 2.7).

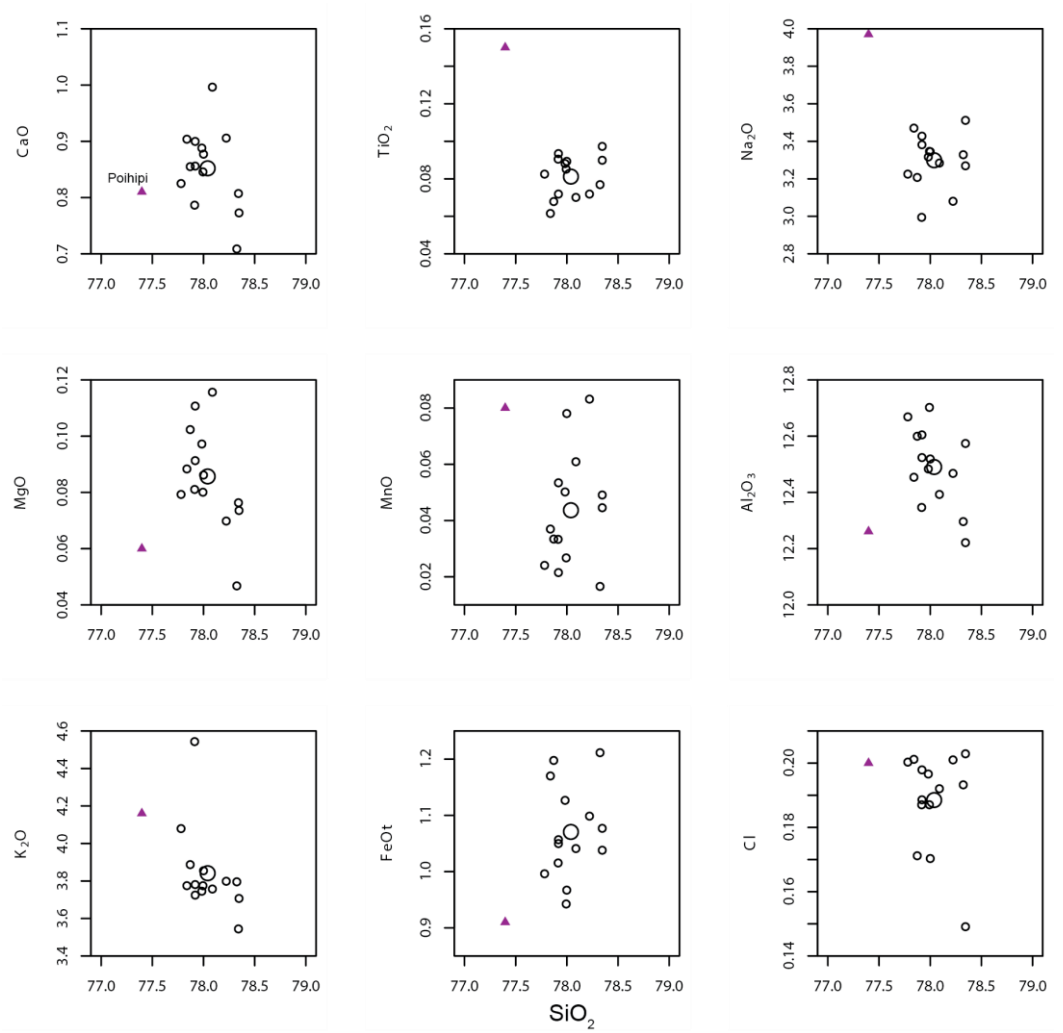

Figure 55. Major and minor element vs. SiO_2 glass chemistry for sample HR17 (hollow circle, mean represented by larger symbol), compared with Poihipi Tephra (filled triangle) mean data from Smith et al. (2005).

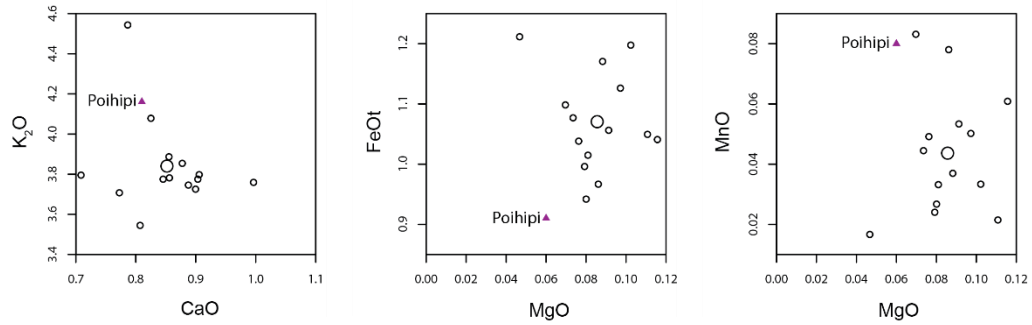

Figure 56. Plots of K_2O vs. CaO (left), FeOt vs. MgO (centre), and MnO vs. MgO (right) for sample HR17 (hollow circle, mean represented by larger symbol), compared with Poihipi Tephra (filled triangle) mean data from Smith et al. (2005).

Sample HR20 is from the upper part of a 0.4-m-thick unit which underlies Taupo Unit Y on the outcrop, with a 0.2-m-thick buried soil between the two units. The unit is around 1 m above the c. 39 ka sinter and must therefore be younger in age than the sinter, and hence known tephras older than 39 ka have not been used for comparisons. The unit from which HR20 was taken was described as potentially being two units graded into each other, and the glass geochemistry supports this possibility.

Overall the data points align best in the SiO_2 plots with Okaia Tephra and Oruanui/Kawakawa tephra, in particular for K_2O, FeOt, Cl, and TiO_2. In some cases, however, the data are more closely correlated with Rotoma Tephra, as with the CaO and MgO plots, and Rotoma Tephra is still reasonably close in the K_2O and TiO_2 plots. In some cases there is a split of points which could indicate that both Rotoma and Kawakawa tephras may be present, but more microprobe data would need to be collected to determine whether this is an appropriate conclusion.

The unit HR20 was taken from is tentatively identified as predominantly Oruanui/Kawakawa, with an associated age of c. 25.4 ka (Vandergoes et al., 2013) Given the unit is quite high up in the stratigraphy and ~1 m above the c. 39 ka sinter, the identification is very tentative. Kawakawa is usually fine-grained and sticky, field (physical) properties which were not noted at the time of observation but could be present nonetheless.

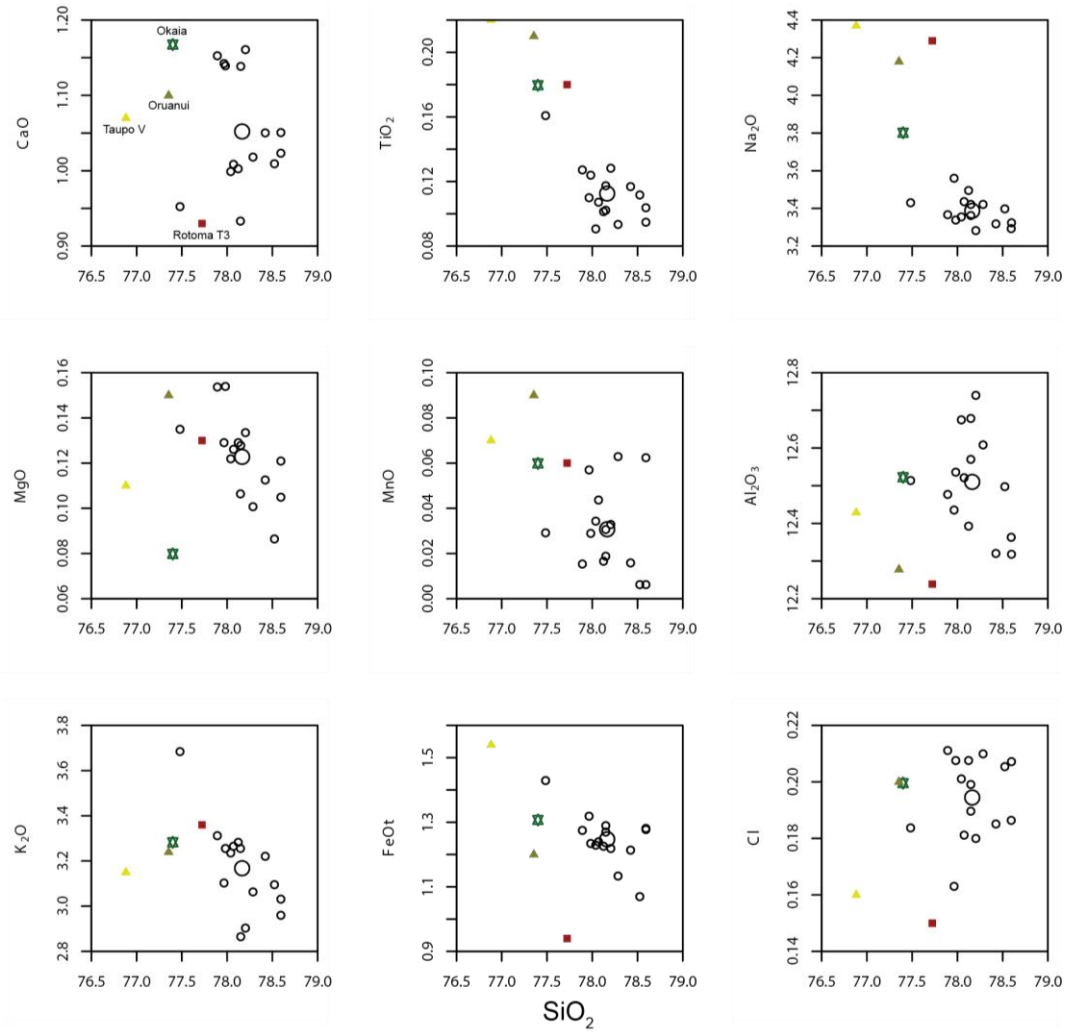

Figure 57. Major and minor element vs. SiO_2 glass chemistry for sample HR20 (hollow circle; mean represented by a larger hollow circle), compared with Taupo Unit V and Oruanui/Kawakawa (filled triangles), Okaia (star), and Rotoma T1 (filled square) from Smith et al. (2005).

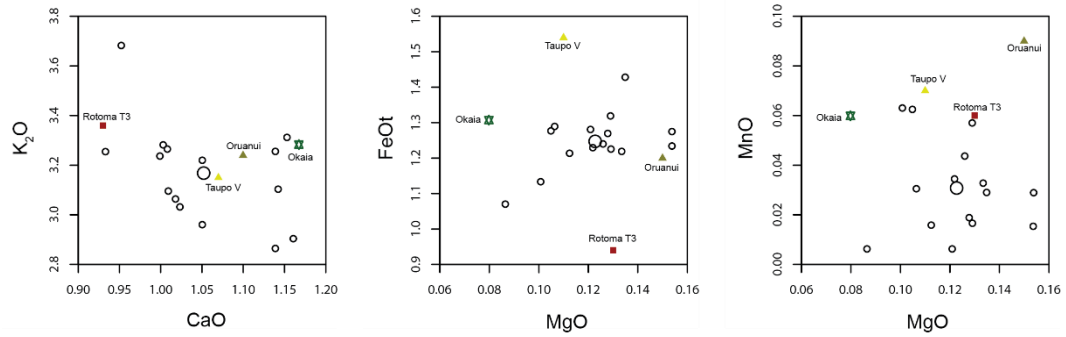

Figure 58. Plots of K_2O vs. CaO (left), FeOt vs. MgO (centre), and MnO vs. MgO (right) for sample HR20 (hollow circle; mean represented by a larger hollow circle), compared with Taupo Unit V and Oruanui/Kawakawa (filled triangles), Okaia (star), and Rotoma T1 (filled square) from Smith et al. (2005).

5.4: Conclusions

Using major and minor element analyses from volcanic glass derived by EMPA, and comparison with mean data of glasses from known tephras from the TVZ, most of the samples were able to be identified (Table 10).

Samples HT13, HT16, HT17, HT18, HT33, HT35, HT20, and HT25 from the Meade-Hossack trench were identified as Rotoma Tephra. HT10, HT11, and CR31 from the Meade-Hossack trench and Core 3 were identified as Rotorua Tephra. HT12, HT36, and CR32 from the Meade-Hossack trench and Core 3 were identified as Okareka Tephra. HR20 from the outcrop was identified tentatively as Kawakawa Tephra. HR17 from the outcrop was identified as Poihipi Tephra. HP9 and HP11 from the pit at the base of the outcrop were identified as Tahuna Tephra. HR13 and HR 15 from the outcrop were not able to be identified, but are constrained as being older than the c. 39 ka sinter and younger than the c. 40 cal. ka Tahuna tephra. Henceforth ages given within the ^{14}C timescale and reported as ka are actually cal. ka.

Table 10. Summary of samples and tephra identifications made on the basis of glass major and minor elemental EMPA-derived data, and corresponding ages from [a]Lowe et al. (2013), [b]A. Rae (pers. comm., 2014), and [c]Smith and Shane (2002).*

Sample	Identification	Age (cal. yr. BP)
HT13	Rotoma Tephra	9423 ± 120[a]
HT16		
HT17		
HT18		
HT33		
HT35		
HT20	Rotoma Tephra (w/Rotorua Tephra)	9423 ± 120[a]
HT25		
HT10	Rotorua Tephra	15635 ± 412[a]
HT11		
CR31		
HT12	Okareka Tephra (w/ Rotorua Tephra)	21858 ± 290[a]
HT36	Okareka Tephra	21858 ± 290[a]
CR32		
HR20	Kawakawa Tephra	25358 ± 162[a]
HR17	Poihipi Tephra	28446 ± 670[a]
HR13	Uncorrelated	>c. 39000[b], <c. 40000[c]
HR15		
HP9	Tahuna Tephra	c. 40000[c]
HP11		

*Additionally the Taupo and Kaharoa tephras, as well as Ohakuri Ignimbrite, were identified in the field and/or via mineralogy.

There is uncertainty around the identifications made in the study, and it would be worthwhile gathering more EPMA data for samples that were not analysed and also for samples that turned out to be heterogeneous. The EPMA data were perhaps somewhat limited in quality, with several discrepancies detected on multiple elements despite precautions taken to choose appropriate block preparation, operating conditions, and beam positions.

In addition to more EPMA data, for a more definitive identification, trace element data could be collected by LA-ICP-MS. It would be particularly useful for TVZ tephras as many are compositionally similar with regard to their major elements. However, at present there is a lack of available comparison data for trace element composition of TVZ-derived volcanic

glass and these data would also need to be gathered, preferably from samples obtained from type sections of the tephras.

More broadly speaking, an effort should be made in the scientific community to make geochemical data more accessible, as means do not necessarily tell the whole story, and it can be more useful to have a “cloud” of data for comparison rather than a single point.

Chapter 6: Restoration of tectonic deformation in the Meade-Hossack trench

6.1: Introduction

Trench restoration is a form of analysis which involves removing deformation and reconstructing the thickness and orientation of stratigraphic units in stages, recording the amount of displacement and rotation needed as the analysis progresses. Restoration can be used to calculate cumulative displacement over time, and in volcanic zones can be used to assess time associations between volcanic events and fault rupture events.

A previous study on the Whirinaki Fault (Canora-Catalán et al., 2008) used trench logs to obtain estimates for the single-event displacements (SED), recurrence intervals, and slip rates on two individual fault strands. A summary of results for the Fitzpatrick trench on the northwest section of the west strand and the Matthews trench on the southeast section of the east strand of the Whirinaki Fault is presented in Table 11. The Meade-Hossack trench is on the northeast section of the east strand of the Whirinaki Fault (Figure 59. Data obtained from trench restoration will be compared with those for both the Fitzpatrick and Matthews trenches.

Table 11. Summary of rupture history and slip rates from the Fitzpatrick (west strand) and Matthews (east strand) trenches on the Whirinaki Fault (Canora-Catalán et al., 2008).

Trench	Event	Timing	SED (m)	Slip rate (mm/yr)
Fitzpatrick (west)	F1	< 1.7 ka	0.8	0.3 ± 0.1
	F2	>1.7, <5.5 or 8 ka	0.9	
	F3	>5.5 or 8, <9.5 ka	1	
	F4	9.5 ka	0.7	
	F5	>15.8, <21.8 ka	0.7	0.1 ± 0.1
Matthews (east)	M1	432 ± 102 cal. yr BP	0.2	1.4 ± 0.2
	M2	501 ± 63 cal. yr BP	0.5	
	M3	>9.5, <15.8 ka	2	0.2 ± 0.1
	M4	>21.8, <27 ka	4	0.4 ± 0.1

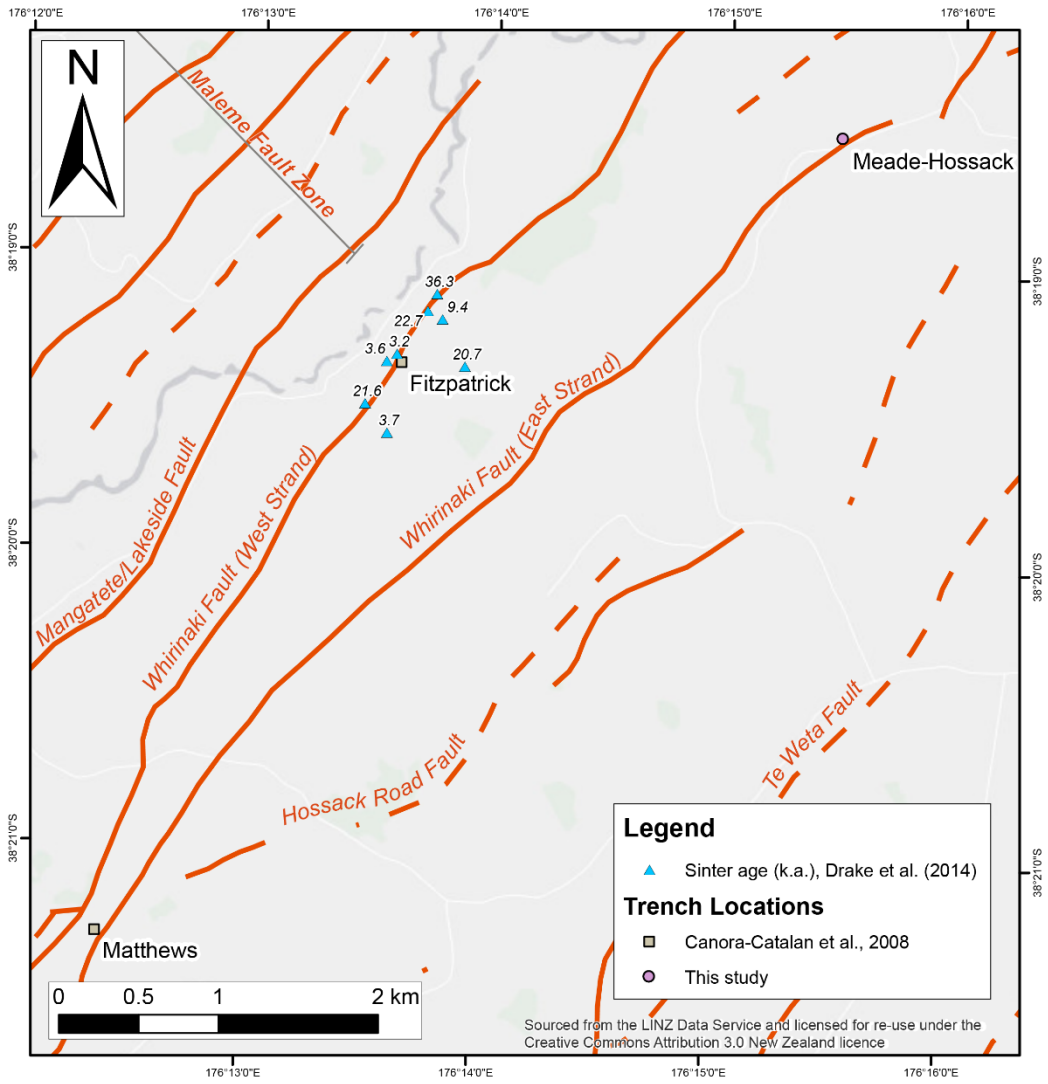

Figure 59. Location of paleoseismic trenches on the Whirinaki Fault. The locations of the Fitzpatrick and Matthews trenches (Canora-Catalán et al., 2008) are represented as squares, the Meade-Hossack trench is represented with a circle. Locations of dated sinters from Drake et al. (2014) are represented with triangles and labelled with their ages.

The aim of restoring the Meade-Hossack trench is to use the identified tephra units as a means to constrain the ages of fault rupture events, and to obtain estimates for SED that can be used in calculating slip rates for the time periods provided by the stratigraphic framework, and rupture recurrence intervals. The fault activity will also be compared against the ages of sinters at the Meade-Hossack site and those on the west strand of the Whirinaki Fault found by Drake et al. (2014).

6.2: Methods

Adobe Illustrator was used to perform a detailed restoration of deformation in the Meade-Hossack trench, following examples given in the data supplements to Villamor et al. (2007, 2011). Each step of the restoration is described in detail, including the horizontal and vertical batters that the restoration crosses, the number of events restored, the active fault planes on which the deformation occurred, the amount of deformation associated with each event restored given as SED, and the timing of the event as determined by the bracketing stratigraphic units. A series of figures was produced for each wall of the trench to display the progression of displacement.

6.3: Results

6.3.1: Restoration of deformation in the SW wall

Figure 60 shows the trench log of the SW wall as it was mapped in the field in November 2014, with labelled units identified from geochemical data. The subunits of Taupo Y mapped in the trench (Taupo Ignimbrite, Taupo Pumice Lapilli, and Rotongaio Ash) have been merged into one synchronous unit, which does not affect constraints for the ages of fault rupture events. The topsoil contains hard white pumice lapilli in the base, which are assumed to represent the Kaharoa Tephra. Unidentified units have been merged as Unit 30x. The bottom unit in the core is labelled as 50; it is unidentified and does not bear any resemblance to the other units in the trench. It is possible that Unit 50, a pale grey (low chroma) colour, is a reduced tephra (having been below the water table). It may correlate to part of Unit 30x, or possibly alluvium or Kawakawa Tephra. The base of Unit 50 is assumed to be directly on top of sinter, as that was the point at which the vibrocore was obstructed from further penetration. However, the vibrocore could have been obstructed for other reasons such as hitting a boulder, or other mechanical failure.

The restoration of the SW wall will proceed given the appropriate criteria are present for each event: progressive displacement, and the presence of a tephra mantling the displacement.

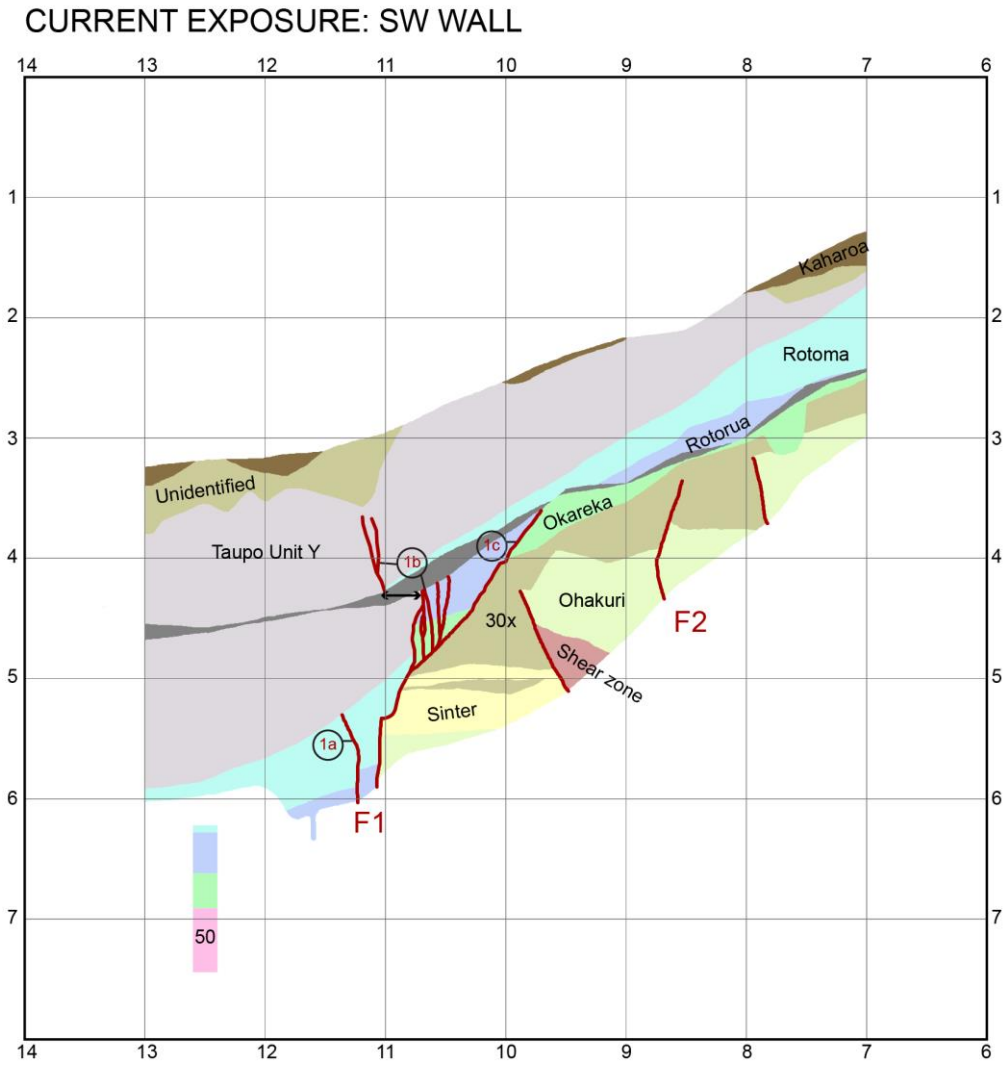

Figure 60. Partial trench and core log of the SW wall of the Meade-Hossack trench, Whirinaki Fault.

Two fault planes were mapped on the SW wall, labelled F1, and F2, with subsidiary ruptures of F1 labelled as 1a, 1b, and 1c.

F1 has the most recent movement, with fracturing and fissuring of Taupo Unit Y on F1b. The fracturing in Taupo Unit Y on 1b is likely to be a continuation of the fracturing in the Rotorua and Okareka tephras below the bench, as indicated by the arrowed line. The discrepancy in continuity is attributable to several factors: fault planes are rarely straight, the trench may

not be cut perpendicular to the fault, and the soft sediment in which the faulting has occurred lends itself to more convolute deformations.

F2 affects Ohakuri Ignimbrite, sinter, and Unit 30x (between c. 240 ka and c. 22 ka), and is associated with a zone of sheared material between horizontal batters 9 and 10.

The youngest unit displaced is Taupo Unit Y (Figure 60). The result of the first restoration step is shown in Figure 61. The stratigraphy of Core 1 was extrapolated to corresponding units on the hanging wall where possible. Restoration involved the removal of fracturing of Taupo Unit Y at rupture 1b, vertical displacement of Taupo Unit Y, Rotoma, Rotorua, and Okareka tephras on the hanging wall at rupture 1b, and restoration of eroded and/or altered material in the upper part of Taupo Unit Y. The gap left in the log is attributable to the aforementioned complex nature of faulting in softer sediments.

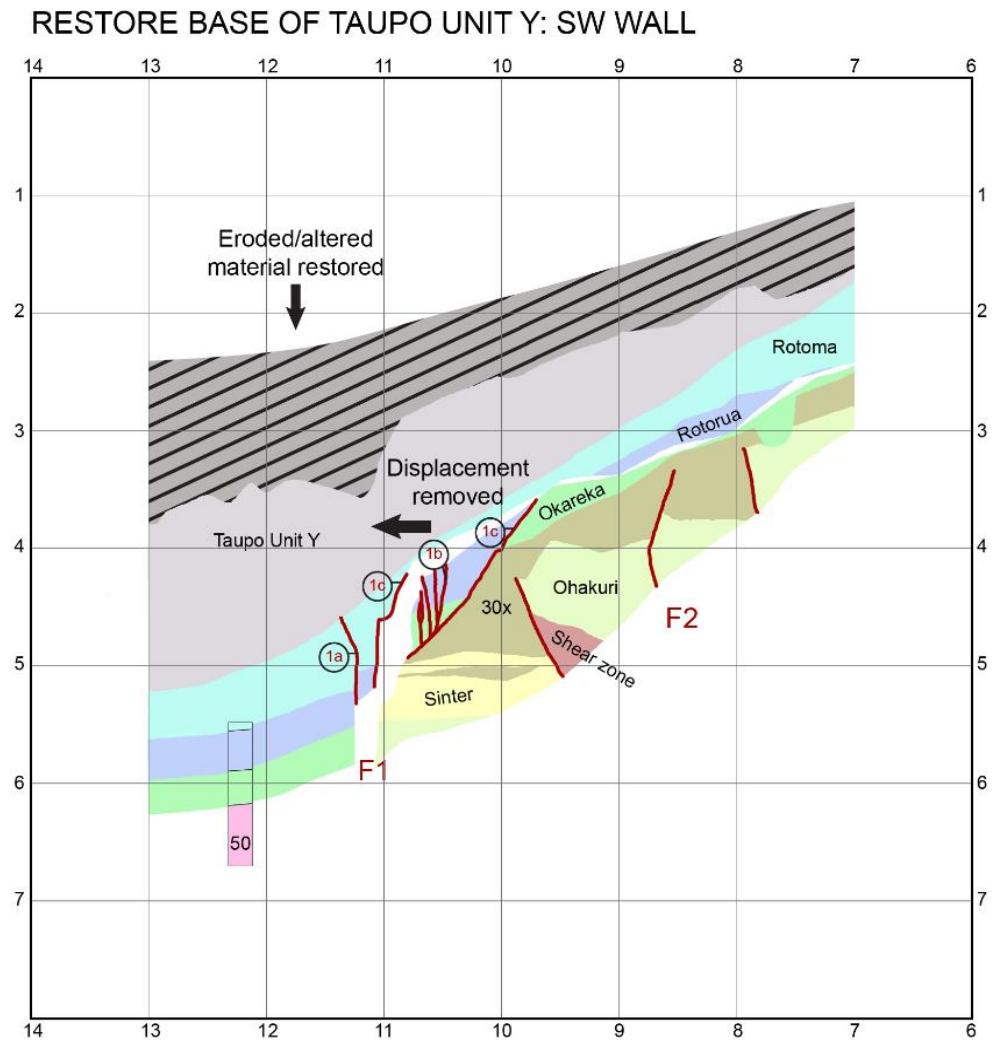

Figure 61. First stage of restoration of the SW wall of the Meade-Hossack trench log, restoring the base of Taupo Unit Y.

Event 1 is represented by the difference between Figures 59 and 60, with Figure 61 showing the geometry of the layers before deformation by Event 1. The event horizon is within the Taupo Ignimbrite.

Restoration is across: Same batters at F1.

Fault planes active: F1 (1b only)

SED: 0.55 m

Timing of event: Pre-Kaharoa Tephra, post Taupo Unit Y, 0.63 ka < Event 1 < 1.8 ka

The second youngest unit affected by deformation is the Rotoma Tephra. The result of the restoration is shown in Figure 62. Restoration involved removing vertical displacements of 0.15 m and 0.7 m on ruptures 1a and 1b, removing the cracking at rupture 1b, and restoring eroded material from the upper part of the Rotoma Tephra. The bases of the Rotorua and Okareka tephras on the hanging wall are aligned with the extrapolated stratigraphy from Core 1, and can be considered partially restored.

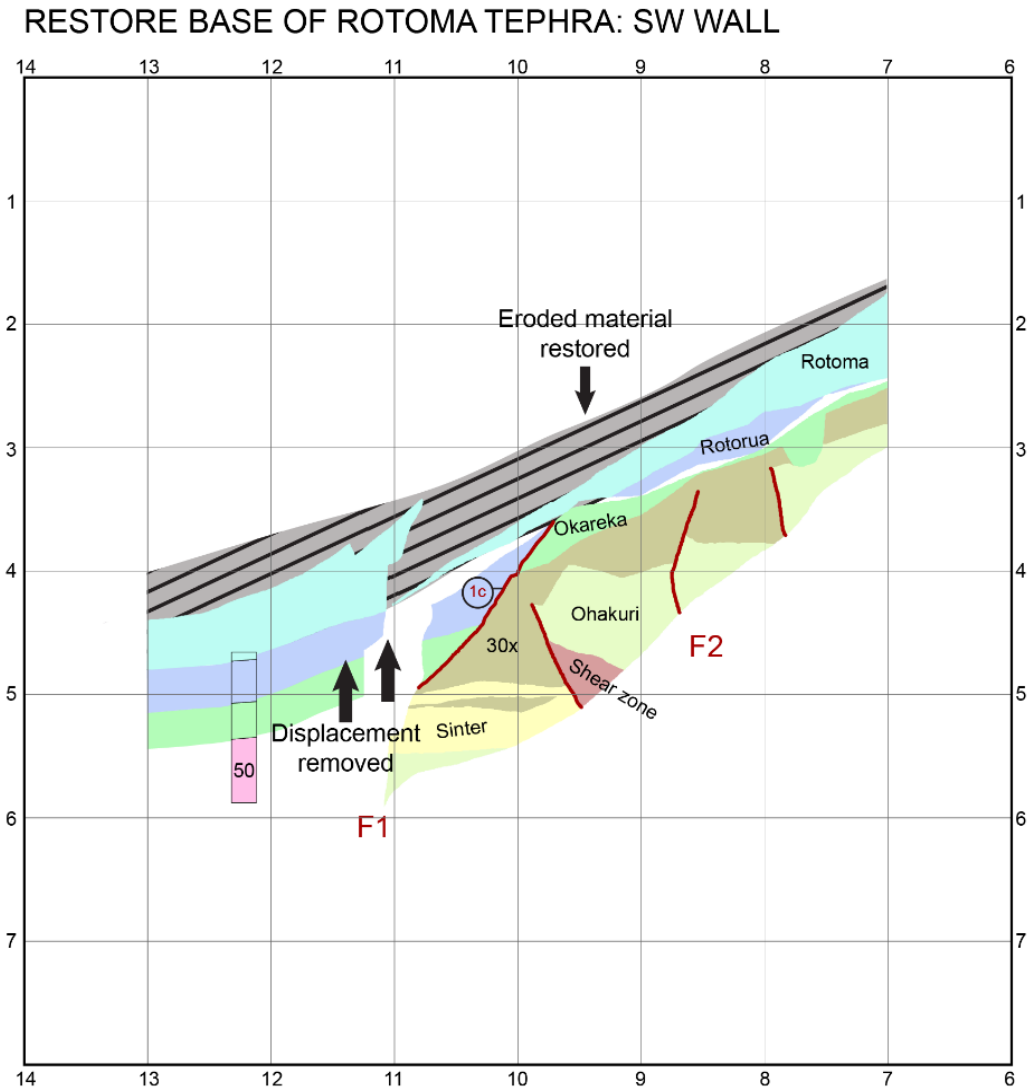

Figure 62. Second stage of restoration of the SW wall of the Meade-Hossack trench log, restoring the base of Rotoma Tephra.

Event 2 is represented by the difference between Figures 60 and 61, with Figure 61 showing the geometry of the layers before deformation by Event 2. The event horizon is at the top of Rotoma Tephra.

Restoration is across: Different batters at F1.

Fault planes active: F1 (1a and 1b)

SED: 0.85 m

Timing of event: Pre- Taupo Unit Y, post Rotoma Tephra, 1.8 ka < Event 2 < 9.4 ka

The third youngest unit affected by deformation is the Rotorua tephra. The result of the restoration is shown in Figure 63. Restoration involved removing displacement from Rotorua and Okareka tephras at rupture 1c by moving 0.8 m laterally and 0.9 m vertically (or 1.2 m along a hypotenuse), which restores the base of both units.

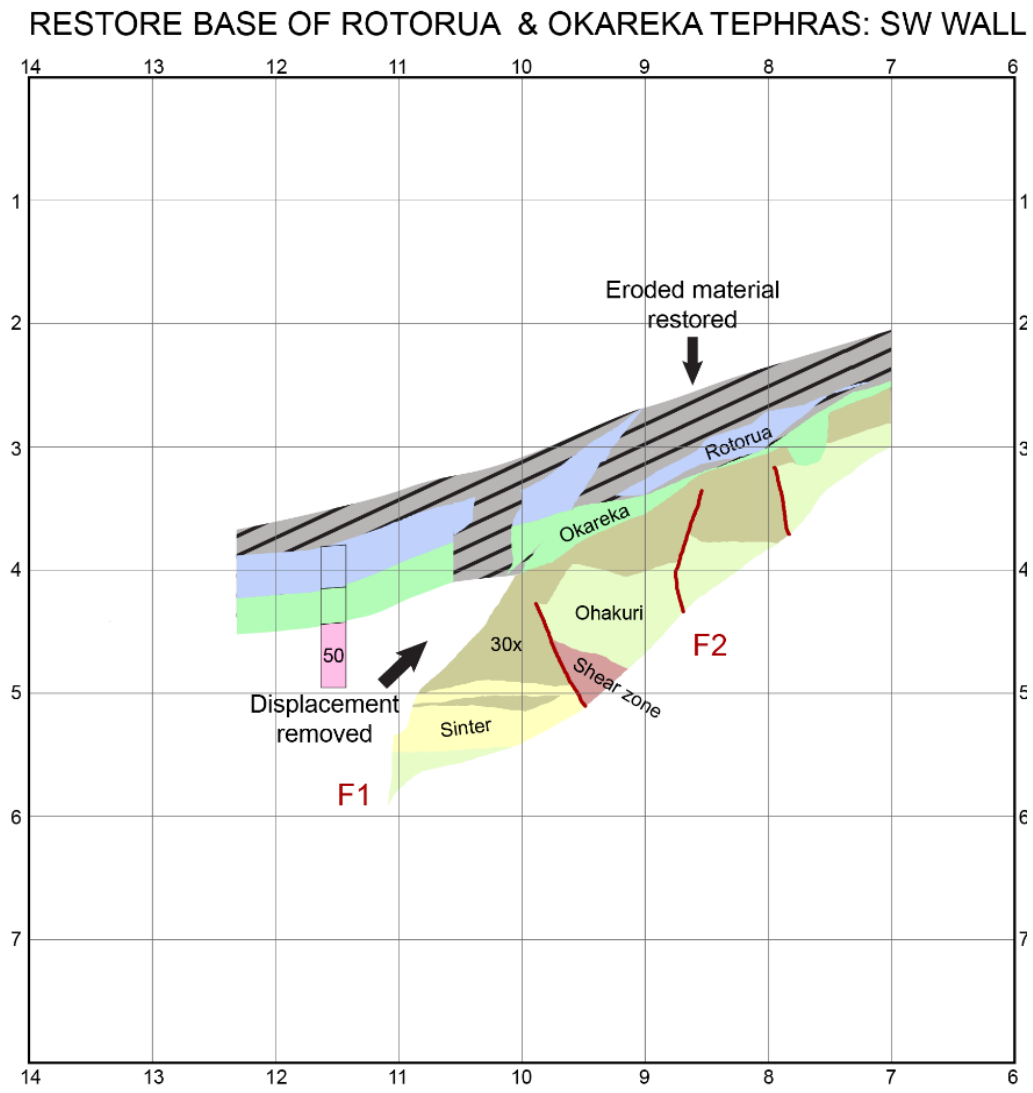

Figure 63. Third stage of restoration of the SW wall of the Meade-Hossack trench log, restoring the base of Rotorua and Okareka tephras.

Event 3 is represented by the difference between Figures 61 and 62, with Figure 63 showing the geometry of the layers before deformation by Event 3. The event horizon is at the top of Rotorua Tephra.

Restoration is across: Different batters at F1.

Fault planes active: F1 (1c only)

SED: 1.2 m

Timing of event: Pre-Rotoma Tephra, post Rotorua Tephra 9.4 ka < Event 3 < 15.6 ka

The oldest unit affected by deformation on the SW wall is Unit 30x. Restoration (Figure 64) involved removing the sinters, removing Unit 50 as it was assumed to be younger than the sinters, removing displacement from the unidentified unit and Ohakuri Ignimbrite by moving 0.2 m laterally and 0.85 m vertically (0.87 m along a hypotenuse), removing sheared material and a further 0.26 m of displacement, removing drag folding from Ohakuri Ignimbrite, a 21° rotation to bring the units up 0.5 m and match the slope, and restoring eroded material.

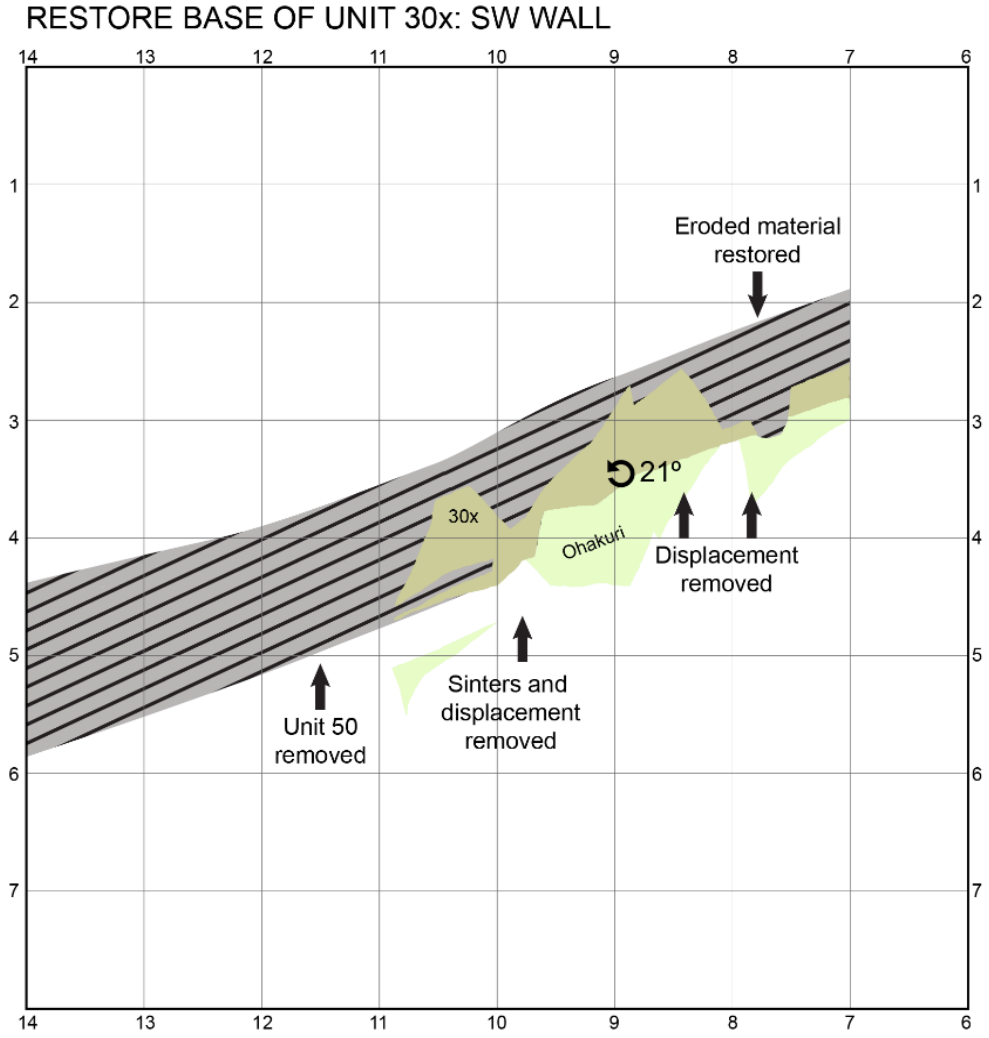

Figure 64. Final stage of restoration of the SW wall of the Meade-Hossack trench log, restoring the base of the unidentified unit.

Event 4 is represented by the difference between Figures 62 and 63, with Figure 64 showing the geometry of the layers before deformation by Event 4. The event horizon is within the unidentified unit.

Restoration is across: Different batters at F2.

Fault planes active: F2

SED: 1.63 m

Timing of event: Pre-Okareka Tephra, post Ohakuri Ignimbrite, 21.8 ka < Event 4 < c. 240 ka

6.3.2: Comments on deformation in the NE wall

Figure 65 shows the trench log of the NE wall as it was mapped in the field in November 2014, with units as identified from EMPA data. As with the SW wall, the subunits of Taupo Y mapped in the trench (Taupo Ignimbrite, Taupo Pumice Lapilli, and Rotongaio Ash) have been merged into one unit. Three fault planes were mapped on the NE wall, labelled F1, F2, and F3. F1 has the most recent movement, displacing Taupo Unit Y, and is associated with some fissuring in Okareka Tephra between horizontal batters 10 and 11. F2 and F3 both affect Ohakuri Ignimbrite, sinter, and an unidentified unit of between c. 240 ka and c. 22 ka in age.

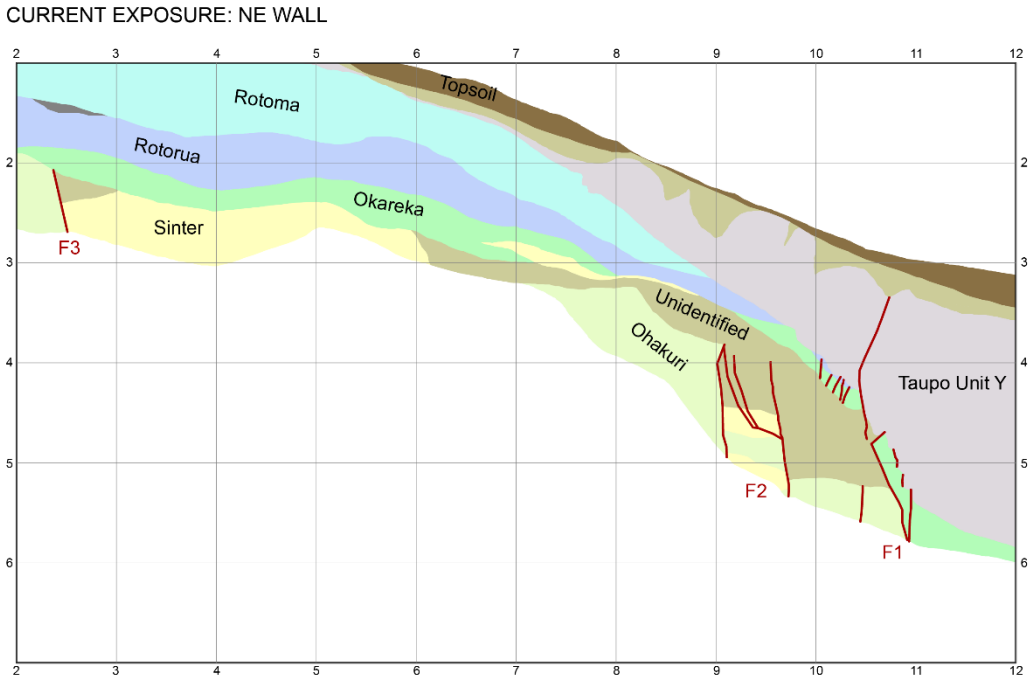

Figure 65. Partial trench log of the NE wall of the Meade-Hossack trench, Whirinaki Fault.

The NE wall will not be restored in this study, as only three of the four events observed on the SW wall are represented. The Rotorua and Rotoma tephras are not present on the downthrown section, and the deformation of the Okareka Tephra (displacement, drag folding, and colluvial wedge formation) cannot be adequately constrained. The criteria for restoration cannot be fulfilled in this case as the displacements are not mantled and at least one known event may be missing from the record. Where possible, SED values have been measured from the trench logs and are provided in Appendix 3.

The absence of the Rotoma and Rotorua tephras on the NE wall highlights a common limitation of the paleoseismic trenching technique: that spatial variability and fault behaviour can affect the stratigraphy within lateral distances of just a few metres, particularly in softer, more erodible deposits.

6.3.3: Slip rates

The displacement values from the restoration of the trench logs and the age constraints were used to estimate average slip rates for each of the trench walls, using the simple formula:

$$fault\ slip\ rate\ \left(\frac{mm}{yr}\right) = \frac{displacement\ (mm)}{number\ of\ years}$$

The values used and the results of slip rate calculations are presented in Table 12. The average offset of the Ohakuri Ignimbrite on the Whirinaki Fault, a value of 112 ± 32 m (Canora-Catalán et al., 2008), has been added to the pre-Okareka displacement values obtained from the restoration in order to give a more accurate long-term slip rate for event MH5. Where possible, measurements from the NE wall (Appendix 3.1) have been included in calculations of mean displacement values. For simplicity, a uniform distribution has been assumed when dealing with uncertainties.

Table 12. Slip rates for each phase of movement identified from the Meade-Hossack trench logs. Starred events have incorporated measurements from the NE wall into mean values.

Event	Constraining Ages (ka)	ΔTime (yrs)	Mean Displacement (mm)	Mean Slip Rate (mm/yr)
MH1*	1.8 – 0.63	1082 ± 24	940 ± 551	0.87 ± 0.37
MH2	9.4 – 1.8	7705 ± 176	850 ± 141	0.11 ± 0.20
MH3	15.6 – 9.4	6212 ± 752	1200 ± 141	0.20 ± 0.22
MH4*	21.8 – 15.6	6223 ± 992	800 ± 141	0.13 ± 0.27
MH5*	240 – 21.8	218142 ± 14552	113790 ± 45622	0.53 ± 0.24

The mean slip rate for the Whirinaki Fault at the Meade-Hossack trench from the Ohakuri Ignimbrite to the Okareka Tephra is 0.53 ± 0.24 mm/yr, after which it then drops to 0.13 ± 0.27 mm/yr until the Rotorua tephra is deposited. From the time of deposition of the Rotorua Tephra to that of the Rotoma Tephra, the slip rate increases to 0.20 ± 0.22 mm/yr, and then it drops to 0.11 ± 0.20 mm/yr until the emplacement of Taupo Unit Y. The rate then rises again to 0.87 ± 0.37 mm/yr until the Kaharoa Tephra is deposited.

The long-term slip rate of around 0.5 mm/yr post-Ohakuri and pre-Okareka is comparable to the slip rate for the same period of 0.45 ± 0.15

mm/yr calculated in Canora-Catalán et al. (2008), as is the lower cumulative slip rate for the period between Rotorua tephra deposition and emplacement of Taupo Unit Y, 0.3 ± 0.05 mm/yr versus 0.07 ± 0.01 mm/yr in the Meade-Hossack trench. The similarity with the Matthews and Fitzpatrick slip rates continues with a sharp increase in slip rate to 0.75 mm ± 0.28 mm/yr after the emplacement of Taupo Unit Y until the present day in the Meade-Hossack trench, compared to the rate of 1.4 ± 0.2 mm/yr reported in Canora-Catalán et al. (2008).

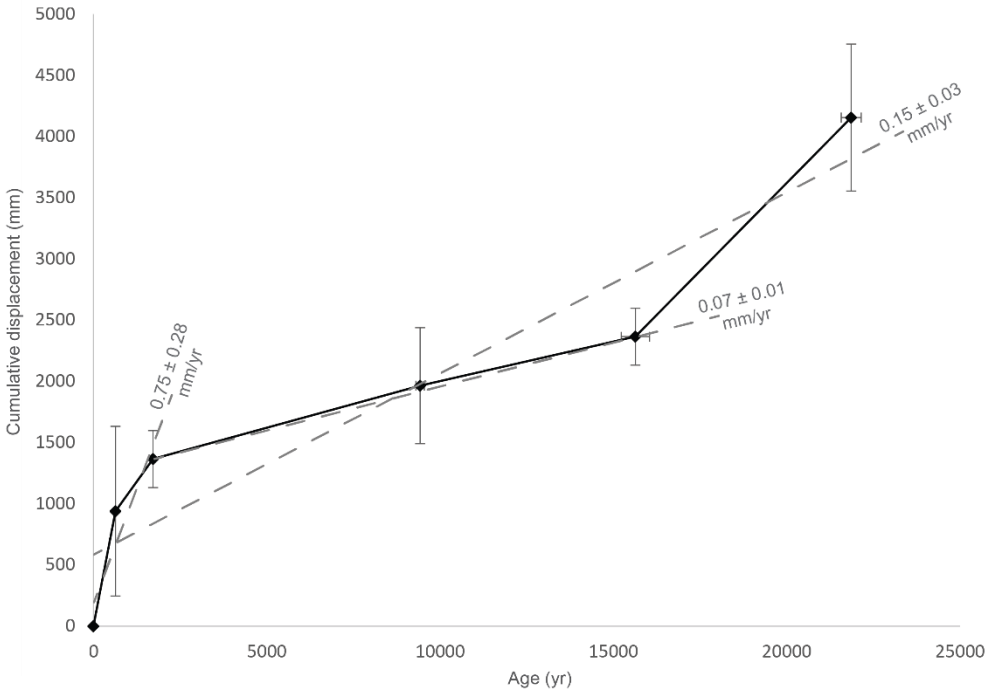

Figure 66. Displacement-age plot for the Meade-Hossack trench, showing cumulative vertical displacement from present day to Okareka Tephra deposition.

There are some limiting factors which impact the accuracy of the slip rates calculated. Having more identified units in the trench log would affect the age constraints for fault ruptures, potentially changing the values for the number of years and the amount of displacement occurring within that time period. The restoration process itself is qualitative and can provide only estimated values of displacement with uncertainties of ± 0.1 m. The ages of the tephras also have uncertainties attached and are subject to adjustment as different dating and statistical techniques arise. The uncertainties are crucial to include for practical uses of trench data, such as in seismic hazard assessments.

6.3.4: Rupture recurrence interval

The recurrence interval of ruptures (T) is calculated using the formula $T = N/n$, where N is the number of years in the time period in question, and n is the number of rupture events recorded within that timeframe.

Based on the Meade-Hossack trench data, the recurrence interval range for the northeast section of the east strand of the Whirinaki Fault during the last 21.8 kyr, including four rupture events, is 1.8–5.4 kyr.

The recurrence interval range fits within the range based on the Matthews trench on the southeast section of the east strand for the same time period, though the minimum recurrence is lower by ~1 kyr and the maximum recurrence is higher by ~2 kyr in the southeast section. The comparison with the range for the Fitzpatrick trench on the west strand yields roughly the same minimum recurrence, but the maximum recurrence for the Fitzpatrick trench is over double that of the Meade-Hossack trench. The recurrence interval range for the Meade-Hossack trench is closer to that calculated for the whole Whirinaki fault, which is 1–4 kyr (Canora-Catalán et al., 2008).

6.4: Interpretation

A summary of events of the past 30,000 years is presented in Figure 67, along with comparisons with other events from the Matthews and Fitzpatrick trenches on the southeast section of the east strand of the Whirinaki Fault studied by Canora-Catalán et al. (2008). Included on the summary diagram are some of the sinter emplacement intervals observed in the trench and on the outcrop at the Meade-Hossack site, and sinter emplacement intervals on the west strand of the Whirinaki Fault (Figure 59) from a study by Drake et al. (2014). MH5 has been excluded from the summary figure because it is too poorly constrained (> 21.8 ka, < 240 ka).

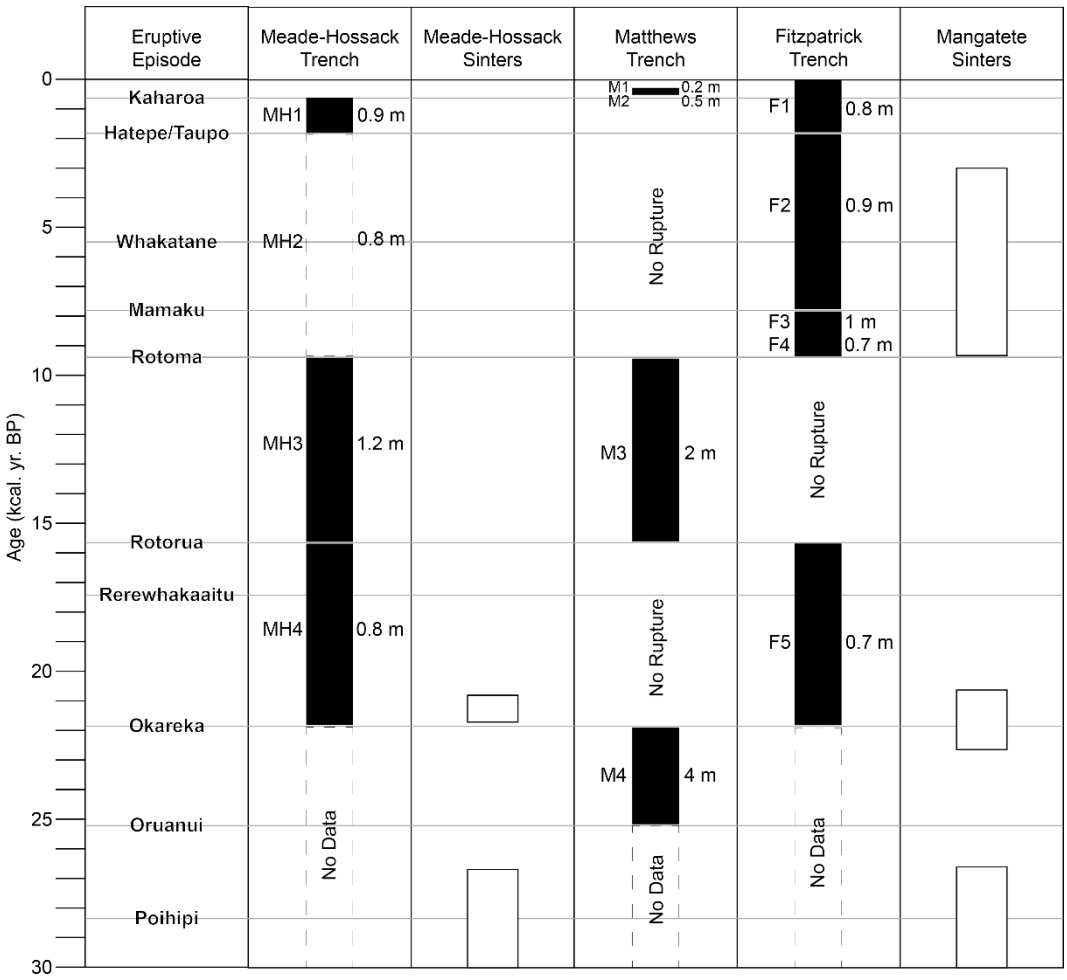

Figure 67. Summary of faulting events in the Meade-Hossack trench, compared with faulting events in the Matthews and Fitzpatrick trenches from Canora-Catalán et al. (2008), sinter formation at the Meade-Hossack site (trench and outcrop), and sinter formation at Mangatete, TVZ, from Drake et al. (2014). For the trenches, event number and SED are on the left and right side of the bars, respectively.

Rupture events in the Meade-Hossack trench appear to be influenced by movements along both the southeast section of the east strand, and the west strand, which is geographically closer (Figure 59). The influence of both strands may explain why the rupture recurrence interval range is closer to that of the entire Whirinaki Fault, rather than either the Matthews or Fitzpatrick trenches.

The MH1 SED post-Hatepe is comparable to that of F1, though it is possible that MH1 is recorded as a single event when it may have been two, and it is also possible that the MH1 rupture occurred after the Kaharoa eruption and did not reach the surface. The MH2 rupture event is poorly

constrained between the Rotoma and Hatepe eruptive episodes, a period of no rupture in the Matthews trench. The SED of MH2 is similar to that of F2, which occurred after the Mamaku Tephra (which has an age of 7940 ± 257 cal. yr BP; Lowe et al., 2013); and before Taupo Unit Y. Alternatively, MH2 could be correlated with either F3 or F4. MH3 occurs during a period of no recorded rupture in the Fitzpatrick trench, but within the same timeframe as M3 in the Matthews trench. The SED of MH3 is less than that of M3, 1.2 m and 2 m, respectively. MH4 occurs during a period of no rupture in the Matthews trench, but within the same time period and with a similar SED to F5. Although there is a pre-Okareka rupture in the Meade-Hossack trench, it is too poorly constrained to be able to correlate with M4.

Sinter development on the northeast section of the east strand of the Whirinaki Fault mirrors that of the Mangatete sinters on the west strand around the time of the Poihipi and Okareka eruptions. However, sinter development appears to have ceased entirely at the Meade-Hossack site after the post-Okareka sinter was formed, while emplacement continued between the Rotoma and Hatepe eruptive episodes on the west strand. It is possible that the MH3 rupture event, or a combination of MH3 and MH4, affected fluid flow to the Meade-Hossack site and prevented further hydrothermal activity.

6.5: Conclusions

The trench restoration obtained a mean cumulative vertical displacement value for the site of 3.79 ± 0.97 m. The mean slip rates for the northeast section of the east strand of the Whirinaki Fault vary from 0.53 ± 0.24 mm/yr from c. 240 ka to 21.8 ka, 0.12 ± 0.03 mm/yr from 21.8 to 1.8 ka, and 0.87 ± 0.37 mm/yr from 1.8 to 0.63 ka The rupture recurrence interval range for the northeast section of the east strand of the Whirinaki Fault is 1.8–5.4 kyr. The tephrostratigraphy erected in Chapter 5 enabled this restoration to be developed.

The fast-slow-fast pattern of slip rate and the rupture recurrence interval in the past c. 22 kyr are comparable to those of a previous study on

the Whirinaki Fault. However, the timing of events and the recurrence interval range suggest that the Meade-Hossack site appears to have been influenced by fault rupture on both the southeast section of the east strand, as well as by activity on the west strand.

Sinter development at the Meade-Hossack site in the past c. 30 kyr is very similar to that on the west strand of the Whirinaki Fault, but ceased after the MH3 rupture event, while it continued after the Rotoma Tephra on the west strand. Fluid flow may have been blocked off or diverted elsewhere after MH3, ceasing hydrothermal activity at Meade-Hossack.

Chapter 7: Geological history of the Meade-Hossack site and implications of tephrochronology on seismic and geothermal studies

7.1: Introduction

Using the findings presented mainly in chapters 3 to 6, it is possible to place the chronology of events at the Meade-Hossack site into the broader area of the Ngakuru Graben and relate faulting and hydrothermal activity at the site to that at other locations on both east and west strands of the Whirinaki Fault.

The following chapter includes a geological history of events in chronological order, a discussion on geothermal development and possible paleoenvironments at the Meade-Hossack site, and an assessment of the role of tephrochronology for seismic and geothermal investigations. The conclusions presented in this chapter encompass the study as a whole.

7.2: Geological history

The main geological events affecting the Meade-Hossack site have been tied into events established from the Matthews and Fitzpatrick trenches (Canora-Catalán et al., 2008) and the sinter development on the west strand of the Whirinaki Fault (Drake et al., 2014) to form a geological history for Ngakuru Graben since the Ohakuri eruption. Where possible, paleoenvironmental features have been inferred and included.

1) **c. 240 ka:** Shortly following the eruption of the Mamaku Ignimbrite c. 240 ka from either the Rotorua Caldera (Gravley et al., 2007) or the Kapenga Caldera (vent area adjacent to the Horohoro Bluffs) (Esler, 2010), the Ohakuri Ignimbrite (with a similar numerical age c. 240 ka) was erupted from the single-event Ohakuri Caldera (Gravley et al., 2007) approximately 17 km southwest of the present-day location of the Meade-Hossack trench site. The Ohakuri Ignimbrite was emplaced across the area of the trench site.
2) The top of the Ohakuri Ignimbrite was weathered and eroded. Post-eruption subsidence after the paired Mamaku and Ohakuri events contributed to basin formation (Gravley et al., 2007).

3) A lake system developed within the basin and lake sediments were deposited, forming the Huka Group. Over time, the lakes shrank in size and the sediments were at least partially eroded away.
4) The unidentified unit or units (classified here as 30x) were emplaced onto the surface of the Ohakuri Ignimbrite and/or associated lake sediments and reworked deposits of the Huka Group.
5) Siliceous sinters formed within the Ohakuri Ignimbrite (or Huka Group) and in the lower part of Unit 30x. The upper part of Unit 30x was then partially eroded by surface processes.
6) The Ohakuri Ignimbrite, sinters, and unidentified units were faulted in several places by event MH5. The scarp formed by the largest displacement contributed to the formation of a shallow paleovalley. The faulting also resulted in a zone of fault breccia comprised of clasts of sinter and silicified Ohakuri Ignimbrite (or Huka Group).
7) **c. 40 ka:** The Tahuna Tephra was erupted from an undetermined source vent likely to be within the Taupo Volcanic Centre (Smith and Shane, 2002), and was deposited at the field site, though only preserved on the hillock to the west of the trench site. Concurrent with the deposition of the Tahuna Tephra, a hydrothermal explosion produced a vent breccia.
8) **c. 39 ka:** Plant-rich sinter accumulated on the northeast section of the east strand of the Whirinaki Fault, at a rate of ~0.06 mm/yr as constrained by the overlying/underlying units of known age. At the same time, plant-rich Mangatete sinters continued to accumulate on the west strand of the Whirinaki Fault. In both cases, the sinters were deposited on terraces distal to the source vent(s) of alkali chloride springs.
9) **28.4 ka:** The Poihipi Tephra was erupted from an area around 6 km northeast of present-day Tapuaehara Bay in the Taupo Volcanic Centre, marked by two lava domes which formed during the same eruptive episode (Wilson et al. 2009), and was deposited across the Ngakuru Graben landscape.
10) Sinter continued to form on the hill at the Meade-Hossack site, at a rate of ~0.1 mm/yr as constrained by overlying/underlying units, as well as on the west strand of the Whirinaki Fault. At both locations,

sinter development ceased prior to the Oruanui eruption. The Poihipi Tephra was eroded from the lower-lying areas at the Meade-Hossack site.

11) **25.4 ka:** The caldera-forming Oruanui eruption (generating Kawakawa Tephra) occurred in the Taupo Volcanic Centre, resulting in the emplacement of fine-grained fall deposits and a non-welded ignimbrite across most of the North Island of New Zealand (Wilson, 2001; Wilson et al., 2006).
12) Rupture event M4 occurred in the southeast section of the east strand of the Whirinaki Fault, causing a vertical displacement of 4 m. On the west strand, sinter development recommenced.
13) **21.8 ka:** The Okareka eruptive episode occurred at Tarawera Volcano in the Okataina Volcanic Centre (Shane et al., 2008). The Okareka Tephra was deposited across the area of the trench site, mantling the paleovalley.
14) Slightly below the surface, a siliceous sinter formed within the Okareka Tephra in the area below and to the northeast of the hill at the Meade-Hossack site. Plant-rich sinters continued to form on the west strand of the Whirinaki Fault.
15) Rupture events MH4 on the northeast section of the east strand and F5 on the west strand caused vertical displacements of 0.8 m and 0.7 m, respectively. Sinter development then ceased at both locations.
16) **15.6 ka:** The Rotorua eruptive episode occurred from the Okareka Embayment of the Okataina Volcanic Centre (Kilgour & Smith, 2008), with Rotorua Tephra from the resulting plinian eruption plume deposited across the area of the trench site.
17) Rupture event M3 occurred in the southeast section of the east strand of the Whirinaki Fault, triggering a slightly smaller rupture event (MH3) in the northeast section and causing deepening of the paleovalley at the Meade-Hossack site.
18) **9.4 ka:** The Rotoma eruption episode began at the Haroharo linear vent zone in the Okataina Volcanic Centre (Smith et al., 2006). Rotoma tephra was deposited across the area of the trench site.

19) Rupture events F4 and F3 occurred on the west strand of the Whirinaki Fault, totalling 1.7 m vertical displacement. Sinter development of several different types recommenced on the west strand, with lithofacies indicative of a deepening environment of deposition.
20) **7.9 ka:** The Mamaku eruption episode began at the Haroharo linear vent zone in the Okataina Volcanic Centre strand (Smith et al., 2006), producing the fallout deposits observed at the Fitzpatrick site on the west strand of the Whirinaki Fault.
21) Rupture event MH2 occurred on the northeast section of the east strand of the Whirinaki Fault, and F2 occurred on the west strand, with displacements of 0.8 m and 0.9 m, respectively.
22) Sinter development ceased on the west strand of the Whirinaki Fault.
23) **1.8 ka:** The Hatepe eruption episode occurred at the Taupo Volcanic Centre. In the area of the trench site, a thin layer of Rotongaio Ash from the phreatomagmatic phase of the eruption was deposited, followed by a thicker deposit of the Taupo Pumice Lapilli from the following Taupo plinian fallout phase. The climactic Taupo Ignimbrite was emplaced, creating a gently undulating to rolling landscape.
24) Rupture event MH1 occurred on the northeast section of the east strand of the Whirinaki Fault, and F1 occurred on the west strand, causing vertical displacements of 0.9 m and 0.8 m respectively.
25) **0.63 ka:** The Kaharoa eruption occurred at Tarawera Volcano. Kaharoa Tephra was deposited across the area of the trench site.
26) Rupture events M2 and M1 occurred on the southeast section of the east strand of the Whirinaki Fault, totalling 0.7 m of displacement.

7.3: Geothermal development

The sinters at the Meade-Hossack site appear to be similar to some of the types found near the Fitzpatrick trench on the west strand of the Whirinaki Fault. Unit 40x from the trench has thin, wavy grey laminae. Unit 42 from the trench also has the same colour and laminations, but also has

the round pore-like structures frequently containing infilled material in a radial pattern. Units 40x and 42 resemble the domal stromatolitic type of sinter described by Drake et al. (2014), formed from alkali-chloride springs in a mid-temperature (45-55°C), mid-apron pool of at least 1 m depth. The sinters on the outcrop also show similarities, one with the plant-rich sinters described by Drake et al. (2014), containing many silicified reeds in random to subparallel orientations, and the thinner sinters more fitting with the tufted sinter with lenticularoids, which form in a similar environment to the domal stromatolitic type. The plant-rich sinter on the outcrop indicates that the location was on the outer edges of the paleogeothermal field at the time of deposition, and the move to domal stromatolitic and tufted sinters by the time the Okareka Tephra was deposited indicates a deepening environment over time (Drake et al., 2014).

One of the difficulties faced with attempting to reconstruct the geothermal development and paleoenvironment of the Meade-Hossack site is that it is unclear whether some of the sinters observed are *in situ*, or large *ex situ* blocks that have been transported by debris flows or emplaced as a result of a hydrothermal vent explosion. The large, terrace-like sinter exposed in the trench in the top of the Ohakuri Ignimbrite is most likely *in situ*, but less exposed sinters such as that within the Okareka Tephra in the trench, and a plant-rich sinter on the small knoll just south of the outcrop could be *ex situ*. Further studies could attempt to date the plant-rich sinter on the hillock using ^{14}C to determine whether it is of a similar age to the c. 39 ka sinter on the outcrop.

7.4: Role of tephrochronology in seismic and geothermal studies

The following section is a discussion assessing the application of tephrochronology to paleoseismic and geothermal work, taking into consideration the limitations encountered over the course of this study.

Tephrochronology and the associated techniques have the potential to be useful tools when undertaking either or both paleoseismic

investigations and geothermal studies. In ideal circumstances, tephras are well-preserved, easily identifiable by field and lab observations, and provide correlatable markers of known ages with which to constrain events. However, circumstances are often less than ideal.

Aside from Taupo Unit Y, the tephras at the Meade-Hossack site were largely unidentifiable in the field, necessitating lengthier and costlier investigation via lab analyses of their constituents. Ferromagnesian mineral assemblages helped in determining the source volcanic centre for samples, but their relative abundances did not correlate well with those documented in previous studies to enable identification of the discrete eruptive episode for each tephra.

EPMA provided quantitative data on the major and minor element composition of the volcanic glass shards from the tephras, but despite taking prescribed precautionary steps to prepare blocks correctly, select appropriate grains for analysis, and set operating conditions to reduce volatile losses, the analyses were still impacted by technical issues and could not be fully completed for all samples given the time and budgetary constraints. In addition to the technical problems, the major and minor element geochemistry of the samples were frequently very similar even for stratigraphically separate units. One option for further work to overcome this similarity would be to obtain trace element data for the glass shards using LA-ICP-MS (e.g., Pearce, 2014; Pearce et al., 2011, 2014), but a problem arises for Late Quaternary TVZ tephras in that there are currently few comparative data available from the type sections of each tephra. Another option would be to analyse the biotite in the ferromagnesian separates for each sample using EPMA, as there are comparative data available for some TVZ biotites (e.g. Shane et al., 2003a, 2003b).

Nevertheless, a tephrostratigraphic framework comprising (from younger to older) Kaharoa, Taupo, Rotoma, Rotorua, Okareka, Kawakawa, Poihipi, and Tahuna tephras, along with Ohakuri Ignimbrite, was able to be constructed for the site using the EMPA-derived glass compositional data together with the tephras' physical properties and stratigraphic positions. In turn, the identification of these tephras (albeit tentatively in some cases) allowed their known ages (developed using Bayesian statistical approaches

and dendrochronology: Lowe et al., 2013) to be transferred to the Meade-Hossack site and hence the chronology of geological events established in Section 7.2 was able to be constructed.

At the Meade-Hossack site, the issue of spatial variability complicated the reconstruction of events. Displacement events were not equally represented on each of the trench walls due to complex fault behaviour in soft sediments. Unconformities were also abundant across both the trench and the outcrop, affecting the age constraints. Further identification work could remove some of the unconformities to improve the resolution of the data, but variations in paleotopography, climate, and tectonism over time have likely contributed to the complete erosion of some units.

The sinters at the Meade-Hossack site were not analysed in detail, but tephra identification gave better constraint for the ages of the sinters, and the study established a possible link between the paleohydrothermal system at the Meade-Hossack site and the sinters near the Fitzpatrick trench on the west strand of the Whirinaki Fault. However, this study assumes the sinters in the trench and the outcrop are *in situ*, when it is possible that some may be *ex situ* blocks. Hydrothermal alteration of tephras may also have played a role in complicating the identification of tephras by changing the geochemistry of the volcanic glass shards.

Overall, the use of tephrochronology has demonstrably been a key part of this investigation and can therefore aid investigations into dynamic paleoenvironments of tectonically and geothermally active areas. However, problems may arise in correlating tephras where data (such as EMPA-derived glass-shard major element compositions) are inadequate or ambiguous, meaning that further detailed analyses are required for unequivocal correlations (such as the use of LA-ICP-MS to acquire trace element data for glass shards). Consequently, here are criteria that need to be fulfilled at every stage of investigation in order to glean high-resolution data appropriate for developing system evolution models or applications in seismic hazard assessments.

7.5: Conclusions

The combination of stratigraphy, ferromagnesian mineralogy, and major and minor element compositions of glass shards was sufficient to identify eight tephras (some tentatively) in the Meade-Hossack trench, namely Kaharoa, Taupo, Rotoma, Rotorua, Okareka, Kawakawa, Poihipi, and Tahuna tephras. These tephras have well-established ages derived from dendrochronology and 14C dating or from Bayesian-based age modelling based on 14C ages and stratigraphy (Lowe et al., 2013). Therefore these ages were able to be transferred using tephrochronology to the Meade-Hossack sequences, thereby providing a chronostratigraphic framework to evaluate and date the history of events and deposition inferred at the site including faulting and hydrothermal activity.

A history of displacement was observed in the trench, with five discernible fault rupture events. The sinters at the site are younger than c. 240 kyr and older than ~16 kyr, with apparent periods of quiescence between times of sinter deposition, and a deepening paleoenvironment, with pool depth increasing up to 1 m from c. 39 ka to ~16 ka. Periods of hydrothermal activity and quiescence at the Meade-Hossack site mirror those observed on the west strand of the Whirinaki Fault from c. 30 ka to ~10 ka. The Meade-Hossack site experienced a greater vertical displacement than the Fitzpatrick site on the west strand during this time, changing the fluid flow regime which led to cessation of hydrothermal activity on the east strand. Fault rupture at the Meade-Hossack site is influenced by both the southeast section of the east strand and the northwest section of the west strand of the Whirinaki Fault.

This study is the first known use of tephrochronology to constrain ages for both fault rupture and hydrothermal activity at a single site. The results improve understanding of the complex rupture behaviour of the Whirinaki Fault and provide evidence for relationships between not only the northern and south sections of the east strand, but also between the west and east strands, a possible indicator of cross-faulting at depth, which could explain the paired hydrothermal activity on both strands until ~10 ka. The data collected from the trench restoration may also be useful for seismic

hazard assessment modelling, as the Whirinaki Fault is one of the major faults in the central TVZ.

Plenty of opportunity remains for future work on the Meade-Hossack site and the wider area of the Ngakuru Graben. The samples collected during this study could be used with different techniques to further refine age constraints for events in the Meade-Hossack site. For example, EPMA on biotite crystals for major element data could further test the identifications made and constrain other unknown tephras. SEM imaging of the samples tentatively identified here as the Ohakuri Ignimbrite, based on stratigraphic position and field characteristics, could be used to test this hypothesis, or alternatively suggest an origin within the Huka Group if diatoms were found to be present. Cores 1 and 2 from the trench could be sampled and analysed by EPMA to verify tephra identifications.

Trace element data from LA-ICP-MS analyses would also help to constrain the list of possible source eruptions for any given tephra. However at this time there is little available trace element data for Late Quaternary TVZ tephras, from their respective type sections, to use for comparison. Researchers therefore have the opportunity to significantly increase the knowledge base by incorporating LA-ICP-MS analyses into studies on known tephras, whether the localities are in the Ngakuru Graben or elsewhere.

The sample at the Meade-Hossack site containing riebeckite could be further investigated to verify whether a Mayor Island cryptotephra is present within that unit, including further mineralogy to ascertain the presence of both riebeckite and aegerine, as well as EPMA of a larger number of shards (>100). The presence of the Mayor Island M5 eruptive at the Meade-Hossack site, which is based on the identification of the enclosing unit as Okareka Tephra, could have implications for studies on the paleo wind directions around the time of this eruption, as well as possibly being the first onshore report of the M5 eruptive.

To enhance the record of fault rupture events in the Ngakuru Graben, more trenches could be excavated on different sections of the Whirinaki Fault, with more time allowed for each trench in order to gather higher-

resolution data. The logical next choice would be the southwest section of the west strand, to complete all four quadrants of the fault. Other faults in the area such as Mangatete/Lakeside, Hossack Road, and Te Weta could also be trenched to build up a wider picture of fault history and stress transfer in the Ngakuru Graben, and whether activity can be related back to large-scale TVZ events like caldera formation.

Detailed geophysical work could help reveal the extent of the fossil geothermal fields in the Ngakuru Graben. The report by Alder and Sharp (1988) included low level magnetic, induced polarisation (IP), and resistivity surveys close to the Meade-Hossack site, but these techniques have evolved since that time and the data quality has improved as a result. It may be possible to not only find the extent of the geothermal fields on the Whirinaki Fault, but to better delineate the boundary of the Kapenga caldera.

Some of the Meade-Hossack samples exhibited signs of hydrothermal alteration. Investigation of alteration was outside the scope of this study but would nonetheless be an interesting project suitable for a student. The alteration mineralogy can be used as an indicator of the pH and temperature ranges of the hydrothermal fluids involved at the Meade-Hossack site and may provide more clues as to the evolution of the paleoenvironment and whether the fluid types are the same as those on the west strand of the Whirinaki Fault.

The study supports the use of tephrochronological methods for constraining the ages of hydrothermal deposits and fault rupture events in order to gain insight into the complex interrelationships between fault segments and geothermal systems in an active rift setting. Tephras must be well-preserved and solid comparison data must be available for tephrochronology to be reliable for seismic and geothermal investigations. Although the scope of this study was limited to contextualising the faulting and hydrothermal activity into a broader geological history, there are implications for future work on the model of fluid flow over time, and seismic hazard assessments in the region.

References

Alder, G.A. & Sharp, B.M. (1988). Report on geology, geochemistry, geophysics and drilling PL 311941 (Thomsons), Central North Island. *Mineral Report Series*, *MR671*. Wellington, New Zealand: Ministry of Economic Development.

Berryman, K., Villamor, P., Nairn, I., Van Dissen, R., Begg, J. & Lee, J. (2008). Late Pleistocene surface rupture history of the Paeroa fault, Taupo Rift, New Zealand. *New Zealand Journal of Geology and Geophysics*, *51*(2), 135-158. doi:10.1080/00288300809509855

Bertrand, E. A., Caldwell, T. G., Hill, G. J., Wallin, E. L., Bennie, S. L., Cozens, N., Onacha, S. A., Ryan, G. A., Walter, C., Zaino, A. & Wameyo, P. (2012). Magnetotelluric imaging of upper-crustal convection plumes beneath the Taupo Volcanic Zone, New Zealand. *Geophysical Research Letters*, *39*(2). doi:10.1029/2011GL050177

Bibby, H. M., Caldwell, T. G., Davey, F. J. & Webb, T. H. (1995). Geophysical evidence on the structure of the Taupo Volcanic Zone and its hydrothermal circulation. *Journal of Volcanology and Geothermal Research*, *68*(1), 29-58. doi:10.1016/0377-0273(95)00007-H

Brathwaite, R. L. (2003). Geological and mineralogical characterization of zeolites in lacustrine tuffs, Ngakuru, Taupo Volcanic Zone, New Zealand. *Clays and Clay Minerals*, *51*(6), 589-598. doi:10.1346/CCMN.2003.0510601

Buck, M. D., Briggs, R. M. & Nelson, C. S. (1981). Pyroclastic deposits and volcanic history of Mayor Island. *New Zealand Journal of Geology and Geophysics*, *24*(4), 449-467. doi:10.1080/00288306.1981.10422737

Campbell, K. A., Buddle, T. F. & Browne, P. R. L. (2003). Late Pleistocene siliceous sinter associated with fluvial, lacustrine, volcaniclastic and landslide deposits at Tahunaatara, Taupo Volcanic Zone, New Zealand. *Transactions of the Royal Society of Edinburgh: Earth Sciences*, *94*(4), 485-501. doi:10.1017/S0263593300000833

Canora-Catalán, C., Villamor, P., Berryman, K., Martínez-Díaz, J. J. & Raen, T. (2008). Rupture history of the Whirinaki Fault, an active normal fault in the Taupo Rift, New Zealand. *New Zealand Journal of Geology and Geophysics*, *51*(4), 277-293. doi:10.1080/00288300809509866

Chambefort, I., Lewis, B., Wilson, C. J. N., Rae, A. J., Coutts, C., Bignall, G. & Ireland, T. R. (2014). Stratigraphy and structure of the Ngatamariki geothermal system from new zircon U–Pb geochronology: Implications for Taupo Volcanic Zone evolution. *Journal of Volcanology and Geothermal Research*, *274*, 51-70. doi:10.1016/j.jvolgeores.2014.01.015

Danišík, M., Shane, P., Schmitt, A. K., Hogg, A., Santos, G. M., Storm, S., Evans, N. J., Fifield, L. K. & Lindsay, J. M. (2012). Re-anchoring the late Pleistocene tephrochronology of New Zealand based on concordant radiocarbon ages and combined $^{238}U/^{230}Th$ disequilibrium and (U–Th)/He zircon ages. *Earth and Planetary Science Letters*, *349*, 240-250. doi:10.1016/j.epsl.2012.06.041

Downs, D. T., Rowland, J. V., Wilson, C. J. N., Rosenberg, M. D., Leonard, G. S. & Calvert, A. T. (2014a). Evolution of the intra-arc Taupo-Reporoa Basin within the Taupo Volcanic Zone of New Zealand. *Geosphere*, *10*(1), 185-206. doi:10.1130/GES00965.1

Downs, D. T., Wilson, C. J. N., Cole, J. W., Rowland, J. V., Calvert, A. T., Leonard, G. S. & Keall, J. M. (2014b). Age and eruptive center of the Paeroa Subgroup ignimbrites (Whakamaru Group) within the Taupo Volcanic Zone of New Zealand. *Geological Society of America Bulletin*, B30891-1. doi:10.1130/B30891.1

Drake, B. D., Campbell, K. A., Rowland, J. V., Guido, D. M., Browne, P. R. & Rae, A. (2014). Evolution of a dynamic paleo-hydrothermal system at Mangatete, Taupo Volcanic Zone, New Zealand. *Journal of Volcanology and Geothermal Research*, *282*, 19-35. doi:10.1016/j.jvolgeores.2014.06.010

Esler, W. R. (2010). An introduction to the Rotorua Basin and Okataina Volcanic Centre: an iconoclastic view. In: Lowe, D.J., Neall, V.E., Hedley, M., Clothier, B., Mackay, A. *Guidebook for Pre-conference North Island, New Zealand 'Volcanoes to Oceans' field tour (27-30 July), 19th World Soils Congress, International Union of Soil Sciences, Brisbane. Soil and Earth Sciences Occasional Publication No. 3,* 4.23 – 4.29. Massey University, Palmerston North.

Froggatt, P. C. (1983). Toward a comprehensive Upper Quaternary tephra and ignimbrite stratigraphy in New Zealand using electron microprobe analysis of glass shards. *Quaternary Research*, *19*(2), 188-200. doi:10.1016/0033-5894(83)90004-2

Froggatt, P. C. (1992). Standardization of the chemical analysis of tephra deposits. Report of the ICCT working group. *Quaternary International*, *13*, 93-96. doi:10.1016/1040-6182(92)90014-S

Gravley, D. M., Wilson, C. J. N., Leonard, G. S., & Cole, J. W. (2007). Double trouble: paired ignimbrite eruptions and collateral subsidence in the Taupo Volcanic Zone, New Zealand. *Geological Society of America Bulletin*, *119*(1-2), 18-30. doi: 10.1130/B25924.1

Green, R. M., Bebbington, M. S., Cronin, S. J. & Jones, G. (2014). Automated statistical matching of multiple tephra records exemplified using five long maar sequences younger than 75ka, Auckland, New Zealand. *Quaternary Research*, *82*(2), 405-419. doi:10.1016/j.yqres.2014.06.004

Grindley, G. W. (1959). *Sheet N85—Waiotapu*. Geological map of New Zealand 1:63360. Wellington, New Zealand: New Zealand Department of Scientific and Industrial Research.

Hall, M. & Hayward, C. (2014). Preparation of micro-and crypto-tephras for quantitative microbeam analysis. *Geological Society, London, Special Publications*, *398*, SP398-5. doi:10.1144/SP398.5

Heise, W., Bibby, H. M., Caldwell, T. G., Bannister, S. C., Ogawa, Y., Takakura, S. & Uchida, T. (2007). Melt distribution beneath a young continental rift: the Taupo Volcanic Zone, New Zealand. *Geophysical Research Letters*, *34*(14). doi:10.1029/2007GL029629

Hogg, A. G. & McCraw, J. D. (1983). Late Quaternary tephras of Coromandel Peninsula, North Island, New Zealand: a mixed peralkaline and calcalkaline tephra sequence. *New Zealand Journal of Geology and Geophysics*, *26*(2), 163-187. doi:10.1080/00288306.1983.10422515

Hogg, A. G., Higham, T. F., Lowe, D. J., Palmer, J. G., Reimer, P. J. & Newnham, R. M. (2003). A wiggle-match date for Polynesian settlement of New Zealand. *Antiquity*, *77*(295), 116-125. doi:10.1017/S0003598X00061408

Hogg A.G., Lowe D.J., Palmer J., Boswijk, G. & Ramsey, C.B. (2012) Revised calendar date for the Taupo eruption derived by ^{14}C wiggle-matching using a New Zealand kauri ^{14}C calibration data set. *The Holocene*, *22*, 439-449. doi:10.1177/0959683611425551

Holland, G. R. (2000). *The Whirinaki sinter, Taupo Volcanic Zone*. Unpublished MSc thesis, University of Auckland, Auckland, New Zealand.

Houghton, B. F., Weaver, S. D., Wilson, C. J. & Lanphere, M. A. (1992). Evolution of a Quaternary peralkaline volcano: Mayor Island, New Zealand. *Journal of Volcanology and Geothermal Research*, *51*(3), 217-236. doi:10.1016/0377-0273(92)90124-V

Howorth, R. (1975). New formations of late Pleistocene tephras from the Okataina Volcanic Centre, New Zealand. *New Zealand Journal of Geology and Geophysics*, *18*(5), 683-712. doi:10.1080/00288306.1975.10421569

Janoušek, V., Farrow, C. M. & Erban, V. (2006). Interpretation of whole-rock geochemical data in igneous geochemistry: introducing Geochemical Data Toolkit (GCDkit). *Journal of Petrology 47*(6), 1255-1259. doi:10.1093/petrology/egl013

Janoušek, V., Farrow, C. M., Erban, V. & Trubač, J. (2011). Brand new geochemical data toolkit (GCDkit 3.0) – is it worth upgrading and browsing documentation? (Yes!). *Geologicke výzkumy na Morave a ve Slezsku*, *18*, 26-30.

Jones, B., Renaut, R. W., Torfason, H. & Owen, R. B. (2007). The geological history of Geysir, Iceland: A tephrochronological approach to the dating of sinter. *Journal of the Geological Society*, *164*(6), 1241-1252. doi:10.1144/0016-76492006-178

Juvigné, É. & Porter, S. C. (1985). Mineralogical variations within two widespread Holocene tephra layers from Cascade Range Volcanoes, USA. *Géographie physique et Quaternaire*, *39*(1), 7-12. doi:10.7202/032580ar

Kaya, E., O'Sullivan, M. J. & Yeh, A. (2014). Three-Dimensional model of the deep geothermal resources in the Taupo-Reporoa Basin, New Zealand. *Journal of Volcanology and Geothermal Research*, *284*, 46-60. doi:10.1016/j.jvolgeores.2014.07.015

Kennedy, N. & Froggatt, P. (1984). Recognition of Tuhua Tephra (c. 6,200 BP) at Rotorua. *Geological Society of New Zealand Newsletter*, *66*, 17-18.

Kilgour, G. N. & Smith, R. T. (2008). Stratigraphy, dynamics, and eruption impacts of the dual magma Rotorua eruptive episode, Okataina Volcanic Centre, New Zealand. *New Zealand Journal of Geology and Geophysics*, *51*(4), 367-378. doi:10.1080/00288300809509871

Kuehn, S. C., Froese, D. G. & Shane, P. A. R. (2011). The INTAV intercomparison of electron-beam microanalysis of glass by tephrochronology laboratories: results and recommendations. *Quaternary International*, *246*(1), 19-47. doi:10.1016/j.quaint.2011.08.022

Kuehn, S. C. (2014). Reducing uncertainty in tephra correlation through improved geochemical characterization and better data reporting practices. In M. Bursik, S. C. Kuehn, S. Pouget & K. Wallace (Eds.), *Tephra 2014: Maximising the potential of tephra for multidisciplinary science*.

Leonard G.S., Begg J.G. & C.J.N. Wilson (2010) Geology of the Rotorua area: scale 1:250,000. *Institute of Geological and Nuclear Sciences 1:250,000 geological map 5*. Institute of Geological and Nuclear Sciences, Lower Hutt, New Zealand.

Lowe, D. J. (1988a). Late Quaternary volcanism in New Zealand: towards an integrated record using distal airfall tephras in lakes and bogs. *Journal of Quaternary Science*, *3*(2), 111-120. doi:10.1002/jqs.3390030202

Lowe, D. J. (1988b). Stratigraphy, age, composition, and correlation of late Quaternary tephras interbedded with organic sediments in Waikato lakes, North Island, New Zealand. *New Zealand Journal of Geology and Geophysics*, *31*(2), 125-165. doi:10.1080/00288306.1988.10417765

Lowe, D. J. (2011). Tephrochronology and its application: A review. *Quaternary Geochronology*, *6*(2), 107-153. doi:10.1016/j.quageo.2010.08.003

Lowe, D. J. & Alloway, B. V. (2015). Tephrochronology. In W. J. Rink & J. W. Thompson (Eds.), *Encyclopaedia of Scientific Dating Methods* (783-799). Dordrecht, The Netherlands: Springer. doi:10.1007/978-94-007-6304-3_19

Lowe, D.J. & Tonkin, P.J. (2010). Unravelling upbuilding pedogenesis in tephra and loess sequences in New Zealand using tephrochronology. In R. J. Gilkes & N. Prakongkep (Eds.), *Proceedings of the 19th World Congress of Soil Science "Soil Solutions for a Changing World" (1-6 Aug., 2010, Brisbane), Symposium 1.3.2 Geochronological techniques and soil formation* (34-37). Published on DVD and at http://www.iuss.org

Lowe, D. J., Newnham, R. M. & Ward, C. M. (1999). Stratigraphy and chronology of a 15 ka sequence of multi-sourced silicic tephras in a montane peat bog, eastern North Island, New Zealand. *New Zealand Journal of Geology and Geophysics*, *42*(4), 565-579. doi:10.1080/00288306.1999.9514863

Lowe, D. J., Shane, P. A. R., Alloway, B. V. & Newnham, R. M. (2008). Fingerprints and age models for widespread New Zealand tephra marker beds erupted since 30,000 years ago: a framework for NZ-INTIMATE. *Quaternary Science Reviews*, *27*, 95-126. doi:10.1016/j.quascirev.2007.01.013

Lowe, D. J., Blaauw, M., Hogg, A. G. & Newnham, R. M. (2013). Ages of 24 widespread tephras erupted since 30,000 years ago in New Zealand, with re-evaluation of the timing and palaeoclimatic implications of the late glacial cool episode recorded at Kaipo bog. *Quaternary Science Reviews*, *74*, 170-194. doi:10.1016/j.quascirev.2012.11.022

Lutz, S. J., Caskey, S. J., Mildenhall, D. D., Browne, P. R. L. & Johnson, S. D. (2002). Dating sinter deposits in northern Dixie Valley, Nevada: The paleoseismic record and implications for the Dixie Valley geothermal system. In *Proceedings 27th Workshop on Geothermal Reservoir Engineering* (284-290).

Manighetti, B., Palmer, A., Eden, D., & Elliot, M. (2003). An occurrence of Tuhua Tephra in deep-sea sediments from offshore eastern North Island, New Zealand. *New Zealand Journal of Geology and Geophysics*, *46*(4), 581-590. doi: 10.1080/00288306.2003.9515031

Martin, R., Mildenhall, D. C., Browne, P. R., & Rodgers, K. A. (2000). The age and significance of in-situ sinter at the Te Kopia thermal area, Taupo Volcanic Zone, New Zealand. *Geothermics*, *29*(3), 367-375. doi:10.1016/S0375-6505(00)00008-0

McCalpin, J. P. (2009). Field techniques in paleoseismology—terrestrial environments. *International Geophysics*, *95*, 29-118. doi:10.1016/S0074-6142(09)95002-1

McClymont, A. F., Villamor, P. & Green, A. G. (2009). Fault displacement accumulation and slip rate variability within the Taupo Rift (New Zealand) based on trench and 3-D ground-penetrating radar data. *Tectonics*, *28*(4), 446-451. doi:10.1029/2008TC002334

Molloy, C., Shane, P. & Augustinus, P. (2009). Eruption recurrence rates in a basaltic volcanic field based on tephra layers in maar sediments: implications for hazards in the Auckland volcanic field. *Geological Society of America Bulletin*, *121*(11-12), 1666-1677. doi:10.1130/B26447.1

Morgan, G. B. & London, D. (2005). Effect of current density on the electron microprobe analysis of alkali aluminosilicate glasses. *American Mineralogist*, *90*(7), 1131-1138. doi:10.2138/am.2005.1769

Payne, S. J., Hackett, W. R., & Smith, R. P. (2009). Paleoseismology of volcanic environments. *International Geophysics*, *95*, 271-314. doi:10.1016/S0074-6142(09)95004-5

Pearce, N. J. G. (2014). Towards a protocol for the trace element analysis of glass from rhyolitic shards in tephra deposits by laser ablation ICP-MS. *Journal of Quaternary Science*, *29*(7), 627-640. doi:10.1002/jqs.2727

Pearce, N. J. G., Westgate, J. A., Perkins, W. T. & Wade, S. C. (2011). Trace element microanalysis by LA-ICP-MS: the quest for comprehensive chemical characterisation of single, sub-10 μm volcanic glass shards. *Quaternary International*, *246*(1-2), 57-81. doi:10.1016/j.quaint.2011.07.012

Pearce, N. J., Abbott, P. M. & Martin-Jones, C. (2014). Microbeam methods for the analysis of glass in fine-grained tephra deposits: A SMART perspective on current and future trends. *Geological Society, London, Special Publications*, *398*, SP398-1. doi:10.1144/SP398.1

Preston, L. J., Benedix, G. K., Genge, M. J. & Sephton, M. A. (2008). A multidisciplinary study of silica sinter deposits with applications to silica identification and detection of fossil life on Mars. *Icarus*, *198*(2), 331-350. doi:10.1016/j.icarus.2008.08.006

Reimer, P., Bard, E., Bayliss, A., Beck, J., Blackwell, P., Bronk Ramsey, C., Buck, C., Cheng, H., Edwards, R., Friedrich, M., Grootes, P., Guilderson, T., Haflidason, H., Hajdas, I., Hatté, C., Heaton, T., Hoffmann, D., Hogg, A., Hughen, K., Kaiser, K., Kromer, B., Manning, S., Niu, M., Reimer, R., Richards, D., Scott, E., Southon, J., Staff, R., Turney, C. & van der Plicht, J. (2013). IntCal13 and Marine13 radiocarbon age calibration curves 0–50,000 years cal BP. *Radiocarbon*, *55*(4), 1869-1887. doi:10.2458/azu_js_rc.55.16947

Rowland, J. V. & Sibson, R. H. (2004). Structural controls on hydrothermal flow in a segmented rift system, Taupo Volcanic Zone, New Zealand. *Geofluids*, *4*(4), 259-283. doi:10.1111/j.1468-8123.2004.00091.x

Rowland, J. V. & Simmons, S. F. (2012). Hydrologic, magmatic, and tectonic controls on hydrothermal flow, Taupo Volcanic Zone, New Zealand: Implications for the formation of epithermal vein deposits. *Economic Geology*, *107*(3), 427-457. doi:10.2113/econgeo.107.3.427

Seebeck, H. (2008). The interrelationships between faulting and volcanism in the Okataina Volcanic Centre, New Zealand. Unpublished MSc thesis, Victoria University of Wellington, Wellington, New Zealand.

Shane, P. A. R., Smith, V. C., Lowe, D. J. & Nairn, I. A. (2003a). Re-identification of c. 15,700 cal yr BP tephra bed at Kaipo Bog, eastern North Island: implications for dispersal of Rotorua and Puketarata tephra beds. *New Zealand Journal of Geology and Geophysics*, *46*(4), 591-596. doi:10.1080/00288306.2003.9515032

Shane, P. A. R., Smith, V. & Nairn, I. A. (2003b). Biotite composition as a tool for the identification of Quaternary tephra beds. *Quaternary Research*, *59*(2), 262-270. doi:10.1016/S0033-5894(03)00012-7

Shane, P., Nairn, I. A., Martin, S. B. & Smith, V. C. (2008). Compositional heterogeneity in tephra deposits resulting from the eruption of multiple magma bodies: Implications for tephrochronology. *Quaternary International*, *178*(1), 44-53. doi:10.1016/j.quaint.2006.11.014

Smith, V. C. & Shane, P. (2002). Geochemical characteristics of the widespread Tahuna Tephra. *New Zealand Journal of Geology and Geophysics*, *45*(1), 103-107. doi:10.1080/00288306.2002.9514962

Smith, V. C., Shane, P. & Nairn, I. A. (2005). Trends in rhyolite geochemistry, mineralogy, and magma storage during the last 50 kyr at Okataina and Taupo volcanic centres, Taupo Volcanic Zone, New Zealand. *Journal of Volcanology and Geothermal Research*, *148*(3), 372-406. doi:10.1016/j.jvolgeores.2005.05.005

Smith, V. C., Shane, P., Nairn, I. A. & Williams, C. M. (2006). Geochemistry and magmatic properties of eruption episodes from Haroharo linear vent zone, Okataina Volcanic Centre, New Zealand during the last 10 kyr. *Bulletin of Volcanology*, *69*(1), 57-88. doi:10.1007/s00445-006-0056-7

Villamor, P. & Berryman, K. (2001). A late Quaternary extension rate in the Taupo Volcanic Zone, New Zealand, derived from fault slip data. *New Zealand Journal of Geology and Geophysics*, *44*(2), 243-269. doi:10.1080/00288306.2001.9514937

Villamor, P. & Berryman, K. R. (2006). Evolution of the southern termination of the Taupo Rift, New Zealand. *New Zealand Journal of Geology and Geophysics*, *49*(1), 23-37. doi:10.1080/00288306.2006.9515145

Villamor, P., Berryman, K. R., Nairn, I. A., Wilson, K., Litchfield, N. & Ries, W. (2011). Associations between volcanic eruptions from Okataina volcanic center and surface rupture of nearby active faults, Taupo rift, New Zealand: Insights into the nature of volcano-tectonic interactions. *Geological Society of America Bulletin*, *123*(7-8), 1383-1405. doi:10.1130/B30184.1

Vucetich, C. G. & Pullar, W. A. (1969). Stratigraphy and chronology of late Pleistocene volcanic ash beds in central North Island, New Zealand. *New Zealand Journal of Geology and Geophysics*, *12*(4), 784-837. doi:10.1080/00288306.1969.10431112

Vucetich, C. G. & Pullar, W. A. (1973). Holocene tephra formations erupted in the Taupo area, and interbedded tephras from other volcanic sources. *New Zealand Journal of Geology and Geophysics*, *16*(3), 745-780. doi:10.1080/00288306.1973.10431394

Vucetich, C. G. & Howorth, R. (1976). Late Pleistocene tephrostratigraphy in the Taupo district, New Zealand. *New Zealand Journal of Geology and Geophysics*, *19*(1), 51-69. doi:10.1080/00288306.1976.10423550

Wilson, C. J. N. (1985). The Taupo eruption, New Zealand II. The Taupo ignimbrite. *Philosophical Transactions of the Royal Society of London A: Mathematical, Physical and Engineering Sciences*, *314*(1529), 229-310. doi:10.1098/rsta.1985.0020

Wilson, C. J. N. (1993). Stratigraphy, chronology, styles and dynamics of late Quaternary eruptions from Taupo volcano, New Zealand. *Philosophical Transactions of the Royal Society of London. Series A: Physical and Engineering Sciences*, *343*(1668), 205-306. doi:10.1098/rsta.1993.0050

Wilson, C. J. N. (2001). The 26.5 ka Oruanui eruption, New Zealand: an introduction and overview. *Journal of Volcanology and Geothermal Research*, *112*(1-4), 133-174. doi:10.1016/S0377-0273(01)00239-6

Wilson, C. J. N. & Walker, G. P. L. (1985). The Taupo eruption, New Zealand I. General aspects. *Philosophical Transactions of the Royal Society of London A: Mathematical, Physical and Engineering Sciences*, *314*(1529), 199-228. doi:10.1098/rsta.1985.0019

Wilson, C. J. N., Houghton, B. F., McWilliams, M. O., Lanphere, M. A., Weaver, S. D. & Briggs, R. M. (1995). Volcanic and structural evolution of Taupo Volcanic Zone, New Zealand: a review. *Journal of Volcanology and Geothermal Research*, *68*(1), 1-28. doi:10.1016/0377-0273(95)00006-G

Wilson, C. J. N., Blake, S., Charlier, B. L. A. & Sutton, A. N. (2006). The 26.5 ka Oruanui eruption, Taupo volcano, New Zealand: development, characteristics and evacuation of a large rhyolitic magma body. *Journal of Petrology*, *47*(1), 35-69. doi:10.1093/petrology/egi066

Wilson, C. J. N., Gravley, D. M., Leonard, G. S. & Rowland, J. V. (2009). Volcanism in the central Taupo Volcanic Zone, New Zealand: tempo, styles and controls. In T. Thordarson, S. Self, G. Larsen, S. K. Rowland & A. Hoskuldsson (Eds.), *Studies in Volcanology: The Legacy of George Walker. Special Publications of IAVCEI*, *2*, 225-247. London, UK: The Geological Society.

Wittke, J. H. (2006). *EMP*. Retrieved from https://www4.nau.edu/microanalysis/Microprobe/ProbeIntro-EMP.html.

Wohletz, K. H. (1983). Mechanisms of hydrovolcanic pyroclast formation: Grain-size, scanning electron microscopy, and experimental studies. *Journal of Volcanology and Geothermal Research*, *17*(1), 31-63. doi:10.1016/0377-0273(83)90061-6

Zervas, D., Nichols, G. J., Hall, R., Smyth, H. R, Lüthje, C. & Murtagh, F. (2009). SedLog: a shareware program for drawing graphic logs and log data manipulation. *Computers & Geosciences*, *35*, 2151-2159. doi:10.1016/j.cageo.2009.02.009

Appendices

Appendix 1: Field sample and PETLAB codes

Field sample #	PETLAB Database #
HP1	W150500
HP2	W150501
HP3	W150502
HP4	W150503
HP5	W150504
HP6	W150505
HP7	W150506
HP8	W150507
HP9	W150508
HP10	W150509
HP11	W150510
HP12	W150511
HR1	W150512
HR2	W150513
HR3	W150514
HR4	W150515
HR5	W150516
HR6	W150517
HR7	W150518
HR8	W150519
HR9	W150520
HR10	W150521
HR11	W150522
HR12	W150523
HR13	W150524
HR14	W150525
HR15	W150526
HR16	W150527
HR17	W150528
HR18	W150529
HR19	W150530
HR20	W150531
HR21	W150532
HR30	W150533
HR31	W150534
HR32	W150535
HR33	W150536
HT1	W150537
HT2	W150538
HT3	W150539
HT4	W150540
HT5	W150541
HT6	W150542
HT7	W150543

Field sample #	PETLAB database #
HT10	W150544
HT11	W150545
HT12	W150546
HT13	W150547
HT14	W150548
HT15	W150549
HT16	W150550
HT17	W150551
HT18	W150552
HT19	W150553
HT20	W150554
HT22	W150555
HT23	W150556
HT24	W150557
HT25	W150558
HT26	W150559
HT27	W150560
HT28	W150561
HT29	W150562
HT30	W150563
HT31	W150564
HT32	W150565
HT33	W150566
HT34	W150567
HT35	W150568
HT36	W150569
CR31	W150570
CR32	W150571
C101	W150572
C102	W150573
C103	W150574
C104	W150575
C105	W150576
C106	W150577
C107	W150578
C108	W150579
C201	W150580
C202	W150581
C203	W150582
C204	W150583
C205	W150584
CORE1	W150585
CORE2	W150586
CORE3	W150587

Appendix 2: Electron Microprobe

2.1: Operating conditions

Instrument model: JEOL JXA-8230 SuperProbe

Beam diameter: 10 μm

Beam voltage: 15 kV

Probe current: 8 Å

Software version: PC-SEM Version 3.0.1.9

PC-EPMA Version 1.9.2.0

EOS Subsystem Version 1.9.3.0

Stage Subsystem Version 2.8.5

Notes: Asynchronous measurement, ZAF correction on oxides.

2.2: Standards

Element (wt. %)	ATHO-G	VG-568
SiO_2	75.6	76.96
Al_2O_3	12.2	12.17
TiO_2	0.255	0.08
FeOt	3.27	1.08
MnO	0.106	0.02
MgO	0.103	0.03
CaO	1.7	0.45
Na_2O	3.75	3.52
K_2O	2.64	4.93
P_2O_5	0.025	0
Cl (ppm)	430	1013

2.3: Element analysis conditions

Mass spectrometer	CH1	CH2	CH3	CH4	CH5
Element	Ca	Na	Si	K	Mn
	Ti	Mg	Al	Fe	P
					Cl

2.4: Peak and background count times

Element	Peak Count Time (s)	Background Count Time (s)
Ca	30	15
Ti	30	15
Na	10	10
Mg	30	15
Si	30	15
Al	30	15
K	30	15
Fe	30	15
Mn	30	15
P	30	15
Cl	30	15

2.5: Block mount maps and sample codes

POLISHED SIDE

UNPOLISHED SIDE

I

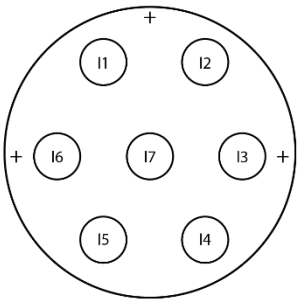

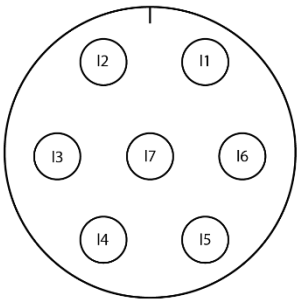

Block Code	Sample
I1	HT10
I2	HT11
I3	HT12
I4	HT13
I5	HT16
I6	HT17
I7	HT18

II

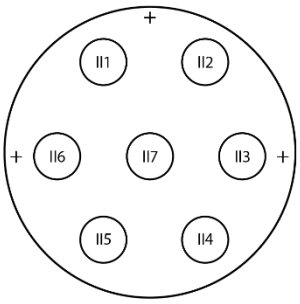

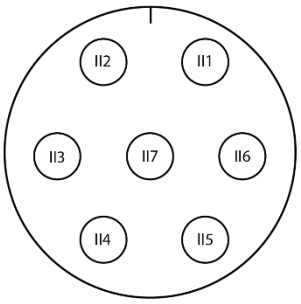

Block Code	Sample
II1	HT30
II2	HR4
II3	HR5
II4	HR6
II5	HR8
II6	HR17
II7	HR18

III

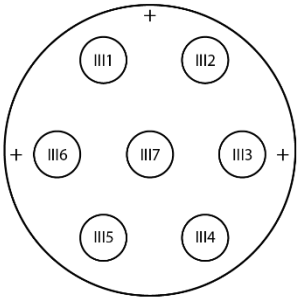

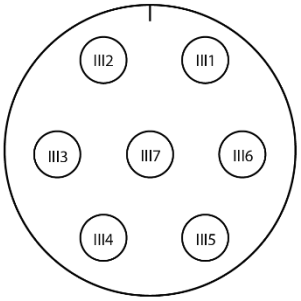

Block Code	Sample
III1	HP4
III2	HP5
III3	HP6
III4	HT28
III5	HR10
III6	HR9
III7	HT27

V

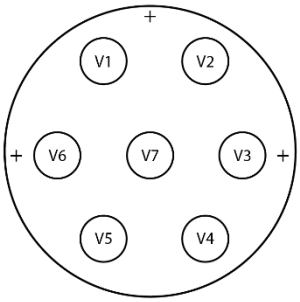

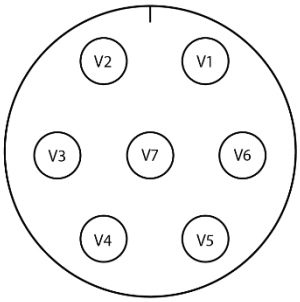

Block Code	Sample
V1	HP9
V2	HT07
V3	HT33
V4	HT35
V5	HT36
V6	HP1
V7	CR31

VI

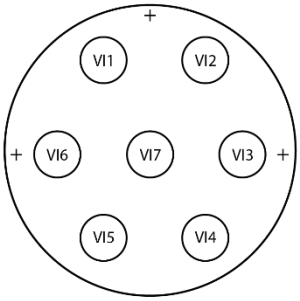

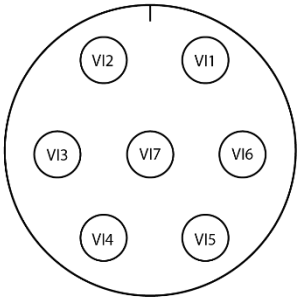

Block Code	Sample
VI1	HT20
VI2	HT25
VI3	HP11
VI4	HR13
VI5	HR15
VI6	HR17
VI7	HR20

2.6: Raw electron microprobe data in wt.%

Comment	CaO	TiO_2	Na_2O	MgO	SiO_2	Al_2O_3	K_2O	FeO	MnO	P_2O_5	Cl	Total
ATHO	1.76	0.261	3.677	0.074	76.377	12.327	2.699	3.424	0.088	0	0.037	100.716
ATHO	1.739	0.21	3.805	0.077	76.054	12.223	2.753	3.407	0.102	0.012	0.039	100.412
VG568	0.452	0.086	3.339	0.022	77.057	12.276	5.023	1.046	0.012	0	0.114	99.401
VG568	0.476	0.065	3.245	0.013	76.928	12.216	5.048	1.132	0.02	0.002	0.091	99.215
I1-01	0.711	0.063	3.333	0.059	76.634	12.331	4.203	0.904	0.062	0.016	0.134	98.42
I1-02	0.013	0	0.011	0	100.353	0.03	0	0.064	0.005	0.016	0	100.492
I1-03	0.604	0.052	3.465	0.049	77.721	12.401	4.386	0.774	0.058	0.014	0.147	99.638
I1-04	0.642	0.072	3.42	0.045	77.743	12.474	4.291	0.831	0.059	0	0.176	99.713
I1-05	1.382	0.22	3.686	0.245	76.819	13.049	2.922	1.358	0.075	0.028	0.131	99.885
I1-06	1.36	0.21	3.827	0.274	76.772	13.008	2.922	1.313	0.078	0.059	0.123	99.918
I1-07	1.316	0.209	3.551	0.194	77.525	12.963	3.072	1.428	0.041	0.009	0.133	100.411
I1-08	0.735	0.064	3.44	0.065	74.826	12.205	3.584	0.816	0.077	0.016	0.173	95.962
I1-09	1.354	0.198	3.432	0.197	77.513	12.683	3.076	1.311	0.045	0.023	0.152	99.95
I1-10	10.32	0	5.256	0.024	56.427	27.728	0.202	0.355	0.025	0	0	100.337
I1-11	0.589	0.061	3.279	0.041	73.61	11.875	4.109	0.737	0.053	0.012	0.156	94.487
I1-12	0.631	0.072	3.312	0.032	75.408	12.197	4.245	0.816	0.064	0	0.167	96.906
I1-13	0.6	0.04	3.111	0.056	75.102	12.145	4.098	0.816	0.088	0	0.168	96.186
I1-14	0.595	0.04	3.38	0.062	75.04	12.118	3.971	0.816	0.08	0	0.169	96.233
I1-15	0.734	0.056	3.14	0.073	74.921	12.216	4.069	0.819	0.053	0.014	0.145	96.207
I1-16	0.651	0.069	3.513	0.044	77.109	12.396	4.415	0.788	0.058	0.017	0.148	99.175
I1-17	0.554	0.049	3.278	0.042	75.01	12.071	4.148	0.822	0.062	0	0.156	96.157
I1-18	9.315	0	5.304	0.018	57.317	26.762	0.268	0.412	0	0.015	0.008	99.417
I1-19	0.592	0.058	3.141	0.065	74.886	12.051	4.286	0.705	0.104	0.012	0.158	96.022

Comment	CaO	TiO_2	Na_2O	MgO	SiO_2	Al_2O_3	K_2O	FeO	MnO	P_2O_5	Cl	Total
I1-20	0.64	0.048	3.322	0.051	77.709	12.491	4.264	0.816	0.03	0	0.172	99.504
ATHO	1.721	0.232	3.658	0.119	76.317	12.448	2.795	3.262	0.133	0.019	0.043	100.737
ATHO	1.713	0.251	3.738	0.102	75.982	12.401	2.738	3.222	0.06	0.014	0.045	100.256
VG568	0.441	0.071	3.376	0.032	77.23	12.253	4.96	1.288	0	0.017	0.095	99.742
VG568	0	0	0	0	0.005	0.002	0	0	0	0.001	1.226	0.957
I2-01	0.702	0.046	3.255	0.058	75.324	12.255	4.113	0.921	0.051	0	0.152	96.843
I2-02	0.574	0.061	3.273	0.047	75.646	12.207	4.192	0.851	0.043	0	0.154	97.013
I2-03	1.369	0.198	3.521	0.218	75.235	12.724	2.973	1.38	0.04	0.037	0.102	97.774
I2-04	0.602	0.07	3.359	0.038	74.899	12.009	4.186	0.787	0.048	0.003	0.165	96.129
I2-05	1.402	0.22	3.549	0.192	74.96	12.801	2.946	1.247	0.069	0.042	0.127	97.526
I2-06	0.645	0.06	3.406	0.048	76.002	12.282	4.312	0.882	0.066	0.014	0.162	97.842
I2-07	6.342	0.004	7.186	0	60.885	24.566	0.528	0.184	0.015	0.003	0.007	99.718
I2-08	1.333	0.19	3.546	0.205	74.057	12.346	2.858	1.352	0.12	0.033	0.139	96.148
I2-09	0.629	0.059	3.173	0.077	74.72	11.887	4.181	0.784	0.082	0	0.135	95.697
I2-10	0.726	0.046	3.137	0.091	74.518	12.218	4.073	0.901	0.043	0.012	0.157	95.887
I2-11	8.673	0	5.707	0	57.774	26.459	0.307	0.26	0.019	0.026	0.007	99.23
I2-12	0.617	0.059	3.339	0.059	74.903	12.067	4.307	0.803	0.066	0.021	0.155	96.361
I2-13	0.633	0.043	3.365	0.077	75.499	12.09	4.179	0.762	0.048	0	0.158	96.818
I2-14	5.673	0	7.058	0.014	62.311	23.508	0.673	0.101	0.011	0	0.005	99.353
I2-15	0.741	0.075	3.283	0.077	75.753	12.266	4.1	0.863	0.042	0	0.162	97.325
I2-16	0.603	0.074	3.362	0.05	75.399	12.106	4.155	0.876	0.041	0	0.16	96.79
I2-17	1.406	0.211	3.645	0.276	76.777	12.917	2.991	1.425	0.043	0.042	0.108	99.817
I2-18	1.442	0.218	3.487	0.239	77.014	13.043	3.057	1.387	0.056	0.021	0.149	100.079
I2-19	0.618	0.082	3.284	0.036	75.057	12.155	4.087	0.828	0.064	0.002	0.163	96.339

Comment	CaO	TiO_2	Na_2O	MgO	SiO_2	Al_2O_3	K_2O	FeO	MnO	P_2O_5	Cl	Total
I2-20	0.639	0.046	3.226	0.053	74.657	11.929	4.199	0.914	0.062	0	0.165	95.853
ATHO	1.719	0.233	3.821	0.068	75.998	12.377	2.749	3.256	0.144	0.01	0.031	100.399
ATHO	1.608	0.232	3.648	0.105	76.182	12.333	2.701	3.338	0.116	0.024	0.037	100.316
VG568	0.444	0.093	3.345	0.04	77.542	12.251	4.89	1.012	0.044	0.009	0.106	99.752
VG569	0.418	0.061	3.242	0.036	77.441	12.203	5.105	1.028	0.046	0.023	0.115	99.692
I3-01	1.302	0.241	3.724	0.257	76.393	13.044	3.072	1.487	0.075	0.037	0.137	99.738
I3-02	0.606	0.058	3.191	0.063	74.936	12.019	4.33	0.927	0.073	0.012	0.148	96.33
I3-03	0	0.01	0.018	0	100.429	0.055	0.008	0.019	0	0.016	0	100.555
I3-04	0.72	0.079	3.172	0.066	74.815	12.096	4.072	0.911	0.02	0.017	0.141	96.077
I3-05	9.763	0.045	5.137	0.014	56.774	27.173	0.194	0.339	0	0	0	99.439
I3-06	1.273	0.192	3.219	0.207	75.818	12.58	2.996	1.342	0.069	0.019	0.127	97.813
I3-07	6.451	0	6.703	0.006	60.075	24.301	0.52	0.143	0.022	0.029	0.001	98.251
I3-08	0.639	0.078	3.49	0.067	76.922	12.344	4.377	0.813	0.059	0	0.146	98.902
I3-09	4.423	0.003	7.706	0.015	63.083	22.715	0.702	0.165	0	0.002	0.002	98.816
I3-10	0	0.01	0.01	0.009	100.772	0.028	0.014	0.032	0	0.005	0	100.88
I3-11	5.76	0	7.02	0.001	61.51	23.78	0.559	0.146	0.005	0.009	0.004	98.793
I3-12	0.617	0.057	3.321	0.05	75.834	12.146	4.028	0.74	0.054	0.012	0.133	96.962
I3-13	9.112	0.006	5.719	0.025	57.486	26.666	0.259	0.317	0.015	0.015	0.002	99.622
I3-14	7.086	0	6.376	0	59.725	25.068	0.461	0.231	0.002	0	0	98.949
I3-15	0.764	0.078	3.123	0.064	74.963	11.996	4.026	0.943	0.036	0.012	0.16	96.129
I3-16	0	0.005	0	0.004	101.02	0.02	0	0	0.015	0	0	101.064
I3-17	1.382	0.22	3.692	0.205	76.042	12.89	2.801	1.459	0.093	0.033	0.135	98.922
I3-18	10.493	0.014	5.031	0.006	56.048	27.963	0.187	0.276	0	0.036	0	100.054
I3-19	0.02	0	0	0.002	0.023	0.002	0.003	0	0	0.007	1.075	0.889

Comment	CaO	TiO_2	Na_2O	MgO	SiO_2	Al_2O_3	K_2O	FeO	MnO	P_2O_5	Cl	Total
I3-20	10.303	0.009	4.882	0.033	55.917	27.579	0.2	0.466	0	0.02	0.006	99.414
ATHO	1.75	0.232	3.636	0.12	75.997	12.224	2.804	3.359	0.111	0.037	0.031	100.294
ATHO	1.737	0.24	3.695	0.1	76.23	12.272	2.863	3.438	0.147	0.016	0.033	100.764
VG568	0.438	0.059	3.195	0.037	77.044	12.088	4.99	1.015	0.001	0.005	0.102	98.951
VG568	0.432	0.085	3.248	0.027	77.003	12.208	5.116	0.964	0.02	0.016	0.085	99.185
I4-01	0.79	0.12	3.573	0.121	76.595	12.472	3.296	0.927	0.098	0.03	0.178	98.16
I4-02	0.685	0.108	3.711	0.091	78.281	11.683	3.23	0.759	0.043	0.026	0.171	98.749
I4-03	0.771	0.137	3.47	0.152	75.694	12.34	3.576	1.012	0.078	0.014	0.126	97.342
I4-04	0.736	0.094	3.365	0.102	77.479	12.433	3.396	0.911	0.046	0	0.146	98.675
I4-05	0.781	0.09	3.616	0.106	77.418	12.32	3.435	0.927	0.077	0	0.164	98.897
I4-06	0.788	0.116	3.619	0.107	77.583	12.297	3.445	1.006	0.053	0.014	0.152	99.146
I4-07	6.305	0.006	7.078	0	61.134	24.161	0.543	0.196	0.011	0	0	99.434
I4-08	0.786	0.102	3.633	0.117	77.87	12.474	3.361	0.841	0.103	0.026	0.145	99.425
I4-09	0.855	0.091	3.644	0.13	77.224	12.459	3.196	0.93	0.068	0.028	0.137	98.731
I4-10	0.771	0.125	3.64	0.1	77.731	12.197	3.456	0.984	0.067	0	0.158	99.193
I4-11	0.766	0.103	3.442	0.096	74.311	11.928	3.174	1.003	0.047	0.009	0.146	94.992
I4-12	0.771	0.097	3.645	0.118	77.484	12.425	3.312	0.936	0.078	0.012	0.166	99.007
I4-13	0.787	0.106	3.323	0.105	77.424	12.336	3.421	0.794	0.017	0.032	0.148	98.46
I4-14	0.749	0.097	3.511	0.097	75.218	12.198	3.361	0.885	0.054	0.007	0.158	96.299
I4-15	0.933	0.12	3.5	0.11	75.3	12.024	3.138	1.019	0.079	0.033	0.159	96.379
I4-16	0.767	0.098	3.596	0.116	77.77	12.321	3.477	0.857	0.041	0.012	0.156	99.176
I4-17	0.704	0.093	3.474	0.11	75.348	11.79	3.325	0.797	0.078	0.004	0.154	95.842
I4-18	0.777	0.112	3.687	0.122	76.853	12.309	3.489	0.882	0.049	0.023	0.156	98.424
I4-19	0.774	0.122	3.522	0.128	77.247	12.29	3.345	0.895	0.061	0	0.145	98.496

Comment	CaO	TiO_2	Na_2O	MgO	SiO_2	Al_2O_3	K_2O	FeO	MnO	P_2O_5	Cl	Total
I4-20	9.748	0	5.333	0	56.449	27.13	0.165	0.253	0.02	0.014	0.009	99.119
ATHO	1.737	0.223	3.696	0.103	75.84	12.328	2.718	3.286	0.075	0	0.035	100.033
ATHO	1.747	0.213	3.379	0.087	75.716	12.285	2.796	3.267	0.112	0.009	0.042	99.644
VG568	0.444	0.066	3.346	0.02	77.324	12.157	5.064	0.996	0	0.009	0.086	99.493
VG569	0.468	0.063	3.251	0.053	76.895	12.08	5.071	1.145	0.009	0	0.118	99.126
I5-01	0.766	0.086	3.48	0.113	75.593	11.841	3.29	0.85	0.077	0	0.169	96.227
I5-02	0.754	0.111	3.474	0.118	77.774	12.412	3.497	0.882	0.057	0.014	0.127	99.191
I5-03	0.76	0.115	3.653	0.081	77.846	12.553	3.415	1.012	0.075	0.019	0.147	99.643
I5-04	0.76	0.088	3.539	0.135	77.491	12.403	3.4	0.965	0.054	0	0.175	98.971
I5-05	12.259	0	4.299	0.01	53.236	29.506	0.137	0.326	0.041	0	0	99.814
I5-06	0.763	0.103	3.505	0.114	77.556	12.278	3.332	0.768	0.067	0.005	0.152	98.609
I5-07	7.673	0	6.207	0.021	59.005	25.457	0.297	0.269	0.015	0.026	0	98.97
I5-08	0.737	0.102	3.376	0.137	75.022	12.094	3.189	0.787	0.069	0.033	0.131	95.647
I5-09	0.762	0.117	3.765	0.103	77.318	12.401	3.381	0.828	0.074	0.003	0.152	98.87
I5-10	0.767	0.086	3.696	0.095	75.876	12.091	3.158	1.031	0.04	0.012	0.168	96.982
I5-11	0.859	0.101	3.554	0.147	76.88	12.306	3.318	0.898	0.067	0.009	0.145	98.251
I5-12	0.719	0.106	3.445	0.105	75.503	12.11	3.106	0.816	0.033	0.012	0.15	96.071
I5-13	0.734	0.089	3.367	0.11	75.382	11.826	3.251	0.888	0.036	0.009	0.162	95.817
I5-14	0.806	0.077	3.622	0.12	75.92	12.252	3.103	0.949	0.057	0	0.146	97.019
I5-15	0.748	0.108	3.428	0.109	75.149	12.086	3.223	0.929	0.046	0.024	0.166	95.979
I5-16	0.778	0.09	3.547	0.112	77.644	12.495	3.532	0.93	0.067	0	0.159	99.318
I5-17	0.772	0.108	3.512	0.105	76.8	12.378	3.334	0.841	0.069	0.005	0.153	98.042
I5-18	0.818	0.104	3.783	0.115	77.568	12.433	3.34	0.936	0.109	0.021	0.161	99.352
I5-19	0.826	0.1	3.614	0.105	77.13	12.224	3.269	0.838	0.043	0	0.162	98.274

Comment	CaO	TiO_2	Na_2O	MgO	SiO_2	Al_2O_3	K_2O	FeO	MnO	P_2O_5	Cl	Total
I5-20	0.748	0.108	3.671	0.108	75.535	11.903	3.177	0.806	0.049	0.023	0.164	96.255
ATHO	1.723	0.257	3.625	0.096	75.871	12.269	2.754	3.544	0.11	0.016	0.043	100.298
ATHO	1.748	0.221	3.666	0.103	76.086	12.254	2.666	3.143	0.131	0.026	0.045	100.079
VG568	0.461	0.069	3.413	0.024	77.291	12.084	4.929	1.164	0.035	0	0.115	99.559
VG568	0.428	0.076	3.108	0.027	76.652	12.116	5.021	1.047	0.033	0.019	0.099	98.604
I6-01	0.936	0.124	3.758	0.12	77.237	12.298	3.12	1.025	0.077	0.021	0.14	98.824
I6-02	0.801	0.132	2.955	0.107	72.179	11.678	3.157	1.243	0.057	0	0.161	92.434
I6-03	0.938	0.145	3.458	0.126	77.596	12.233	3.238	1.038	0.096	0	0.135	98.973
I6-04	0.804	0.1	3.276	0.118	74.088	11.703	3.087	1.034	0.077	0	0.137	94.393
I6-05	0.831	0.112	3.325	0.107	74.731	11.842	3.214	0.898	0.019	0.028	0.164	95.234
I6-06	0.897	0.155	3.668	0.149	77.687	12.349	3.173	1.095	0.051	0.021	0.143	99.356
I6-07	0.873	0.121	3.513	0.154	75.123	11.963	3.272	1.059	0.057	0	0.109	96.219
I6-08	0.816	0.107	3.348	0.116	74.736	11.919	3.224	1.021	0.026	0	0.154	95.432
I6-09	0.894	0.14	3.67	0.143	77.269	12.216	3.349	1.031	0.067	0.024	0.147	98.917
I6-10	0.825	0.117	3.349	0.127	74.681	11.824	3.171	0.828	0.031	0.002	0.165	95.083
I6-11	0.817	0.123	3.226	0.121	74.115	11.662	3.194	0.895	0.044	0.018	0.14	94.323
I6-12	0.9	0.135	3.559	0.143	77.341	12.091	3.266	0.98	0.085	0	0.141	98.609
I6-13	8.4	0	6.006	0.01	58.374	25.981	0.281	0.177	0	0	0.006	99.234
I6-14	0.87	0.144	3.542	0.129	77.916	12.445	3.415	1.107	0.08	0.01	0.142	99.768
I6-15	0.854	0.119	3.328	0.092	74.569	11.876	3.234	1.091	0.083	0	0.158	95.368
I6-16	0.879	0.125	3.314	0.134	76.054	11.995	3.232	1.158	0.063	0	0.171	97.086
I6-17	0.86	0.092	2.97	0.133	75.62	11.969	3.191	1.079	0.038	0	0.141	96.061
I6-18	0.63	0.072	3.422	0.053	76.597	12.371	4.339	0.85	0.082	0	0.163	98.542
I6-19	0.809	0.128	3.08	0.107	74.332	11.85	3.168	0.933	0.042	0.024	0.15	94.589

Comment	CaO	TiO_2	Na_2O	MgO	SiO_2	Al_2O_3	K_2O	FeO	MnO	P_2O_5	Cl	Total
I6-20	0.874	0.129	3.356	0.128	75.198	11.963	3.191	1.012	0.07	0.014	0.136	96.04
ATHO	1.575	0.233	4.403	0.093	75.37	12.381	2.803	3.477	0.105	0.047	0.049	100.525
ATHO	1.7	0.241	3.91	0.097	75.83	12.246	2.767	3.238	0.126	0.01	0.047	100.201
VG568	0.427	0.086	3.628	0.037	76.946	12.109	5.006	1.04	0.032	0	0.117	99.402
VG568	0.45	0.074	3.302	0.027	77.139	12.074	4.946	1.158	0.015	0	0.086	99.252
I7-01	0.705	0.098	3.461	0.113	75.945	11.984	3.631	1.012	0.079	0.019	0.17	97.179
I7-02	0.931	0.125	3.51	0.124	77.995	12.423	3.26	1.037	0.096	0.007	0.147	99.622
I7-03	0.812	0.081	3.672	0.116	77.959	12.515	3.383	1.059	0.062	0.04	0.163	99.825
I7-04	0.67	0.107	3.377	0.072	77.082	12.127	3.857	0.816	0.063	0.033	0.177	98.341
I7-05	0.723	0.091	3.624	0.121	78.28	12.435	3.524	0.927	0.028	0.051	0.15	99.92
I7-06	2.261	0.231	4.335	0.227	73.225	14.755	2.465	1.999	0.049	0.047	0.161	99.719
I7-07	1.51	0.254	3.984	0.289	74.742	13.205	2.675	2.107	0.079	0.023	0.174	99.003
I7-08	0.892	0.119	3.609	0.112	75.473	11.942	3.249	1.075	0.054	0.031	0.132	96.658
I7-09	6.78	0	6.647	0.024	60.501	24.345	0.373	0.361	0	0	0.004	99.034
I7-10	0.688	0.084	3.623	0.104	78.049	12.465	3.845	0.834	0.068	0.024	0.152	99.902
I7-11	1.3	0.192	3.857	0.151	75.526	12.76	3.104	1.651	0.084	0.016	0.126	98.739
I7-12	0.757	0.097	3.428	0.072	77.381	12.313	3.264	0.952	0.078	0.009	0.142	98.461
I7-13	0.776	0.092	3.504	0.129	77.994	12.348	3.431	0.876	0.09	0.002	0.181	99.382
I7-14	0.765	0.086	3.416	0.117	77.04	12.368	3.667	1.05	0.049	0.026	0.138	98.691
I7-15	0.766	0.092	3.617	0.101	76.873	12.317	3.408	0.99	0.042	0	0.14	98.314
I7-16	1.021	0.152	3.733	0.117	76.832	12.46	3.218	1.547	0.088	0.026	0.145	99.306
I7-17	0.764	0.104	3.591	0.108	77.816	12.361	3.466	0.969	0.057	0.005	0.143	99.352
I7-18	0.733	0.091	3.369	0.112	75.385	12.084	3.507	0.835	0.035	0	0.15	96.267
I7-19	0.733	0.092	3.412	0.098	75.844	11.937	3.595	0.904	0.043	0.023	0.153	96.799

Comment	CaO	TiO_2	Na_2O	MgO	SiO_2	Al_2O_3	K_2O	FeO	MnO	P_2O_5	Cl	Total
I7-20	5.984	0.094	5.081	0.103	64.53	21.168	1.257	1.061	0.031	0.033	0.072	99.398
ATHO	1.74	0.234	3.589	0.096	76.124	12.31	2.821	3.244	0.123	0.059	0.039	100.37
ATHO	1.745	0.266	3.673	0.09	75.914	12.203	2.758	3.43	0.121	0.021	0.041	100.253
VG568	0.432	0.063	4.378	0.022	76.878	12.225	5.076	0.973	0	0	0.084	100.112
VG568	0.442	0.097	3.495	0.029	77.577	12.068	5.035	1.072	0.035	0	0.113	99.937
ATHO	1.755	0.233	3.452	0.098	76.645	12.509	2.708	3.299	0.087	0.007	0.036	100.821
ATHO	1.721	0.259	3.659	0.099	76.662	12.381	2.844	3.265	0.159	0.042	0.038	101.12
VG568	0.428	0.106	3.325	0.023	77.205	12.229	4.868	1.048	0.043	0.019	0.113	99.381
VG568	0.425	0.077	3.407	0.046	77.284	12.156	5.006	1.093	0.054	0.016	0.103	99.644
IV1-01	0.846	0.106	3.482	0.135	75.594	12.117	3.213	1.014	0.065	0.033	0.205	96.764
IV1-02	0.803	0.125	3.313	0.131	75.141	12.244	2.981	0.96	0.062	0.007	0.198	95.92
IV1-03	0.798	0.118	3.582	0.133	76.732	12.226	3.315	0.875	0.007	0.028	0.155	97.934
IV1-04	0.737	0.108	3.419	0.124	76.122	12.112	3.373	0.916	0.049	0.016	0.176	97.112
IV1-05	0.841	0.1	3.572	0.141	78.324	12.66	3.243	0.986	0.044	0.03	0.142	100.051
IV1-06	0.83	0.132	3.413	0.135	75.902	12.177	3.349	0.871	0.072	0.037	0.175	97.054
IV1-07	0.855	0.095	3.6	0.127	76.15	12.261	3.17	0.856	0.062	0.017	0.198	97.346
IV1-08	0.801	0.137	3.585	0.129	75.541	12.205	3.355	0.91	0.075	0	0.153	96.856
IV1-09	0.78	0.126	3.38	0.12	75.981	12.111	3.392	0.922	0.063	0.005	0.15	96.996
IV1-10	0.824	0.14	3.444	0.138	74.843	12.015	3.175	0.91	0.078	0.024	0.19	95.738
IV1-11	0.823	0.137	3.48	0.115	76.313	12.285	3.278	0.875	0.002	0.068	0.17	97.508
IV1-12	0.814	0.127	3.45	0.125	75.908	12.29	3.332	0.872	0.077	0.003	0.181	97.138
IV1-13	0.827	0.133	3.589	0.126	77.244	12.394	3.307	0.919	0.056	0.035	0.161	98.755
IV1-14	0.835	0.108	3.751	0.133	78.155	12.509	3.347	0.818	0.106	0.009	0.202	99.927
IV1-15	0.819	0.101	3.462	0.152	74.204	12.062	2.942	0.976	0.017	0.017	0.184	94.894

Comment	CaO	TiO_2	Na_2O	MgO	SiO_2	Al_2O_3	K_2O	FeO	MnO	P_2O_5	Cl	Total
IV1-16	0.82	0.13	3.576	0.129	76.283	12.104	3.32	0.982	0.051	0.019	0.172	97.547
IV1-17	0.835	0.108	3.625	0.141	75.921	12.285	3.31	0.868	0.073	0.007	0.198	97.326
IV1-18	0.812	0.13	3.545	0.111	75.411	12.194	3.088	0.893	0.044	0.012	0.164	96.367
IV1-19	0.831	0.135	3.206	0.134	74.386	12.093	2.907	0.884	0.058	0.021	0.196	94.807
IV1-20	0.817	0.117	3.422	0.13	76.437	12.198	3.248	0.669	0.014	0.009	0.156	97.182
ATHO	1.734	0.245	3.651	0.129	76.802	12.373	2.741	3.321	0.11	0.023	0.039	101.159
ATHO	1.764	0.238	3.634	0.096	76.281	12.18	2.751	3.466	0.119	0.03	0.036	100.587
VG568	0.471	0.071	3.457	0.025	77.241	12.165	5.117	1.112	0	0	0.114	99.747
VG568	0.395	0.055	3.395	0.031	76.431	12.04	5.014	2.654	0	0.017	0.095	100.106
IV2-01	0.759	0.089	2.973	0.07	77.341	12.337	4.271	1.033	0.067	0.01	0.181	99.09
IV2-02	0.773	0.074	2.978	0.086	77.551	12.498	4.336	1.008	0.011	0.019	0.18	99.473
IV2-03	0.725	0.098	2.961	0.061	76.345	12.223	4.355	0.903	0.031	0.016	0.177	97.855
IV2-04	0.714	0.088	3.236	0.099	76.818	12.098	4.371	0.926	0.07	0.002	0.176	98.558
IV2-05	0.734	0.101	3.064	0.117	77.247	12.297	4.321	0.945	0.052	0	0.187	99.023
IV2-06	0.714	0.105	3.064	0.093	76.446	12.224	4.438	0.96	0.033	0.003	0.186	98.224
IV2-07	0.753	0.096	3.015	0.114	76.506	12.271	4.359	0.954	0.032	0.01	0.181	98.25
IV2-08	0.735	0.101	3.064	0.086	76.446	12.122	0.351	0	0.054	0.005	0.168	93.094
IV2-09	0.762	0.088	3.166	0.119	76.438	12.256	4.351	1.014	0	0.014	0.181	98.348
IV2-10	0.677	0.083	3.222	0.055	77.249	12.069	4.37	1.147	0.049	0.033	0.201	99.11
IV2-11	0.765	0.1	3.06	0.074	77.436	12.592	4.319	0.938	0.047	0.005	0.194	99.486
IV2-12	0.77	0.095	3.1	0.09	77.259	12.321	4.469	0.954	0.085	0	0.193	99.292
IV2-13	0.706	0.116	3.202	0.089	77.385	12.395	4.431	1.043	0.03	0.01	0.186	99.551
IV2-14	0.765	0.09	2.883	0.091	76.896	12.29	4.438	0.84	0.043	0	0.195	98.487
IV2-15	0.773	0.092	3.166	0.132	77.294	12.403	4.458	0.976	0.077	0.031	0.224	99.575

Comment	CaO	TiO_2	Na_2O	MgO	SiO_2	Al_2O_3	K_2O	FeO	MnO	P_2O_5	Cl	Total
IV2-16	0.745	0.082	2.906	0.108	76.061	12.114	4.396	1.002	0.073	0	0.2	97.642
IV2-17	0.763	0.089	2.907	0.085	76.434	12.242	4.305	1.024	0.044	0.01	0.183	98.045
IV2-18	0.782	0.099	3.077	0.1	77.025	12.314	4.451	0.935	0.04	0.01	0.221	99.004
IV2-19	0.766	0.094	3.084	0.067	77.224	12.264	4.417	0.891	0.068	0.007	0.189	99.028
IV2-20	0.791	0.097	2.922	0.095	77.063	12.426	4.418	0.954	0.049	0.009	0.207	98.984
ATHO	1.748	0.235	3.677	0.083	76.5	12.217	2.791	3.331	0.11	0.037	0.046	100.765
ATHO	1.777	0.246	3.691	0.079	76.49	12.397	2.81	3.35	0.112	0.023	0.043	101.008
VG568	0.441	0.084	3.195	0.03	77.147	12.1	4.971	1.16	0	0	0.086	99.195
VG568	0.439	0.078	3.344	0.014	77.481	12.184	4.985	0.986	0.03	0.003	0.104	99.625
IV3-01	0.73	0.099	2.735	0.071	73.261	11.628	3.869	1.236	0.019	0	0.17	93.78
IV3-02	0.817	0.129	3.347	0.139	75.386	11.945	3.014	0.923	0.036	0	0.204	95.894
IV3-03	0.783	0.08	3.196	0.109	74.725	11.846	3.207	0.907	0.095	0.01	0.206	95.118
IV3-04	0.824	0.112	3.268	0.127	74.389	11.942	3.024	0.992	0.081	0	0.198	94.912
IV3-05	0.796	0.105	3.312	0.144	74.966	11.89	3.138	0.913	0.063	0.03	0.198	95.51
IV3-06	0.003	0.008	0.013	0	101.128	0.029	0.013	0.038	0	0.027	0	101.259
IV3-07	0.787	0.121	3.13	0.104	74.536	11.832	2.991	0.872	0.047	0.009	0.187	94.574
IV3-08	0.764	0.101	3.332	0.115	74.203	11.769	3.124	0.812	0.032	0.023	0.186	94.419
IV3-09	0.693	0.083	3.225	0.058	73.378	11.824	3.477	1.267	0.051	0.014	0.185	94.213
IV3-10	0.823	0.119	3.448	0.155	74.72	11.853	3.192	0.982	0.035	0.031	0.202	95.514
IV3-11	0.703	0.099	3.175	0.053	73.506	11.612	3.211	1.109	0.043	0.014	0.155	93.645
IV3-12	0.738	0.095	3.241	0.111	74.166	11.8	3.066	0.866	0.065	0.049	0.158	94.319
IV3-13	0.849	0.104	3.318	0.151	74.673	12.01	3.017	0.878	0.052	0.003	0.206	95.215
IV3-14	0.667	0.069	2.998	0.066	74.094	11.687	3.459	1.053	0.063	0.005	0.141	94.27
IV3-15	0.813	0.111	3.317	0.139	74.127	11.861	3.023	0.78	0.051	0.037	0.201	94.415

Comment	CaO	TiO_2	Na_2O	MgO	SiO_2	Al_2O_3	K_2O	FeO	MnO	P_2O_5	Cl	Total
IV3-16	0.802	0.11	3.261	0.136	74.33	12.003	3.137	0.907	0.061	0.038	0.149	94.9
IV3-17	0.78	0.113	3.398	0.123	74.628	11.787	3.086	0.904	0.033	0.007	0.17	94.991
IV3-18	0.746	0.121	3.335	0.12	75.202	11.791	3.182	0.888	0.001	0	0.004	95.389
IV3-19	0.543	0.097	3.02	0.057	73.547	11.61	3.43	1.052	0	0.003	0.085	93.425
IV3-20	0.789	0.119	3.035	0.14	73.514	11.814	3.011	0.783	0.049	0.023	0.207	93.437
ATHO	1.764	0.23	4.36	0.12	75.825	12.201	2.717	3.291	0.08	0	0.026	100.608
ATHO	1.74	0.234	3.896	0.125	76.026	12.395	2.803	3.226	0.067	0.033	0.038	100.574
VG568	0.431	0.065	3.328	0.031	77.501	12.108	4.89	1.306	0.012	0.009	0.103	99.761
VG568	0.456	0.053	3.3	0.032	77.217	12.166	5.07	1.22	0.016	0	0.111	99.616
IV4-01	1.123	0.168	3.624	0.218	72.871	12.459	2.61	1.232	0.102	0.059	0.193	94.615
IV4-02	1.111	0.152	3.633	0.182	72.851	12.526	2.688	1.099	0.068	0.007	0.174	94.452
IV4-03	1.147	0.181	3.749	0.179	76.209	13.114	2.886	1.134	0.105	0.063	0.166	98.896
IV4-04	1.075	0.184	3.484	0.186	73.654	12.436	2.67	1.138	0.102	0	0.178	95.067
IV4-05	0.838	0.115	3.585	0.162	75.703	12.145	3.314	1.005	0.015	0.038	0.191	97.068
IV4-06	1.064	0.156	1.884	0.172	71.248	12.087	4.003	1.147	0.095	0.028	0.165	92.012
IV4-07	1.141	0.153	3.575	0.216	73.686	12.537	2.736	1.239	0.073	0	0.157	95.478
IV4-08	1.106	0.167	3.661	0.184	73.531	12.512	2.714	1.258	0.08	0.002	0.192	95.364
IV4-09	1.145	0.179	3.689	0.191	73.484	12.544	2.715	1.096	0.095	0.012	0.174	95.285
IV4-10	1.102	0.174	3.631	0.177	73.769	12.503	2.707	1.154	0.08	0.009	0.171	95.438
IV4-11	1.136	0.155	3.899	0.227	73.67	12.908	2.614	1.22	0.069	0.03	0.19	96.075
IV4-12	1.138	0.197	3.662	0.185	73.368	12.554	2.699	1.315	0.073	0.037	0.193	95.377
IV4-13	1.1	0.206	3.55	0.208	73.833	12.578	2.818	1.22	0.118	0	0.194	95.781
IV4-14	1.126	0.157	3.589	0.208	72.845	12.493	2.684	1.254	0.085	0.016	0.142	94.567
IV4-15	1.142	0.166	3.669	0.183	73.401	12.448	2.701	1.166	0.079	0.042	0.19	95.144

Comment	CaO	TiO_2	Na_2O	MgO	SiO_2	Al_2O_3	K_2O	FeO	MnO	P_2O_5	Cl	Total
IV4-16	1.135	0.172	3.501	0.201	73.701	12.642	2.745	1.22	0.053	0.03	0.156	95.521
IV4-17	1.113	0.179	3.796	0.226	73.875	12.571	2.761	1.204	0.08	0.023	0.169	95.959
IV4-18	1.118	0.158	3.677	0.19	73.501	12.643	2.729	1.324	0.057	0.054	0.178	95.589
IV4-19	1.149	0.171	3.732	0.202	73.453	12.464	2.524	1.229	0.069	0.028	0.164	95.148
IV4-20	1.13	0.161	3.761	0.209	73.756	12.546	2.692	1.324	0.095	0	0.195	95.825
ATHO	1.679	0.209	5.168	0.086	75.405	12.304	2.711	3.461	0.18	0.005	0.031	101.232
ATHO	1.784	0.22	3.925	0.086	76.06	12.317	2.786	3.248	0.102	0	0.036	100.556
VG568	0.428	0.068	3.549	0.036	77.623	12.089	5	1.255	0.006	0.014	0.089	100.137
VG568	0.452	0.078	3.491	0.031	77.789	12.181	5.101	1.194	0.01	0.014	0.098	100.417
IV5-01	0.721	0.102	3.039	0.076	74.473	11.611	3.661	0.888	0.037	0.014	0.14	94.73
IV5-02	9.187	0	5.794	0.02	58.03	26.598	0.226	0.383	0.009	0.012	0	100.259
IV5-03	0.709	0.091	2.819	0.069	74.501	11.765	4.392	0.903	0.1	0.021	0.162	95.495
IV5-04	2.329	0.387	4.004	0.552	72.696	14.217	2.345	2.13	0.067	0.076	0.187	98.948
IV5-05	1.928	0.286	3.475	0.441	70.452	13.427	2.352	1.839	0.139	0.077	0.141	94.525
IV5-06	11.517	0.023	4.474	0.056	54.922	28.486	0.124	0.421	0.012	0	0	100.035
IV5-07	9.679	0.013	4.98	0.042	57.254	26.656	0.173	0.452	0	0.015	0.002	99.266
IV5-08	10.771	0.016	4.859	0.053	55.856	28.071	0.158	0.487	0	0	0.001	100.272
IV5-09	2.332	0.325	4.095	0.396	72.319	14.378	2.341	1.626	0.08	0.073	0.137	98.071
IV5-10	11.12	0	4.89	0.033	55.684	28.593	0.173	0.436	0.009	0	0	100.938
IV5-11	1.876	0.305	3.771	0.421	71.21	13.276	2.463	1.869	0.112	0.057	0.149	95.475
IV5-12	2.334	0.39	3.862	0.516	72.187	14.119	2.363	2.008	0.111	0.089	0.19	98.126
IV5-13	1.718	0.269	3.777	0.395	72.416	13.257	2.449	1.538	0.117	0.031	0.164	96.094
IV5-14	2.027	0.345	3.437	0.479	70.134	13.448	2.284	1.715	0.089	0.057	0.181	94.155
IV5-15	2.028	0.313	3.508	0.53	70.178	13.404	2.301	1.853	0.073	0.042	0.159	94.353

Comment	CaO	TiO_2	Na_2O	MgO	SiO_2	Al_2O_3	K_2O	FeO	MnO	P_2O_5	Cl	Total
IV5-16	0.797	0.117	2.286	0.129	72.919	11.543	4.099	0.852	0.057	0.01	0.191	92.957
IV5-17	1.835	0.265	3.416	0.408	71.005	13.07	2.345	1.585	0.071	0.073	0.153	94.191
IV5-18	2.286	0.383	3.752	0.574	72.692	13.944	2.213	1.9	0.102	0.073	0.171	98.051
IV5-19	9.534	0.02	5.31	0.014	57.504	27.046	0.162	0.247	0.018	0	0	99.855
IV5-20	9.695	0.015	5.466	0.049	57.072	26.918	0.192	0.537	0.017	0.043	0	100.004
ATHO	1.721	0.223	3.663	0.094	75.867	12.132	2.375	3.313	0.087	0.003	0.044	99.512
ATHO	1.755	0.255	3.658	0.086	76.032	12.205	2.675	3.31	0.106	0.024	0.03	100.129
VG568	0.439	0.061	3.334	0.044	77.105	12.07	5.092	1.016	0.033	0.012	0.101	99.284
VG568	0.422	0.078	3.351	0.054	76.986	12.015	5.016	1.591	0.02	0.009	0.098	99.618
IV6-01	9.137	0.035	5.682	0.035	57.836	26.451	0.268	0.316	0.005	0.017	0	99.782
IV6-02	0.794	0.069	3.25	0.076	75.43	12.032	3.593	1.13	0.03	0.021	0.187	96.57
IV6-03	0.789	0.084	3.436	0.082	75.092	12.012	3.714	1.073	0.057	0.009	0.177	96.485
IV6-04	1.107	0.135	3.531	0.134	73.721	12.708	3.734	1.686	0.07	0.036	0.18	97.001
IV6-05	0.598	0.101	3.233	0.049	75.332	11.672	3.851	1.111	0.02	0	0.17	96.099
IV6-06	0.718	0.1	3.311	0.105	75.537	12.039	3.565	0.846	0.046	0.016	0.176	96.419
IV6-07	0.617	0.093	3.395	0.07	75.545	11.652	3.823	1.07	0.039	0	0.209	96.466
IV6-08	0.981	0.146	3.736	0.167	75.168	12.428	3.024	1.197	0.086	0.014	0.146	97.06
IV6-09	0.781	0.071	3.048	0.111	75.71	12.125	3.834	1.14	0.004	0	0.182	96.965
IV6-10	1.118	0.165	3.489	0.149	73.598	12.852	3.322	1.55	0.058	0.002	0.191	96.451
IV6-11	0.825	0.115	3.672	0.152	76.099	12.221	3.466	1.01	0.064	0.012	0.141	97.745
IV6-12	0.762	0.077	3.035	0.086	75.717	12.195	4.152	1.054	0.021	0	0.243	97.287
IV6-13	0.788	0.086	3.763	0.106	78.598	12.594	3.382	0.893	0.038	0.031	0.143	100.39
IV6-14	0.775	0.081	3.236	0.086	75.165	11.912	3.827	0.997	0.032	0.045	0.191	96.304
IV6-15	0.824	0.076	3.314	0.093	75.421	12.012	3.552	0.94	0.038	0	0.151	96.387

Comment	CaO	TiO_2	Na_2O	MgO	SiO_2	Al_2O_3	K_2O	FeO	MnO	P_2O_5	Cl	Total
IV6-16	0.825	0.082	3.196	0.088	73.943	11.976	3.41	0.925	0.009	0.019	0.149	94.588
IV6-17	1.04	0.149	3.19	0.131	74.565	11.943	3.5	1.222	0.032	0	0.179	95.911
IV6-18	0.747	0.07	3.174	0.09	75.723	12.072	4.014	0.912	0.023	0	0.164	96.952
ATHO	1.747	0.219	3.407	0.102	76.771	12.269	2.704	3.317	0.096	0.035	0.047	100.703
ATHO	1.735	0.243	3.764	0.072	76.476	12.299	2.794	3.455	0.109	0.033	0.034	101.006
VG568	0.438	0.08	3.355	0.039	77.239	12.022	4.838	1.229	0.032	0	0.125	99.369
VG568	0.439	0.058	3.292	0.038	77.33	12.238	5.038	1.124	0.05	0.012	0.098	99.695
IV6-19	0.707	0.073	2.388	0.058	75.3	12.051	3.678	0.865	0.042	0.007	0.185	95.312
IV6-20	0.985	0.125	3.051	0.151	74.269	11.98	3.33	1.038	0.016	0.047	0.141	95.101
V1-01	0.744	0.082	0.147	0.012	0.004	0	0.003	0.022	0.026	0	0.157	1.162
V1-02	0.873	0.097	3.343	0.118	0.003	0	2.783	0.8	0.045	0.018	0.155	8.2
V1-03	0.848	0.07	3.198	0.116	75.988	12.205	3.64	1.06	0.045	0	0.186	97.314
V1-04	1.041	0.083	3.113	0.143	21.865	3.912	3.393	1.147	0.043	0.023	0.175	34.899
V1-05	0.893	0.122	3.017	0.114	75.394	11.876	4.143	1.252	0.029	0	0.178	96.978
V1-06	0.01	0	0	0	101.795	0.036	0	0.095	0.005	0.014	0	101.955
V1-07	0.855	0.102	2.951	0.061	75.888	12.062	4.167	0.854	0.048	0	0.165	97.116
V1-08	1.137	0.163	3.397	0.154	74.012	12.845	3.685	1.537	0.049	0.014	0.171	97.125
V1-09	0.89	0.135	3.277	0.104	75.334	12.077	3.814	1.273	0.071	0.062	0.179	97.176
V1-10	1.029	0.139	3.038	0.136	75.42	11.966	3.755	1.037	0.037	0.014	0.144	96.683
V1-11	0.912	0.106	3.117	0.085	75.741	11.987	3.911	0.983	0.059	0	0.179	97.04
V1-12	0.752	0.131	2.52	0.108	75.365	12.239	4.757	1.099	0.037	0.024	0.241	97.219
V1-13	6.273	0.001	6.701	0.006	61.638	24.555	0.599	0.23	0.027	0.019	0	100.049
V1-14	1.112	0.15	2.743	0.127	72.867	12.535	3.678	1.603	0.074	0.002	0.204	95.049
V1-15	0.841	0.087	3.444	0.087	75.913	12.086	3.605	0.965	0.044	0.024	0.171	97.228

Comment	CaO	TiO_2	Na_2O	MgO	SiO_2	Al_2O_3	K_2O	FeO	MnO	P_2O_5	Cl	Total
V1-16	0.877	0.127	3.169	0.114	75.871	12.1	3.864	1.374	0.055	0.021	0.194	97.722
V1-17	0.845	0.077	3.332	0.084	75.604	11.993	3.823	1.205	0.029	0.007	0.183	97.141
V1-18	0.904	0.08	3.281	0.079	76.337	12.184	3.719	0.991	0.02	0.009	0.193	97.753
V1-19	0.762	0.082	2.845	0.068	75.202	11.809	4.066	1.258	0	0.016	0.164	96.235
V1-20	0.909	0.117	3.098	0.102	75.434	12.11	3.958	1.246	0.028	0	0.164	97.129
ATHO	1.777	0.249	3.809	0.1	76.6	12.271	2.732	3.453	0.109	0.038	0.037	101.167
ATHO	1.755	0.253	3.8	0.111	76.452	12.343	2.791	3.274	0.072	0	0.044	100.885
VG568	0.464	0.083	3.48	0.018	77.805	12.206	5.022	1.11	0.052	0.002	0.104	100.323
VG568	0.437	0.067	3.443	0.032	77.82	12.243	5.102	1.073	0.028	0.021	0.109	100.35
V2-01	0.639	0.067	3.397	0.068	77.696	12.482	4.25	0.859	0.049	0.003	0.16	99.634
V2-02	4.28	0.017	7.741	0.039	64.445	22.811	0.842	0.148	0	0.016	0.004	100.342
V2-03	0.012	0	0	0.014	101.215	0.117	0.02	0	0	0	0.006	101.383
V2-04	9.355	0.013	5.642	0.006	58.194	27.227	0.316	0.293	0.025	0.003	0.001	101.075
V2-05	7.895	0	6.252	0.022	59.642	25.898	0.308	0.189	0	0.017	0.008	100.229
V2-06	0.737	0.05	3.26	0.086	77.627	12.332	4.196	0.891	0.07	0	0.183	99.391
V2-07	6.527	0	6.781	0.021	61.047	24.423	0.472	0.243	0.022	0.015	0.005	99.555
V2-08	0.839	0.149	3.598	0.082	78.89	12.566	3.267	1.039	0.054	0.024	0.152	100.626
V2-09	0.611	0.088	3.022	0.082	78.426	12.075	4.57	0.802	0.039	0.01	0.163	99.851
V2-10	0.873	0.128	3.501	0.108	78.595	12.629	3.45	1.029	0.061	0	0.128	100.473
V2-11	0.754	0.081	3.332	0.084	76.07	12.332	3.849	0.946	0.085	0.021	0.17	97.686
V2-12	0.771	0.071	3.158	0.06	76.212	12.098	4.042	0.988	0.036	0.016	0.164	97.579
V2-13	5.767	0.007	7.46	0.012	62.924	24.229	0.587	0.195	0.011	0	0	101.192
V2-14	8.452	0	6.051	0.022	59.334	26.693	0.31	0.318	0	0	0.012	101.189
V2-15	0.63	0.044	3.471	0.058	77.769	12.676	4.427	0.796	0.022	0.009	0.16	100.026

Comment	CaO	TiO_2	Na_2O	MgO	SiO_2	Al_2O_3	K_2O	FeO	MnO	P_2O_5	Cl	Total
V2-16	0.008	0.017	0	0	101.822	0.018	0.007	0	0	0.007	0.003	101.881
V2-17	6.603	0.005	6.598	0.005	61.582	25.056	0.609	0.233	0	0.022	0.002	100.715
V2-18	7.101	0.01	6.574	0.009	60.474	24.918	0.464	0.293	0	0	0	99.843
V2-19	8.496	0.008	5.765	0.028	59.597	26.25	0.369	0.284	0.005	0	0	100.802
V2-20	7.946	0.004	6.112	0.016	61.036	26.098	0.391	0.281	0	0	0	101.884
ATHO	1.728	0.243	4.282	0.091	76.695	12.372	2.722	3.242	0.114	0.002	0.043	101.524
ATHO	1.736	0.227	3.888	0.103	76.557	12.426	2.716	3.35	0.118	0	0.051	101.16
VG568	0.424	0.074	3.378	0.031	78.305	12.174	5.01	0.995	0	0.003	0.108	100.478
VG568	0.441	0.074	3.347	0.034	77.791	12.06	4.805	1.005	0.009	0	0.113	99.653
V3-01	0.722	0.072	3.587	0.071	78.892	12.476	3.823	0.914	0.082	0.003	0.162	100.767
V3-02	0.689	0.084	3.522	0.121	78.698	12.448	3.74	0.882	0.068	0.003	0.177	100.392
V3-03	9.196	0.031	5.8	0.021	58.212	26.867	0.29	0.233	0	0.034	0	100.684
V3-04	1.281	0.177	3.773	0.174	76.797	13.173	3.01	1.96	0.089	0.042	0.14	100.584
V3-05	6.77	0.002	6.836	0	60.993	24.827	0.402	0.192	0.033	0	0.002	100.057
V3-06	0.688	0.088	3.535	0.084	78.444	12.378	3.74	0.875	0.057	0	0.137	99.995
V3-07	0.698	0.127	3.592	0.095	78.6	12.499	3.831	0.98	0.009	0.005	0.158	100.558
V3-08	0.79	0.093	3.669	0.09	78.919	12.691	3.503	0.916	0.036	0	0.149	100.822
V3-09	0.019	0	0.003	0	0.05	0.259	0	0.042	0.022	0	1.187	1.314
V3-10	0.011	0	0.01	0	0.03	0.164	0.005	0	0	0	1.397	1.302
V3-11	1.332	0.17	3.837	0.177	76.638	13.21	3.056	1.736	0.098	0.05	0.135	100.409
V3-12	0.84	0.109	3.707	0.121	78.195	12.509	3.348	0.92	0.087	0.047	0.152	100.001
V3-13	5.811	0	7.166	0.003	61.973	24.273	0.477	0.132	0.025	0.038	0.004	99.901
V3-14	0.741	0.098	3.545	0.135	77.627	12.466	3.351	0.894	0.046	0.009	0.159	99.035
V3-15	0.632	0.097	3.273	0.089	78.229	12.415	3.918	0.9	0.058	0	0.162	99.736

Comment	CaO	TiO_2	Na_2O	MgO	SiO_2	Al_2O_3	K_2O	FeO	MnO	P_2O_5	Cl	Total
V3-16	0.688	0.093	3.51	0.11	78.886	12.63	3.953	1.026	0.054	0.007	0.156	101.078
V3-17	1.238	0.188	3.664	0.174	76.496	13.071	3.011	1.798	0.052	0.052	0.156	99.865
V3-18	0.805	0.095	3.55	0.127	76.965	12.273	3.344	0.972	0.059	0	0.16	98.314
V3-19	0.799	0.129	3.637	0.121	78.732	12.599	3.459	0.963	0.041	0.012	0.165	100.62
V3-20	0.324	0.034	0.913	0.029	21.752	4.853	1.252	0.447	0.038	0.014	0.622	30.138
ATHO	1.785	0.232	3.764	0.091	76.888	12.542	2.603	3.49	0.119	0.019	0.032	101.558
ATHO	1.734	0.24	3.889	0.076	76.853	12.369	2.746	3.286	0.107	0.007	0.033	101.333
VG568	0.446	0.074	3.394	0.039	77.583	12.269	5.075	1.032	0.031	0	0.111	100.029
VG568	0.441	0.069	3.288	0.035	77.494	12.243	5.079	1.022	0.028	0	0.089	99.768
V4-01	0.767	0.103	3.313	0.079	78.125	12.539	3.221	0.982	0.053	0.016	0.15	99.314
V4-02	0.813	0.12	3.771	0.105	78.295	12.692	3.4	0.893	0.044	0.023	0.16	100.28
V4-03	0.681	0.107	3.716	0.114	78.423	12.501	3.841	0.88	0.039	0	0.15	100.418
V4-04	0.717	0.1	3.547	0.102	78.681	12.505	3.706	0.848	0.076	0	0.156	100.403
V4-05	0.879	0.108	3.449	0.161	77.379	12.335	3.377	0.981	0.042	0.016	0.149	98.842
V4-06	0.744	0.091	3.448	0.11	77.958	12.597	3.615	0.804	0.069	0.002	0.132	99.54
V4-07	0.768	0.096	3.739	0.094	78.982	12.617	3.431	0.845	0.059	0	0.164	100.758
V4-08	0.762	0.108	3.65	0.123	77.466	12.404	3.479	0.896	0.048	0.014	0.158	99.072
V4-09	0.612	0.076	3.446	0.083	78.399	12.499	3.884	0.855	0.039	0.007	0.151	100.017
V4-10	0.797	0.094	3.572	0.145	78.282	12.575	3.429	0.972	0.095	0.003	0.146	100.077
V4-11	0.754	0.111	3.656	0.115	78.685	12.605	3.74	0.978	0.049	0.023	0.158	100.838
V4-12	0.761	0.105	3.636	0.096	77.728	12.386	3.346	0.88	0.076	0.009	0.166	99.152
V4-13	0.777	0.099	3.579	0.103	78.24	12.48	3.124	0.927	0.065	0.007	0.139	99.509
V4-14	0.635	0.04	3.225	0.065	77.324	12.383	4.433	0.835	0.043	0	0.156	99.104
V4-15	0.8	0.144	3.471	0.126	78.472	12.34	3.443	1.031	0.055	0.016	0.135	100.003

Comment	CaO	TiO_2	Na_2O	MgO	SiO_2	Al_2O_3	K_2O	FeO	MnO	P_2O_5	Cl	Total
V4-16	1.381	0.179	3.655	0.147	76.418	12.941	3.082	1.683	0.07	0.023	0.163	99.705
V4-17	0.72	0.104	3.703	0.125	78.439	12.404	3.534	0.962	0.052	0.016	0.153	100.177
V4-18	0.665	0.107	3.417	0.081	76.591	12.206	3.472	0.886	0.044	0	0.17	97.601
V4-19	0.713	0.061	3.612	0.094	78.267	12.62	4.113	0.94	0.069	0	0.175	100.625
V4-20	0.674	0.106	3.578	0.105	78.786	12.533	3.941	0.927	0.05	0.019	0.159	100.842
ATHO	1.74	0.222	3.835	0.108	76.488	12.155	2.781	3.418	0.116	0.022	0.05	100.924
ATHO	1.747	0.237	3.872	0.102	77.013	12.403	2.822	3.547	0.116	0.029	0.044	101.922
VG568	0.435	0.048	3.337	0.045	77.701	12.268	5.155	1.103	0.016	0.021	0.107	100.212
VG568	0.423	0.077	3.366	0.027	77.793	12.113	5.1	1.034	0.012	0	0.093	100.017
V5-01	0.735	0.1	3.505	0.085	78.702	12.545	3.831	1.034	0.049	0.021	0.163	100.733
V5-02	0.978	0.167	2.764	0.146	73.31	11.58	3.338	1.081	0.031	0.019	0.115	93.503
V5-03	0.788	0.091	3.856	0.107	78.482	12.585	3.392	0.933	0.071	0.007	0.175	100.448
V5-04	0.747	0.12	3.382	0.091	76.586	12.097	3.659	0.902	0.064	0.007	0.145	97.767
V5-05	0.637	0.038	3.378	0.057	76.318	12.234	4.332	0.883	0.059	0	0.155	98.056
V5-06	6.484	0.006	6.919	0.015	61.636	24.894	0.408	0.201	0.007	0	0.005	100.574
V5-07	0.784	0.098	3.65	0.119	78.777	12.602	3.481	0.873	0.053	0.038	0.155	100.595
V5-08	1.026	0.129	3.723	0.111	76.209	12.476	3.037	1.676	0.108	0.017	0.159	98.635
V5-09	0.818	0.105	3.686	0.083	78.367	12.47	3.285	0.864	0.028	0.031	0.147	99.851
V5-10	0.996	0.148	3.344	0.147	74.578	12.139	3.182	1.402	0.072	0.035	0.136	96.148
V5-11	0.805	0.107	3.587	0.113	78.908	12.468	3.477	0.918	0.064	0.012	0.144	100.571
V5-12	1.479	0.164	3.666	0.2	76.519	13.357	3.051	1.852	0.08	0.023	0.127	100.489
V5-13	0.787	0.103	3.625	0.107	78.505	12.49	3.369	0.924	0.065	0.026	0.167	100.13
V5-14	1.003	0.161	3.57	0.138	76.532	12.624	3.059	1.57	0.069	0.024	0.162	98.875
V5-15	0.635	0.097	3.559	0.079	78.499	12.394	3.842	0.921	0.063	0.028	0.164	100.244

Comment	CaO	TiO_2	Na_2O	MgO	SiO_2	Al_2O_3	K_2O	FeO	MnO	P_2O_5	Cl	Total
V5-16	0.838	0.102	3.634	0.091	77.956	12.423	3.262	0.893	0.039	0.007	0.162	99.37
V5-17	8.725	0	5.632	0.012	59.072	26.419	0.28	0.224	0	0	0	100.364
V5-18	0.837	0.116	3.513	0.127	77.458	12.307	3.419	0.988	0.048	0.009	0.131	98.923
V5-19	0.697	0.099	3.727	0.105	78.253	12.454	3.752	0.972	0.034	0	0.157	100.215
V5-20	1.481	0.186	3.643	0.164	75.149	12.997	3.04	1.731	0.071	0.036	0.134	98.602
ATHO	1.759	0.232	3.825	0.115	76.845	12.353	2.752	3.234	0.109	0.016	0.04	101.271
ATHO	1.788	0.233	3.754	0.096	76.798	12.348	2.609	3.472	0.142	0.036	0.043	101.309
VG568	0.418	0.05	3.328	0.037	78.305	12.248	4.82	1.205	0.014	0.014	0.102	100.518
VG568	0.423	0.052	3.591	0.037	77.92	12.128	5.007	1.104	0.014	0.005	0.09	100.351
V6-01	6.46	0.008	6.998	0.016	61.499	24.557	0.466	0.195	0.037	0	0	100.236
V6-02	6.348	0.012	6.916	0.024	61.988	24.519	0.471	0.199	0	0.003	0.001	100.481
V6-03	10.251	0.01	5.229	0.032	56.98	27.888	0.175	0.302	0.022	0	0	100.889
V6-04	7.003	0	6.689	0.014	61.168	25.147	0.349	0.261	0.017	0.012	0.009	100.667
V6-05	9.196	0.006	5.468	0.013	58.335	26.623	0.326	0.334	0	0	0	100.301
V6-06	0	0	0.007	0	102.174	0.046	0.005	0	0.006	0.005	0.002	102.245
V6-07	0	0.015	0	0.016	101.535	0.049	0	0.003	0.014	0.009	0.003	101.643
V6-08	0.006	0	0.008	0	101.682	0.042	0	0.019	0.001	0	0	101.758
V6-09	8.085	0	6.008	0.017	59.347	26.018	0.356	0.252	0.034	0.015	0.009	100.139
V6-10	6.608	0	6.909	0.001	61.601	24.684	0.394	0.183	0.039	0.003	0	100.422
V6-11	0.014	0	0.015	0	101.606	0.024	0	0	0.022	0	0.008	101.687
V6-12	7.332	0	6.574	0.006	60.746	25.345	0.417	0.268	0.005	0.021	0	100.714
V6-13	5.791	0	7.216	0	62.826	24.04	0.614	0.145	0	0	0	100.632
V6-14	5.295	0	7.484	0	63.175	23.746	0.58	0.221	0	0.009	0	100.51
V6-15	0.017	0	0.002	0	101.822	0.025	0.013	0	0.007	0.004	0	101.89

Comment	CaO	TiO_2	Na_2O	MgO	SiO_2	Al_2O_3	K_2O	FeO	MnO	P_2O_5	Cl	Total
V6-16	8.203	0	6.039	0	59.669	26.128	0.356	0.29	0.012	0.027	0	100.724
V6-17	9.034	0.004	5.631	0.023	58.42	26.844	0.292	0.341	0.037	0	0.007	100.631
V6-18	6.166	0.004	6.889	0.001	62.031	24.63	0.451	0.164	0	0	0	100.336
V6-19	7.274	0.011	6.558	0	60.604	25.255	0.363	0.177	0.01	0.034	0	100.286
V6-20	9.095	0	5.617	0.022	58.32	26.753	0.211	0.243	0.005	0.015	0.004	100.284
ATHO	1.768	0.268	3.823	0.093	77.452	12.572	2.704	3.456	0.091	0.014	0.044	102.275
ATHO	1.736	0.247	4.395	0.129	76.484	12.405	2.702	3.396	0.098	0.009	0.045	101.636
VG568	0.416	0.061	3.374	0.022	77.952	12.27	5.072	1.061	0.032	0.026	0.105	100.367
VG568	0.445	0.071	3.346	0.027	78.265	12.119	5.071	1.171	0.028	0.003	0.106	100.628
V7-01	7.576	0	6.202	0.031	59.975	25.404	0.313	0.23	0.006	0.005	0.008	99.748
V7-02	6.013	0.011	7.146	0	61.991	24.463	0.56	0.148	0	0	0.002	100.334
V7-03	5.544	0	7.106	0.005	62.789	24.142	0.635	0.189	0.004	0	0	100.414
V7-04	0.005	0.007	0.022	0.001	102.055	0.047	0.018	0.003	0	0.004	0	102.162
V7-05	0.658	0.059	3.333	0.071	77.951	12.585	4.3	0.909	0.086	0	0.159	100.075
V7-06	0.631	0.068	3.492	0.033	77.938	12.53	4.279	0.893	0.064	0.002	0.161	100.055
V7-07	0.002	0.003	0	0	101.251	0.082	0	0.013	0.007	0.038	0	101.396
V7-08	0.021	0.01	0.067	0.018	100.608	0.371	0.074	0.041	0.014	0	0	101.224
V7-09	0.622	0.066	3.26	0.045	78.036	12.132	4.37	0.84	0.076	0.01	0.159	99.58
V7-10	0.008	0.02	0	0	101.941	0.035	0.021	0.105	0	0	0.002	102.132
V7-11	1.273	0.224	3.41	0.221	77.679	12.916	3.088	1.202	0.038	0.045	0.105	100.177
V7-12	0.873	0.144	3.588	0.147	78.763	12.467	3.439	0.985	0.022	0	0.117	100.519
V7-13	0.757	0.07	3.097	0.103	76.965	12.278	4.354	0.896	0.053	0.014	0.167	98.716
V7-14	0.608	0.06	3.5	0.061	77.685	12.533	4.461	0.82	0.071	0.038	0.161	99.962
V7-15	0.756	0.074	3.097	0.071	75.159	12.214	4.063	0.944	0.065	0	0.166	96.572

Comment	CaO	TiO_2	Na_2O	MgO	SiO_2	Al_2O_3	K_2O	FeO	MnO	P_2O_5	Cl	Total
V7-16	0.07	0	0.047	0.01	99.969	0.861	0.065	0.003	0.042	0	0	101.067
V7-17	1.373	0.217	3.659	0.248	77.884	13.002	3.02	1.436	0.05	0	0.171	101.021
V7-18	0	0.006	0	0.008	102.175	0.031	0.002	0.006	0	0	0.006	102.233
V7-19	0.608	0.073	3.277	0.055	75.241	12.143	4.152	0.799	0.063	0	0.149	96.526
V7-20	1.441	0.226	3.645	0.259	77.16	12.838	3.026	1.36	0.037	0.014	0.137	100.112
ATHO	1.797	0.242	3.86	0.097	76.746	12.421	2.597	3.441	0.087	0.01	0.035	101.325
ATHO	1.747	0.249	3.57	0.093	76.719	12.286	2.72	3.391	0.088	0.043	0.048	100.943
VG568	0.428	0.099	3.291	0.031	78.399	12.224	5.008	1.064	0.022	0.023	0.092	100.66
VG568	0.447	0.073	3.399	0.016	78.462	12.295	5.005	1.309	0.034	0	0.091	101.11
VI1-01	0.714	0.111	0.003	0.001	0.005	0	0	0.003	0.082	0.014	0.126	1.031
VI1-02	0.755	0.095	0.02	0.003	0.003	0	0	0.012	0.079	0.005	0.133	1.075
VI1-03	0.629	0.11	2.75	0.101	0	0	0.001	0	0.025	0.005	0.141	3.73
VI1-04	0.776	0.102	3.762	0.126	29.401	5.022	3.386	0.877	0.04	0	0.177	43.629
VI1-05	1.223	0.194	3.746	0.165	76.671	13.03	3.128	1.675	0.07	0	0.138	100.009
VI1-06	0.817	0.122	3.408	0.107	78.312	12.675	3.3	0.991	0.047	0.021	0.156	99.921
VI1-07	0.747	0.053	3.196	0.054	76.01	12.26	4.052	1.026	0.053	0	0.184	97.593
VI1-08	0.888	0.1	3.694	0.131	79.124	12.823	3.304	0.893	0.029	0.016	0.147	101.116
VI1-09	1.408	0.224	3.713	0.239	77.83	13.1	3.026	1.381	0.074	0.023	0.13	101.119
VI1-10	11.372	0	4.418	0.052	55.701	28.782	0.177	0.441	0.009	0	0.006	100.957
VI1-11	0.622	0.044	3.506	0.05	78.805	12.658	4.317	0.928	0.095	0.031	0.154	101.175
VI1-12	1.159	0.115	3.311	0.124	74.928	12.356	3.017	1.505	0.055	0	0.158	96.692
VI1-13	0.927	0.137	3.585	0.156	78.938	12.553	3.311	1.089	0.044	0.003	0.137	100.849
VI1-14	0.722	0.079	3.586	0.103	77.718	12.391	3.673	1.035	0.058	0.01	0.169	99.506
VI1-15	0.967	0.156	3.394	0.201	78.771	12.635	3.435	1.278	0.059	0.023	0.124	101.015

Comment	CaO	TiO_2	Na_2O	MgO	SiO_2	Al_2O_3	K_2O	FeO	MnO	P_2O_5	Cl	Total
VI1-16	1.284	0.194	3.65	0.17	77.443	13.361	2.943	1.833	0.09	0.024	0.12	101.085
VI1-17	1.231	0.192	3.666	0.164	76.219	12.946	3.074	1.621	0.085	0.028	0.137	99.332
VI1-18	14.094	0.028	3.179	0.08	52.766	30.924	0.098	0.681	0.02	0	0	101.87
VI1-19	0.012	0	0	0	102.294	0.028	0	0	0	0.004	0	102.338
VI1-20	0.849	0.111	3.604	0.127	78.225	12.511	3.283	0.982	0.059	0.014	0.147	99.879
ATHO	1.646	0.258	4.297	0.09	76.252	12.221	2.423	3.326	0.121	0.002	0.048	100.673
ATHO	1.729	0.234	4.085	0.111	76.885	12.395	2.722	3.276	0.094	0.021	0.035	101.579
VG568	0.42	0.086	3.242	0.011	77.702	12.203	5.009	1.073	0.031	0.005	0.097	99.857
VG568	0.425	0.064	3.389	0	77.632	12.186	5.061	1.108	0.038	0	0.09	99.973
VI7-01	0.968	0.107	3.258	0.083	75.319	11.987	2.969	1.026	0.006	0	0.197	95.876
VI7-02	0.62	0.054	3.181	0.072	76.37	12.257	4.344	0.745	0.071	0.009	0.157	97.845
VI7-03	0.992	0.098	3.109	0.099	74.218	11.675	2.795	1.206	0.059	0.005	0.176	94.392
VI7-04	1.125	0.124	3.285	0.15	76.011	12.176	3.232	1.244	0.015	0.016	0.206	97.538
VI7-05	1.142	0.11	3.56	0.129	77.943	12.432	3.102	1.319	0.057	0.016	0.163	99.936
VI7-06	0.927	0.118	2.537	0.128	74.587	11.842	4.283	1.086	0.023	0.012	0.151	95.66
VI7-07	0.97	0.089	3.259	0.096	74.601	12.015	2.919	1.08	0.06	0.005	0.2	95.249
VI7-08	0.971	0.098	3.385	0.125	75.644	11.999	3.178	1.187	0.016	0.023	0.201	96.782
VI7-09	0.968	0.103	3.299	0.121	74.959	12.022	3.135	1.19	0.042	0	0.174	95.974
VI7-10	1.087	0.112	3.265	0.122	74.603	12.103	2.735	1.212	0.018	0.023	0.181	95.42
VI7-11	0.886	0.097	3.192	0.101	74.195	11.934	3.09	1.224	0.029	0.005	0.189	94.899
VI7-12	0.959	0.087	3.221	0.117	74.928	12.169	3.107	1.18	0.033	0.017	0.193	95.967
VI7-13	0.973	0.09	3.16	0.115	74.747	11.715	2.883	1.218	0.006	0	0.197	95.06
VI7-14	1.096	0.121	3.099	0.126	73.848	12.03	2.742	1.151	0.031	0.017	0.17	94.393
VI7-15	0.987	0.082	2.528	0.15	73.631	11.676	3.633	0.946	0.025	0.026	0.186	93.828

Comment	CaO	TiO_2	Na_2O	MgO	SiO_2	Al_2O_3	K_2O	FeO	MnO	P_2O_5	Cl	Total
VI7-16	0.918	0.155	3.307	0.13	74.681	12.062	3.55	1.377	0.028	0	0.177	96.345
VI7-17	1.103	0.12	3.233	0.149	75.515	12.139	3.152	1.195	0.028	0.002	0.201	96.792
VI7-18	1.06	0.105	3.249	0.121	74.204	12.017	2.815	1.226	0.034	0.014	0.174	94.98
VI7-19	0.852	0.126	1.931	0.12	74.285	11.765	4.41	1.148	0.032	0.019	0.175	94.824
VI7-20	0.999	0.111	3.156	0.107	74.598	11.719	3.063	1.154	0.015	0.024	0.176	95.082
ATHO	1.723	0.226	4.304	0.086	76.559	12.393	2.722	3.463	0.081	0.04	0.044	101.631
ATHO	1.734	0.236	3.783	0.088	76.349	12.31	2.75	3.453	0.111	0	0.044	100.848
VG568	0.461	0.083	3.482	0.025	77.41	12.163	5.108	1.113	0.058	0.026	0.109	100.013
VG568	0.445	0.072	3.309	0.014	77.684	12.259	5.092	1.182	0	0	0.098	100.133
VI2-01	0.974	0.115	3.13	0.115	74.262	11.882	0.003	0	0.068	0.025	0.182	90.715
VI2-02	0.838	0.127	2.997	0.236	0.008	0	0	0.006	0.004	0	0	4.216
VI2-03	0.887	0.144	3.509	0.141	78.73	12.436	3.267	0.984	0.033	0.012	0.15	100.259
VI2-04	0.779	0.126	3.735	0.124	77.08	12.291	3.365	0.952	0.082	0.002	0.144	98.648
VI2-05	0.696	0.057	3.307	0.053	77.73	12.564	2.633	0.473	0.053	0	0.152	97.684
VI2-06	0.01	0	0	0.007	101.71	0.053	0	0	0	0	0	101.78
VI2-07	0.845	0.126	3.564	0.108	78.52	12.33	3.473	1.033	0.081	0.024	0.158	100.226
VI2-08	0.896	0.123	3.721	0.153	73.307	11.888	0	0	0.001	0	0	90.089
VI2-09	0.858	0.138	3.491	0.12	78.355	12.246	0	0.022	0.037	0.014	0.107	95.364
VI2-10	0.003	0.014	0.005	0	101.404	0.037	0.009	0	0	0	0.008	101.478
VI2-11	0.004	0	0	0	0.038	0.502	0.009	0	0	0.004	0.92	1.269
VI2-12	0.62	0.047	3.292	0.059	76.532	12.284	4.299	0.769	0.031	0.017	0.152	98.068
VI2-13	12.734	0.026	3.619	0.062	53.936	29.468	0.215	0.563	0.037	0.032	0	100.692
VI2-14	0.785	0.082	3.517	0.141	77.991	12.554	3.381	0.996	0.069	0.003	0.161	99.644
VI2-15	0.871	0.109	3.382	0.113	76.273	12.204	3.159	0.996	0.028	0	0.147	97.249

Comment	CaO	TiO_2	Na_2O	MgO	SiO_2	Al_2O_3	K_2O	FeO	MnO	P_2O_5	Cl	Total
VI2-16	0.775	0.067	3.325	0.1	78.122	12.535	4.269	0.926	0.076	0.003	0.152	100.316
VI2-17	0.882	0.153	3.447	0.121	76.931	12.266	3.189	0.898	0.025	0	0.141	98.021
VI2-18	0.94	0.135	3.456	0.124	78.083	12.523	3.312	0.848	0.034	0.014	0.125	99.566
VI2-19	0.732	0.076	3.41	0.078	78.197	12.514	4.095	1.03	0.021	0.026	0.192	100.328
VI2-20	0.723	0.104	3.483	0.097	77.898	12.396	3.697	0.958	0.064	0.024	0.152	99.562
ATHO	1.723	0.217	3.79	0.08	75.979	12.137	2.744	3.261	0.127	0.002	0.03	100.083
ATHO	1.691	0.218	3.754	0.11	76.189	12.139	2.792	3.308	0.108	0.014	0.039	100.353
VG568	0.431	0.079	3.49	0.015	77.211	12.04	4.976	1.014	0.017	0.026	0.094	99.372
VG568	0.431	0.046	3.315	0.03	77.33	12.184	4.958	1.059	0.055	0.002	0.088	99.478
VI3-01	0.897	0.073	3.35	0.098	75.83	12.116	3.604	1.125	0.014	0.014	0.182	97.262
VI3-02	0.817	0.074	3.296	0.076	75.894	12.027	3.696	0.996	0.039	0.038	0.198	97.106
VI3-03	0.726	0.077	3.339	0.07	75.928	11.961	3.752	1.207	0.058	0	0.164	97.245
VI3-04	0.836	0.062	3.061	0.103	74.85	11.987	3.894	1.055	0.037	0	0.188	96.031
VI3-05	0.832	0.093	3.124	0.078	76.122	12.327	3.584	0.971	0.023	0.036	0.196	97.342
VI3-06	0.75	0.096	2.65	0.108	75.84	11.731	4.698	0.993	0.052	0.029	0.233	97.127
VI3-07	0.665	0.084	1.844	0.048	73.647	11.62	4.752	1.251	0.036	0.021	0.221	94.139
VI3-08	0.82	0.066	3.181	0.086	74.466	11.94	3.545	1.071	0.029	0.012	0.185	95.359
VI3-09	0.85	0.07	3.183	0.099	76.042	12.113	3.61	0.986	0.049	0.04	0.184	97.184
VI3-10	0.847	0.073	3.103	0.087	75.747	12.06	3.75	1.011	0.017	0.029	0.194	96.874
VI3-11	0.916	0.065	3.177	0.096	75.96	12.381	3.72	0.977	0.026	0.017	0.202	97.491
VI3-12	0.89	0.097	3.367	0.103	75.509	12.245	3.711	1.087	0.04	0.017	0.197	97.219
VI3-13	0.78	0.085	3.266	0.071	74.393	12.045	3.688	0.986	0.013	0.038	0.172	95.498
VI3-14	0.772	0.091	3.406	0.05	75.573	11.867	3.837	0.948	0.028	0	0.126	96.67
VI3-15	0.869	0.097	3.091	0.082	75.532	12.155	3.593	1.121	0.063	0.033	0.188	96.782

Comment	CaO	TiO_2	Na_2O	MgO	SiO_2	Al_2O_3	K_2O	FeO	MnO	P_2O_5	Cl	Total
VI3-16	0.902	0.11	3.207	0.083	75.859	12.092	3.851	0.766	0.027	0.002	0.149	97.014
VI3-17	0.882	0.066	3.234	0.066	75.781	11.968	3.835	1.021	0.043	0.024	0.181	97.06
VI3-18	0.77	0.084	2.848	0.065	75.03	12.211	4.276	0.961	0.002	0	0.162	96.372
VI3-19	0.688	0.101	3.047	0.067	75.212	11.985	3.872	1.055	0.025	0.012	0.148	96.179
VI3-20	0.868	0.107	3.268	0.064	75.111	11.987	3.645	1.411	0.039	0.01	0.169	96.641
ATHO	1.741	0.224	3.857	0.092	76.181	12.245	2.831	3.279	0.111	0.021	0.033	100.608
ATHO	1.684	0.258	3.605	0.105	76.378	12.234	2.799	3.381	0.16	0.017	0.053	100.662
VG568	0.446	0.07	3.354	0.041	76.907	12.12	4.916	0.98	0.052	0	0.094	98.959
VG568	0.424	0.098	3.367	0.007	77.607	12.226	4.89	1.162	0.027	0.026	0.099	99.911
VI4-01	0.823	0.118	2.974	0.111	74.216	11.875	3.969	0.964	0.05	0.005	0.16	95.229
VI4-02	8.282	0	5.798	0.02	58.906	25.867	0.326	0.255	0	0	0	99.454
VI4-03	6.13	0	6.802	0.016	61.943	24.107	0.707	0.192	0	0	0.005	99.901
VI4-04	9.513	0	5.355	0.037	57.182	27.038	0.268	0.302	0.048	0	0	99.743
VI4-05	0.925	0.083	2.983	0.06	75.895	12.208	3.676	0.873	0.033	0	0.198	96.889
VI4-06	0.013	0.002	0	0.009	100.876	0.071	0	0	0.012	0.021	0.012	101.013
VI4-07	0.82	0.088	3.298	0.057	75.926	12.039	3.69	1.002	0.037	0.003	0.189	97.106
VI4-08	0	0.007	0.002	0.006	101.127	0.038	0	0.048	0.017	0	0	101.245
VI4-09	0.819	0.069	3.12	0.101	75.761	11.999	3.662	1.087	0.031	0.012	0.188	96.807
VI4-10	0.873	0.068	3.195	0.096	75.911	12.08	3.675	1.011	0.031	0	0.199	97.094
VI4-11	0.01	0	0.016	0	101.367	0.033	0	0.041	0	0	0.014	101.478
VI4-12	7.225	0.007	6.442	0.018	60.479	24.962	0.599	0.236	0	0.003	0.009	99.978
VI4-13	5.146	0	7.403	0	62.773	23.603	0.849	0.148	0.016	0	0	99.938
VI4-14	9.698	0.013	5.307	0.018	57.248	27.163	0.193	0.315	0.023	0	0	99.978
VI4-15	8.769	0	5.586	0.011	58.282	26.177	0.237	0.189	0.005	0	0.001	99.257

Comment	CaO	TiO_2	Na_2O	MgO	SiO_2	Al_2O_3	K_2O	FeO	MnO	P_2O_5	Cl	Total
VI4-16	0.016	0	0.018	0	0.032	0.208	0.014	0.047	0	0	0.739	0.907
VI4-17	0.78	0.052	3.366	0.076	75.433	12.126	3.642	1.077	0.05	0.04	0.191	96.79
VI4-18	5.234	0.006	7.449	0	62.703	23.378	0.558	0.293	0	0.012	0	99.633
VI4-19	0.781	0.093	3.301	0.069	75.3	12.244	3.629	0.958	0.042	0.003	0.184	96.562
VI4-20	7.652	0	6.108	0.014	59.794	25.584	0.538	0.277	0.007	0.01	0.005	99.988
ATHO	1.718	0.239	3.606	0.109	76.351	12.4	2.77	3.216	0.062	0.04	0.034	100.537
ATHO	1.782	0.237	3.887	0.098	76.724	12.337	2.746	3.228	0.137	0.024	0.045	101.235
VG568	0.466	0.07	3.497	0.027	77.096	12.078	4.993	1.071	0.007	0.003	0.108	99.392
VG568	0.473	0.058	3.313	0.039	77.555	12.134	4.999	1.065	0.021	0	0.113	99.744
VI5-01	0	0	0	0.014	101.414	0.016	0.006	0	0	0	0.007	101.455
VI5-02	10.187	0.016	5.158	0.025	56.556	27.826	0.248	0.409	0.013	0.017	0.004	100.458
VI5-03	0.746	0.066	3.442	0.067	74.553	12.022	3.622	1.018	0.026	0	0.156	95.683
VI5-04	9.828	0.006	5.043	0.026	57.052	27.505	0.22	0.365	0.002	0	0.004	100.05
VI5-05	6.313	0	6.568	0.012	61.458	24.348	0.613	0.132	0	0	0	99.444
VI5-06	8.592	0.015	5.651	0.01	58.615	26.366	0.29	0.289	0	0.007	0	99.835
VI5-07	0.046	0.013	0	0	0.094	0.269	0.004	0	0	0	1.113	1.288
VI5-08	0.879	0.109	3.52	0.064	74.937	12.177	3.752	1.42	0.034	0.005	0.145	97.009
VI5-09	0.703	0.071	3.342	0.075	75.59	11.803	3.745	1.021	0.027	0.01	0.18	96.526
VI5-10	0.891	0.095	3.057	0.099	76.594	12.174	3.667	0.977	0.079	0	0.195	97.784
VI5-11	6.331	0	6.429	0.003	61.499	24.673	0.683	0.151	0	0	0.005	99.773
VI5-12	0.201	0.002	3.014	0	66.378	18.925	11.286	0.069	0	0.008	0.002	99.885
VI5-13	0.896	0.107	3.215	0.062	74.683	12.183	3.572	1.339	0.04	0.007	0.181	96.244
VI5-14	8.605	0	5.643	0.017	58.414	26.213	0.26	0.179	0	0.015	0	99.346
VI5-15	8.585	0	5.769	0.024	58.498	26.06	0.387	0.28	0.033	0.012	0.004	99.651

Comment	CaO	TiO_2	Na_2O	MgO	SiO_2	Al_2O_3	K_2O	FeO	MnO	P_2O_5	Cl	Total
VI5-16	0.888	0.153	3.271	0.103	75.908	12.208	3.786	1.231	0.065	0.042	0.169	97.786
VI5-17	0.844	0.094	3.263	0.062	76.034	12.133	3.706	1.131	0.023	0	0.201	97.446
VI5-18	0.821	0.096	2.931	0.097	75.732	11.973	3.5	0.939	0.07	0.007	0.218	96.335
VI5-19	0.773	0.119	3.395	0.059	75.737	11.817	3.766	1.25	0.037	0.019	0.181	97.112
VI5-20	0.886	0.147	3.409	0.104	75.616	12.072	3.654	1.241	0.036	0	0.154	97.284
ATHO	1.716	0.257	3.716	0.096	76.669	12.384	2.723	3.391	0.062	0.024	0.043	101.071
ATHO	1.759	0.242	3.844	0.109	76.115	12.313	2.702	3.335	0.116	0.002	0.033	100.563
VG568	0.446	0.079	3.369	0.014	77.505	12.061	4.966	1.049	0.025	0.005	0.089	99.588
VG568	0.465	0.054	3.362	0.02	77.405	12.057	4.966	1.131	0.055	0	0.115	99.604
VI6-01	6.352	0.012	6.756	0.005	61.599	24.601	0.49	0.189	0	0.007	0	100.011
VI6-02	5.405	0.003	7.41	0.01	63.072	23.645	0.56	0.223	0	0.005	0.003	100.335
VI6-03	0.883	0.07	3.004	0.068	76.259	12.154	3.703	1.071	0.081	0	0.196	97.445
VI6-04	0.008	0	0.019	0	0.167	0.418	0.005	0.015	0	0	0.972	1.385
VI6-05	5.812	0.001	6.916	0	62.309	24.271	0.554	0.23	0	0.017	0.009	100.117
VI6-06	0.819	0.065	3.071	0.098	74.59	12.069	3.723	1.147	0.032	0.007	0.164	95.748
VI6-07	0.867	0.086	3.239	0.095	76.153	12.191	3.657	1.1	0.049	0.023	0.192	97.609
VI6-08	0.772	0.086	3.126	0.073	74.921	12.024	3.39	0.993	0.047	0.005	0.194	95.587
VI6-09	8.021	0.017	6.183	0.025	59.473	25.792	0.357	0.245	0.021	0.015	0	100.149
VI6-10	0.835	0.07	3.299	0.108	76.012	12.296	3.689	1.024	0.021	0.014	0.184	97.51
VI6-11	0.855	0.087	3.259	0.084	76.002	12.198	3.756	0.942	0.076	0.012	0.166	97.4
VI6-12	0.965	0.068	3.181	0.112	75.628	12.002	3.64	1.008	0.059	0	0.186	96.807
VI6-13	0.682	0.074	3.204	0.045	75.377	11.834	3.653	1.166	0.016	0	0.186	96.195
VI6-14	0.88	0.06	3.379	0.086	75.813	12.13	3.677	1.14	0.036	0	0.196	97.353
VI6-15	0.757	0.087	2.882	0.078	74.991	11.883	4.373	0.977	0.032	0.007	0.18	96.206

Comment	CaO	TiO_2	Na_2O	MgO	SiO_2	Al_2O_3	K_2O	FeO	MnO	P_2O_5	Cl	Total
VI6-16	0.823	0.083	3.257	0.078	75.914	12.364	3.674	0.917	0.026	0.014	0.182	97.291
VI6-17	0.877	0.091	3.342	0.089	75.974	12.211	3.632	1.03	0.052	0.012	0.193	97.459
VI6-18	0.791	0.079	3.091	0.076	74.564	12.145	3.91	0.955	0.023	0.038	0.192	95.821
VI6-19	0.723	0.051	3.028	0.089	67.819	12.074	3.293	0.879	0.038	0.002	0.235	88.178
VI6-20	0.746	0.094	3.392	0.071	75.66	11.802	3.581	1.04	0.043	0	0.144	96.541
ATHO	1.741	0.248	3.717	0.119	77.075	12.389	2.776	3.292	0.096	0.029	0.047	101.518
ATHO	1.669	0.23	3.717	0.092	76.387	12.415	2.835	3.207	0.092	0.003	0.034	100.673
VG568	0.432	0.064	3.297	0.041	77.6	12.15	5.07	1.071	0	0	0.118	99.816
VG568	0.442	0.077	3.36	0.022	77.377	12.063	4.89	1.169	0	0	0.09	99.47

2.7: Adjustment to data and resulting plots

As noted in Chapter 5, the EPMA data appear to have been affected by losses of some elements and excesses of others. Using the Rotorua Tephra correlation as a basis for the discrepancies, a table has been constructed for adjustment of the normalised data to have more straightforward correlation plots. The plots from adjusted data have not been presented in the main body of the study as they are based on the assumption that all data collected suffers from the same discrepancies in the same amounts. Given that the data collected for the standards did not exhibit the same issue, the discrepancy may be an indicator of problems with the block preparation or attributable to natural compositional variations. In an effort to keep the elements balanced, Al_2O_3 was not adjusted as much as it could be.

Element (Oxide)	Discrepancy (wt. %)	Adjustment Made (wt. %)
SiO_2	+0.6	-0.6
CaO	+0.05	-0.05
TiO_2	-0.08	+0.08
Na_2O	-0.6	+0.6
MgO	N/A	N/A
Al_2O_3	+0.2	-0.03
K_2O	N/A	N/A
FeOt	N/A	N/A
MnO	N/A	N/A
Cl	N/A	N/A

Appendix 3: Fault rupture data

3.1: Displacement values for NE wall of the Meade-Hossack trench

The displacement values for the NE wall were estimated from the trench logs using a measured grid, and carry an uncertainty of ±0.1 m. The displacement of the Ohakuri Ignimbrite across the rest of the Whirinaki Fault (112 ± 32 m) has been excluded.

Approx. age range (ka)	Displacement (mm)	Cumulative displacement (mm)
240-21.8	1950	4080
21.8-15.6	800	2130
15.6-9.4	0	1330
9.4-1.8	0	1330
1.8-0.63	1330	1330

3.2: Values used for calculation of slip rates

Event	Min. displacement (mm)	Max. displacement (mm)	Mean displacement (mm)	Error displacement (± mm)	Age (cal yr. BP)	Error age (± cal yr. BP)
MH1	550	1330	940	551.54	636	12
MH2	750	950	850	141.42	1718	5
MH3	1100	1300	1200	141.42	9423	120
MH4	700	900	800	141.42	15635	412
MH5	81530	146050	113790	45622.53	21858	290

Event	Min. ΔT (yr)	Max. ΔT (yr)	Mean ΔT (yr)	Error ΔT (yr)	Min. slip rate (mm/yr)	Max. slip rate (mm/yr)	Mean slip rate (mm/yr)	Error slip rate (± mm/yr)
MH1	1065	1099	1082	24.04	0.50	1.25	0.87	0.37
MH2	7580	7830	7705	176.78	0.10	0.13	0.11	0.20
MH3	5680	6744	6212	752.36	0.16	0.23	0.20	0.22
MH4	5521	6925	6223	992.78	0.10	0.16	0.13	0.27
MH5	207852	228432	218142	14552.26	0.36	0.70	0.53	0.24